UNIVERSITY OF OKLAHOMA

GRADUATE COLLEGE

ANALYSIS OF THE FORMATION OF SOLID AND HOLLOW FIBERS IN THE MELT BLOWING PROCESS: EXPERIMENTS AND MODELING

A Dissertation

SUBMITTED TO THE GRADUATE FACULTY

in partial fulfillment of the requirements for the

degree of

Doctor of Philosophy

By

Vishnu Tej Marla
Norman, Oklahoma
2005

UMI Number: 3244726

UMI Microform 3244726

ProQuest Information and Learning Company
300 North Zeeb Road
P.O. Box 1346
Ann Arbor, MI 48106-1346

ANALYSIS OF THE FORMATION OF SOLID AND HOLLOW FIBERS IN THE MELT BLOWING PROCESS: EXPERIMENTS AND MODELING

A Dissertation Approved for the
SCHOOL OF CHEMICAL, BIOLOGICAL AND MATERIALS ENGINEERING

BY

_____
Dr. Robert Shambaugh

_____
Dr. Dimitrios Papavassiliou

_____
Dr. Lance Lobban

_____
Dr. Brian Grady

_____
Dr. Ramkumar Parthasarathy

_____
Mr. David Nelson

ACKNOWLEDGEMENTS

I would like to thank the following people without whom this present work would never have been possible:

Dr. R. L. Shambaugh, for his financial support and guidance during my stay in graduate school. In addition to our frequent discussion on Polymer Processing Technology, I have thoroughly enjoyed our numerous discussions on world history, culture, current affairs, philosophy and mythology. It has been a privilege working for you and I will always cherish the ideal student-teacher relationship we had.

Dr. D. V. Papavassiliou, for being my co-advisor and for his calming influence and encouragement from time to time.

Dr. L. L. Lobban, for serving on my committee.

Dr. B. P. Grady, for serving on my committee, for his instruction in Polymer Science, for his help on several projects and for answering so many of my doubts and questions.

Dr. R. N. Parthasarathy, for serving on my committee, for his instruction in Turbulence and Viscous Fluid Dynamics, and for his help on various aspects of my research.

Mr. D. L. Nelson, for serving on my committee, for his understanding, and for his valuable guidance and tips in helping me understand the importance of approaching a problem both from a fundamental and practical perspective.

Eric Moore and Diana Ortiz, for being great lab partners and friends through the ups and downs, for patiently teaching me to use all the equipment in the laboratory, and for making work an enjoyable place.

My Elder brother Krishna Menon, for standing by me during one of the most difficult times of my life. Thanks Knon.

Jessica, John, Brent and DeJuan, for helping me with on-line fiber diameter measurements in melt spinning and for keeping the lab atmosphere lively and entertaining.

Aaron Smith, for his incredible dedication, and hard work in helping me with on-line fiber diameter measurements in melt blowing and in the Laval nozzles project.

Christopher Fogle, for his help in the swirl die project.

Holly Krutka, for helping me understand the CFD aspect of melt blowing dies.

To all my friends in OU, who made my stay in the United States, the most memorable period of my life.

My Elder brother Krishna Marla and sister-in-law Geetanjali, for helping me prepare for so many of my presentations and for their support and concern through the rough times.

And finally, to my Parents, because whatever I am today it is because of them. Mom, Dad – I owe this to you

TABLE OF CONTENTS

LIST OF ILLUSTRATIONS

CHAPTER 1

CHAPTER 2

CHAPTER 3

CHAPTER 4

CHAPTER 5

CHAPTER 6

CHAPTER 7

LIST OF TABLES

ABSTRACT

A comprehensive mathematical model for the melt blowing process was developed. The predictions of the model were compared with experimental data obtained using both annular dies and slot dies. Favorable agreement was obtained between experimental data and model predictions. A novel process in which hollow fibers are manufactured using the melt blowing process was simulated and the effect of hollowness on the fiber properties was investigated. The results from these simulations were used as the basis for design of experiments with the swirl die, which is used in the deposition of adhesives. It was seen that in the case of hollow fibers made using the swirl die, hollowness causes a significant increase in line speeds or laydown frequency of the fiber.

A calibration procedure for an Infrared camera is described that quantify the errors involved in the temperature measurement of small targets. In order to improve upon the empirical correlation employed in the model of the melt blowing process, a new model for the heat transfer coefficient had to be introduced. An unsteady state approach was used to determine the heat transfer coefficient from fine polymer filaments to air in both cross flow and parallel flow. The results obtained for cross flow compared favorably with the well-established correlation of McAdams. The results for heat transfer coefficient in parallel flow were found to lie in between the values obtained by other research groups. On-line measurements of fiber diameter and fiber temperature in the melt spinning and melt blowing process were made. These results were compared with the predictions of a previously developed melt spinning model and the 3D melt blowing

model respectively. The heat transfer correlation developed in this study (for parallel flow) was used in the model. The temperature profile predicted by the above models compared favorably with experimental data. On using the commonly used heat transfer correlation of Kase and Matsuo in the 3D melt blowing model, it was found that the model severely overpredicted the fiber temperature. However, the choice of heat transfer correlation did not significantly affect the model predictions of the fiber diameter profile.

CHAPTER 1

INTRODUCTION

1.1 Introduction to Melt Blowing

Melt Blowing is a single step process for converting polymer pellets into fiber form. In this process, an extruder assembly and gear pump discharge precise quantities of molten polymer from a tiny orifice. High velocity streams of hot air exert a tremendous forwarding force on the molten polymer, thereby accelerating the polymer and forming fibers having diameters typically in the range of 1-100 μm. These fibers are usually collected on a meshed-screen or a rotating drum in the form of a soft, fluffy mass known as a 'web' or a 'mat'. A schematic of the process is shown in Figure 1. Compare this with the melt spinning process shown in Figure 2, where the attenuating force is provided by a mechanical roll placed some distance below the die. Since the mat in melt blowing is produced exclusively by cohesive attachment and interlocking of fibers with one another, it is known as a 'nonwoven' material (note that it does not involve knitting or weaving). Nonwovens find wide application in the filtration industry, geo-textile industry, in the manufacture of surgical disposables, baby diapers, absorbent materials, upholstery, automobile interiors, paper towels etc.

Critical to the formation of a uniform mat is the choice of the die geometry. While there are many types of dies to choose from, the end goal remains the same: minimizing the pounds of air per pound of resin for a desired fiber diameter. Melt blowing involves phenomena such as simultaneous heat and momentum transfer, turbulence and structural

changes of the polymer along the threadline. This makes it a very appealing and interesting process to study from the standpoint of a chemical engineer, fluid dynamicist and also from the perspective of a polymer scientist.

In this regard, a brief literature review in each of the following areas pertaining to melt blowing is given in the next section: melt blowing die geometries, turbulent jets, experimental measurements of fiber properties such as diameter, temperature, and, finally, modeling efforts undertaken in the past.

1.2 Literature Review

1.2.1 Melt Blowing Die Geometries

Some of the earliest dies were designed at the Naval Research Laboratory by Wente[1] in the mid 1950's. The goal of his research was to produce fibers as small as 0.1 micron in diameter. Figure 3 shows a perspective view of the die. As can be seen, individual orifices were slots, which were machined into a flat surface and then matched with identical slots machined in a similar surface. When these two surfaces are put together, they form a row of orifices, each orifice being around 0.3 mm in diameter. The typical number of holes per inch was 20. Wente considered the effect of the angle between the converging air streams to be an important factor in determining the web characteristics. He found that an angle of 90° resulted in a lot of turbulence and the fibers laid down on the collection screen in a very random fashion. An angle of 30°, however, resulted in loosely coiled bundles of fibers called "ropes" which were undesirable for filtration purposes. At the same time the fiber attenuation was a lot higher for a given gas

velocity with this angle. Hence, he reached a compromise by selecting an angle of 60°. (It turns out that almost 5 decades after Wente's work, 60° still remains the most preferred angle in the industry for this type of die.)

Hartmann et al.[2] addressed the problem of turbulence by introducing directional changes and baffles in the flow distribution chamber preceding the air slots. In addition, they introduced a guide passageway open at both ends around 5 cm below the orifice, which served to keep the fibers out of contact with each other. Substantial contact occurred just shortly before leaving the guide and this resulted in a fleece of very good uniformity. The die they used was a modified form of Wente's design. Harding et al.[3] then designed an outset die with a sharp nosepiece. Here again, a 60° angle was used between the converging air streams.

Although the above configuration proved to be very efficient in terms of air consumption, the cost of machining orifices on such sharp nosepieces was very high. Harding et al.[3] found that the setback was crucial to producing a shot-free web and an optimum was observed at 0.15 mm. Keller et al.[4] gave a detailed description on the melt blowing process with specifications on slot width, nosepiece width, optimum operating conditions and means to reduce turbulence and thereby ensure uniform flow through the air slots. Butin et al.[5] thoroughly described the melt blowing process for producing non-woven mats by controlled degradation of the resin. They found that in order to obtain good web characteristics, it is important to reduce the resin viscosity to 50-300 poise at the die exit. In addition, they also addressed the problem of 'rope formation' in melt

blowing and found that unlike spunbonded mats, the morphology of melt-blown mats was non-oriented as seen under a polarizing microscope.

Another melt blowing die configuration is shown in Figure 4. In this type of die, the air flows in the annulus with the polymer being discharged through the inner core. The annular die, therefore, has air flowing parallel to the fiber direction. Page et al.[6] claimed that this type of die configuration produced a better component of air velocity in the direction of the extruded resin. Another die geometry, shown in Figure 5, consists of a nozzle used for spraying hot melt adhesive in fiber form in a controlled, spiral pattern upon a substrate. The six equally spaced air holes receive pressurized air and the air is directed tangentially to the adhesive resin discharged through the orifice. This imparts a spiral motion to the fibers so that they are formed in a compact spray pattern for deposition onto a substrate.[7,8] The goal of this process is not necessarily to produce fine fibers but rather to spray adhesives onto a substrate in a controlled manner. The 6 air holes are machined such that their centers are equidistant from the adhesive-issuing orifice. Each of these air holes is inclined at 30° with respect to the longitudinal axis of the adhesive-issuing orifice. In addition, the longitudinal axis of each air jet bore is inclined 10° with respect to a vertical plane, which passes through the longitudinal axis of the center orifice and the center of the respective air hole. This type of die finds application in the manufacturing of baby diapers and cardboard boxes.

1.2.2 Turbulent Jets in Melt Blowing

The round jet has received considerable attention starting from Tollmien[9] and Schlichting[10], who theoretically developed analytical solutions for the centerline velocity decay, jet half width etc. These were later experimentally verified by other researchers.[11] Isothermal annular jets used in melt blowing were studied extensively by Uyttendaele and Shambaugh.[12], and non-isothermal jets were studied by Majumdar and Shambaugh.[13]

The dual rectangular jet commonly used in the melt blowing industry has been well studied. Harpham and Shambaugh,[14,15] and Tate and Shambaugh[16,17] measured the air velocity field below these dual rectangular jets using pitot tubes, and the temperature field using fine thermocouple probes. These jets had air slots inclined at an angle of 60° or 70° with the horizontal and adjustable plates that could be set for different slot widths using feeler gages. The studies mentioned above reported the velocity and temperature fields for different slot widths, mass flowrates, nosepiece inset and outset values, etc and presented dimensionless correlations.

Knowledge of the airflow field below the die is important in the modeling of the fiber formation process in melt blowing. Several techniques other than the conventional pitot-tube method have been used by researchers in analyzing the flow field. Lai and Nasr[18] investigated the velocity field resulting from two parallel plane jets by laser Doppler anemometry (LDA). Krutka et al.[19] made use of computational fluid dynamics (CFD) in predicting the air flow pattern of a dual rectangular jet. They validated their results by comparing the results with the experimental data obtained experimentally by

other research groups.[14-17] While Krutka et al. worked mainly with slot dies, Moore et al.[20] used CFD to analyze the flow fields below annular melt blowing dies. CFD simulations are less time consuming compared to experiments. They are also far more economical and can describe the flow field at distances close to the die, which are very difficult to measure in the laboratory. Also, CFD simulations predict other properties like velocity fluctuations in a flow field, velocity components in the vertical and lateral direction etc which give useful insights in the efficient design of a melt blowing die.

1.2.3 Experimental Measurements in Melt Blowing

The various fiber properties that have been measured online in melt blowing include fiber diameter, fiber velocity, fiber temperature, fiber vibration frequency and fiber vibration amplitudes. Bansal and Shambaugh[21] made use of high-speed flash photography to measure the diameter of the fiber as it was being formed and an Infrared camera was used to measure the temperature profile. Wu and Shambaugh[22] used LDV to measure the velocity of the fiber along the threadline. Moore et al.[23] used an ensemble laser diffraction (ELD) technique to determine the fiber diameter distribution at any location below a melt blowing die. Bresee and Qureshi[24] used a pulsed laser in conjunction with a rapid framing rate camera to acquire the fiber diameter in the melt blowing process. Zhao and Wadsworth[25] used a 51 cm long rigid mechanical arm to collect the fiber at different locations along the melt blowing spinline and analyzed the collected fibers using an optical microscope and an image analyzing software. Haberkorn et al.[26] used a forward laser light scattering (LLS) technique to determine the

fiber diameter along the spinline. Wallen et al.[27] used small angle light scattering to study the fiber diameter and orientation in the melt blowing process. Bresee and Ko[28] used a digital IR thermometer with adjustable emissivity for temperature measurements of fibers in melt blowing. They inserted a probe into the fiber stream and measured the temperature of the fiber as they collected on the probe surface.

The impinging high air velocity streams in melt blowing result in a region of turbulence below the die face. Turbulence can induce transverse motion of the fiber, thereby causing it to flap about the longitudinal axis of the polymer orifice with a certain frequency. Chhabra and Shambaugh[29] used laser Doppler velocimetry and high-speed strobe photography to measure the frequency and amplitude of the flapping fiber. Rao and Shambaugh[30] extended Uyttendaele and Shambaugh's[31] one-dimensional model to a two-dimensional model by accounting for fiber motion in a plane. Marla and Shambaugh[32,33] further expanded this model into a 3D model, which described the motion of the fiber in 3D space. Rao and Shambaugh observed that their model underpredicted the fiber amplitudes. The velocity fluctuations induced in the flow field due to the inherent turbulence in the system are difficult to account for in the model. Marla and Shambaugh used the lateral velocity profiles generated by the CFD simulations of Krutka et al.[19] to better estimate the fiber amplitudes.

1.3 Motivation

It has been shown that only a fraction of the air in melt blowing is used to attenuate the polymer while the rest is dissipated.[34] This means that there is tremendous

room for improvement in the area of melt blowing die design. Also, there is a need for a model that would predict the fiber properties *a priori* and compare the performances of different die geometries before the dies are put to use for mass production of melt blowing mats. Such a model would result in saving valuable time and resources. Finally, there is a constant need for improving existing fiber-making technologies in order to increase line speeds or production rates, improve product quality and decrease cost of operation. If the mathematical model could be modified so as to simulate any modifications/changes to existing processes, to define processing limits and to give some insights on the operating conditions for smooth and stable processing of the new process, it would result in tremendous cost savings. The results from any model must be verified with experimental data. Only when the predictions of the model have been compared with experimental data and favorable agreement is obtained, can one proceed to simulating new processes and place confidence in its predictions. The ability of a model to predict accurate trends in the absence of experimental data is a measure of its usefulness and importance.

1.4 Objective and Scope of Work

In view of the above, the goal of the present study is the *development of a mathematical model for melt blowing, the results of which could be used in the subsequent design of experiments*.

Although, every subsequent Chapter in this study has an introduction section, an overview of the thesis chapters is given. Chapter 2 discusses the development of a three-

dimensional model of the melt blowing process, formulation of equations and experimental verification. In Chapter 3, a novel method for manufacturing hollow fibers, viz. melt blowing, is presented. By making modifications to the model developed in Chapter 2, the new process for manufacturing hollow fibers is simulated, followed by a discussion on the trends predicted by the model. In Chapter 4, the process of fiber spinning using a unique kind of melt blowing die known as swirl die is discussed. The effect of changing the operating conditions on the fiber diameter and the swirl frequency is presented. One of the key findings from the modeling work in Chapter 3 was that inducing hollowness in the fibers increases the outer fiber diameter and the fiber vibration frequency. By using these predictions as the basis for design of experiments, the swirl die was modified in order to manufacture hollow fibers and experiments were conducted to investigate the effect of hollowness on the outer diameter and frequency of the swirled fiber.

Chapters 5-7 discuss the development of a new heat transfer correlation for use in the 3D model developed in Chapter 2. Starting from the calibration procedure for an Infrared (IR) camera (Chapter 5), to the use of an unsteady state approach in determining the heat transfer coefficient of fine polymer filaments (Chapter 6), this study was an attempt to develop better empirical correlations for estimating transport properties. It should be noted here that these empirical correlations are an input to the 3D melt blowing model and hence the accuracy of the predictions of fiber properties from the model are dependent on the accuracy of the empirical correlations. Finally, in Chapter 7, results of on-line measurements of fiber diameter and temperature in the melt spinning and melt

blowing process are presented. These are compared with the predictions from the model when both the newly developed heat transfer correlation and the commonly used heat transfer correlation of Kase and Matsuo[35] are used. In Chapter 8, the main conclusions drawn from this study, the impact and the significance of this work and the recommended directions of future research are discussed.

Formatting Note

Chapters 2-7 in this thesis were written with the intent of submitting each for publication in a journal. Each of the Chapters is in a different stage of this publication process. For example, Chapter 2 is the abridged version of the author's work published as two journal articles, the details of which are given on the first page of the Chapter. Each Chapter has an introduction section of its own and certain details such as experimental setup may be repeated in some Chapters. It is hoped that the reader understands the need for this repetition.

References

(1) Wente, V. A. Superfine Thermoplastic Fibers. *Ind. Eng. Chem.* **1956,** *48*(8), 1342-1346.

(2) Hartmann, L.; Riedmuller, W.; Muller, G. Apparatus and Process for Production of Filaments. US Patent 3,379,811, April 23, **1968**.

(3) Harding, J. W.; Keller, J. P.; Buntin, R. R. Melt-Blowing Die for Producing Nonwoven Mats. US Patent 3,825,380, July 23, **1974**.

(4) Keller, J. P.; Prentice, J. S.; Harding, J. W. Process for Producing Melt-Blown Nonwoven Synthetic Polymer Mat Having High Tear Resistance. US Patent 3,755,527, Aug. 28, **1973**.

(5) Butin, R. B.; Keller, J. P.; Harding, J. W. Non-woven Mats by Melt Blowing. US Patent 3,849,241, Nov. 19, **1974**.

(6) Page, R. J. Melt Blowing Apparatus with Parallel Air Stream Fiber Attenuation. US Patent 3,954,361, May 4, **1976**.

(7) Fort, W. C. Continuous Hot Melt Adhesive Applicator. US Patent 5,700,322, Dec. 23, **1997**.

(8) Ziecker, R. A.; Boger, B. B.; Smyrna, L. Adhesive Spray Gun and Nozzle Attachment. US Patent 4,785,996, Nov. 22, **1988**.

(9) Tollmien, W. Berechnung turbulenter Ausbreitungsvorgange. *ZAMM*, **1926,** *6*, 468. Also in NACA Tech. Memo. *1085*, **1945**.

(10) Schlichting, H. *Boundary Layer Theory*; McGraw Hill: New York, 1979; pp 745-747.

(11) Obot, N. T.; Graska, M. L.; Trabold, T. A. Near Field Behavior of Round Jets at Moderate Reynolds Numbers. *Can. J. Chem. Eng.* **1984,** *62*(5), 587-593.

(12) Uyttendaele, M. A. J.; Shambaugh, R. L. Flow Field of Annular Jets at Moderate Reynolds Numbers. *Ind. Eng. Chem. Res.* **1988,** *28*(11), 1735-1740.

(13) Majumdar, B.; Shambaugh, R. L. Velocity and Temperature Fields in Annular Jets. *Ind. Eng. Chem. Res.* **1991**, *30*(6), 1300-1306.

(14) Harpham, A. S.; Shambaugh, R. L. Flow Field of Practical Dual Rectangular Jets. *Ind. Eng. Chem. Res.* **1996,** *35*(10), 3776-3781.

(15) Harpham, A. S.; Shambaugh, R. L. Velocity and Temperature Fields of Dual Rectangular Jets. *Ind. Eng. Chem. Res.* **1997,** *36*(9), 3937-3943.

(16) Tate, B. D.; Shambaugh, R. L. Modified Dual Rectangular Jets for Fiber Production. *Ind. Eng. Chem. Res.* **1998,** *37*(9), 3772-3779.

(17) Tate, B. D.; Shambaugh, R. L. Temperature Fields below Melt-Blowing Dies of Various Geometries. *Ind. Eng. Chem. Res.* **2004,** *43*(17), 5405-5410.

(18) Lai, J. C. S.; Nasr, A. Two Parallel Plane Jets: Comparison of the Performance of Three Turbulence Models. *P. I. Mech. Eng. G-J Aer.* **1998**, *G6*, 379-391.

(19) Krutka, K. M.; Shambaugh, R. L.; Papavassiliou, D. V. Analysis of a Melt-Blowing Die: Comparison of CFD and Experiments. *Ind. Eng. Chem. Res.* **2002,** *41*(20), 5125-5138.

(20) Moore, E.M.; Shambaugh, R.L.; Papavassiliou D.V. Analysis of Isothermal Annular Jets: Comparison of CFD and Experimental Data. *J. Appl. Polym. Sci*. **2004,** *94*(3), 909-922.

(21) Bansal, V.; Shambaugh, R. L. On-line Determination of Diameter and Temperature during Melt Blowing of Polypropylene. *Ind. Eng. Chem. Res.* **1998,** *37*(5), 1799-1806.

(22) Wu, T. T.; Shambaugh, R. L. Characterization of the Melt Blowing Process with Laser Doppler Velocimetry. *Ind. Eng. Chem. Res.* **1992,** *31*(1), 379-389.

(23) Moore, M, M.; Shambaugh, R. L.; Papavassiliou, D. V. Ensemble Laser Diffraction for Online Measurement of Fiber Diameter Distribution During the Melt Blowing Process. *Int. Nonwovens. J.* **2004,** *13*(2), 42-47.

(24) Bresee, R. R.; Qureshi, U. A. Fiber Motion Near the Collector During Melt Blowing Part 1: General Considerations. *Int. Nonwovens. J.* **2002,** *11*(2), 27-34.

(25) Zhao, R.; Wadsworth, L. C. Attenuating PP/PET Bicomponent Melt Blown Microfibers. *Polym. Eng. Sci*. **2003,** *43*(2), 463-469.

(26) Haberkorn, H.; Hahn, K.; Breur, H.; Dorrer, H. D.; Matthies, P. On the Neck-Like Deformation in High-Speed Spun Polyamides. *J. Appl. Polym. Sci*. **1993,** *47*, 1551-1579.

(27) Wallen, J.; Fellers, J. F..; Bresee, R. R. Small Angle Light Scattering Studies of the Fiber Attenuation Process During Melt Blowing. *Int. Nonwovens. J.* **1995,** *7*(3), 49-50.

(28) Bresee, R. R.; Ko, W. C. Fiber Formation During Melt Blowing. *Int. Nonwovens. J.* **2003,** *12*(2), 21-28.

(29) Chhabra, R.; Shambaugh, R. L. Experimental Measurements of Fiber Threadline Vibrations in the Melt-Blowing Process. *Ind. Eng. Chem. Res.* **1996**, *35*(11), 4366-4374.

(30) Rao, R. S.; Shambaugh, R. L. Vibration and Stability in the Melt Blowing Process. *Ind. Eng. Chem. Res.* **1993,** *32*(12), 3100-3111.

(31) Uyttendaele, M. A. J.; Shambaugh, R. L. Melt Blowing: General Equation Development and Experimental Verification. *AIChE J.* **1990,** *36*(2), 175-186.

(32) Marla, V. T.; Shambaugh, R. L. Three-Dimensional Model of the Melt Blowing Process. *Ind. Eng. Chem. Res.* **2003**, *42*(26), 6993-7005.

(33) Marla, V. T.; Shambaugh, R. L. Modeling of the Melt Blowing Performance of Slot Dies. *Ind. Eng. Chem. Res.* **2004**, *43*(11), 2789-2797.

(34) Shambaugh, R. L. A Macroscopic View of the Melt Blowing Process for Producing Microfibers. *Ind. Eng. Chem. Res.* **1988,** *27*(12), 2363-2372

(35) Kase, S.; Matsuo, T. Studies on Melt Spinning. I. Fundamental Equations on the Dynamics of Melt Spinning. *J. Polym. Sci., Part A*. **1965,** *3*, 2511-2554.

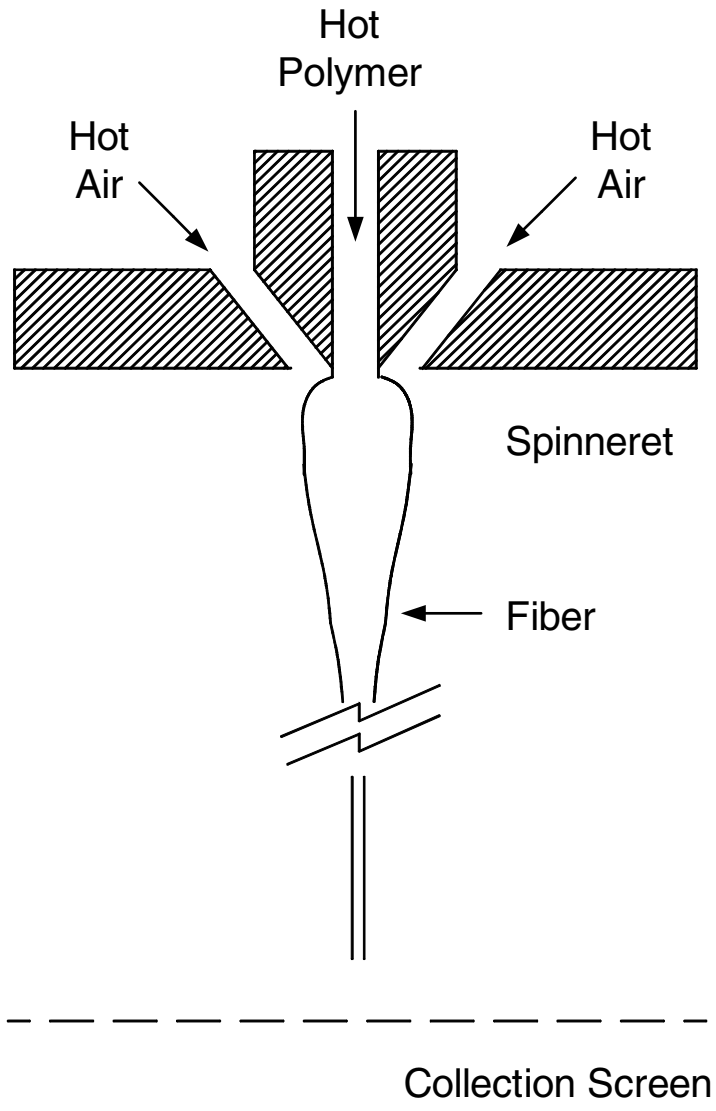

Figure 1. Schematic of the melt blowing process.

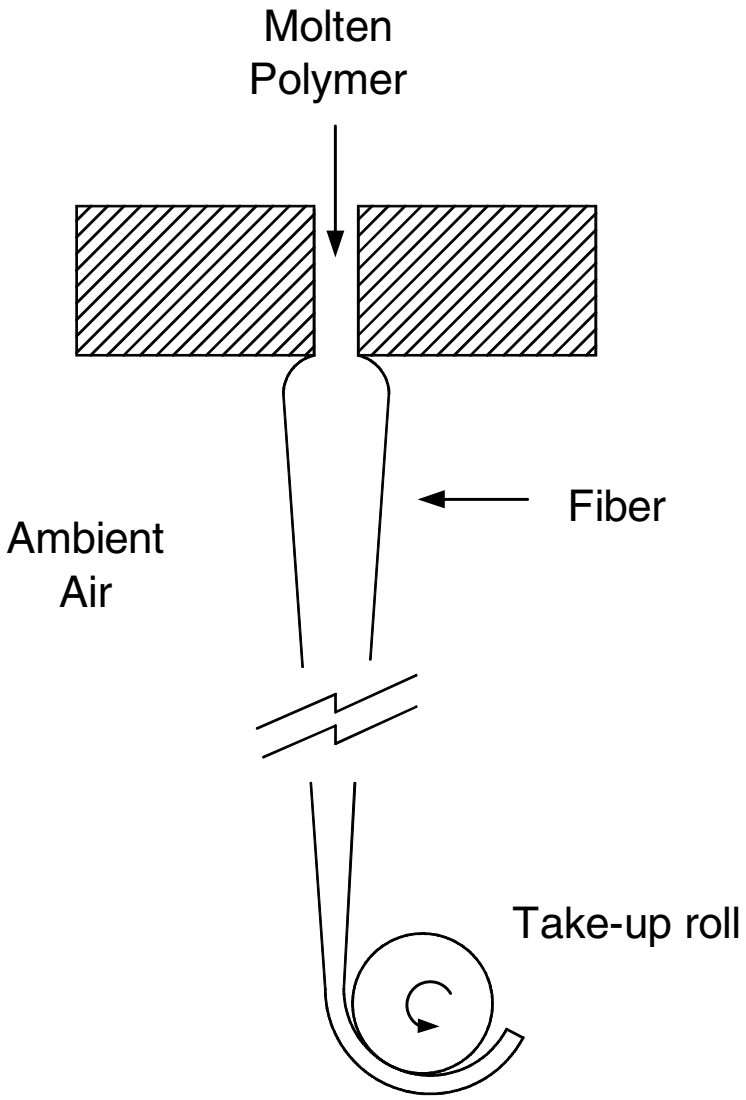

Figure 2. Schematic of the melt spinning process.

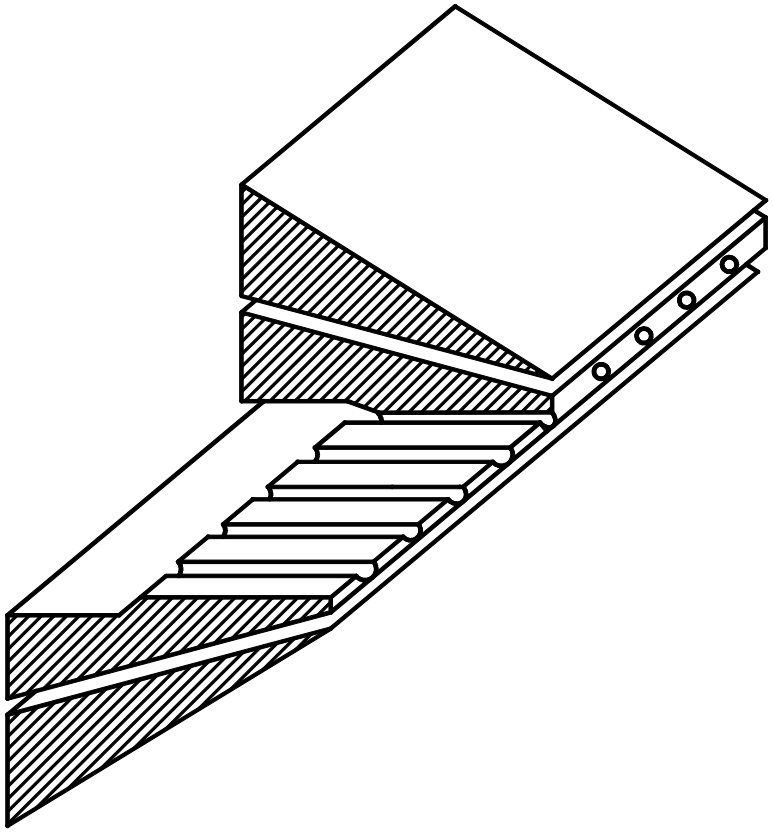

Figure 3. A typical slot die that is used to produce melt blown fibers.

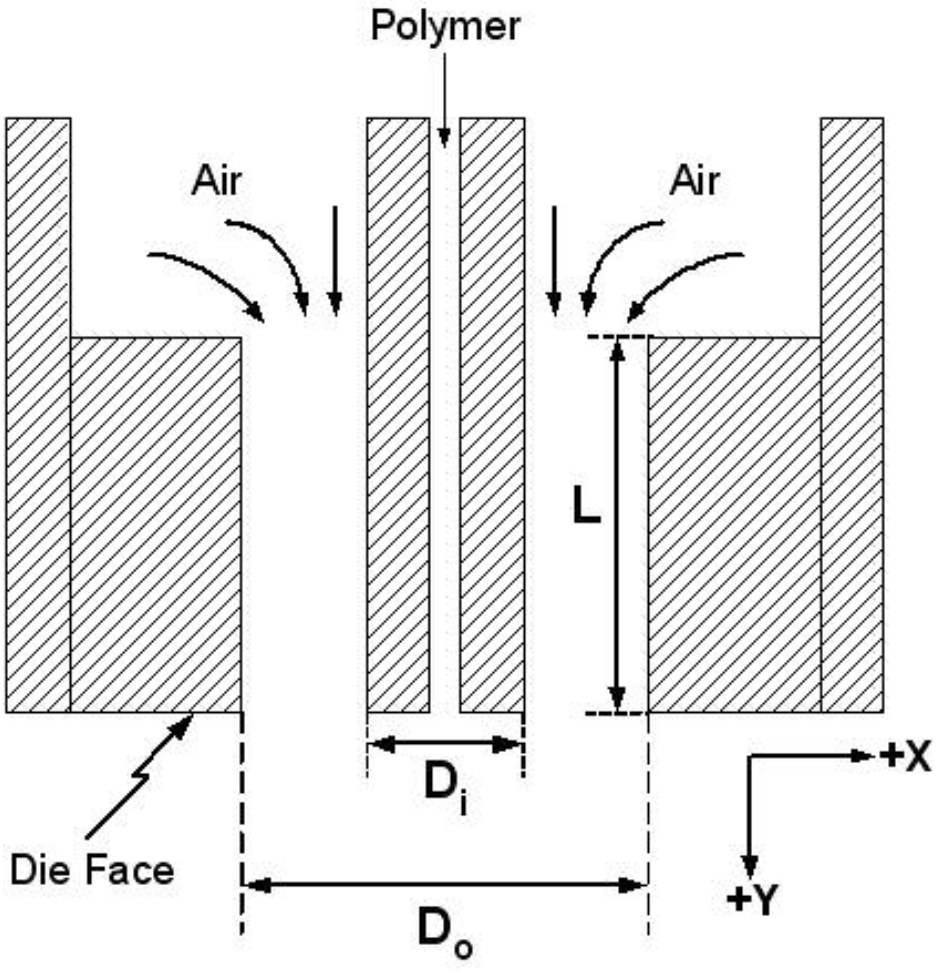

Figure 4. A schematic of an annular die that is used to produce melt blown fibers.

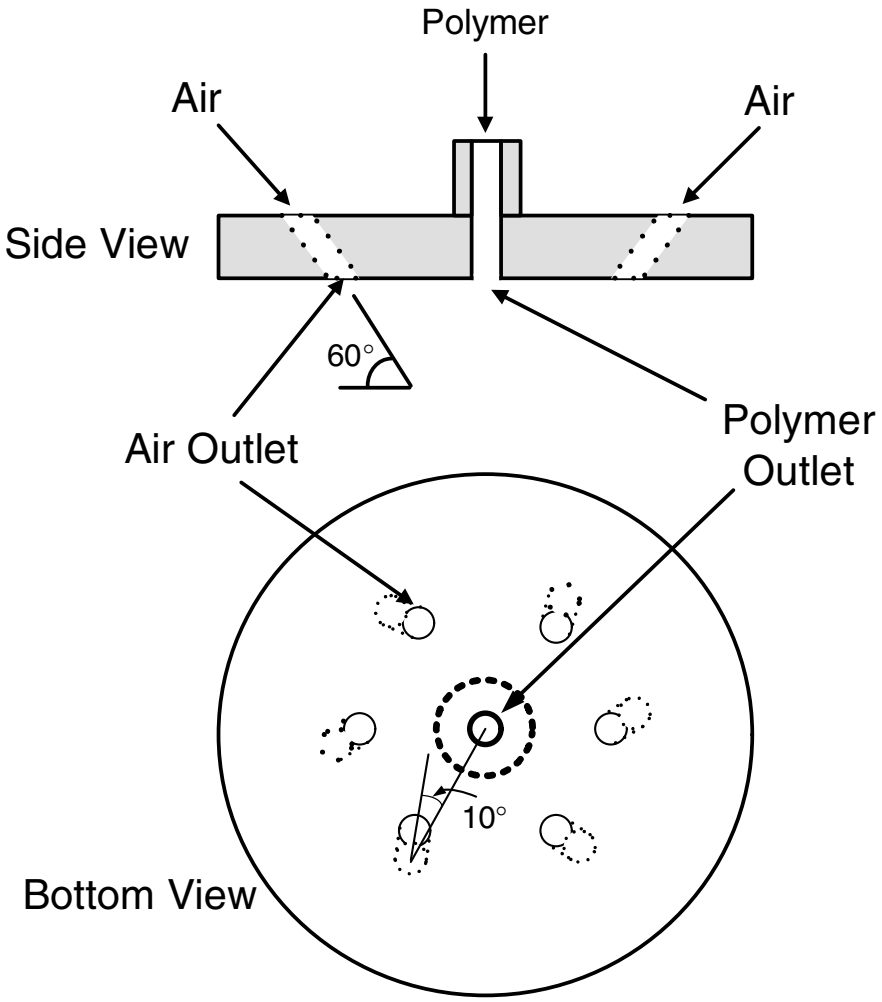

Figure 5. Schematic of the swirl die used for deposition of adhesives.

CHAPTER 2

MANUFACTURE OF SOLID FIBERS IN THE MELT BLOWING PROCESS: EXPERIMENTS AND THREE DIMENSION MODELING

Contents of this Chapter have been reproduced from the following sources:

Reproduced with permission from *Ind. Eng. Chem. Res.* **2003**, *42,* 6993-7005. Copyright 2003 Am. Chem. Soc.

Reproduced with permission from *Ind. Eng. Chem. Res.* **2004**, *43,* 2789-2797. Copyright 2004 Am. Chem. Soc.

ABSTRACT

A model has been developed that can predict the three-dimensional motion of a fiber as it is being formed below a melt blowing die. The model involves the simultaneous solution of the momentum, energy, and continuity equations. The model equations are solved numerically with both Newtonian and viscoelastic constitutive equations. Predicted parameters include fiber attenuation, vibration frequency, vibration amplitude, temperature, and stress. The predicted results compare favorably with experimental data.

2.1 Introduction

Overview of Melt Blowing Process

Melt blowing is used commercially as a one-step process for converting polymer resin directly into a nonwoven mat of fibers. Figure 1 shows a typical melt blowing process in which a molten polymer is pressurized and forced through a fine capillary.

The polymer stream is then rapidly attenuated by the drawing force exerted by high velocity air. The fiber collects and forms a mat on an open screen. Because weaving (or knitting) is not used to form the mat, the mat is referred to as a type of nonwoven. Such nonwovens are of great commercial importance.

The primary difference between melt blowing and conventional melt spinning is that a draw roll, rather than a gas stream, provides the attenuating force in melt spinning. In melt spinning, the gas into which the fiber is spun not only exerts a drag force on the filament but also cools the filament. In contrast, the gas used in melt blowing provides a substantial forwarding force and, because the gas is heated approximately to the polymer temperature, the gas prevents polymer solidification at distances close to the melt blowing die. Lack of a draw roll permits melt blowing at very high speeds: 30,000 m/min is possible with any common melt blowing head, while commercial melt spinning operations run at maximum of 6,000 m/min.

2.2 Past Modeling Work On Melt Blowing

Since melt blowing has much in common with conventional melt spinning, a brief review of the literature on melt spinning is in order. Though melt spinning was developed commercially by Du Pont in the 1930's, only since the 1960's have mathematical models been developed for melt spinning. Ziabicki and Kedzierska,[1,2] Ziabicki,[3] Kase and Matsuo,[4] and Matovich and Pearson[5] developed the basic momentum, continuity, and energy balances that apply to a spinning threadline. They, however, applied these equations only to low molecular weight, inelastic fluids. Since most real polymers have

material properties that are highly dependent on deformation rate, Fisher and Denn[6] extended previous work to include polymers with a power law viscosity and constant shear modulus. Gagon and Denn[7] modeled the melt spinning of a viscoelastic fluid with the inclusion of heat transfer, inertial, and air drag effects.

Melt blowing (see Fig.1) is particularly difficult to model because the lower end of the spinline is free to move. Thus, establishing a lower boundary condition is tricky. Uyttendaele and Shambaugh[8] solved this problem by assuming that the spinline has a "freeze point" where attenuation ceases. The rheological force at this freeze point is balanced by the gravity and air drag forces acting on the frozen segment of the filament. Uyttendaele and Shambaugh's model is a one-dimensional model in that only forces acting in the axial direction are included in the momentum balance. For relatively low spinning speeds, their model does a good job of predicting fiber attenuation under the action of the hot air stream. Rao and Shambaugh[9] expanded the one-dimensional model into a two-dimensional model that accounted for fiber motion in a plane. Since many melt blowing dies are planar in configuration,[10] modeling in two-dimensions was a reasonable approximation. In fact, the Rao-Shambaugh model does predict fiber vibration frequencies that are experimentally verifiable. However, the amplitudes of these vibrations are underpredicted. The next logical step is the expansion of the melt blowing model into three dimensions. Though such an expansion adds much to the complexity and computational time required, it is felt that such and expansion will accurately predict fiber motions in three dimensions.

2.3 Model Formulation

Figure 1 shows a vibrating filament exiting from a melt blowing die. It is assumed that: (a) the process is time dependent, and (b) the force exerted by the air on the fiber can have components in the x, y, and w directions. Through the use of planes drawn perpendicular to the y axis, the space below the die head is divided into a series of control volumes (CV). Each CV contains an element of the fiber; the mass of each element is assumed to be centered in a "bead" located at the center of the fiber element. The planes between adjacent control volumes are control surfaces (CS). An arbitrary CV and the fiber element within the CV are identified by the subscript "*i*". The upper and lower control surfaces of this CV are identified by the subscripts "*l*" and "$l + \Delta l$", respectively. At any time t, the fiber element *i* has coordinates (x_i, y_i , w_i) and velocity $v_{f,i} = (v_{f,x,i}, v_{f,y,i}, v_{f,w,i})$. Figure 2 shows an arbitrary fiber element within a control volume.

These additional assumptions were made to facilitate the solution to the model:

The fiber does not offer any resistance to bending.

The fluid forces on each element of the fiber may be assumed to be the same as those acting on an element of a straight cylinder of the same diameter and inclination.

The fiber tension is dependent only on the polymer velocity gradient along the fiber axis; this fiber axis is defined as the "z" direction. Relative to the x, y, and w directions, this z direction changes from fiber element to fiber element. Also, this z direction is time dependent.

Three-dimensional (x, y, and w) motions are considered.

Continuity Equation

In difference form the continuity equation for an element "*i*" is

$$- (\rho_f v_{f,y} A)\Big|_{i,l} + (\rho_f v_{f,y} A)\Big|_{i,l+\Delta l} + \frac{\Delta m_i}{\Delta t} = 0 \qquad (1)$$

where ρ_f is fiber density, A is the fiber cross-sectional area at a control surface, m_i is the mass of the element, and t is time.

Momentum Equations

As suggested by Figure 2, the external forces acting on a fiber element are the gravitational force in the downward direction, the aerodynamic force, and the rheological force. The aerodynamic force vector acting on the element can be resolved into three components – F_x , F_y and F_w - that correspond to forces in, respectively, the x, y and w directions. For the x momentum balance, the rheological force at the upper CS is $F_{rheo,\,x,\,l}$, while the rheological force at the lower CS is $F_{rheo,\,x,\,l+\Delta l}$. In difference form the x momentum balance for an arbitrary element *i* is

$$(F_x - F_{rheo,x,l} + F_{rheo,x,l+\Delta l})\Big|_i = -(v_{f,x}\rho_f v_{f,y} A)\Big|_{i,l} + (v_{f,x}\rho_f v_{f,y} A)\Big|_{i,l+\Delta l} + v_{f,x,i}\frac{\Delta m_i}{\Delta t} + m_i \frac{\Delta v_{f,x,i}}{\Delta t} \qquad (2)$$

The y momentum balance is

$$(m_i g_y + F_y - F_{rheo,y,l} + F_{rheo,y,l+\Delta l})\Big|_i = -(v_{f,y}{}^2 \rho_f A)\Big|_{i,l} + (v_{f,y}{}^2 \rho_f A)\Big|_{i,l+\Delta l} + v_{f,y,i}\frac{\Delta m_i}{\Delta t} + m_i \frac{\Delta v_{f,y,i}}{\Delta t} \tag{3}$$

Finally, the w momentum balance is

$$(F_w - F_{rheo,w,l} + F_{rheo,w,l+\Delta l})\Big|_i = -(v_{f,w}\rho_f v_{f,y} A)\Big|_{i,l} + (v_{f,w}\rho_f v_{f,y} A)\Big|_{i,l+\Delta l} + v_{f,w,i}\frac{\Delta m_i}{\Delta t} + m_i \frac{\Delta v_{f,w,i}}{\Delta t} \tag{4}$$

Energy Equation

To further develop the continuity, momentum and energy equations, the orientation of the fiber element within the CV must be known. Figure 3 shows a fiber element in three-dimensional space. The angle ϕ is the angle between the fiber axis and the w axis. The projection of the fiber upon the x-y plane is shown in Figure 3. This projection makes an angle α with the y axis. The range of ϕ is $0 \le \phi \le 180°$, while the range of α is $-90° \le \alpha \le 90°$. Let Δz be the axial length of fiber that is contained within the control volume. Then, based on the geometry shown in Figure 3,

$$\Delta z = \frac{\Delta l}{\cos(\alpha)\cos(90-\phi)} \tag{5}$$

The Δz defines the length of fiber element from which convective heat transfer occurs. The energy balance equation for the fiber element is

$$\begin{aligned} &-\left(\rho_f C_{p,f}\left[\left(T_f v_{f,y} A\right)\Big|_l - \left(T_f v_{f,y} A\right)\Big|_{l+\Delta l}\right]\right)\Big|_i + \left[C_{p,f}\left(T_f \frac{\Delta m}{\Delta t} + m\frac{\Delta T_f}{\Delta t}\right)\right]\Big|_i \\ &= -\left[h\pi \frac{d_l + d_{l+\Delta l}}{2} \frac{\Delta l}{\cos(\alpha)\cos(90-\phi)}\left(T_f - T_a\right)\right]\Big|_i \end{aligned} \tag{6}$$

where $C_{p,f}$ is the fiber heat capacity, T_f is the fiber temperature, T_a is the air temperature, h is the convective heat transfer coefficient, and d_l and $d_{l+\Delta l}$ are, respectively, the fiber diameters at the upper and lower control surfaces.

The Set of ODE's (Ordinary Differential Equations)

In the limit as $\Delta t \rightarrow 0$, equations (1), (2), (3), (4) and (6) can be rearranged to give

$$\frac{dm_i}{dt} = -\left[\left(\rho_f v_{f,y} A\right)\Big|_{l+\Delta l} - \left(\rho_f v_{f,y} A\right)\Big|_l\right]\Big|_i \tag{7}$$

$$\frac{dv_{f,x,i}}{dt} = \begin{pmatrix} -v_{f,x,i}\frac{dm_i}{dt} - \left[\left(\rho_f v_{f,y} A v_{f,x}\right)\Big|_{l+\Delta l} - \left(\rho_f v_{f,y} A v_{f,x}\right)\Big|_l\right]\Big|_i \\ + \left(F_x - F_{rheo,x,l} + F_{rheo,x,l+\Delta l}\right)\Big|_i \end{pmatrix} / m_i \tag{8}$$

$$\frac{dv_{f,y,i}}{dt} = \begin{pmatrix} -v_{f,y,i}\frac{dm_i}{dt} - \left[(\rho_f v_{f,y} A v_{f,y})\big|_{l+\Delta l} - (\rho_f v_{f,y} A v_{f,y})\big|_l\right]\Big|_i \\ +(mg_y + F_y - F_{rheo,y,l} + F_{rheo,y,l+\Delta l})\big|_i \end{pmatrix} / m_i \tag{9}$$

$$\frac{dv_{f,w,i}}{dt} = \begin{pmatrix} -v_{f,w,i}\frac{dm_i}{dt} - \left[(\rho_f v_{f,y} A v_{f,w})\big|_{l+\Delta l} - (\rho_f v_{f,y} A v_{f,w})\big|_l\right]\Big|_i \\ +(F_w - F_{rheo,w,l} + F_{rheo,w,l+\Delta l})\big|_i \end{pmatrix} / m_i \tag{10}$$

$$\frac{dT_{f,i}}{dt} = \begin{pmatrix} -C_{p,f,i}T_{f,i}\frac{dm_i}{dt} - \left[(\rho_f v_{f,y} A C_{p,f} T_f)\big|_{l+\Delta l} - (\rho_f v_{f,y} A C_{p,f} T_f)\big|_l\right]\Big|_i \\ -\left[h\pi\frac{d_l + d_{l+\Delta l}}{2}\Delta z(T_f - T_a)\right]\Big|_i \end{pmatrix} / (m_i C_{p,f,i}) \tag{11}$$

Two additional differential equations are provided from the relations

$$\frac{dx_{f,i}}{dt} = v_{f,x,i} \tag{12}$$

$$\frac{dw_{f,i}}{dt} = v_{f,w,i} \tag{13}$$

Equations (7)–(13) are algebraic in nature in the space (y) domain and differential in nature in the time (t) domain. Thus, the solution techniques for ordinary differential equations (ODE's) can be applied to solve the equations with t as the primary

independent variable and y as the secondary independent variable. The dependent variables are the mass (m_i), temperature ($T_{f,i}$), transverse velocity in the x direction ($v_{f,x,i}$), transverse velocity in the w direction ($v_{f,w,i}$), velocity in the y direction ($v_{f,y,i}$), the transverse position in the x direction ($x_{f,i}$), and the transverse position in the w direction ($w_{f,i}$). Thus, there are seven equations with seven unknowns. These equations are solved simultaneously for each CV. Since the fiber elements in each CV are all connected as are beads along a string, the solution for a CV is dependent on the solution of the equations for the adjacent CV's. One has to therefore progressively solve the equations for all the CV's at a given moment in time. Moreover, initial conditions (IC's) are required for all the dependent variables along the length of the fiber. Also, boundary conditions (BC's) are required at the start and end of the fiber length.

To proceed with the solution of equations (7) to (13) one also needs expressions for the fiber cross-sectional areas at the control surfaces (A_l and $A_{l+\Delta l}$), the aerodynamic force components (F_x , F_y and F_w), the rheological force components ($F_{rheo,\,x,\,l}$, $F_{rheo,\,x,\,l+\Delta l}$, $F_{rheo,\,y,\,l}$, $F_{rheo,\,y,\,l+\Delta l}$, $F_{rheo,\,w,\,l}$, $F_{rheo,\,w,\,l+\Delta l}$), and the convective heat transfer coefficient (h). A discussion of how these variables are expressed will now be given.

Cross-sectional Areas of the Fiber at the Control Surfaces

The upper and lower control surfaces (see Fig. 2) are ellipsoidal. The appropriate relations for A_l and $A_{l+\Delta l}$ are

$$A_{i,l} = \pi\left(\frac{{d_{i,l}}^2}{4\cos(\alpha_{i,l})\cos(90-\phi_{i,l})}\right) \tag{14}$$

$$A_{i,l+\Delta l} = \pi\left(\frac{d_{i,l+\Delta l}{}^2}{4\cos(\alpha_{i,l+\Delta l})\cos(90-\phi_{i,l+\Delta l})}\right) \tag{15}$$

where

$$\alpha_{i,l} = \tan^{-1}\left(\frac{x_{f,i} - x_{f,i-1}}{\Delta l}\right) \tag{16}$$

$$\alpha_{i,l+\Delta l} = \tan^{-1}\left(\frac{x_{f,i+1} - x_{f,i}}{\Delta l}\right) \tag{17}$$

$$90 - \phi_{i,l} = \tan^{-1}\left(\frac{w_{f,i} - w_{f,i-1}}{\Delta l}\cos(\alpha_{i,l})\right) \tag{18}$$

$$90 - \phi_{i,l+\Delta l} = \tan^{-1}\left(\frac{w_{f,i+1} - w_{f,i}}{\Delta l}\cos(\alpha_{i,l+\Delta l})\right) \tag{19}$$

The $\alpha_{i,l}$ is the angle at the upper CS between the y axis and the projection of the fiber axis on the x-y plane; the $\alpha_{i,l+\Delta l}$ is similarly defined for the lower CS. (The α_i is the average of these two angles.) The $\phi_{i,l}$ is the angle at the upper CS between the fiber axis (the z direction) and the w axis; the $\phi_{i,l+\Delta l}$ is similarly defined for the lower CS.

Though fiber diameter is not a variable in Equations (7) to (13), fiber diameter is an important parameter in fiber formation processes. Furthermore, knowledge of fiber diameter is needed for use in equations (14) and (15) (and in the aerodynamic force calculation). To determine fiber diameter, a fiber element can be approximated as the frustum of a cone. The mass m_i of the polymer in the element can then be defined as

$$m_i = \rho_f \pi \frac{\Delta l}{12\cos(\alpha_i)\cos(90-\phi_i)}\left(d_{i,l}{}^2 + d_{i,l}d_{i,l+\Delta l} + d_{i,l+\Delta l}{}^2\right) \tag{20}$$

where α_i and ϕ_i are average angles for the fiber element. To calculate the threadline diameter profile at a particular time t, eq. (20) is used by first starting at the top element of the threadline where d_l is known. The bottom diameter $d_{l+\Delta l}$ can then be determined, since m_i is known. The procedure is repeated for each successive element until the entire diameter profile has been determined.

Aerodynamic Force

As a result of the transverse (x and w direction) motions of the fiber, the fiber elements may assume varying orientations with respect to the y axis. Matsui[11] and Majumdar and Shambaugh[12] developed empirical correlations for the friction coefficient in parallel flow at the air-filament interface. Ju and Shambaugh[13] showed how the total force on a filament at an oblique angle to the flow can be correlated by separating the force into parallel and normal components. They developed a correlation for the normal drag force that can be combined with Majumdar and Shambaugh's correlation to evaluate the total force on an oblique filament.

The air velocity and the fiber axis are vectors (lines) that define a plane in which is contained both the parallel drag force and the normal drag force. The orientation of this plane changes with both time and position along the threadline.

For a melt blowing system with transverse fiber motions, the appropriate definition for the parallel drag force is

$$F_{PAR} = C_f (1/2)\rho_a \left(v_{a,eff,PAR}\right)^2 \left(\pi d_f L_f\right) \tag{21}$$

The L_f is the length of the fiber element ($L_f = \Delta z$). The C_f is the skin coefficient which is defined by a modified form of the Matsui (1976) relation as $C_f = \beta(Re_{DP})^{-n}$. The appropriate definition of Re_{DP} for our system is $Re_{DP} = \rho\, v_{a,eff,PAR}\, d_f / \mu_a$. Majumdar and Shambaugh[12] determined that $\beta = 0.78$ and $n = 0.61$ are appropriate values for melt blowing conditions.

The definition of the normal (cross flow) force is

$$F_N = C_{DN}(1/2)\rho_a\left(v_{a,eff,N}\right)^2\left(d_f L_f\right) \tag{22}$$

The C_{DN} is the drag coefficient which was correlated by Ju and Shambaugh[13] as $C_{DN} = 6.958\ Re_{DN}^{-0.4399}(d_f / d_o)^{0.4044}$. The Reynolds number ($Re_{DN}$) is based on the normal component of the air; for our system the appropriate definition for Re_{DN} is $Re_{DN} = \rho_a\, v_{a,eff,N}\, d_f / \mu_a$.

The aerodynamic force correlations and Reynolds numbers just given employ the parallel and normal components of the effective air velocity with respect to the fiber. In the case of a stationary filament the effective air velocity ($\bar{\mathbf{v}}_{a,eff}$) is the same as the actual air velocity ($\bar{\mathbf{v}}_a$). However, a melt blown fiber exhibits both axial and transverse motion. As a result, the effective air velocity as seen by the fiber is different than the actual air velocity.

Consider a fiber element as shown in Figure 3. A unit vector $\bar{\mathbf{f}}_{PAR}$ that is parallel to the fiber axis is

$$\bar{\mathbf{f}}_{PAR} = \sin(\phi)\sin(\alpha)\,\bar{\mathbf{i}} + \sin(\phi)\cos(\alpha)\,\bar{\mathbf{j}} + \cos(\phi)\,\bar{\mathbf{k}} \tag{23}$$

where i , j and k are unit vectors in the x-y-w coordinate system.

To determine $\bar{\mathbf{f}}_N$, the unit vector normal to the fiber, we need to first define the plane in which $\bar{\mathbf{f}}_N$ lies. To define this plane, we need to know the effective (relative) air velocity. The air velocity is

$$\bar{\mathbf{v}}_a = v_{a,x}\,\bar{\mathbf{i}} + v_{a,y}\,\bar{\mathbf{j}} + v_{a,w}\,\bar{\mathbf{k}} \tag{24}$$

The fiber velocity is

$$\bar{\mathbf{v}}_{f,i} = v_{f,x,i}\,\bar{\mathbf{i}} + v_{f,y,i}\,\bar{\mathbf{j}} + v_{f,w,i}\,\bar{\mathbf{k}} \tag{25}$$

The effective (relative) velocity of the air with respect to the fiber is then

$$\bar{\mathbf{v}}_{a,eff} = \left(v_{a,x} - v_{f,x,i}\right)\bar{\mathbf{i}} + \left(v_{a,y} - v_{f,y,i}\right)\bar{\mathbf{j}} + \left(v_{a,w} - v_{f,w,i}\right)\bar{\mathbf{k}} \tag{26}$$

The vectors $\bar{\mathbf{v}}_{a,eff}$ and $\bar{\mathbf{f}}_{PAR}$ determine the plane which contains both the parallel and normal components of the drag force upon the fiber. This plane can be defined by a vector perpendicular to the plane. Let us define

$$\bar{\mathbf{u}} = \bar{\mathbf{f}}_{PAR} \times \bar{\mathbf{v}}_{a,eff} \tag{27}$$

The normal force on the fiber is perpendicular to both $\bar{\mathbf{u}}$ and $\bar{\mathbf{f}}_{PAR}$. Thus,

$$\bar{\mathbf{f}}_N = \frac{\bar{\mathbf{f}}_{PAR} \times \bar{\mathbf{u}}}{\left\| \bar{\mathbf{f}}_{PAR} \times \bar{\mathbf{u}} \right\|} \tag{28}$$

or

$$\bar{\mathbf{f}}_N = \frac{\bar{\mathbf{f}}_{PAR} \times \left(\bar{\mathbf{f}}_{PAR} \times \bar{\mathbf{v}}_{a,eff}\right)}{\left\| \bar{\mathbf{f}}_{PAR} \times \left(\bar{\mathbf{f}}_{PAR} \times \bar{\mathbf{v}}_{a,eff}\right) \right\|} \tag{29}$$

The normal and parallel components of the effective air velocity with respect to the fiber (z) axis are then

$$\bar{\mathbf{v}}_{a,eff,N} = \left(\bar{\mathbf{v}}_{a,eff} \bullet \bar{\mathbf{f}}_N\right)\bar{\mathbf{f}}_N \tag{30}$$

$$\bar{\mathbf{v}}_{a,eff,PAR} = \left(\bar{\mathbf{v}}_{a,eff} \bullet \bar{\mathbf{f}}_{PAR}\right)\bar{\mathbf{f}}_{PAR} \tag{31}$$

The magnitude of the velocities in equations (30) and (31) can be used in equations (21) and (22) to calculate the magnitude of the parallel (F_{PAR}) and normal (F_N) components of the aerodynamic force, respectively. The directions of these force components are described by the unit vectors $\bar{\mathbf{f}}_{PAR}$ and $\bar{\mathbf{f}}_N$, respectively. Since the quantity calculated from equation 21 is always positive, the sign of F_{PAR} must be determined from the sign of the dot product of $\bar{\mathbf{v}}_{a,eff}$ and $\bar{\mathbf{f}}_{PAR}$. Similarly, the sign of F_N must be determined from the sign of the dot product of $\bar{\mathbf{v}}_{a,eff}$ and $\bar{\mathbf{f}}_N$. Specifically,

$$\bar{\mathbf{F}}_{PAR} = F_{PAR}\ \bar{\mathbf{f}}_{PAR} \qquad \text{for } v_{a,eff,PAR} > 0 \tag{32}$$

and

$$\bar{\mathbf{F}}_{PAR} = -F_{PAR}\ \bar{\mathbf{f}}_{PAR} \qquad \text{for } v_{a,eff,PAR} < 0 \tag{33}$$

(where $v_{a,eff,PAR} = \bar{\mathbf{v}}_{a,eff} \bullet \bar{\mathbf{f}}_{PAR}$)

For $\bar{\mathbf{F}}_N$,

$$\bar{\mathbf{F}}_N = F_N\ \bar{\mathbf{f}}_N \qquad \text{for } v_{a,eff,N} > 0 \tag{34}$$

and

$$\bar{\mathbf{F}}_N = -F_N\ \bar{\mathbf{f}}_N \qquad \text{for } v_{a,eff,N} < 0 \tag{35}$$

The total vector aerodynamic force F_T is then

$$\bar{\mathbf{F}}_T = \bar{\mathbf{F}}_{PAR} + \bar{\mathbf{F}}_N \tag{36}$$

Heat Transfer Correlation

When air flow is perpendicular to a fiber, the Nusselt number can be determined from the following correlation[4,14]:

$$Nu_{\psi=90^\circ} = 0.764\,Re_{eff}^{\,0.38} \tag{37}$$

where

$$Re_{eff} = \frac{\rho_a v_{a,eff} d_{f,i}}{\mu_a} \tag{38}$$

The Nusselt number is defined as $Nu = h\, d_f / k_a$, where h is the convective heat transfer coefficient and k_a is the thermal conductivity of the air. The ψ in equation (37) is the angle between the fiber axis and the effective air velocity; $\psi = 90°$ for crossflow. The ψ is defined as

$$\psi_i = \tan^{-1}\left(\frac{\left|v_{a,eff,N}\right|}{\left|v_{a,eff,PAR}\right|}\right) \tag{39}$$

Generally, $\psi \neq 90°$ for melt blowing; i.e., the fiber is oblique to the (effective) air flow. Morgan[15] gives a comprehensive summary of research on heat transfer from fine cylinders oblique to the air stream. With a least-squares fit of the of the experimental

data from Mueller[16] and Champagne et al.,[17] the following relation can be written to predict the Nusselt number for flow oblique to a fiber:

$$\mathrm{Nu/Nu}_{\psi=90^\circ} = 0.590 \sin^{0.849}(\psi) + 0.400 \tag{40}$$

Equation (40), combined with equation (37), can be used to calculate h in our melt blowing system.

Rheological Forces

As described by Uyttendaele and Shambaugh,[8] the axial rheological stress is

$$F_{rheo} = \left(\pi {d_f}^2 / 4\right)\left(\tau^{zz} - \tau^{x'x'}\right) \tag{41}$$

where the z direction is the fiber axial direction and x' is any direction in the cross-sectional plane. For the geometry of our problem, the device of defining the z direction maintains the simple form of the constitutive equations. For a Newtonian fluid, Middleman[18] defines the τ^{zz} and $\tau^{x'x'}$ as

$$\tau^{zz} = 2\eta_f \frac{dv_{f,z}}{dz} \tag{42}$$

$$\tau^{x'x'} = -\eta_f \frac{dv_{f,z}}{dz} \tag{43}$$

Therefore, for the Newtonian case,

$$F_{rheo} = \pi\left(\frac{{d_f}^2}{4} 3\eta_f \frac{dv_{f,z}}{dz}\right) \tag{44}$$

This force acts along the fiber axis. The axial direction is defined by the unit vector f_{PAR} . Then the rheological force is

$$\bar{\mathbf{F}}_{\text{rheo}} = F_{\text{rheo}} \bar{\mathbf{f}}_{\text{PAR}} \tag{45}$$

The x component of the rheological force is

$$F_{\text{rheo,x},i,l} = F_{\text{rheo}} \bar{\mathbf{f}}_{\text{PAR}} \bullet \bar{\mathbf{i}} \tag{46}$$

$$= \left[F_{\text{rheo}} \left(\sin(\phi)\sin(\alpha)\bar{\mathbf{i}} + \sin(\phi)\cos(\alpha)\bar{\mathbf{j}} + \cos(\phi)\bar{\mathbf{k}} \right) \bullet \bar{\mathbf{i}} \right]_{i,l} \tag{47}$$

$$= \left[F_{\text{rheo}} \sin(\phi)\sin(\alpha) \right]_{i,l} \tag{48}$$

Similarly for the y component

$$F_{\text{rheo,y},i,l} = F_{\text{rheo}} \bar{\mathbf{f}}_{\text{PAR}} \bullet \bar{\mathbf{j}} \tag{49}$$

$$= \left[F_{\text{rheo}} \sin(\phi)\cos(\alpha) \right]_{i,l} \tag{50}$$

Finally, for the w component

$$F_{\text{rheo,w},i,l} = F_{\text{rheo}} \bar{\mathbf{f}}_{\text{PAR}} \bullet \bar{\mathbf{k}} \tag{51}$$

$$= \left[F_{\text{rheo}} \cos(\phi) \right]_{i,l} \tag{52}$$

Equations (48), (50), and (52) are force components at the upper control surface. For the bottom control surface, the equations are identical except that l is replaced with $l + \Delta l$.

To use the above rheological component equations, we need to evaluate the fiber velocity gradient at the upper and lower control surface. For the upper surface

$$\left(\frac{dv_{f,z}}{dz}\right)\Bigg|_{i,l} = \frac{\Delta v_{f,z}}{\Delta z} \tag{53}$$

$$= \frac{v_{f,z,i} - v_{f,z,i\text{-}1}}{\Delta z} \tag{54}$$

Then, with the use of equation (5), we can write

$$\left(\frac{dv_{f,z}}{dz}\right)\Bigg|_{i,l} = \frac{v_{f,z,i} - v_{f,z,i\text{-}1}}{\Delta l}\left[\cos(\alpha)\cos(90-\phi)\right]_{i,l} \tag{55}$$

Similarly, the gradient at the lower control surface is

$$\left(\frac{dv_{f,z}}{dz}\right)\Bigg|_{i,l+\Delta l} = \frac{v_{f,z,i+1} - v_{f,z,i}}{\Delta l}\left[\cos(\alpha)\cos(90-\phi)\right]_{i,l+\Delta l} \tag{56}$$

In equations (55) and (56) we need the velocity v_f along the fiber axis rather than the velocity in the x-y-w coordinate system. For element i the following dot product will give v_f :

$$v_{f,z,i} = \left(\bar{\mathbf{v}}_f \bullet \bar{\mathbf{f}}_{PAR}\right)\Big|_i \tag{57}$$

Non-Newtonian Model

Instead of using a simple Newtonian model for the polymer, more complex constitutive equations can be used. Phan-Thien[19] suggested that the behavior of a

polymer in an elongational flow field can be modeled with the following set of constitutive equations:

$$\tau^{zz} = \sum_{i} \tau_i{}^{zz} \tag{58}$$

$$\tau^{x'x'} = \sum_{i} \tau_i{}^{x'x'} \tag{59}$$

$$K_i \tau_i{}^{zz} + \lambda_i \left[v_{f,z} \frac{d\tau_i{}^{zz}}{dz} - 2(1-X)\tau_i{}^{zz} \frac{dv_{f,z}}{dz} \right] = 2G_i \lambda_i \frac{dv_{f,z}}{dz} \tag{60}$$

$$K_i \tau_i{}^{x'x'} + \lambda_i \left[v_{f,z} \frac{d\tau_i{}^{x'x'}}{dz} + (1-X)\tau_i{}^{x'x'} \frac{dv_{f,z}}{dz} \right] = -G_i \lambda_i \frac{dv_{f,z}}{dz} \tag{61}$$

$$K_i = \exp\left[\frac{E}{G_i} \left(2\tau_i{}^{x'x'} + \tau_i{}^{zz} \right) \right] \tag{62}$$

where i= 1, 2, 3, …etc. (Note that i in equations (58) to (62) is a counting variable rather than the element i used elsewhere in our equations.)

Equations (58)-(62) are derived from the application of the Phan-Thien and Tanner rheological model to simple elongational flow. The Phan-Thien and Tanner model allows the use of a discrete spectrum of relaxation times. The factor X is a viscous shear thinning parameter, and E is a parameter related to stress saturation at high extension rates. When both parameters are set equal to zero, the common (upper convected) Maxwell fluid model is recovered.

For our calculations, we assume that i=1 in equations 58-62. Then, equations 58 and 59 become tautologies, and we can drop the subscript i in equations 60-62 (and rid ourselves of two definitions for i in our calculations). In solving the Phan-Thien case, we replace eq. 44 with the more general eq. 41. This adds two variables, τ^{zz} and $\tau^{x'x'}$. We then add the additional variable K, and we use equations 60-62 to handle the three additional variables.

Velocity and Temperature Correlations for Annular die

In order to solve our model equations, the air velocity and temperature need to be known at any position below the melt blowing die. Majumdar[20] and Majumdar and Shambaugh[21] have developed dimensionless correlations for an annular die geometry, and these correlations were used in the modeling work of Rao and Shambaugh.[9] Since we are modeling the same annular geometry in our present work, we will use the same correlations. The correlations for the velocity profiles are as follows:

$$v_{jo}/v_o = 0.077\,Y(d_{AN}) + 1.00 \qquad \text{for } Y(d_{AN}) < 3.093 \tag{63}$$

$$v_{jo}/v_o = 0.249\,Y(d_{AN}) + 0.468 \qquad \text{for } Y(d_{AN}) \geq 3.093 \tag{64}$$

$$v/v_o = \exp(-0.693(\,|r|/r_{1/2})^2) \tag{65}$$

$$\frac{r_{1/2}}{d_{AN}} = 0.112\frac{y}{d_{AN}} + 0.040 \qquad \text{for } \frac{y}{d_{AN}} > 4 \tag{66}$$

See the Nomenclature section for definitions of the symbols.

Similarly, the correlations for the temperature profiles are as follows:

$$\theta_{jo}/\theta_o = 0.033\,Y(d_{AN}) + 1.00 \quad \text{for } Y(d_{AN}) < 4.644 \tag{67}$$

$$\theta_{jo}/\theta_o = 0.221\,Y(d_{AN}) + 0.127 \text{ for } Y(d_{AN}) \geq 4.644 \tag{68}$$

$$\theta/\theta_o = \exp(-0.693(|r|/t_{1/2})^2) \tag{69}$$

$$\frac{t_{1/2}}{d_{AN}} = 0.109\frac{y}{d_{AN}} + 0.155 \qquad \text{for } \frac{y}{d_{AN}} > 4 \tag{70}$$

Again, see the Nomenclature section for definitions of the symbols.

Boundary Conditions

The fiber velocity and temperature are known at the die and are used as boundary conditions at the start of the threadline. For the Newtonian assumption, the rheological force (F_{rheo}) at the die is guessed, and an iterative procedure determines the correct value of this force. As described in Rao and Shambaugh,[9] the iteration along the threadline stops at the "stop point". The stop point is defined as the point at which the air velocity and the fiber velocity become equal. Beyond the stop point, the air is actually pushing the fiber upward. Since it is difficult to transmit a compression force along a thin fiber, the fiber tends to buckle at positions beyond the stop point and the fiber floats down to the collection screen. The fiber segment beyond the stop point does not transmit any forces to the fiber segment above the stop point (F_{rheo} =0 at the stop point).

For the nonnewtonian assumption, τ^{zz} at the die is guessed, and $\tau^{x'x'}$ at the die is set equal to zero (see Gagon and Denn[7]). An iterative procedure then determines the correct value of τ^{zz} at the die.

Parameter Inputs

Except where noted, our simulations were based on the experimental parameters used by Rao and Shambaugh.[9] The single-hole spinneret had a spinneret capillary of 0.5334 mm (0.021 in.) inside diameter. The concentric gas annulus had a 1.656 mm (0.0652 in.) outside diameter and a 0.8256 mm (0.0325 in.) inside diameter. The polymer used was 35 MFR Fina polypropylene whose zero shear rate viscosity can be described with the equation.[8]

$$\eta_f = 0.001985 \exp\left(\frac{5754}{T_f}\right) \tag{71}$$

The threadline calculations were started at an assumed diameter of $d_{f,y=0}$ =949 μm for the die swell (see Rao and Shambaugh, 1993). For the Phan-Thien equations (equations 58-62), G = 28 kPa, X = 0.1, and E = 0.015. The ambient air temperature was 23°C.

2.4 Model Results for Annular Dies

For the fiber, initial sideways velocity and/or position are also needed as initial conditions. For example, the fiber position can be specified as having an initial slope of $\Delta x/\Delta y = 10^{-5}$ in the x direction and a slope of $\Delta w/\Delta y = 10^{-5}$ in the w direction. If no

initial slope or velocity is given, then the simulation shows that the fiber does not vibrate at all, but stays vertical. Figure 4 shows the diameter prediction for such a 3D simulation. Also shown are the corresponding diameter predictions for the 2D Rao and Shambaugh model and the 1D Uyttendaele and Shambaugh model (here and elsewhere in this paper, the 1D model was run with a stop point rather than a freeze point assumption - see Rao and Shambaugh[9]). As can be seen, the 2D and 3D model predictions are identical to each other, and the 1D model prediction varies only slightly from the predictions of the other two models. Since the 1D model involves the solution of the steady state equations, while the other two models involve the solution of time dependent equations, the slight variance in the results is insignificant and is probably related to the numerical solution techniques. Basically, the 3D and 2D solutions collapse into the 1D prediction when no vibration is present. Of course, the 2D and 3D cases on Figure 4 are metastable situations, because, as will be discussed shortly, the fiber will vibrate if an initial nonvertical slope is given for the fiber position. Figure 4 also shows the experimental data of Uyttendaele and Shambaugh. The simulations match the experimental data quite well.

For the more realistic situation wherein the fiber does have some initial perturbation from the vertical, it was found that, no matter what the selected initial position of the fiber (within reason), the simulation settled down to a limited range of fiber diameters after 5 seconds of simulation time. Unless otherwise stated, the simulation predictions for all figures are averages of results for the time period 5 to 15 seconds. Since one microsecond was the time interval typically used in our simulations, then about 15 million iterations were done per run. Of course, a simulation time of 15 seconds took

4-6 hours of actual calculation time on our computer, which was a Dell Precision Workstation 530 with a dual 2.2 GHz Intel Xeon processor.

Figure 5 shows the 3D model's predictions of the fiber diameter profiles. The fiber position was specified as having an initial slope of $\Delta x/\Delta y = 10^{-5}$ in the x direction and a slope of $\Delta w/\Delta y = 10^{-5}$ in the w direction (this causes fiber vibration). Both the Newtonian and the Phan-Thien constitutive equations were used with the 3D model; the diameter profiles are quite similar. The Phan-Thien model predicts a final fiber diameter of around 44 μm in comparison to a final diameter of 40 μm predicted by the Newtonian model. The stop point is located at 14.3 cm in the Phan-Thien model, while the Newtonian model predicts a closer stop point of 12.7 cm. These similar results agree with the conclusion of Uyttendaele and Shambaugh.[8] They stated that, in the melt blowing process, thermal changes are so rapid that it is the temperature dependence of the polymer viscosity that dominates in the prediction of fiber diameter. Hence, the use of a viscoelastic constitutive equation has less an effect on the fiber profile than might be expected.

Figure 6 compares the temperature and velocity profiles obtained from 3D simulations using the Newtonian and Phan-Thien equations. The temperature profiles are almost the same. For the velocity profiles, the Phan-Thien curve lies lower than the Newtonian curve. The lower fiber velocity for the Phan-Thien model is expected since, as Fig. 5 shows, the Phan-Thien model predicts a larger fiber diameter (according to the continuity equation, the fiber velocity is proportional to the inverse of the square of the diameter). The stress profiles for the Newtonian and nonnewtonian 3D models (see Fig.

7) are similar in shape; the Phan-Thien model predicts a maximum stress of 33 kPa at a distance of 2.1 cm from the die, while the Newtonian model predicts a maximum stress of 26 kPa at about the same distance (1.9 cm). Fig. 7 also shows that the stress profiles for the 2D and 1D (Newtonian) models vary only slightly from the profile for the 3D (Newtonian) model.

Figure 8 compares the fiber velocity and stress with the air velocity. The air velocity was determined from the experimental correlations discussed earlier (equations 63-66). The fiber velocity and stress are from the 3D simulation. Because of the configuration of the melt blowing die, the air velocity steadily decreases as distance from the die increases. In contrast, the fiber velocity increases steadily, though the rate of increase goes to zero at the stop point. As required by the stop point criterion, the air velocity and fiber velocity are equal at the stop point. The fiber stress rises to a maximum at about 2 cm from the die, and the stress goes to zero at the stop point. The "noise" in the stress data (between about 8 and 9 cm) is an anomaly that sometimes occurred during the stress simulations.

Rao and Shambaugh[9] used 2 mm as the length of each element in the 2D model. To check if a smaller element might give better convergence for our 3D model, a 1 mm element was also tested. The results of this test are shown in Figure 9. As can be seen, using a 1 mm element results in essentially no difference in the simulated predictions of either diameter or temperature. Hence, 2 mm was the element length used in our 3D simulations – there was no need to use a smaller element size with the corresponding increase in computational time.

Table 1 shows how fiber vibration affects the predicted final diameter and other parameters. For this table, the 1D case corresponds to the 3D case run with no vibration (or, equivalently, the 2D case run with no vibration). As described earlier, the 3D case becomes a metastable 1D case when the initial conditions have no disturbance in either the x or w directions. As the table shows, as the number of vibration modes increases, the fiber diameter decreases. Also, the maximum stress slightly increases as the number of vibration modes increases. This decrease in diameter and increase in stress can be attributed to the whipping and attenuation of the fiber during vibration. For this table, the simulations are Newtonian and are run for 35 MFR polypropylene (see eq. 71), d_f = 949 μm at die swell, and β=0.78. The velocity and temperature correlations used are from Majumdar and Shambaugh[21] for die head "B" (as given in equations 63-70). The diameter profiles are averages for t = 5 to 15 s; $v_{a,die}$ =110.3 m/s, $T_{a,die}$ = 368°C, Q = 0.658 cm^3/min, and $T_{f,die}$ = 310°C.

Figure 10 shows the effect of air velocity on the fiber diameter and temperature. Flow fields are considered that have initial air velocities of 110, 150 and 200 m/s. As expected, the higher velocities cause much more rapid attenuation of the fibers, and the final diameters are smaller when the gas velocity is higher. The increase in air velocity has little effect on the temperature profile of the fiber. Though the higher air velocity results in a higher heat transfer rate to the fiber, the time over which the fiber is exposed to the air is less when the air velocity (and thus the fiber velocity) is higher. These two effects tend to cancel each other out.

Table 2 shows the range of predicted fiber diameters for air velocities of 110, 150 and 200 m/s. For this table, a 3D Newtonian model was used with the same parameters as used for Figure 9. The range lists the maximum and minimum values of diameter that were calculated during the simulation for t = 5 to 15 seconds. As might be expected, the diameter range increases for higher air velocities. Also shown are the ranges for other predicted parameters. Stress increases substantially as air velocity increases.

Figure 11 shows the effect of air velocity on the rheological stress in the fiber. The peak stress increases significantly with the air velocity and, as the air velocity increases, the point of maximum stress moves closer to the die. As was shown earlier (Figures 7 and 8), there sometimes is chatter in the stress profiles in the vicinity of the stop point. However, if one considers the average values, then the stress in the fiber smoothly approaches zero at the stop point.

Figure 12 shows the effect of air velocity on the amplitude of fiber vibration. As shown in the experimental work of Rao and Shambaugh, higher air velocities result in higher amplitudes of fiber vibration. Similar to the definition used in the Rao and Shambaugh 2D model, the amplitude of vibration is defined as the maximum displacement, at a position y, that occurs in the range t = 5-15 s. In the 2D model, only fiber vibrations in the x-y plane were considered (i.e., only x displacements). However, in our 3D model we observe the motion of the fiber in three-space. Hence, the amplitude of the fiber at a position y is calculated as $\sqrt{x_{max}^2 + w_{max}^2}$, where x_{max} and w_{max} are the maximum displacements at the position y below the die (that occur in the range t = 5-15 s) in the x-y plane and the w-y plane, respectively. The amplitude prediction is

significantly higher in the 3D model for each air velocity. For example, for the 200 m/s case, the 3D model predicts a maximum amplitude of 1.25 mm, or a fiber cone diameter of 2.5 mm, which is an increase of almost 50 % over the 2D model predictions. Based on their experimental data, Rao and Shambaugh[9] stated that the 2D model underpredicted fiber amplitude. Hence, the 3D model gives an improved prediction of fiber amplitude.

Figure 13 shows the effect of air velocity on the frequency of vibration. The results obtained with the 2D model are also shown in the figure. Rao and Shambaugh determined the frequency of vibration at a position y by counting the number of times that the fiber element crosses the x=0 line in a 3 second time interval (and dividing by two to get the frequency). However, in the 3D model, two frequencies were measured. One frequency was determined by how many times the fiber element crossed the w-y plane; the other frequency was determined by how many times the fiber element crossed the x-y plane. In all the simulations performed, the frequency of w-y plane crossings was exactly equal to the frequency of x-y plane crossings. This was an expected result because of the radial symmetry in the annular die. Hence, the values shown in the figure can be considered the frequency of vibrations in either plane. At each of the three air velocities, the 3D model predictions were almost identical to the 2D model predictions. For each case, the frequency is essentially constant along the threadline. The 150 m/s air velocity gives the highest frequency (about 91 Hz), while the 200 m/s air velocity gives the lowest frequency (about 26 Hz). The 110 m/s velocity gave an intermediate frequency (about 50 Hz).

2.5 Experiments with Slot Dies

Once the model is developed, it can be extended to any die geometry as long as the air velocity and temperature fields below the die are known. The above sections discussed the predictions of the model for annular dies. In this section, the model predictions for slot dies will be discussed and compared with experimental data. A cross-sectional view of the slot die used in the experiments is shown in Figure 14. The center section is called the nose piece; since the nose piece in Figure 14 is flat on the die face, this particular die is called a blunt die. When there is no flat present, the die is known is a sharp die. Harpham and Shambaugh[22,23] and Tate and Shambaugh[24] have done experimental measurements on both sharp and blunt dies. These investigators used pitot tubes and fine thermocouples to measure the velocity and temperature fields below the melt blowing dies. More recently, Krutka et al.[25] made use of computational fluid dynamics (CFD) in predicting the velocity field of melt blowing dies; they validated their results with the experimental data of Harpham and Shambaugh[22,23] and Tate and Shambaugh.[24] CFD simulations take less time in comparison to data obtained from experiments. The CFD simulations also can describe phenomena that are difficult to measure in the laboratory (such as the flow field at distances very close to the die face). The correlations developed by Harpham and Shambaugh[22,23] and Tate and Shambaugh[24] were used in the model for calculating the centerline air velocity and temperature at any point below the slot die. The lateral velocity profiles for air were obtained from the CFD simulations of Krutka et al.

Figure 15 shows the experimental setup. A Brabender extruder of 19.1 mm (0.75 in.) diameter and 381 mm length was used to melt and pressurize the polymer. The barrel had a 20:1 L/D ratio and a 3:1 compression ratio. The polymer exiting from the extruder was then fed to a modified Zenith pump which pumps controlled quantities of molten polymer through a single-hole melt blowing die. The polymer capillary had an inside diameter of 0.420 mm. The two air slots were set flush with the nosepiece, and the slot widths were 0.65 mm (see Fig. 4). Each slot had a length of 74.6 mm (2.94 in.). The die assembly was heated with two 250 W cartridge heaters. A thermal mass flow meter was used to measure the air flow rate, which was maintained at 100 slpm (21°C and atmospheric pressure). For our die, 100 slpm corresponds to an isothermal die face velocity of 17.3 m/s. Details of the heating equipment for the air lines can be found in Harpham and Shambaugh.[23] From the cross-sectional area of the slots and the air temperature the air velocity at the die exit was calculated and was used as a boundary condition in our simulations. The measurement of the fiber cone diameter was done by taking multiple-image photographs. The camera used was a Nikon N90S equipped with a 105 mm Nikon macro lens. The film used was Kodak Tri-X 400. The illumination for the photographs was provided by a GenRad 1546 digital strobe. Refer Chhabra and Shambaugh[26] for details on the camera settings and the technique for the measurement of the fiber cone diameter. For our measurements, we used a strobe frequency of 5 flashes per second and a camera exposure time of 30 seconds. This gave 150 multiple fiber images on each picture, and the cone diameter was determined by measuring the diameter of this multiple image.

The effect of varying the mass flowrate of the polymer, the air flowrate and the effect of changing the polymer temperature at the die on the final fiber diameter and vibration frequency were studied. These are shown in Table 3. There is good agreement between the final diameter predicted by the model and that obtained from experiments. In almost every case, the model predicts final fiber diameters that are very close to the values measured from experiments. The fiber amplitude is underpredicted in each case, but is of the same order. If turbulence had been included, the simulated fiber amplitudes would probably be even closer to the experimental values.

2.6 Conclusions

A comprehensive 3D model was developed by applying the fundamental transport equations. The 3D model predicts higher amplitudes in comparison to the 2D model in the simulations performed. The results of the model for final fiber diameter match experimental data very well. This analysis was conducted for both annular and slot dies and can be extended to any die geometry as long as the air flow field below the die is known. This model can thus be used to find out the best die geometry for a set of operating conditions.

Nomenclature

C_{DN} = drag force coefficient for the drag force perpendicular to the filament (see eq. 22)

C_f = friction factor for parallel flow of fluid along the filament surface (see eq. 21)

$C_{p,f}$ = fiber heat capacity, J/(kg·K)

d_{AN} = outer diameter of annular die orifice, mm

d_f = diameter of filament, µm

d_o = median diameter of filaments used in the correlation of Ju and Shambaugh (1994); d_o = 78 µm

E = Phan-Thien and Tanner model parameter related to stress saturation at high extension rates

$\bar{\mathbf{f}}_{PAR}$ = unit vector along the fiber axis (z-axis)

$\bar{\mathbf{f}}_N$ = unit vector normal to the fiber axis (z-axis)

F_w = aerodynamic force on the filament in the w direction, N

F_x = aerodynamic force on the filament in the x direction, N

F_y = aerodynamic force on the filament in the y direction, N

F_N = drag force normal to the major axis of the fiber, N

F_{PAR} = drag force parallel to the major axis of the fiber, N

F_{rheo} = rheological force, N

F_T = total force on the fiber, N

G = shear modulus, Pa

h = convective heat transfer coefficient, $W/(m^2 \cdot K)$

k_a = thermal conductivity of air, $W/(m \cdot K)$

K = Phan-Thien and Tanner model variable

l = y value at upper control surface of the control volume; see Fig. 1

$l + \Delta l$ = y value at lower control surface of the control volume; see Fig. 1

L_f = length of an element of the filament (equivalent to Δz), m

m = fiber mass, kg

Nu = Nusselt number for heat transfer between the air and the fiber

Q = polymer rate through the die, cm^3/min

r = $\sqrt{x^2 + w^2}$ = radial coordinate, mm

$r_{1/2}$ = air velocity half-width, mm

Re_{DN} = Reynolds number based on filament diameter and the component of air velocity perpendicular to the filament axis; $Re_{DN} = \rho_a \, v_{a,eff,N} \, d_f / \mu_a$

Re_{DP} = Reynolds number based on filament diameter and the component of air velocity parallel to the filament axis; $Re_{DP} = \rho \, v_{a,eff,PAR} \, d_f / \mu_a$

Re_{eff} = Reynolds number defined by eq. 38

T_a = air temperature, °C

$T_{a,die}$ = air temperature at die (y = 0), °C

T_f = filament temperature, °C

$T_{f,die}$ = filament temperature at die (y = 0), °C

v_a = free stream air velocity, m/s

$v_{a,die}$ = v_{jo} = air velocity at the die (y = 0), m/s

v_f = fiber velocity, m/s

$v_{a,eff,N}$ = component of effective air velocity which is normal to the filament axis, m/s

$v_{a,eff,PAR}$ = component of the effective air velocity which is parallel to the filament axis, m/s

v_o = maximum air velocity at a fixed y, m/s

v_{jo} = $v_{a,die}$ = air velocity at the die (y = 0), m/s

$v_{a,eff}$ = effective, or relative, velocity of air with respect to the fiber, m/s

w = Cartesian coordinate; see Figures 1 and 2.

x = Cartesian coordinate; see Figures 1 and 2

x' = coordinate direction normal to z

X = Phan-Thien and Tanner model parameter related to viscous shear thinning

y = vertical Cartesian coordinate; see Figures 1 and 2

$Y(d_{AN}) = Y/\, d_{AN}((\rho_{a\infty} / \rho_{ao})^{1/2}$

z = coordinate position along the fiber axis

Greek Letters

α = angle between the y axis and the projection of the fiber on the x-y plane; see Fig. 3

β = leading coefficient in the Matsui relation; $C_f = \beta(Re_{DP})^{-n}$

ϕ = angle between the fiber axis and the w axis; see Fig. 3

η_f = zero shear fiber viscosity, Pa•s

θ_{jo} = excess air temperature above ambient at die exit, °C

θ_o = excess air temperature above ambient along the center line (the y axis), °C

μ_a = air viscosity, Pa•s

λ = stress relaxation time, s

ν_a = kinematic air viscosity, m^2/s

ρ_a = air density, kg/m^3

ρ_{ao} = air density along the center line downstream from the nozzle, kg/m^3

$\rho_{a\infty}$ = air density at ambient conditions, kg/m^3

τ = extra stress, Pa

ψ = angle between effective air velocity ($\bar{\mathbf{v}}_{a,eff}$) and the fiber axis; see equations 37-40

Subscripts

a = air

die = die

eff = effective

f = fiber

i = fiber element (control volume) i

N = normal

PAR = parallel

rheo = rheological

x = property along the x axis

y = property along the y axis

w = property along the w axis

Superscripts

x’ = coordinate in direction transverse to the fiber axis

z = coordinate position along the fiber axis

References

(1) Ziabicki, A.; Kedzierska, K. Mechanical Aspects of Fibre Spinning Process in Molten Polymers: 1. Stream Diameter and Velocity Distribution along the Spinning Way. *Kolloid Z.* **1960**, *171*, 51.

(2) Ziabicki, A.; Kedzierska, K. Mechanical Aspects of Fibre Spinning Process in Molten Polymers: 2. Stream Broadening after the Exit from the Channel of Spinneret. *Kolloid Z.* **1961**, *171*, 111.

(3) Ziabicki, A. Mechanical Aspects of Fibre Spinning Process in Molten Polymers: 3. Tensile Force and Stress. *Kolloid Z.* **1961**, *175*, 14.

(4) Kase, S.; Matsuo, T. Studies on Melt Spinning. I. Fundamental Equations on the Dynamics of Melt Spinning. *J. Polym. Sci., Part A* **1965**, *3*, 2541

(5) Matovich, M. A.; Pearson, J. R. A. Spinning a Molten Threadline: Steady-State Isothermal Viscous Flows. *Ind. Eng. Chem. Fundam*. **1969**, *8* (3), 512.

(6) Fisher, R. J.; Denn, M. M. A Theory of Isothermal Melt Spinning and Draw Resonance. *AIChE J*. **1976**, *22* (6), 236.

(7) Gagon, D. K.; Denn, M. M. Computer Simulation of Steady Polymer Melt Spinning. *Polym. Eng. Sci*. **1981**, *21,* 844.

(8) Uyttendaele, M. A. J.; Shambaugh, R. L. Melt Blowing: General Equation Development and Experimental Verification. *AIChE J.* **1990**, *36* (2), 175-186.

(9) Rao, R. S.; Shambaugh, R. L. Vibration and Stability in the Melt Blowing Process. *Ind. Eng. Chem. Res.* **1993**, *32* (12), 3100-3111.

(10) Tate, B. D.; Shambaugh, R. L. Modified Dual Rectangular Jets for Fiber Production. *Ind. Eng. Chem. Res.* **1998**, *37* (9), 3772-3779.

(11) Matsui, M. Air Drag on a Continuous Filament in Melt Spinning. *Trans. Soc. Rheol.* **1976**, *20* (3), 465-473.

(12) Majumdar, B.; Shambaugh, R. L. Air Drag on Filaments in the Melt Blowing Process. *J. Rheol.* **1990**, *34* (4), 591-601.

(13) Ju, Y. D.; Shambaugh, R. L. Air Drag on Fine Filaments at Oblique and Normal Angles to the Air Stream. *Polym. Eng. Sci.* **1994**, *34* (12), 958-964.

(14) Andrews, E. H. Cooling of a Spinning Threadline. *Br. J. Appl. Phys.* **1959**, *10* (1), 39-43.

(15) Morgan, V. T. *Advances in Heat Transfer*; Academic Press: New York, 1975; Vol. 11, pp 239-243.

(16) Mueller, A. C. Heat Transfer from Wires to Air in Parallel Flow. *Trans. Am. Inst. Chem. Eng.* **1942**, *38*, 613-627.

(17) Champagne, F. H.; Sleicher, C. A.; Wehrmann, O. H. Turbulence Measurements with Inclined Hot-Wires. Part 1. Heat Transfer Experiments with Inclined Hot-Wire. *J. Fluid. Mech.* **1967**, *28* (1), 153-175.

(18) Middleman, S. *Fundamentals of Polymer Processing*; McGraw-Hill Book Co.: New York, 1977.

(19) Phan-Thien, N. A Nonlinear Network Viscoelastic Model. *J. Rheol.* **1978**, *22* (3), 259-283.

(20) Majumdar, B. Flow Fields for Annular and Multi-Hole Nozzles and Air Drag in the Melt Blowing Process. M.S. Thesis, University of Oklahoma, Norman, OK, 1990.

(21) Majumdar, B.; Shambaugh, R. L. Velocity and Temperature Fields in Annular Jets. *Ind. Eng. Chem. Res.* **1991**, *30* (6), 1300-1306.

(22) Harpham, A. S.; Shambaugh, R. L. Flow Field of Practical Dual Rectangular Jets. *Ind. Eng. Chem. Res.* **1996,** *35*(10), 3776-3781.

(23) Harpham, A. S.; Shambaugh, R. L. Velocity and Temperature Fields of Dual Rectangular Jets. *Ind. Eng. Chem. Res.* **1997,** *36*(9), 3937-3943.

(24) Tate, B. D.; Shambaugh, R. L. Modified Dual Rectangular Jets for Fiber Production. *Ind. Eng. Chem. Res.* **1998,** *37*(9), 3772-3779.

(25) Krutka, K. M.; Shambaugh, R. L.; Papavassiliou, D. V. Analysis of a Melt-Blowing Die: Comparison of CFD and Experiments. *Ind. Eng. Chem. Res.* **2002,** *41*(20), 5125-5138.

(26) Chhabra, R.; Shambaugh, R. L. Experimental Measurements of Fiber Threadline Vibrations in the Melt-Blowing Process. *Ind. Eng. Chem. Res.* **1996**, *35*(11), 4366-4374.

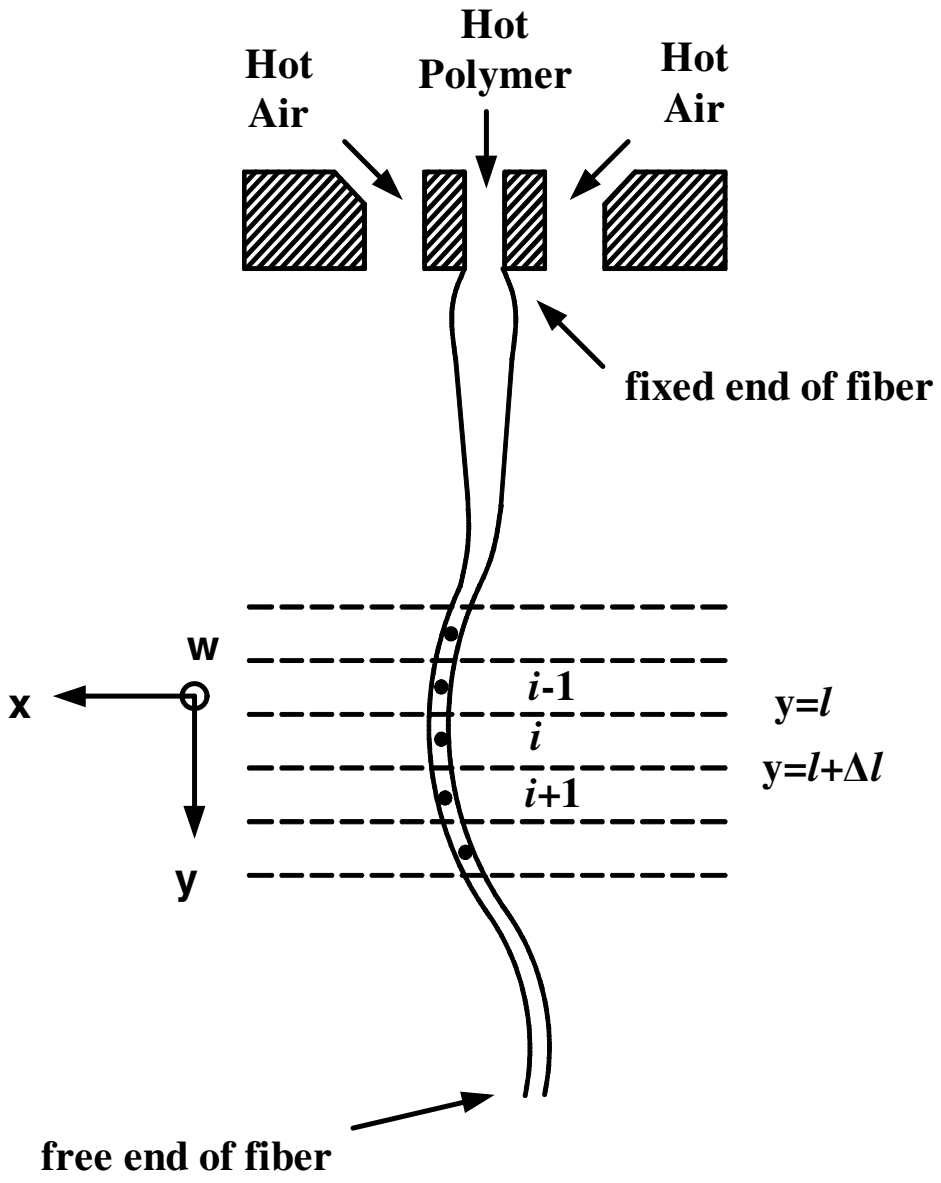

Figure 1. The melt blowing process when fiber vibration is significant. The w-axis is perpendicular and comes out of the plane of the paper.

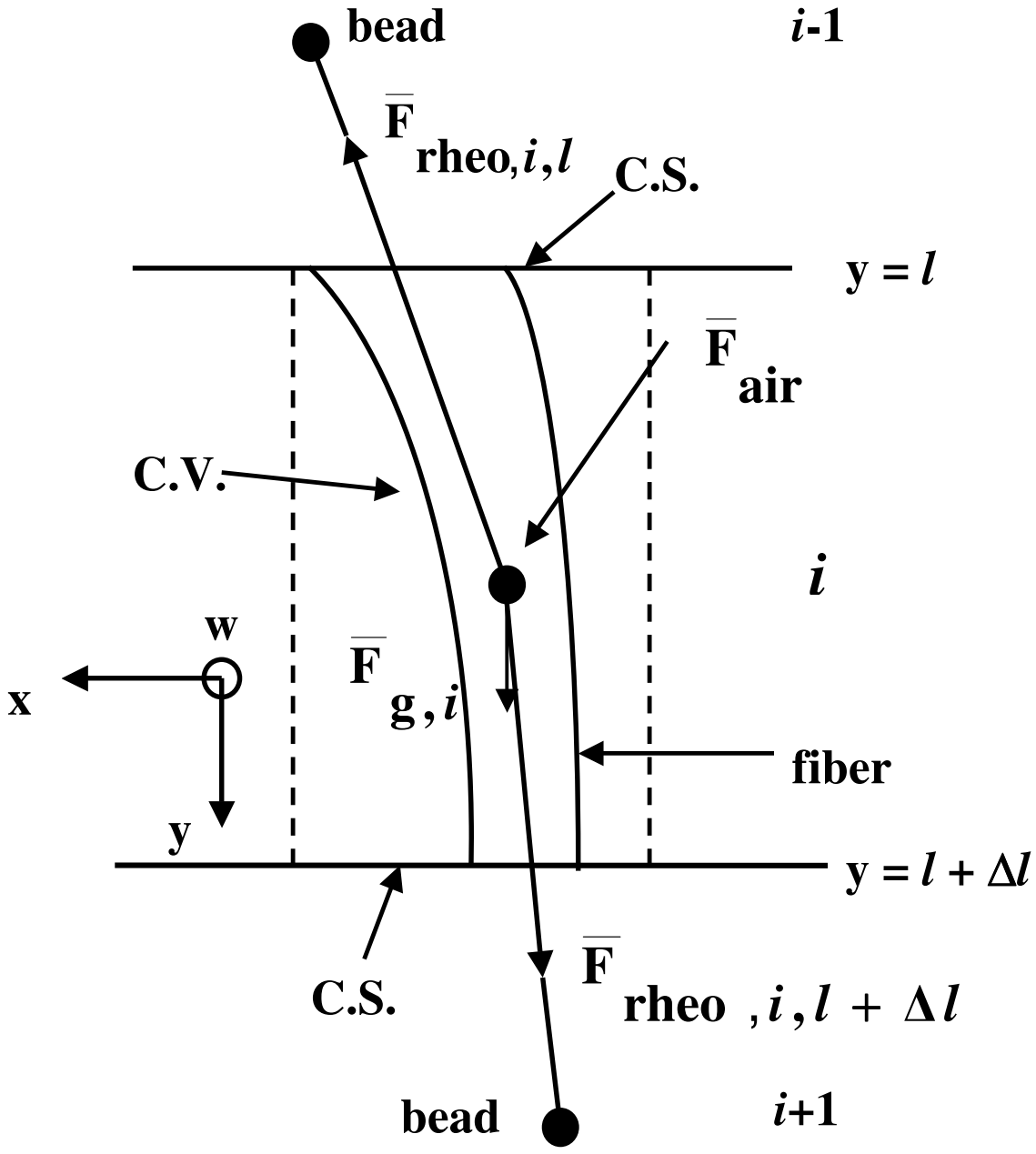

Figure 2. A fiber element contained within a control volume.

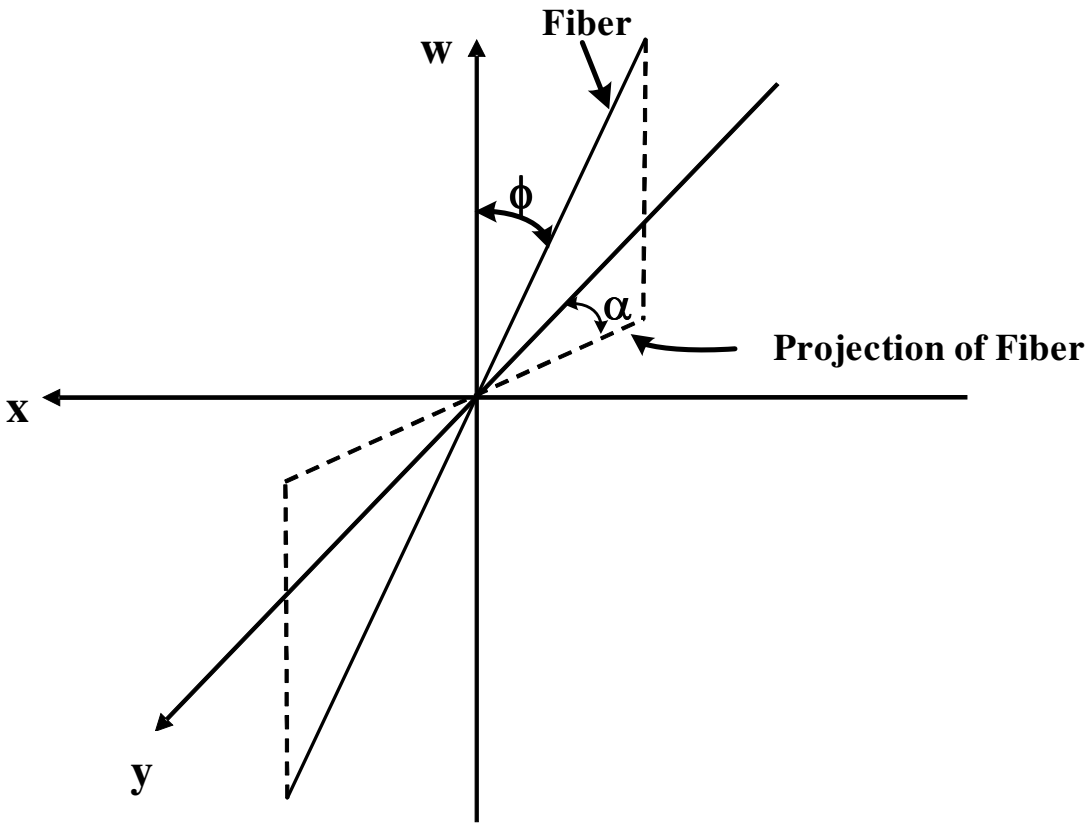

Figure 3. Coordinate system used in the 3D model and the projection of the fiber in the xy plane

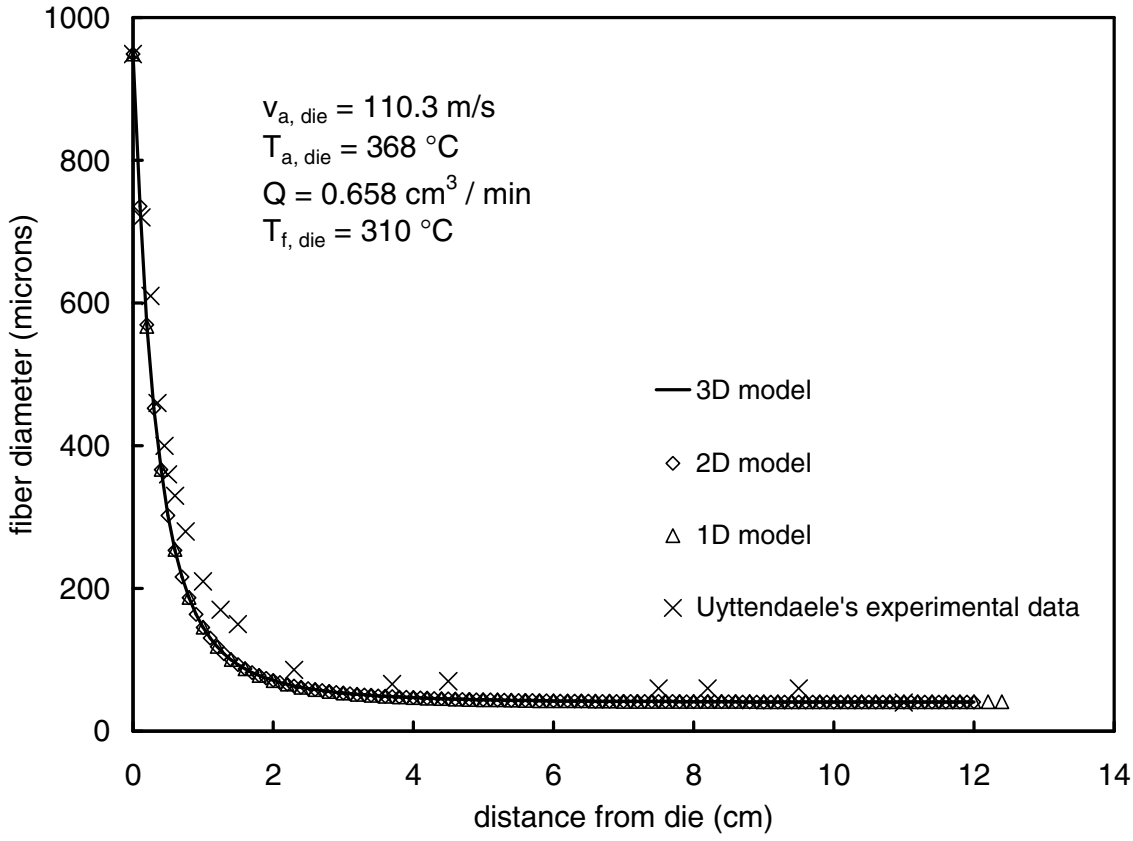

Figure 4. Comparison of the predictions of the present 3D model with the 2D model and the 1D model. The experimental data of Uyttendaele are shown on the figure. The simulations were Newtonian and were run with these experimental conditions used by Uyttendaele: 35 MFR polypropylene (see eq. 71) and df = 949 μm at die swell. The β in the Matsui relation was assumed to be 0.78. The velocity and temperature correlations used are from Majumdar and Shambaugh (1991) for die head "A". The diameter profiles for the 2D and 3D models are averages for t = 5 to 15 s.

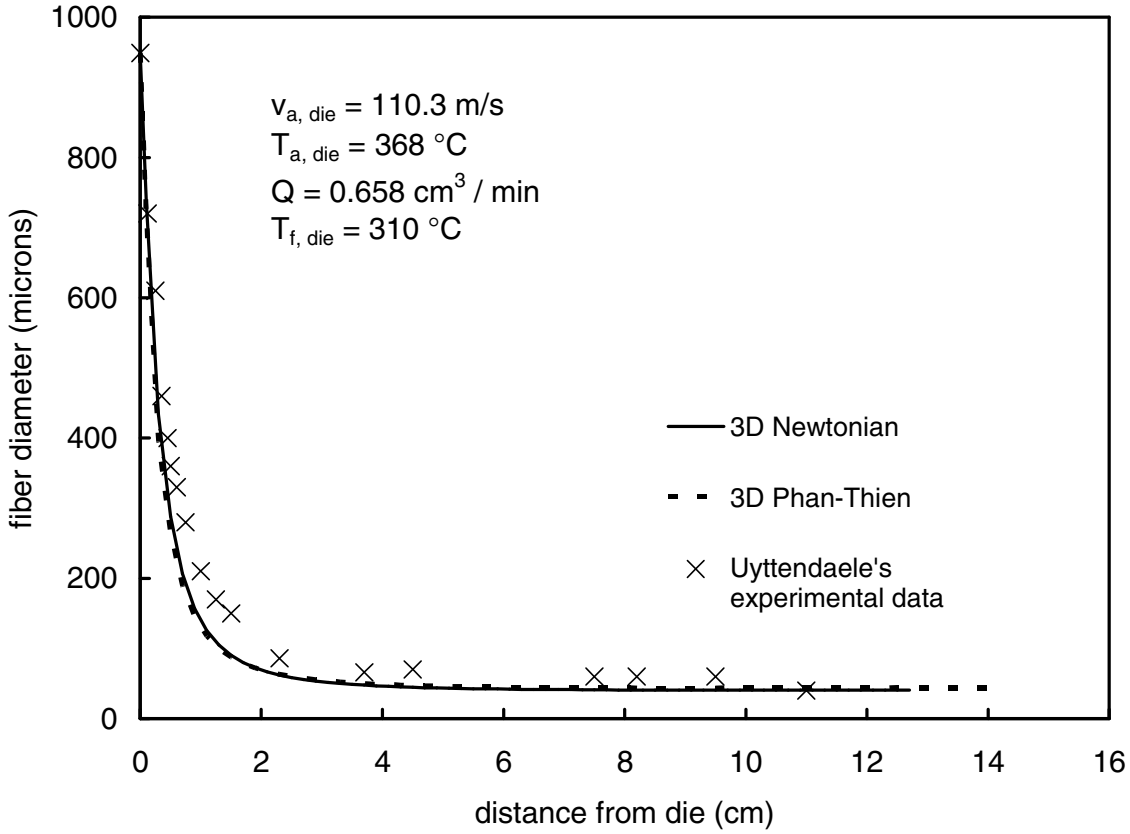

Figure 5. Comparison of fiber diameter profile obtained using a Newtonian constitutive equation with the profile obtained from using a viscoelastic constitutive equation. The profiles are predictions of the 3D model. The experimental data of Uyttendaele are also shown on the figure, and the inputs to the model were the same as listed for Fig. 4. The diameter profiles are averages for t = 5 to 15 s.

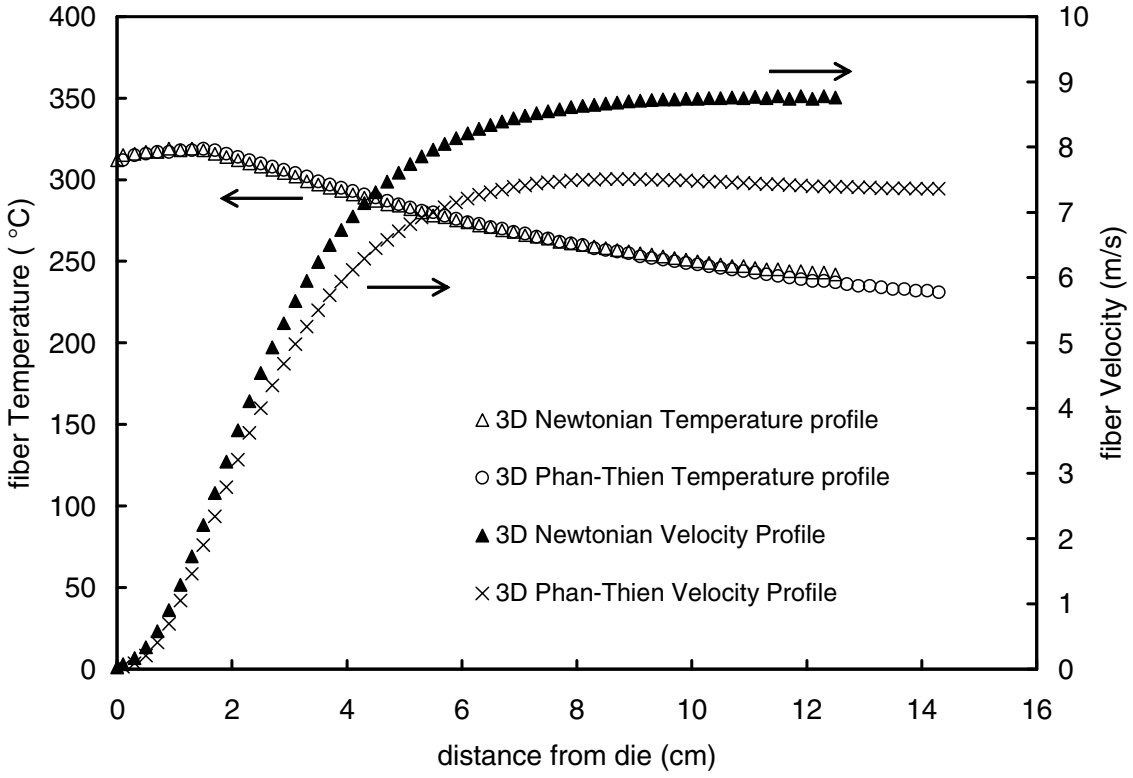

Figure 6. Comparison of fiber temperature and fiber velocity profiles obtained with a Newtonian constitutive equation and with a viscoelastic constitutive equation. The inputs to the model were the same as listed for Fig. 4.

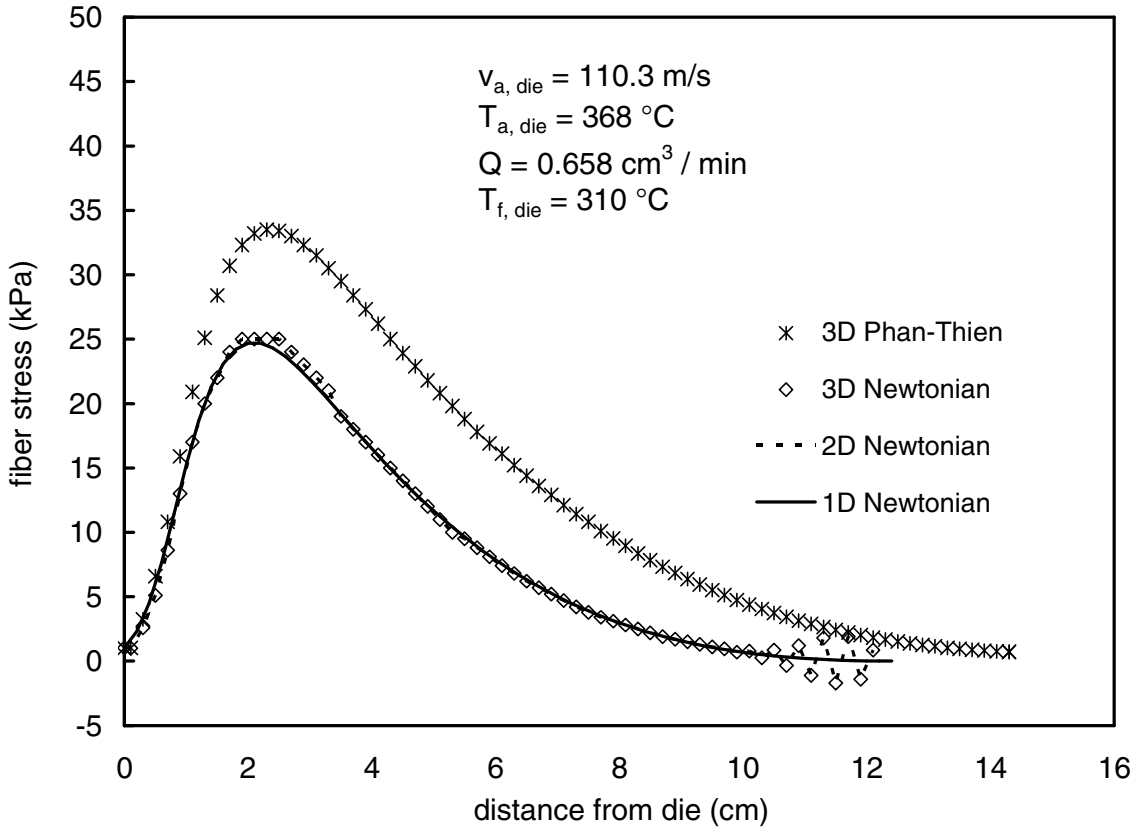

Figure 7. Comparison of fiber stress profile obtained using a viscoelastic constitutive equation in the 3D model with the profiles obtained from using a Newtonian equation in the 1D, 2D and 3D models. The 1D model was Uyttendaele's model modified with the stop point assumption. The inputs to the model were the same as listed for Fig. 4

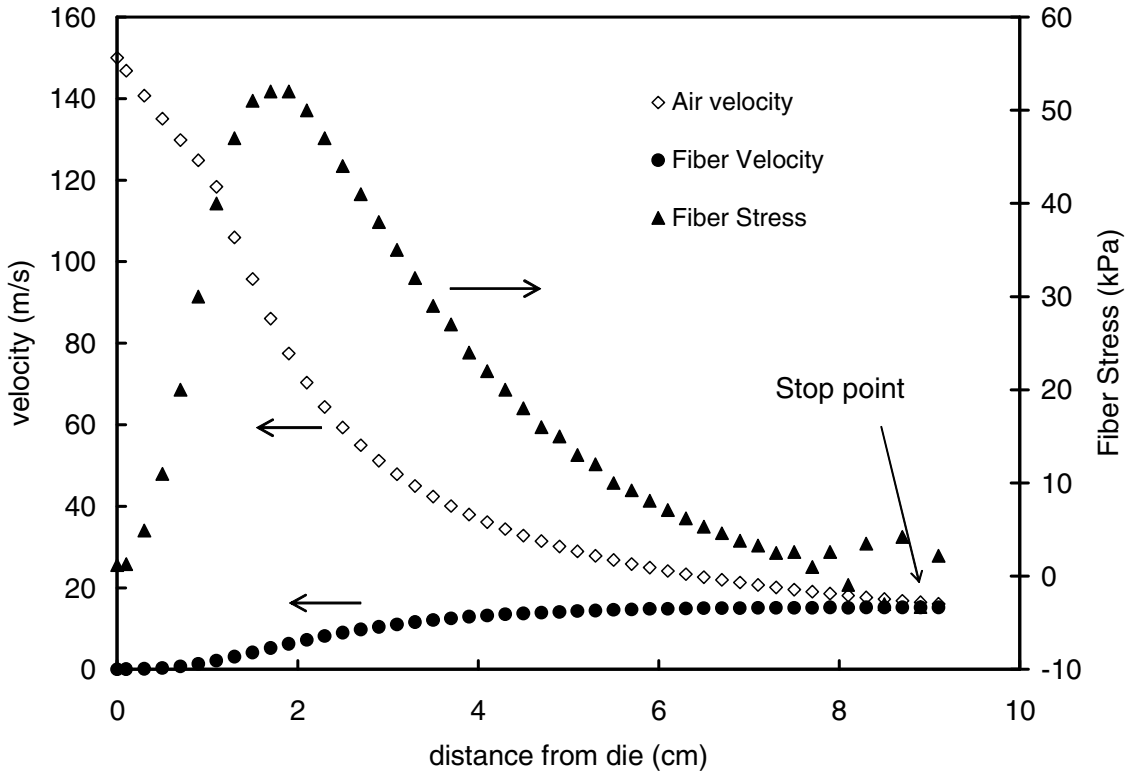

Figure 8. Comparison of fiber velocity, air velocity, and stress along the threadline for 3D Newtonian model. The simulations were run with the experimental conditions used by Rao and Shambaugh (1993): 35 MFR polypropylene (see eq. 71), the velocity and temperature correlations from Majumdar and Shambaugh (1991) for die head "B" (see equations 63-70), and the Phan-Thien parameters listed in this paper. [For this and for all subsequent figures, the correlations for die head "B" were used.] The d_f = 949 μm at die swell, $v_{a,die}$ =150 m/s, $T_{a,die}$ = 368°C, Q = 0.658 cm^3/min, and $T_{f,die}$ = 310°C. The profiles are averages for t = 5 to 15 s

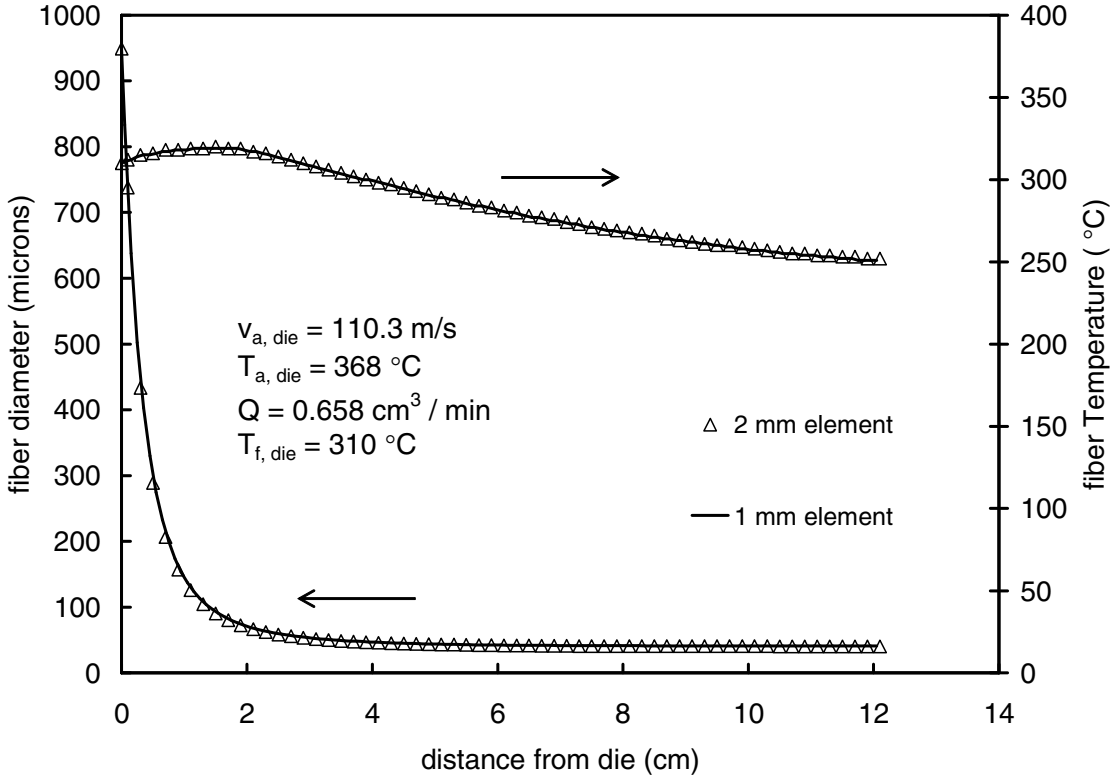

Figure 9. Effect of element step size on the fiber diameter and temperature (3D Newtonian model). Other parameters were the same as listed for Fig. 8

Model	Vibration present	final fiber diameter (μm)	Max elongation rate (s^{-1})	Max stress (kPa)	y location of max elongation rate (cm)	y location of max stress (cm)
1D*	no	41.2	246	24.69	1.80	2.20
1D**	no	41.0	242	24.70	1.75	2.15
2D	yes	40.9	249	24.80	1.85	2.05
3D	yes	40.5	252	25.10	1.90	1.90

Table 1. Effect of Fiber Vibration on Predictions of the 3D Model

*Calculated from Uyttendaele's model modified with the stop point assumption

**Calculated from either 3D or 2D model without fiber vibrations

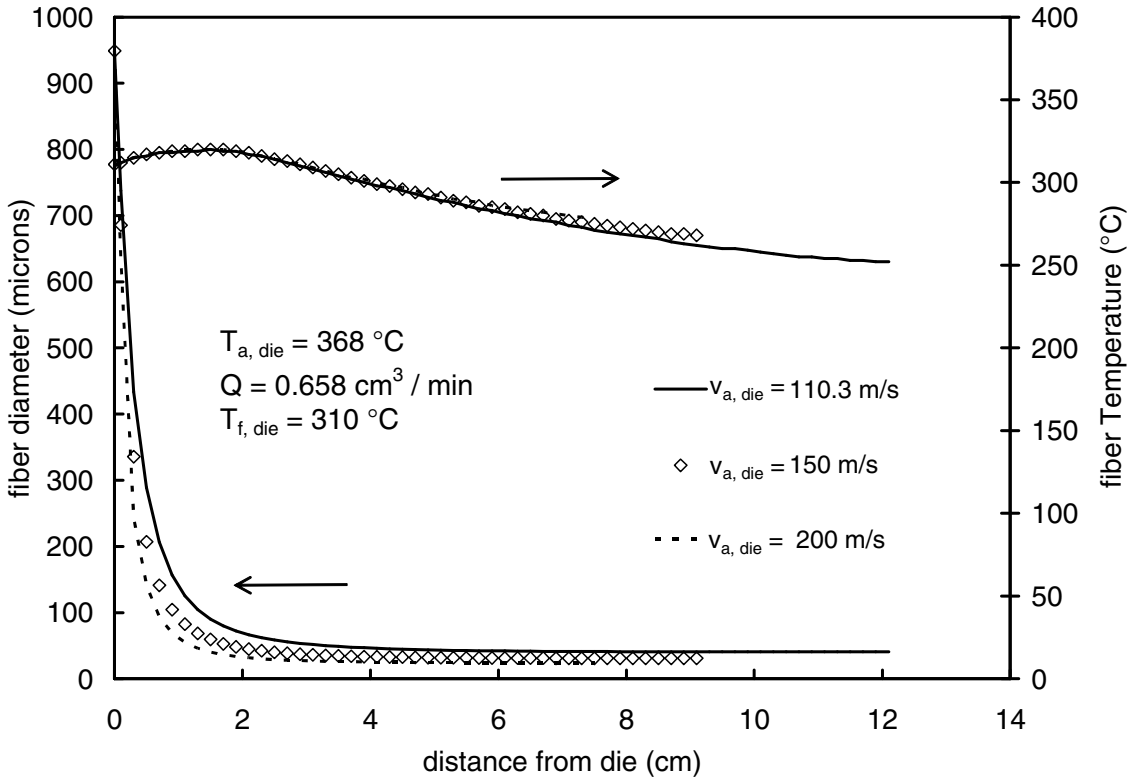

Figure 10. Effect of initial air velocity on fiber diameter and temperature (3D Newtonian model)

Air velocity (m/s)	final fiber diameter (μm)	Max stress (kPa)	y location of max stress (cm)	Peak Amplitude (cm)	Frequency (Hz)
110.3	40.5	25.1	1.9	0.0092	49
150	30.7 – 30.8	52.2	1.7	0.024	91
200	24.0 – 24.3	103 - 105	1.5	0.122	27

Table 2. Range of Fiber Parameters when the Air Velocity Is Varied

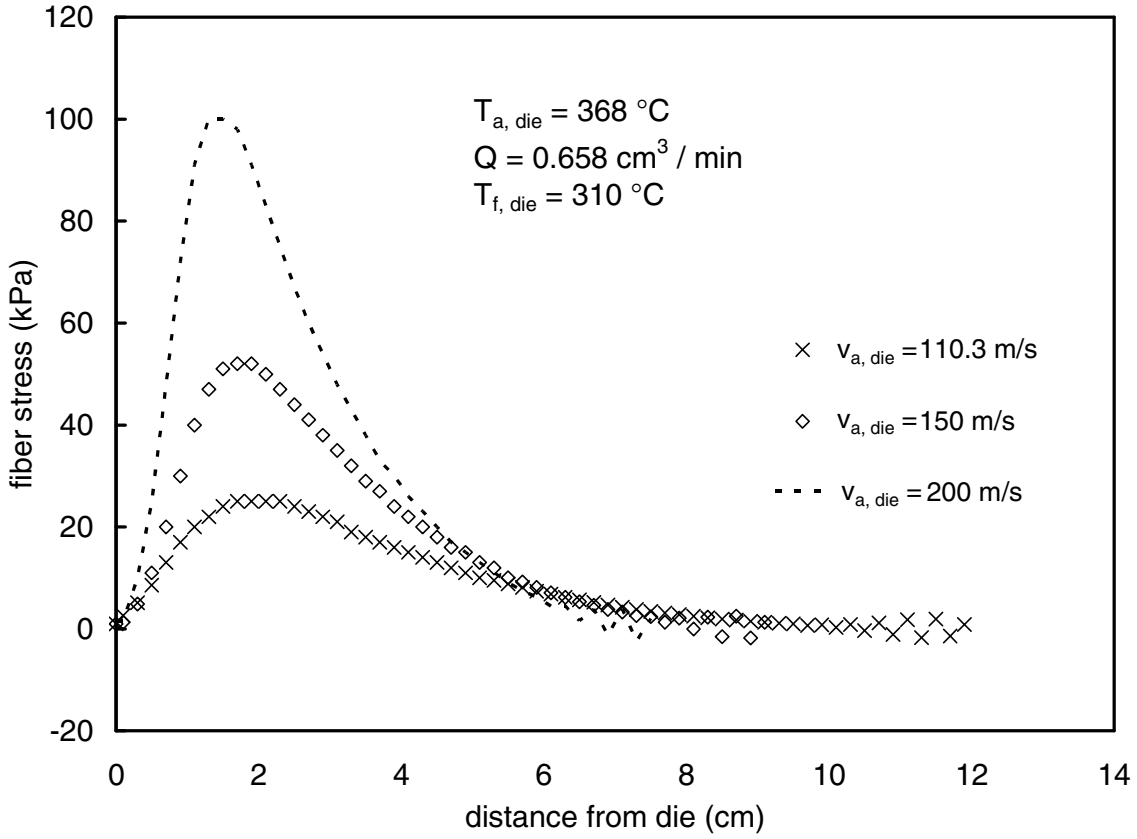

Figure 11. Effect of initial air velocity on rheological stress profile obtained from the 3D Newtonian model.

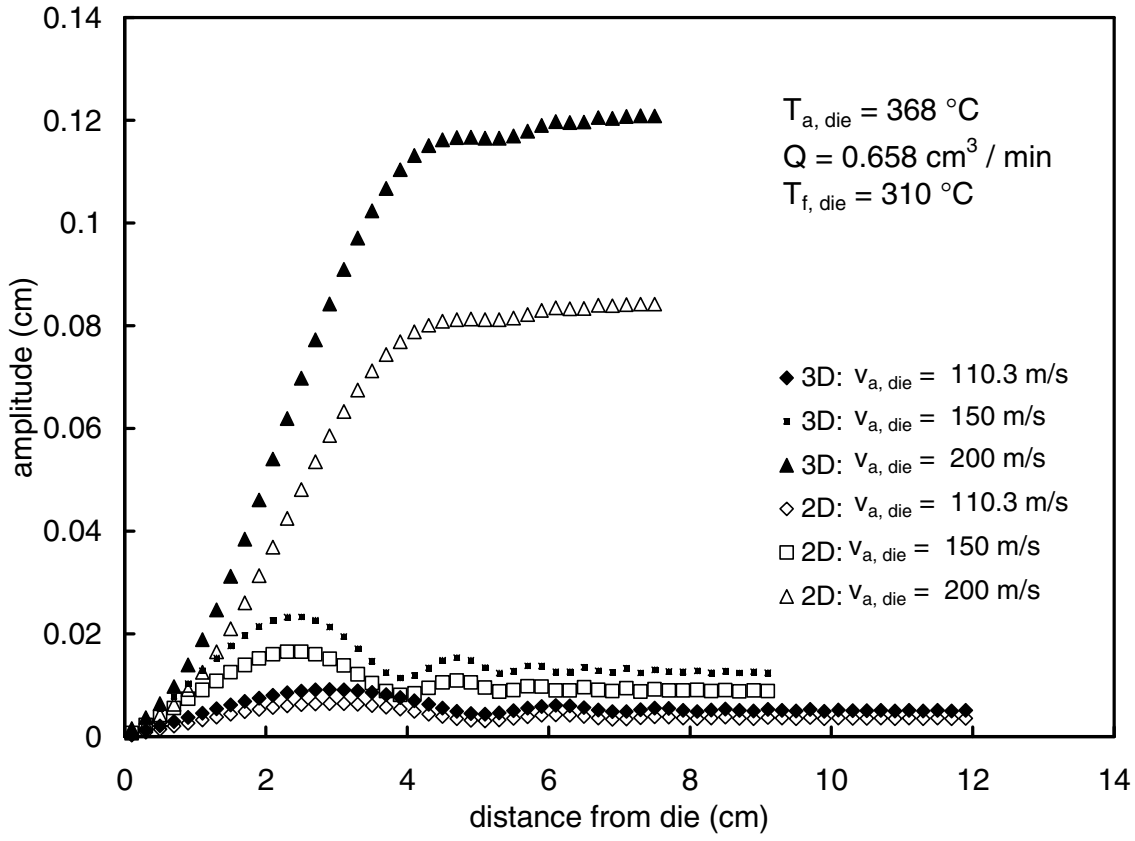

Figure 12. Comparison of amplitude of fiber vibration obtained from the 3D Newtonian model with the 2D Newtonian model. Comparisons are shown for different initial air velocities.

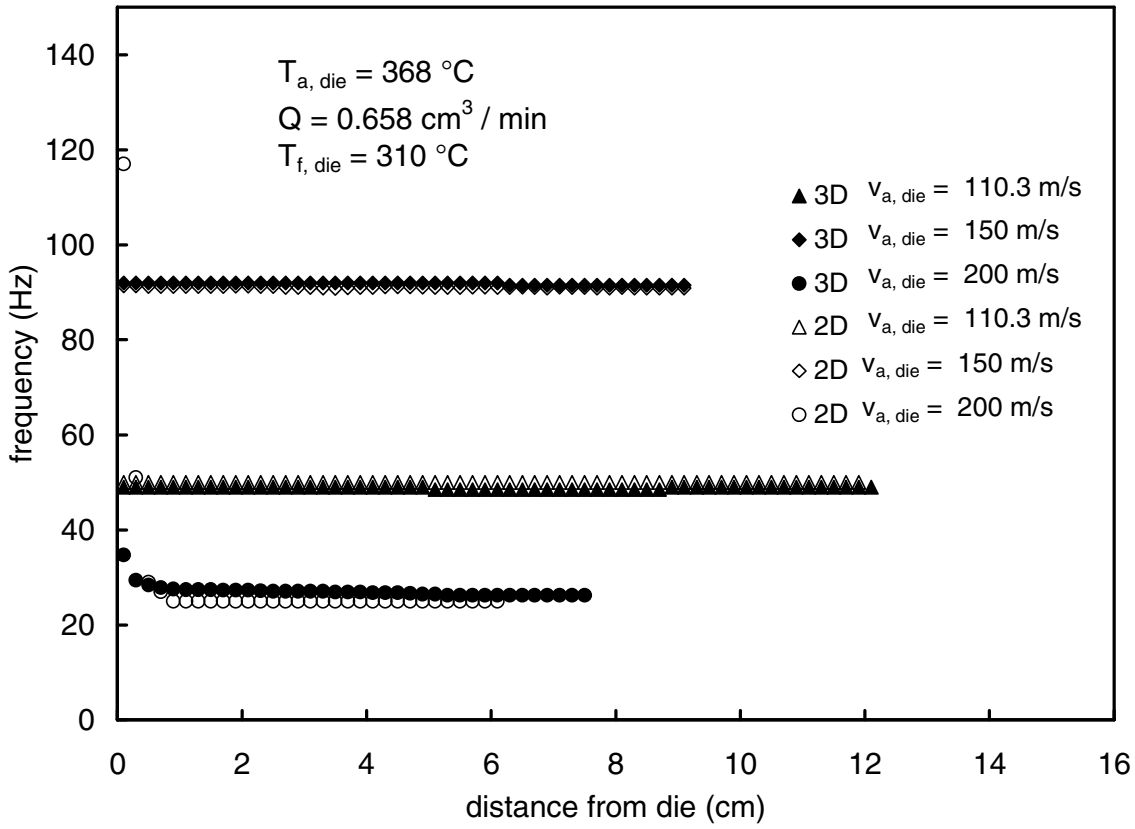

Figure 13. Comparison of frequency of fiber vibration obtained from the 3D model with the 2D model for different initial air velocities. The conditions are same as for Figure 11.

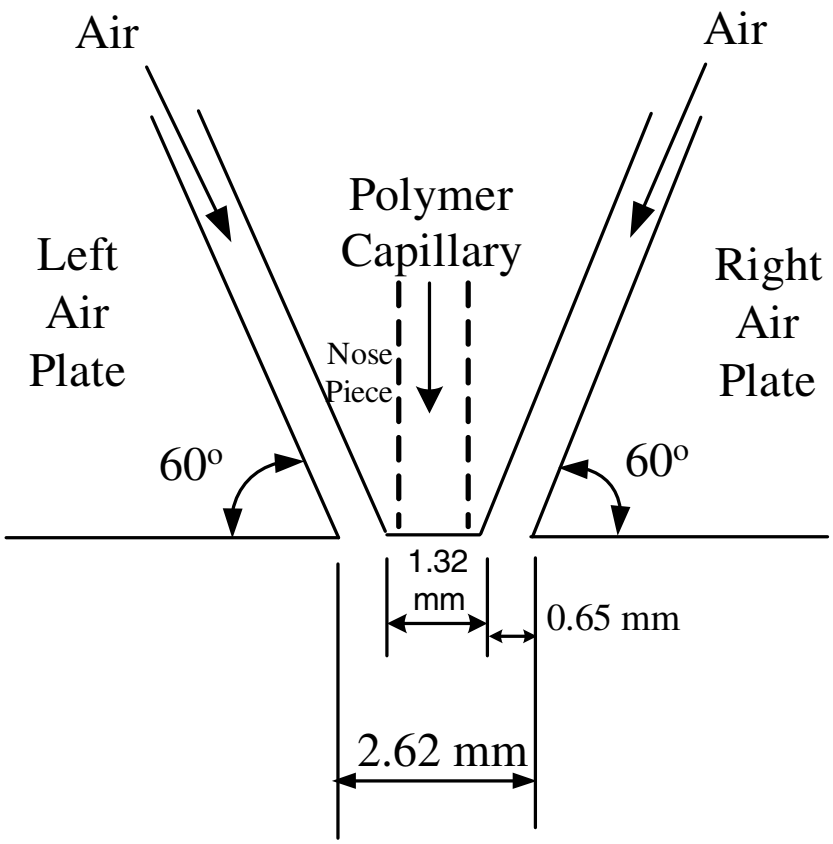

Figure 14. Side view of the air exit region of the experimental die. A width setting of h = 2.62 mm is shown

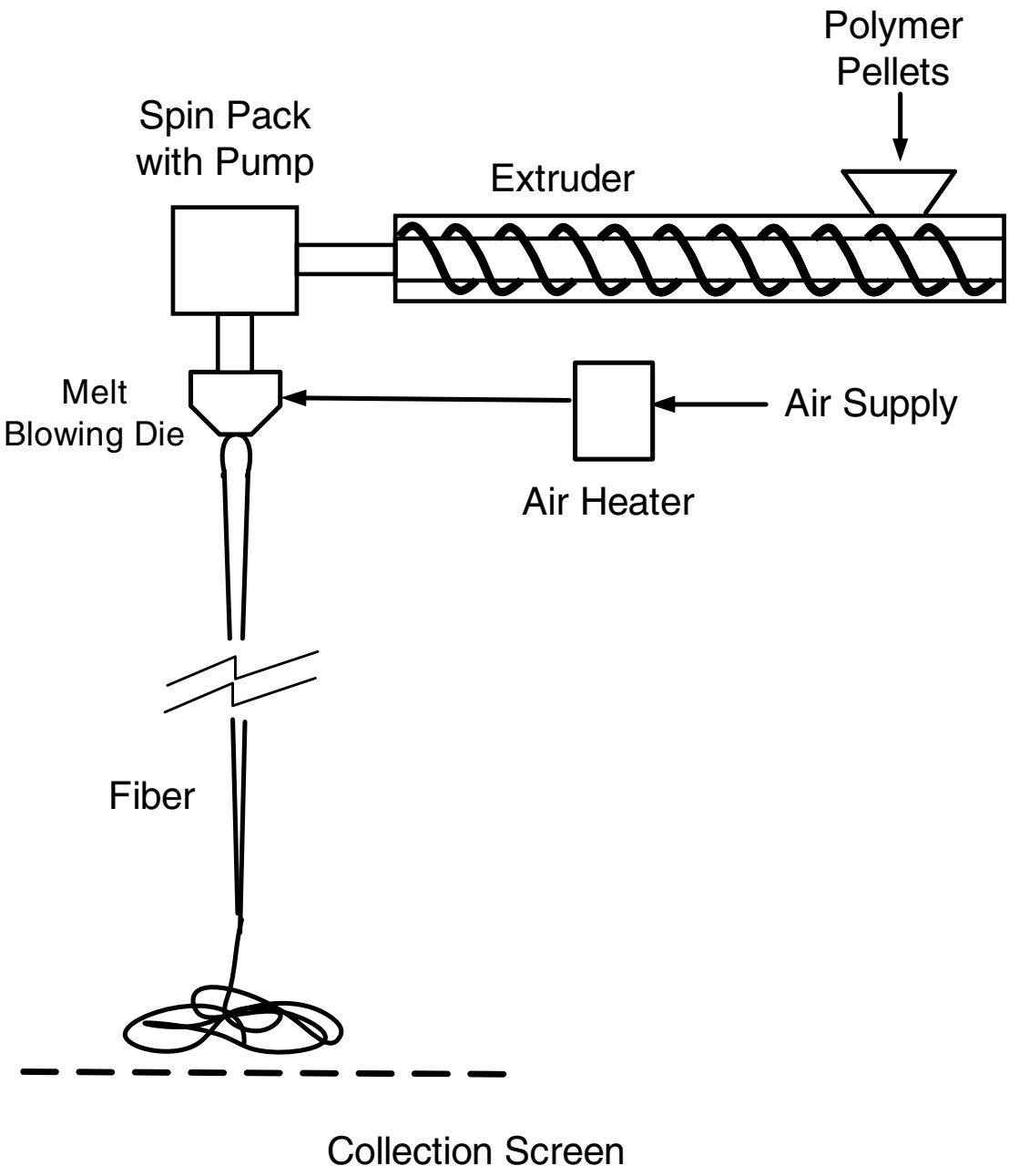

Figure 15. Experimental setup for melt blowing using the slot die.

m (g/min)	$\mathbf{T_{f,die}}$ (°C)	$\mathbf{T_{a,die}}$ (°C)	Final fiber Diameter		Vibration amplitude at y = 4.5 cm	
			Experiment (µm)	**Simulation** (µm)	**Experiment** (mm)	**Simulation** (mm)
0.55	295	330	95 ± 3	95.5 - 96.2	3.00	0.513
1.10	295	330	126 ± 5	134.2 - 135.5	2.625	0.434
0.23	295	330	30 ± 5	56.2 - 56.5	3.375	0.772
0.55	330	330	73 ± 3	74.0 - 75.2	3.75	0.784
0.55	295	380	84 ± 3	85.3 - 86.4	3.215	0.593

Table 3. Summary of results obtained from Experiment and Simulation for different operating conditions

CHAPTER 3

MODELING THE MELT BLOWING OF HOLLOW FIBERS

ABSTRACT

In commercial operation, a melt blowing die is used to produce fine fibers that are solid, not hollow. In this paper, a model was developed to predict what would happen if hollow fibers were produced with a modified melt blowing die. The model involved the simultaneous solution of the momentum, energy, and continuity equations. The model equations were solved numerically. Predicted parameters included fiber hollowness, fiber attenuation, vibration frequency, vibration amplitude, temperature, and stress. Hollowness can affect the laydown pattern of the melt blown fibers.

3.1 Introduction

Hollow fibers have great commercial importance and find wide use as membranes in artificial kidneys, reverse osmosis and ultrafiltration. Other uses for hollow fibers include the production of insulated clothing and fluffy nonwoven materials.[1] Also, from a commercial standpoint, cost savings can be achieved by using hollow fibers since, compared to solid fibers of the same outer diameter, hollow fibers require less polymer. Hollow fiber membranes can be manufactured using dry spinning, wet spinning, or melt spinning. There are two main geometries of spinnerets used in the manufacture of hollow

fibers – annular and segmented (or slit) arc. In the annular geometry, the polymer emerges from the annulus while the lumen fluid flows in the inner core. This arrangement is often referred to as a tube-in-orifice spinneret. In the segmented arc geometry, there is a short distance below the spinneret (prior to where the separate polymer streams coalesce) in which the surrounding air is entrained between the segmented arcs and thereby produces hollowness in the fiber (i.e., some of the surrounding air becomes the lumen fluid).

Several research groups have used experimental measurements and mathematical modeling to investigate the process of manufacturing hollow fibers. Oh et al.[2] used a segmented arc die and obtained the diameter profile by making on-line measurements using a special capturing device, which trapped and froze the filament. The captured filaments were cut with a microtome and the inner and outer fiber diameters were measured with a microscope. They also developed a mathematical model that utilized a finite element method to determine various fiber properties such as inner and outer fiber diameter, temperature, stress, and other parameters along the threadline. Their model indicated that hollow fibers had a greater stress at the solidification point, and this stress was believed to enhance the tensile strength of the fiber. De Rovere and Shambaugh[3] used a tube-in-orifice spinneret geometry to spin hollow and solid fibers from polypropylene. They compared the properties of nonwoven mats made of hollow fibers with mats made from solid fibers. They observed that, for the same outer diameter, the compression-recovery behavior and opacity of mats of hollow fibers were essentially the same as mats of solid fibers. Takarada et al.[4-6] studied the melt spinning process for

making flat, hollow and circular fibers and compared these fibers using experimental and modeling techniques. They made on-line measurements of outer fiber diameter, fiber velocity and threadline tension. A finite difference method was used to solve the transport equations, and they considered both Newtonian and Maxwell models for the constitutive equations. There have been other modeling efforts that examined the sensitivity of fiber equations to changes in process variables.[7,8] Rwei[1] used a C-shaped spinneret and investigated the effect of capillary length, process temperature and shear rate on die-swell and on the formation of hollow fibers. It was observed that, for vinyl polymers such as polypropylene, the die-swell was significant and manufacturing hollow fibers was more difficult for polypropylene than from a condensation polymer. Kim et al.[9] used the thermally induced phase separation (TIPS) process for the formation of hollow fiber membranes and observed the effect of initial composition of melt solution, draw ratio and spinning temperature on the membrane structure. Shen et al.[10] examined the effect of draw ratio, annealing time and temperature, and fiber extension on the microporous membrane structure of polyethylene. De Rovere and Shambaugh[11] spun hollow polypropylene fibers at speeds of 1000-2500 m/min and made on-line measurements of outer fiber diameter using high-speed photography. They formulated a mathematical model and used both a Newtonian equation and a Phan-Thien viscoelastic equation. They concluded that the choice of constitutive equation type was not critically important because of the rapidity of temperature change along the threadline.

All of the above studies involved manufacturing hollow fibers using either dry, wet, or melt spinning. In this paper we propose using melt blowing to manufacture

hollow fibers. Heretofore, melt blowing has not been used for this purpose. Melt Blowing is a single step process for conversion of polymer pellets into nonwoven mats or webs. In melt blowing, high velocity streams of hot air impinge on molten polymer as the polymer is extruded from an array of orifices. These high velocity streams exert a tremendous forwarding or drag force on the molten polymer. This force rapidly attenuate the polymer strands into very fine filaments. Mats made from the melt blowing process are used in baby diapers, wipes, absorbent products, surgical disposables, upholstery, and many other uses. A good overview of the melt blowing process is given by Shambaugh.[12]

In this paper we develop a mathematical model for the formation of hollow fibers via melt blowing and use this model to predict the process conditions needed to produce a range of hollow fibers. In the past, there have been several models developed for melt blowing.[13-15] We will formulate our model by making modifications to equations developed in these previous models. Our steady state model will be based on the model developed by Uyttendaele and Shambaugh[13], while our 3-D model will be based on the work of Marla and Shambaugh.[15] One of the desired outcomes of this modeling work will be the effect of hollowness on fiber vibration frequency. This frequency can affect the uniformity of the fiber mats as well as the line speed – both of these factors are of great commercial importance.

For our modeling of the melt blowing of hollow fibers, we assume a die configuration as shown in Figure 1. While the basic geometry of this die is similar to the die used in the modeling work of Uyttendaele and Shambaugh[13] and Marla and Shambaugh,[15] there is the added complexity of having a center inlet for the lumen fluid

(i.e., the die is now a type of tube-in-orifice spinneret). The assembly shown in Figure 1 involves the following three fluids: lumen fluid (nitrogen gas, in our case), polymer flowing through an annulus, and high-velocity air flowing on the outside of the polymer stream. The mass flow rate of nitrogen gas controls the fiber hollowness. Since the lumen fluid (core fluid) pressure is only slightly greater than the atmospheric pressure, lumen fluid compressibility effects are negligible.[11] The hot air's primary task is what it normally does in melt blowing: the air exerts a substantial drag force that attenuates the fiber.

3.2 Formulation of Steady-state Uni-dimensional (1-D) Model

Under mild melt blowing conditions (when the air velocity is relatively low), fiber vibration is not too severe. In this situation, a 1-D melt blowing model has been found to be adequate; see Uyttendaele and Shambaugh.[13] For the modeling of hollow fiber melt blowing, the equations of Uyttendaele and Shambaugh need to be modified. In particular, the rheological force in hollow fiber melt blowing acts on an annular, rather than a circular, cross-sectional area of the polymer. For the case of melt spinning (not melt blowing) of hollow fibers, the suitable equations have already been developed by de Rovere and Shambaugh.[11] These same equations can also be used to model melt blowing, if we account for the different boundary conditions that occur during melt blowing.

Based on the work of de Rovere and Shambaugh, the application of the continuity equation to both the polymer and lumen streams gives

$$\rho_f A_p v_{f,y} = m_p = \text{constant} \qquad (1)$$

and

$$\rho_n \frac{\pi}{4} D^2 v_{f,y} = m_n = \text{constant} \tag{2}$$

where

$$A_p = \frac{\pi}{4}(d^{\ 2} - D^2) \tag{3}$$

It is implicit in eq 2 that the velocity of the polymer and the lumen fluid are the same.

The differential form of the momentum equation is

$$\frac{d}{dy}\left[A_p(\tau^{yy} - \tau^{x'x'})\right] + \pi d\ C_f \rho_a \frac{v_{rel}^2}{2} + A_p \rho_f g = m_p \frac{dv_{f,y}}{dy} \tag{4}$$

For this 1-D case, the vertical coordinate y corresponds to the coordinate direction along the fiber axis. For the 3-D case that will be discussed below, the coordinate direction along the fiber axis is z and, thus, y must be replaced with z in eq 4.

The equation of energy is

$$m_p C_{\rho,f} \frac{dT_f}{dy} = -\pi h\ d\ (T_f - T_a) \tag{5}$$

Equations 1, 4 and 5 (with eqs 2 and 3) can be solved simultaneously using the 4th order Runge-Kutta method. The dependent variables in this case are the fiber velocity, fiber temperature and fiber stress.

3.3 Formulation of 3-D model

Similar to the development of the 1-D equations, the 3-D equations must account for the fact that the rheological forces act on an annular (or hollow ellipse) cross-sectional

area. With this modification, the ordinary differential equations from Marla and Shambaugh[15] become

$$\frac{dm_i}{dt} = -\left[(\rho_f v_{f,y} A_p)\Big|_{l+\Delta l} - (\rho_f v_{f,y} A_p)\Big|_l\right]\Big|_i \tag{6}$$

$$\frac{dv_{f,x,i}}{dt} = \frac{1}{m_i}\left(-v_{f,x,i}\frac{dm_i}{dt} - \left[(\rho_f v_{f,y} A_p v_{f,x})\Big|_{l+\Delta l} - (\rho_f v_{f,y} A_p v_{f,x})\Big|_l\right]\Big|_i + (F_x - F_{rheo,x,l} + F_{rheo,x,l+\Delta l})\Big|_i\right) \tag{7}$$

$$\frac{dv_{f,y,i}}{dt} = \frac{1}{m_i}\left(-v_{f,y,i}\frac{dm_i}{dt} - \left[(\rho_f v_{f,y} A_p v_{f,y})\Big|_{l+\Delta l} - (\rho_f v_{f,y} A_p v_{f,y})\Big|_l\right]\Big|_i + (mg_y + F_y - F_{rheo,y,l} + F_{rheo,y,l+\Delta l})\Big|_i\right) \tag{8}$$

$$\frac{dv_{f,w,i}}{dt} = \frac{1}{m_i}\left(-v_{f,w,i}\frac{dm_i}{dt} - \left[(\rho_f v_{f,y} A_p v_{f,w})\Big|_{l+\Delta l} - (\rho_f v_{f,y} A_p v_{f,w})\Big|_l\right]\Big|_i + (F_w - F_{rheo,w,l} + F_{rheo,w,l+\Delta l})\Big|_i\right) \tag{9}$$

$$\frac{dT_{f,i}}{dt} = \frac{1}{(m_i C_{p,f,i})}\left(-C_{p,f,i}T_{f,i}\frac{dm_i}{dt} - \left[(\rho_f v_{f,y} A_p C_{p,f} T_f)\Big|_{l+\Delta l} - (\rho_f v_{f,y} A_p C_{p,f} T_f)\Big|_l\right]\Big|_i - \left[h\pi\frac{d_l + d_{l+\Delta l}}{2}\Delta z(T_f - T_a)\right]\Big|_i\right) \tag{10}$$

$$\frac{dx_{f,i}}{dt} = v_{f,x,i} \tag{11}$$

$$\frac{dw_{f,i}}{dt} = v_{f,w,i} \tag{12}$$

Beyond the development given in Marla and Shambaugh, a mass balance on the lumen fluid is needed. This balance is

$$\frac{dM_i}{dt} = -\left[\left(\rho_n v_{f,y} A_h\right)\Big|_{l+\Delta l} - \left(\rho_n v_{f,y} A_h\right)\Big|_{l}\right]\Big|_{i} \tag{13}$$

Refer to the Nomenclature section for definitions of the symbols

Cross-Sectional Areas of the Fiber at the Control Surfaces

In a manner similar to that described in Marla and Shambaugh, the cross-sectional area of the hollow (lumen) portion of the fiber element at any control surface is

$$A_{h,i,l} = \pi\left(\frac{D_{i,l}^{\,2}}{4\cos(\alpha_{i,l})\cos(90-\phi_{i,l})}\right) \tag{14}$$

Refer to Fig. 2. The cross-sectional area of the fiber (polymer) at any control surface is dependent on the hollowness in the fiber. The correct formula for this area is

$$A_{i,l} = \pi\left(\frac{d_{i,l}^{\,2} - D_{i,l}^{\,2}}{4\cos(\alpha_{i,l})\cos(90-\phi_{i,l})}\right) \tag{15}$$

This is the appropriate formula for the A_p used in equations 6-10.

To determine inner fiber diameter, D_i, a hollow fiber element (i.e., an element of the lumen fluid) can be approximated as the frustum of a cone (see Figure 2). The mass M_i of the nitrogen in the hollow element can then be defined as

$$M_i = \rho_n \pi \frac{\Delta l}{12\cos(\alpha_i)\cos(90-\phi_i)}\left(D_{i,l}^{\,2} + D_{i,l}D_{i,l+\Delta l} + D_{i,l+\Delta l}^{\,2}\right) \tag{16}$$

To calculate the inner diameter profile at a particular time t, eq 16 is used by first starting at the top element of the threadline where D_l is known. The bottom diameter $D_{l+\Delta l}$ can then be determined because M_i is known.

Refer again to Fig. 2. The volume of the polymer in the fiber element in the control volume can be calculated by subtracting the volume of the inner frustum (containing the lumen fluid) from the volume contained in the entire control volume (which is also approximately a frustum). Multiplying this volume difference by the polymer density then gives the polymer mass. The appropriate formula is

$$m_i = \rho_f \pi \frac{\Delta l}{12\cos(\alpha_i)\cos(90-\phi_i)}\left(d_{i,l}{}^2 + d_{i,l}d_{i,l+\Delta l} + d_{i,l+\Delta l}{}^2\right) -$$

$$\rho_f \pi \frac{\Delta l}{12\cos(\alpha_i)\cos(90-\phi_i)}\left(D_{i,l}{}^2 + D_{i,l}D_{i,l+\Delta l} + D_{i,l+\Delta l}{}^2\right) \qquad (17)$$

In the above equation, D_l and $D_{l+\Delta l}$ are known from eq 16 and hence $d_{l+\Delta l}$ is the only unknown. Successive application of equations 16 and 17 allows the determination of the entire inner and outer diameter profile. As can be clearly seen from the above equations, when the hollowness is zero, the model collapses to the model developed for solid fibers (see Marla and Shambaugh[15]).

3.4 Model Inputs and Solution Details

For our modeling work, the correlations for estimating the heat transfer coefficient, air velocity, air temperature, polymer viscosity and aerodynamic drag force coefficient

were taken from the paper by Marla and Shambaugh.[15] It has been shown in the past[13,15] that a Newtonian constitutive equation is adequate for modeling melt blowing. (Apparently, it is the temperature dependence of viscosity that is the dominant effect in determining the fiber diameter.) Hence, for our work a Newtonian constitutive equation was used in the momentum equations. This selection substantially reduced the computer time required for the simulations.

The equations were solved for a simulated time of 15 s and, unless otherwise stated, the simulation predictions for all figures are averages of the results for the time period 5-15 s. As shown in Rao and Shambaugh[14], since this time period begins at a time greater than 2 seconds, the time period is located where the predicted properties have reached a constant range of values. The length of each control volume was fixed at 2 mm (as suggested in the 3D model of Marla and Shambaugh). The initial and boundary conditions were also the same as in the 3D model developed previously for solid fibers. However, an additional boundary condition was required to characterize the hollowness at the die. Also, in addition to the outer diameter profile, the inner diameter profile was specified as an initial condition. The maximum outer diameter (die swell) of the polymer near the die exit, d_{die}, was kept constant at 949 μm for all simulations. The initial hollowness at the die was specified, which was equivalent to specifying the lumen fluid flow rate. The percentage hollowness of a hollow fiber was defined as

$$\% \text{ hollowness} = H = \left(\frac{D}{d}\right)^2 \text{ x } 100$$

The density of nitrogen was calculated from the formula[11]

$$\rho_n = \frac{339}{T_f^{1.001}} \tag{17}$$

The velocity of the polymer, $v_{f,die}$, was kept the same for all the simulations unless otherwise stated. (This was set at 0.0155 m/s, corresponding to the value used by Uyttendaele and Shambaugh,[13] Rao and Shambaugh,[14] and Marla and Shambaugh.[15].) Hence, specifying the initial hollowness was equivalent to specifying D_{die}, from which the volumetric flow rate of the lumen fluid was calculated using the equation

$$Q_n = \frac{\pi}{4} D_{die}^2 v_{f,die} \tag{18}$$

In addition to the specification of $d_{die} = d_{f,die} = 949$ μm, the other base conditions for the simulations, unless otherwise specified, were

$v_{f,die} = 0.0155$ m/s

$v_{a,die} = 110.3$ m/s

$T_{f,die} = 310$ °C

$T_{a,die} = 368$ °C

Results and Discussion

For an initial hollowness of 10 %, Figure 3 shows the outer diameter profile obtained from the modified Uyttendaele and Shambaugh (1D) model and the 3D model. There is close agreement between the two models. The final outer diameter predicted by the modified Uyttendaele and Shambaugh model is 41.15 μm, while that predicted by the 3D model is 38.6 μm. For the same initial hollowness of 10 %, Figure 4 shows the inner diameter profile obtained from the two models. Again, the two profiles are very similar

with a final inner diameter of 12.16 μm from the modified Uyttendaele and Shambaugh model and 12.19 μm from the 3D model. Similar agreement between the two models was also found for simulations done with initial hollowness of 25 %, 50 %, and 75 %. Since the diameter predictions of the 1D model and the 3D model are essentially equivalent, all other simulations were done with the 3D model since it yields additional information such as fiber vibration amplitude and frequency. From this point onwards, unless otherwise stated, all presented results were obtained from simulations using the 3D model

Figure 5 compares the outer diameter profiles obtained from the 3D model for simulations done with different initial hollowness. The polymer velocity ($v_{f,die}$) and the initial outer fiber diameter ($d_{f,die}$) were kept constant at 0.0155 m/s and 949 μm, respectively. These values correspond to the values used in previous models.[13-15] Observe that the polymer flow rate, m_p, is not constant, but decreases in proportion to $\left(1-\frac{H}{100}\right)$. Hence, an initial hollowness of 25 % means D_{die} = 474.5 μm. This corresponds to a nitrogen volumetric flow rate of 0.164 ml/min (at 1 atmosphere pressure and 21 ˚C). From the continuity equation and the definition of H, the polymer mass flow rate can be written as

$$m_p = \rho_f \frac{\pi}{4} d_{die}^2 v_{f,die} \left(1 - \frac{H}{100}\right) \qquad (19)$$

From the above formula, it is clear that, as the percent hollowness is increased from 0 to 25 %, the polymer flow rate decreases to 75 % of its flow for a solid fiber. Similarly, polymer flow decreases to 50 % and 25 % for initial hollowness of 50 % and 75 %, respectively. These results are summarized in Table 1. As can be seen in Figure 5, the

attenuation rate increases with increasing hollowness, which results in finer fibers. Also, the final outer diameter decreases steadily with increased hollowness: the final diameter is 40 µm in the case of solid fibers, while the outer diameter is only 20 µm when the hollowness is 75 %. These results are similar to the results obtained by previous researchers for solid fiber spinning. Since increasing the initial hollowness while keeping $v_{f,die}$ constant corresponds to decreasing the polymer flow rate, the results obtained are not unexpected.

In our simulations, the predictions of fiber diameters proceed in the y direction from the spinneret until the stop point is reached. As defined by Rao and Shambaugh,[14] the stop point is where the fiber velocity equals the air velocity. The stop point moves closer to the die as the percent hollowness increases. This is expected because, as hollowness increases, the attenuation rate increases, and the fiber velocity consequently increases more rapidly along the y direction. Thus, the crossover point of the fiber and air velocities moves closer to the die. This phenomenon can be observed in Fig. 5, where the right ends of the simulated profiles correspond to the stop points of the respective simulations.

For the same conditions shown in Fig. 5, Fig. 6 shows how hollowness affects the fiber temperature profile. In the first several centimeters below the spinneret, the more hollow fibers heat more rapidly (in the hot melt blowing air) than the less hollow filaments. Now, a hollow fiber would be expected to heat or cool more quickly than a solid fiber (with the same outer diameter), because the hollow fiber has less mass and, hence, less thermal inertia. However, as shown in Fig. 5, the diameters of the filaments

decrease as a function of hollowness. Finer filaments have less surface area for heat transfer, so this effect would tend to reduce the rate of temperature change of the more hollow filaments. In addition, the finer filaments move more quickly (they have higher v_f), so there is less residence time for heating/cooling in the melt blowing air. This would also tend to reduce the rate of temperature change. These three effects interact to produce the temperature profiles shown in Fig. 6. Beyond about 4 cm from the die, the three effects tend to balance each other out, and the profiles are nearly coincident.

The variation of the percent hollowness along the threadline for simulations performed with different initial hollowness was also examined; see Figure 7. The percent hollowness decreases along the threadline, but the decrease is not drastic. For 10 %, 25 %, and 50 % hollowness, the hollowness at the stop point is, respectively, 9 %, 7 %, and 3 % less than the hollowness starting at the die. These results were similar to those obtained by de Rovere and Shambaugh[11] for hollow fibers produced from the spunbonding process. They observed that the ratio of the inner to outer diameter did not change more than 10-15 % along the threadline. Similar trends in melt spinning were obtained by other researchers as well.[2,7] Also shown on Figure 7 are the profiles when the density of the lumen fluid is assumed constant. These hollowness profiles are independent of threadline position, as is expected from the continuity equations for the polymer and the lumen fluid.

The effect of initial hollowness on the fiber stress is shown in Figure 8. As the initial hollowness increases, the attenuation rate increases (see Fig. 5) and the fiber velocity increases rapidly, resulting in an increase in the fiber velocity gradient. Since the

fiber stress is proportional to the fiber velocity gradient (in the Newtonian constitutive equation), the fiber stress increases. As can be seen in the figure, there is almost an order of magnitude increase in the maximum fiber stress for the 75% hollow fibers compared with the 0% hollow (solid) fibers. Also, the position of the maximum stress moves closer to the die as the hollowness increases. The stress predictions are helpful in understanding such phenomena as fiber crystallization, fiber orientation, and cohesive threadline fracture. The tensile strength of polypropylene drops from 10^6 kPa at room temperature[16] to 30 kPa at 180 °C.[17] This suggests that, under the listed operating conditions, breakup of the fiber stream is possible above 50 % hollowness.

Figure 9 shows the effect of initial hollowness on the amplitude of the fiber vibration. Higher percent hollowness corresponds to lower polymer mass throughput. Since the air velocity is constant, the loading (m_n/m_p) is higher for the higher percent hollowness. Thus, as expected, the amplitude increases as the percent hollowness increases (compare Fig. 9 with the amplitude results in Marla and Shambaugh[15]). The maximum fiber amplitude increases by almost 100 % when the initial hollowness is increased from zero (solid fibers) to 75 %.

The effect of hollowness on fiber vibration frequency is shown in Fig. 10. The fiber frequency increases relatively slowly as the initial hollowness increases from 0 to 50 %. But when the frequency is further increased to 75 %, there is a fairly significant increase to 172 Hz. Overall, the frequency increases by more than 300 % when the hollowness is increased from zero to 75 %. The range of frequencies shown in Fig. 10 is typical for melt blowing.[18]

(With respect to the accuracy of the frequency predictions, keep in mind that the largest step size we used was only 20 μs. Therefore, the sampling frequency was 1/(20 μs) = 50 kHz. Hence, the ratio of sampling frequency to the largest observed frequency = $\frac{50x10^3}{172}$ = 290. Since this ratio is greater than 2, the Nyquist criterion is satisfied.[19] This calculation is for the worst case.)

Effect of Lumen Gas Flow Rate when Polymer Mass Rate is Constant

In Figures 5-10, polymer mass rate was variable. For a constant mass flow rate of 0.5 g/min, Figure 11 shows the effect of lumen gas flow rate on the outer fiber diameter. The lumen gas rate was increased so as to obtain initial hollowness (i.e., hollowness at the die head) of 10, 20, 40, and 50%. The final outer fiber diameter increases from 40 μm to 50 μm (a 25% increase) as the initial fiber hollowness ranges from zero (solid) to 50 %. These results parallel those of De Rovere and Shambaugh.[11] Similar to the solid fiber diameter profile, the diameter profile for the hollow fibers shows rapid attenuation close to the die, followed by an asymptotic behavior till the stop point. The attenuation rate slightly decreases with increase in the lumen gas flow rate.

For a constant polymer rate of 0.5 g/min, Figure 12 shows that increasing the initial hollowness results in an increase in the fiber vibration frequency. The frequency increases from 50 Hz to 67 Hz as we move from solid fibers to fibers with an initial hollowness of 50 %. As was the case in Fig. 10, the frequency remained essentially constant along the threadline. (As a vibrating mechanical system, a threadline generally

exhibits the same frequency at all positions along the threadline.) Since vibration frequency and amplitude can affect the laydown pattern of melt blown fibers, it is possible to use % hollowness as a control variable for optimizing laydown.

Effect of Die Head Temperature

Die head temperature is an important operating parameter in melt blowing. In the previous figures, die head temperature ($T_{f,die}$) was held constant. To investigate the effect of die head temperature, the nitrogen flow rate was adjusted to 0.166 ml/min (at 1 atmosphere pressure and 21°C), which gave an initial hollowness of 20 % while the polymer mass flow rate was kept constant at 0.5 g/min. Under these conditions, Figure 13 shows the outer diameter profile predicted by the model when the temperature at the die is increased from 310°C to 400°C. The attenuation rate increases and the final predicted outer diameter decreases with increase in the die head temperature. This is expected behavior because of the reduction in polymer viscosity at higher die temperatures. Increasing $T_{f,die}$ from 330°C to 400°C also causes the final outer diameter to decrease from 40 µm to 33 µm, while the final inner fiber diameter decreases from 18 µm to 15 µm. These results are similar to those obtained from simulations where the effect of die head temperature on solid fibers was investigated.

Figure 14 shows that the fiber velocity increases rapidly when the temperature at the die head is raised. The final fiber velocity in the 400°C case is almost double that of the 330°C case. The stop point moves progressively closer to the die head as the die head temperature is raised. In addition, the increase in the velocity profile's slope shows that

the fiber acceleration becomes higher in the region close to the die. This acceleration is shown more clearly in Fig. 15. For all gradient profiles, the gradient goes through a maximum between about 1.5 and 2.5 cm from the die. All profiles then decrease and, after 3.5 cm below the die, all exhibit nearly coincident profiles. Yin et al.[20] and Bresee and Ko[21] experimentally measured the peak fiber accelerations in the range of 80,000 to 100,000 m/s^2 for the melt blowing of ordinary solid fibers. Their measured values are higher than the simulated values in Fig. 15 since their operating air velocities are high in comparison to the conditions used in our simulations. However, they obtained a functional form similar to that predicted by our model.

Figure 16 shows that the fiber vibration amplitude increases dramatically with an increase of 70 °C in the die head temperature. This is analogous to the results obtained for solid fibers by Marla and Shambaugh. The amplitude increases to 1.2 mm for the 400°C case, which is almost a 450 % increase compared to the 330°C case. Table 2 shows that the frequency drops with an increase in the die head temperature. The vibration frequency for the 400°C case drops to 1/3rd the value predicted for the 330°C case. These trends, again, parallel those obtained for solid fibers.

3.5 Conclusions

Simulations show that, if hollow fibers are produced in the melt blowing process, there are distinct differences from the ordinary commercial process of melt blowing solid filaments. On the basis of a constant final outside diameter (in the melt blown web), hollow fibers require less polymer, which constitutes a very substantial cost savings.

During the attenuation of hollow fibers, the fibers are subjected to greater stress than solid filaments. This higher stress could result in stronger filaments. Also, the hollow fibers have higher fiber amplitude and higher frequency than solid filaments. These two factors could increase the quality of fiber laydown in terms of web uniformity. Furthermore, these two factors may allow an increase in line speed.

Acknowledgements

This work was supported by an NSF GOALI grant (DMII-0245324). The support of 3M and Procter & Gamble is also gratefully acknowledged.

Nomenclature

A_p = cross-sectional area of the fiber (polymer only) at location y (or for the 3-D model) along the threadline, m^2

A_h = cross-sectional area of the lumen fluid at location y (or z for the 3-D model) along the threadline, m^2

C_f = friction factor for parallel flow of fluid along the filament surface

$C_{p,f}$ =fiber heat capacity, J/(kg·K)

D = inner diameter of the fiber, m

D_{die} = inner diameter of the fiber at the die (y = 0), m

d_{die} = outer diameter of the fiber at the die (y = 0), m

d = outer diameter of the fiber, m

F_w = aerodynamic force on the filament in the w direction, N

F_x = aerodynamic force on the filament in the x direction, N

F_y = aerodynamic force on the filament in the y direction, N

F_{rheo} = rheological force, N

g = gravitational acceleration, m/s^2

H = percent hollowness as defined by eq 19

h = convective heat transfer coefficient, $W/m^2 \cdot K$

l = y value at upper control surface of the control volume; see Fig. 1

$l + \Delta l$ = y value at lower control surface of the control volume; see Fig. 1

m = fiber mass, kg

M = mass of the lumen fluid (nitrogen gas), kg

m_n = mass flow rate of nitrogen, kg/s

m_p = mass flow rate of the polymer, kg/s

Q_n = volumetric flow rate of nitrogen, m^3/s

T_a = air temperature, °C

$T_{a,die}$ = air temperature at die (y = 0), °C

T_f = filament temperature, °C

$T_{f,die}$ = filament temperature at die (y = 0), °C

v_a = free stream air velocity, m/s

$v_{a,die}$ = air velocity at the die (y = 0), m/s

v_f = fiber velocity, m/s

$v_{f,die}$ = fiber velocity at the die (y = 0), m/s

w = Cartesian coordinate; see Fig. 1

x = Cartesian coordinate; see Fig. 1

y = vertical Cartesian coordinate; see Fig. 1

z = coordinate position along the fiber axis

Greek Letters

α = angle between the y axis and the projection of the fiber on the x-y plane; see Marla and Shambaugh, 2003

ϕ = angle between the fiber axis and the w axis; see Marla and Shambaugh, 2003.

ρ_n = density of nitrogen, kg/m^3

ρ_f = fiber density, kg/m^3

τ = extra stress, Pa

Subscripts

a = air

die = die

f = fiber

h = hollow

i = fiber element (control volume) i

n = nitrogen

p = polymer

rheo = rheological

x = property along the x axis

y = property along the y axis

w = property along the w axis

Superscripts

x' = coordinate in direction transverse to fiber axis

z = coordinate position along the fiber axis

y = coordinate position along the fiber axis (only for 1-D model)

References

(1) Rwei, S. P. Formation of Hollow Fibers in the Melt-Spinning Process. *J. Appl. Polym. Sci.* **2001,** *82*, 2896-2902.

(2) Oh, T. H.; Lee, M. S.; Kim, S. Y.; Shim, H. J. Studies on Melt-Spinning Process of Hollow Fibers. *J. Appl. Polym. Sci.* **1997,** *68*, 1209-1217.

(3) De Rovere, A.; Shambaugh, R. L. Melt-Spun Hollow Fibers for Use in Nonwoven Structures. *Ind. Eng. Chem. Res.* **2001,** *40*(1), 176-187.

(4) Takarada, W.; Ito, H.; Kikutani, T.; Okui, N. Studies on High-Speed Melt Spinning of Noncircular Cross-Section Fibers. I. Structural Analysis of As-Spun Fibers. *J. Appl. Polym. Sci.* **2001,** *80*, 1575-1581.

(5) Takarada, W.; Ito, H.; Kikutani, T.; Okui, N. Studies on High-Speed Melt Spinning of Noncircular Cross-Section Fibers. II. On-Line Measurement of the Spin Line, Including Change in Cross-Sectional Shape. *J. Appl. Polym. Sci.* **2001,** *80*, 1582-1588.

(6) Takarada, W.; Ito, H.; Kikutani, T.; Okui, N. Studies on High-Speed Melt Spinning of Noncircular Cross-Section Fibers. III. Modeling of Melt Spinning Process Incorporating Change in Cross-Sectional Shape. *J. Appl. Polym. Sci.* **2001,** *80*, 1589-1600.

(7) Lipscomb, G. G. The Melt Hollow Fiber Spinning Process: Steady-state Behavior, Sensitivity and Stability. *Polym. Adv. Technol.* **1994,** *5*, 745-758.

(8) Lee, M. S.; Kim, S. Y. Effects of Initial Structure on the Deformation Behavior of PP Hollow Fiber in Continuous Drawing. *J. Appl. Polym. Sci.* **2001,** *81*, 2170-2182.

(9) Kim, J. J.; Hwang, R. J.; Kim, Y. U.; Kim, S. S. Operation parameters of melt spinning of polypropylene fiber membranes. *J. Membr. Sci.* **1995,** *108*, 25-36.

(10) Shen, L. Q.; Xu, Z. K.; Xu, Y. Y. Preparation and Characterization of Microporous Polyethylene Hollow Fiber Membranes. *J. Appl. Polym. Sci.* **2002,** *84*, 203-210.

(11) De Rovere, A.; Shambaugh, R. L. Melt-Spun Hollow Fibers: Modeling and Experiments. *Polym. Eng. Sci.* **2001,** *41*(7), 1206-1219.

(12) Shambaugh, R. L. A Macroscopic View of the Melt Blowing Process for Producing Microfibers. *Ind. Eng. Chem. Res.* **1988,** *27*(12), 2363-2372.

(13) Uyttendaele, M. A. J.; Shambaugh, R. L. Melt Blowing: General Equation Development and Experimental Verification. *AIChE J.* **1990,** *36*(2), 175-186.

(14) Rao, R. S.; Shambaugh, R. L. Vibration and Stability in the Melt Blowing Process. *Ind. Eng. Chem. Res.* **1993,** *32*(12), 3100-3111.

(15) Marla, V. T.; Shambaugh, R. L. Three-Dimensional Model of the Melt Blowing Process. *Ind. Eng. Chem. Res.* **2003,** *42*(26), 6993-7005.

(16) Billmeyer, F. W. *Textbook of Polymer Science,* 3rd ed.; Wiley-Interscience: New York, NY, 1984; pp 502-503.

(17) Han, C. D.; Lamonte, R. R. Studies on Melt Spinning, I. Effect of Molecular Structure and Molecular Weight Distribution on Elongational Viscosity. *Trans. Soc. Rheol.* **1972,** *16*(3), 447-472.

(18) Shambaugh, R.L. Polymer Processing Using Pulsating Fluidic Flow. U.S. Patent 5,405,559, 1995.

(19) Chen, C. T. *Digital Signal Processing*, 1st ed.; Cedra A. S., Ed; The Oxford Series in Electrical and Computer Engineering; Oxford University Press: New York, NY, 2001; pp 121

(20) Yin, H.; Yan, Z.; Ko, W. C.; Bresee, R. R. Fundamental Description of the Melt Blowing Process. *Int. Nonwovens. J.* **2000,** *9*(4), 25-28.

(21) Bresee, R. R.; Ko, W. C. Fiber Formation During Melt Blowing. *Int. Nonwovens. J.* **2000,** *12*(2), 21-28.

Outer Diameter (microns)	Inner Diameter (microns)	H_{die}	$v_{f,die}$ (m/s)	m_p (g/min)	m_n (ml/min*)
949	0	0	0.0155	0.5	0
949	300.1	10	0.0155	0.45	0.066
949	474.5	25	0.0155	0.375	0.164
949	671	50	0.0155	0.25	0.329
949	821.8	75	0.0155	0.125	0.493

* at 1 atmosphere pressure and 21 ˚C

Table 1. Summary of simulation conditions used for producing results shown in Figures 5-10

H_{die}	$T_{f,die}$ (˚C)	Fiber frequency (Hz)
20	310	49
20	330	48
20	340	45
20	350	44
20	375	28
20	400	15

Table 2. Variation of fiber vibration frequency with change in the die temperature for an initial hollowness of 20%

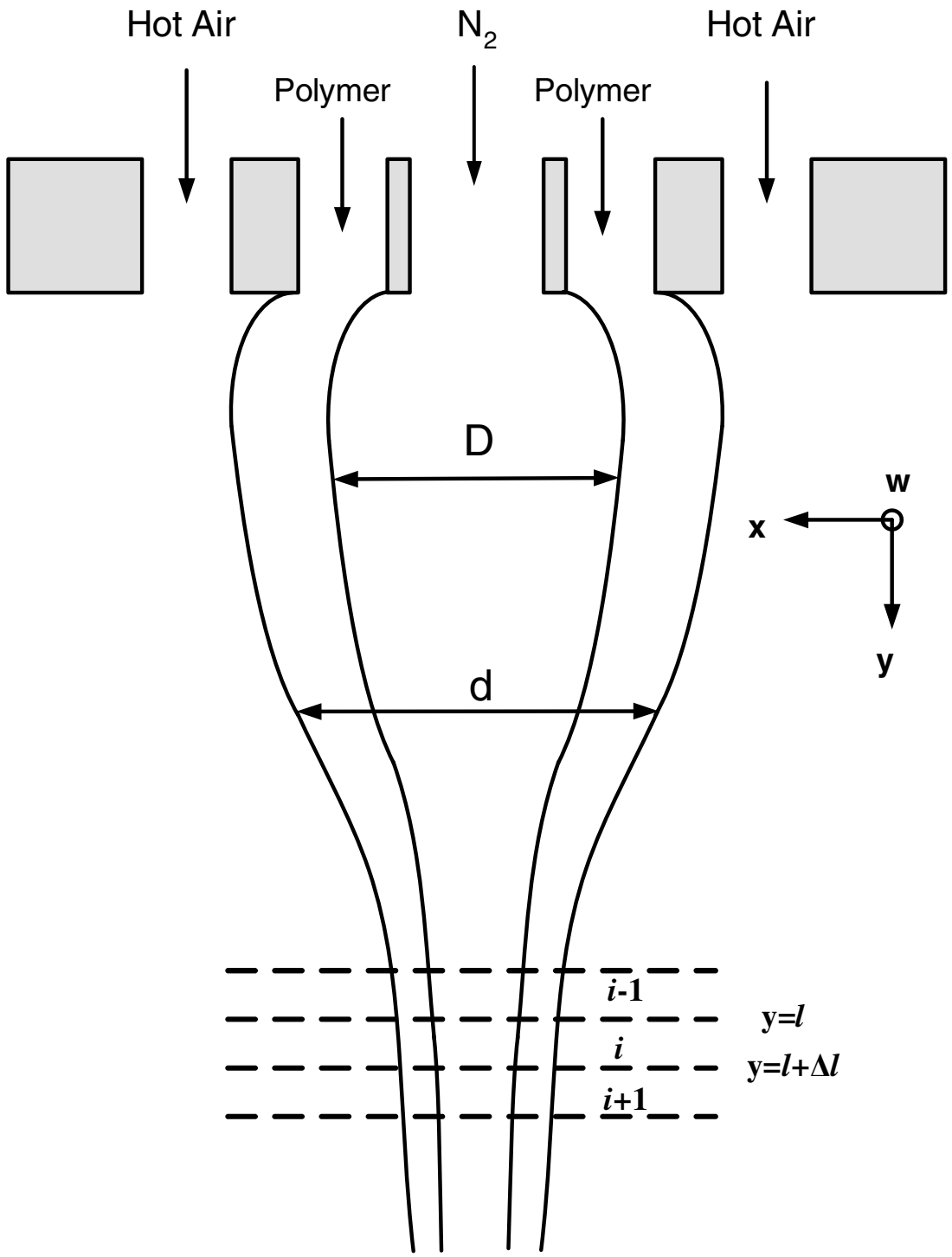

Figure 1. The melt blowing process for producing hollow fibers with an annular die.

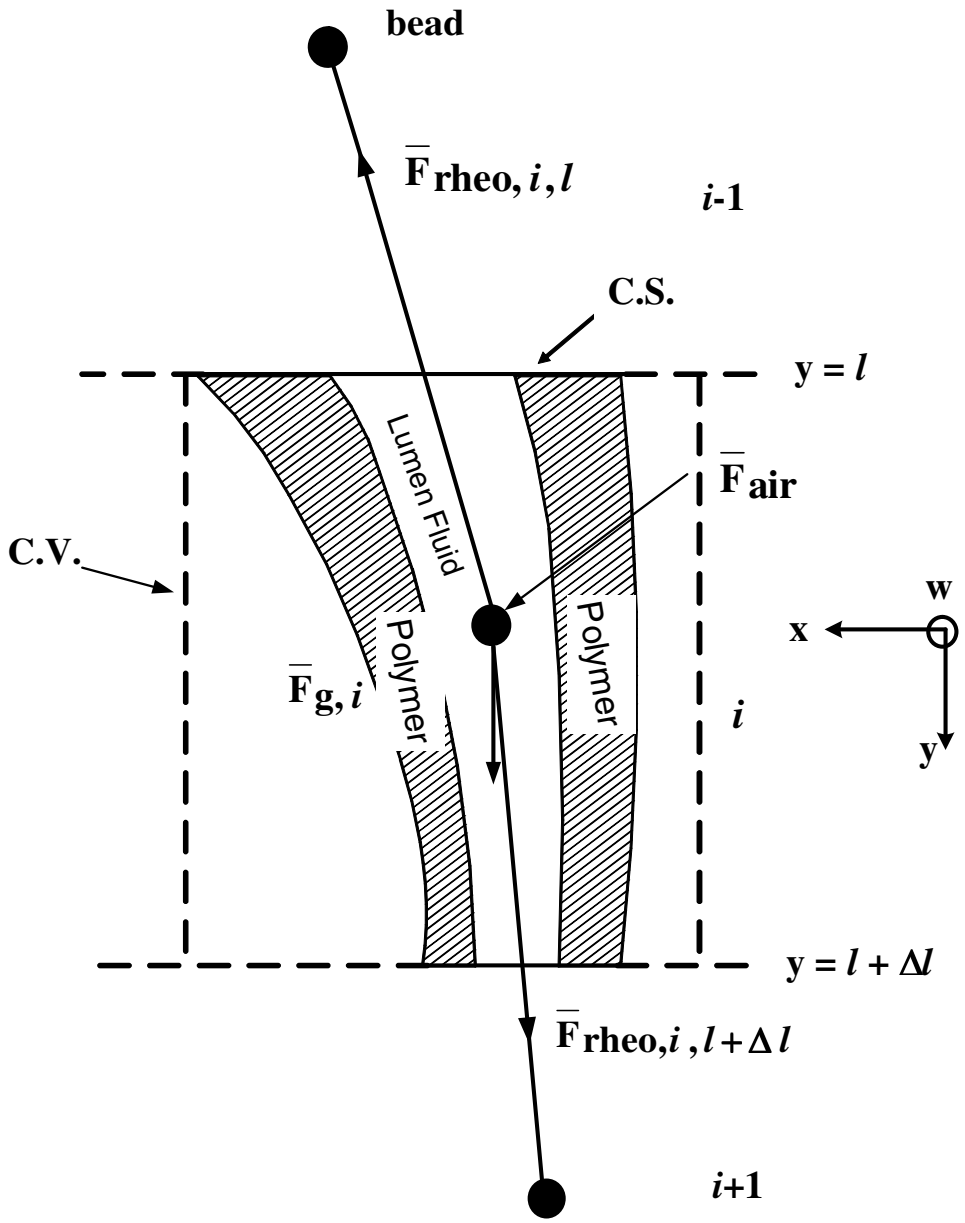

Figure 2. A fiber element contained within a control volume. The inner frustum contains the lumen fluid (nitrogen), while the polymer occupies the hollow outer frustum.

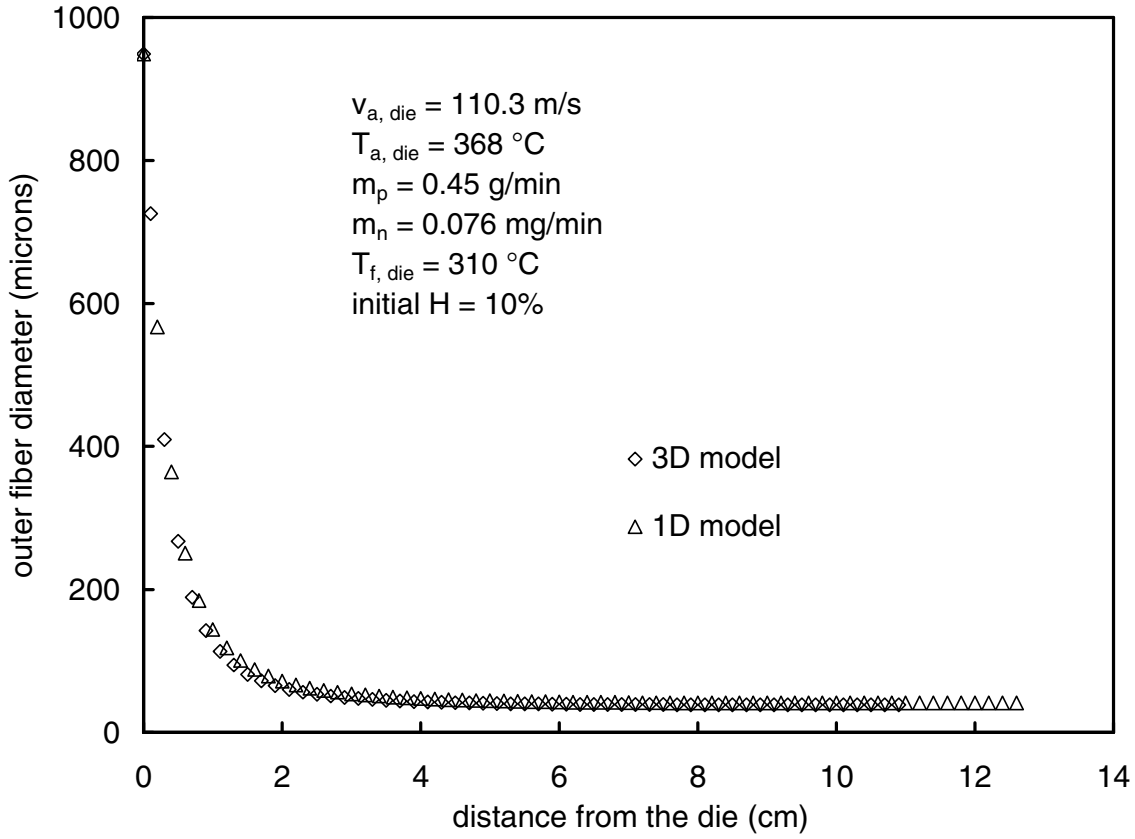

Figure 3. Comparison of the outer fiber diameter profile obtained from the 1D model and the 3D model for an initial H = 10%. Note that the 1D (modified Uyttendaele and Shambaugh) model was solved using the stop point boundary condition.

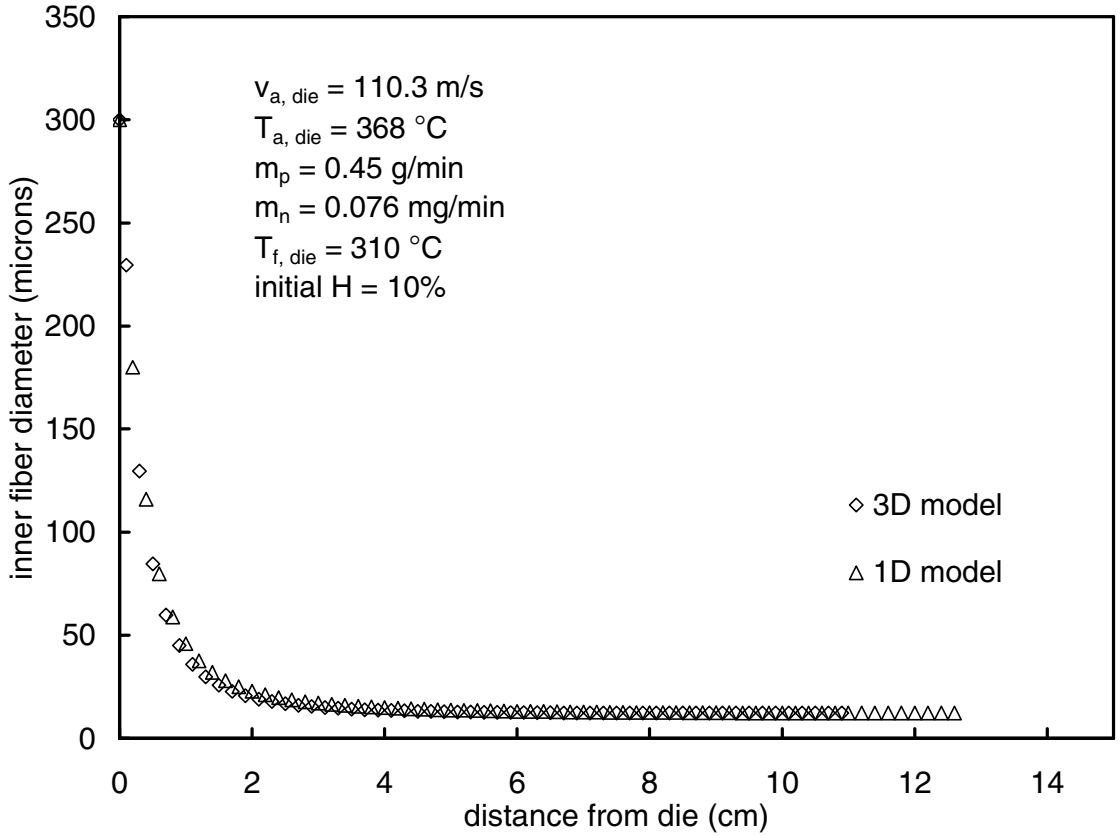

Figure 4. Comparison of the inner fiber diameter profile obtained from the 1D model and the 3D model for an initial H = 10%.

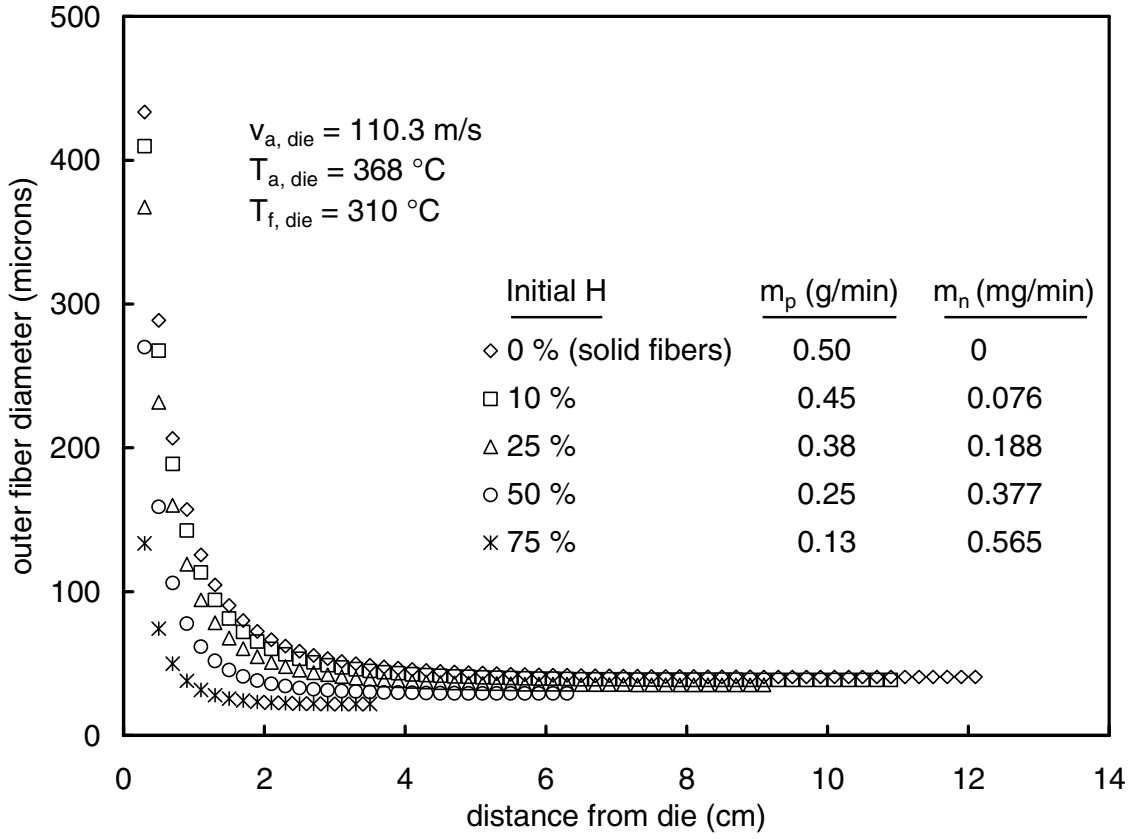

Figure 5. Comparison of outer fiber diameter profiles obtained from the 3D model when the initial hollowness is varied. Note that the mass flowrate of the polymer decreases in proportion to (1- H/100).

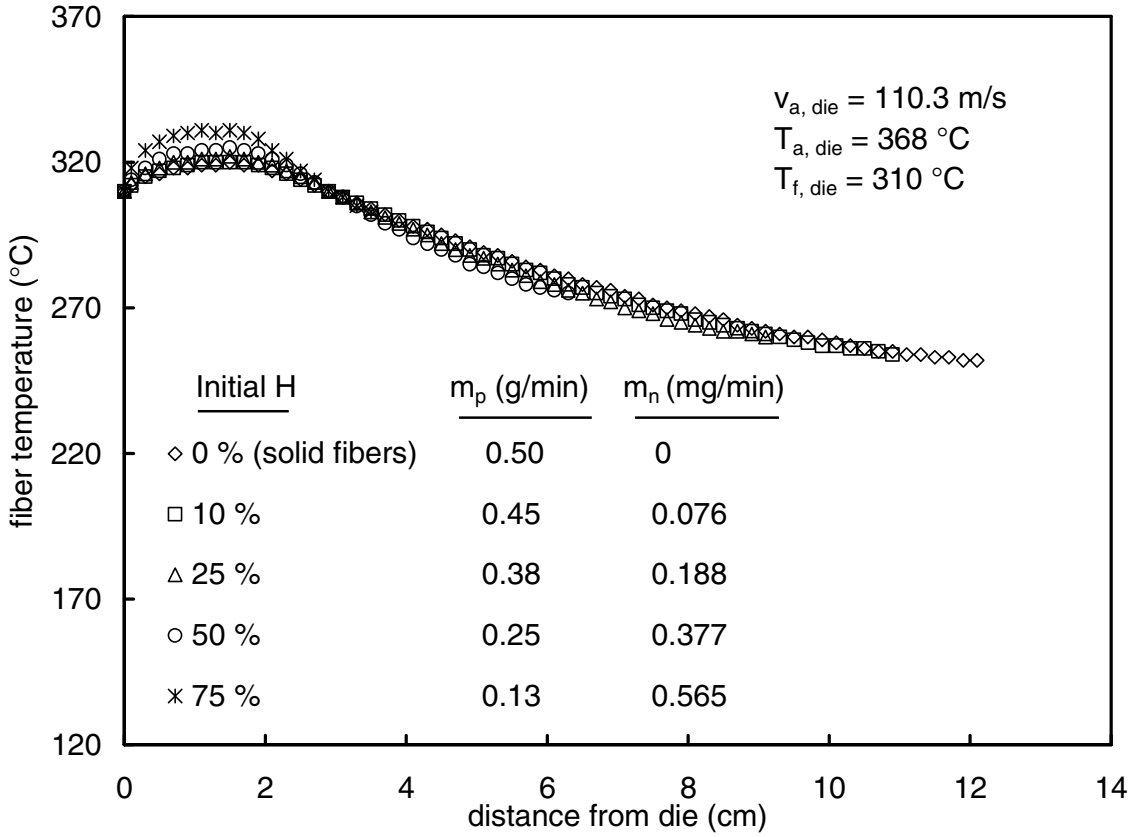

Figure 6. Fiber temperature profiles obtained from the 3D model when the initial hollowness is varied.

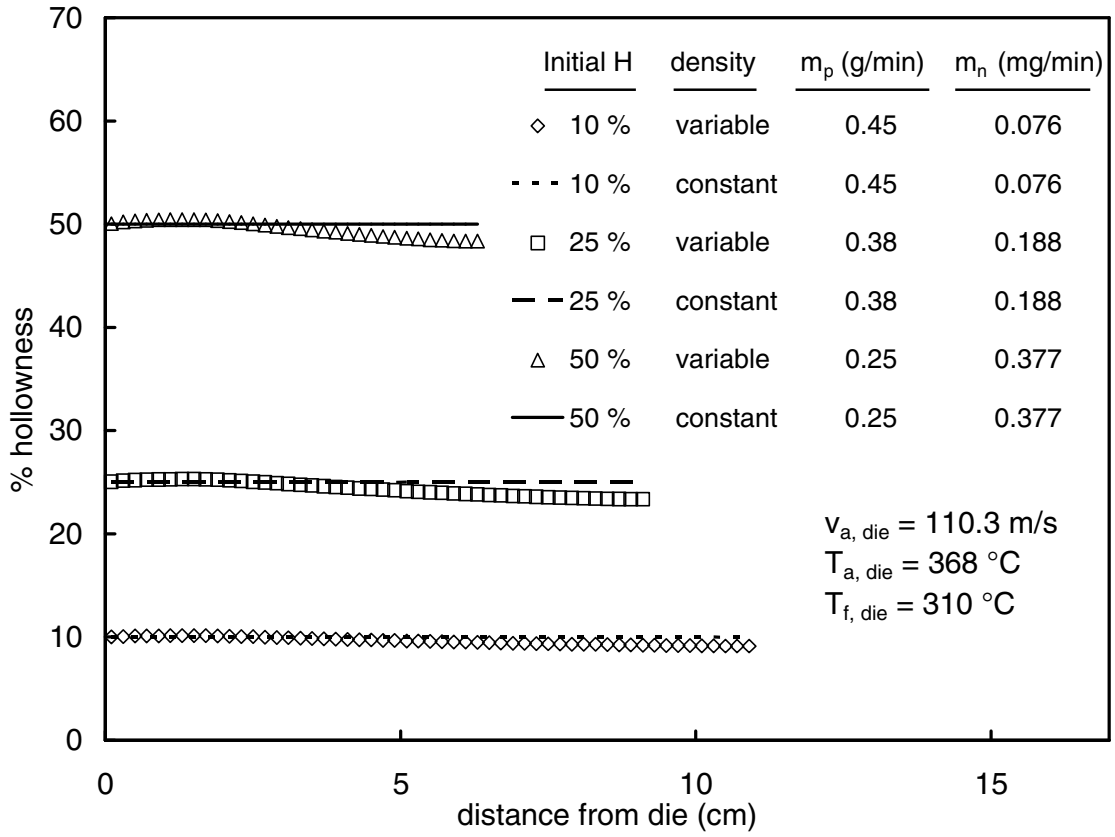

Figure 7. The variation of H along the threadline. Profiles are shown for the case when the lumen fluid density varies with temperature according to eq 17; also shown are the profiles that result if the lumen fluid density is (incorrectly) assumed constant along the threadline.

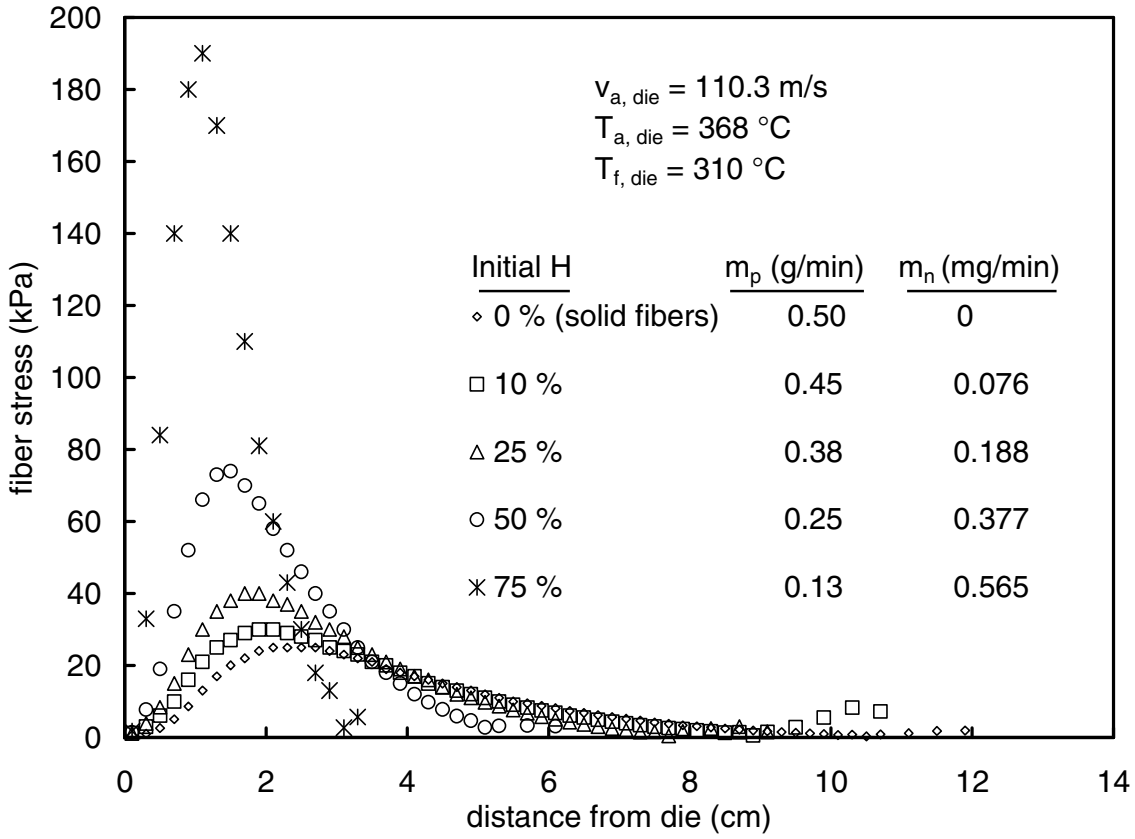

Figure 8. Fiber stress profiles predicted by the 3D model. Initial hollowness is varied from 0 to 75%.

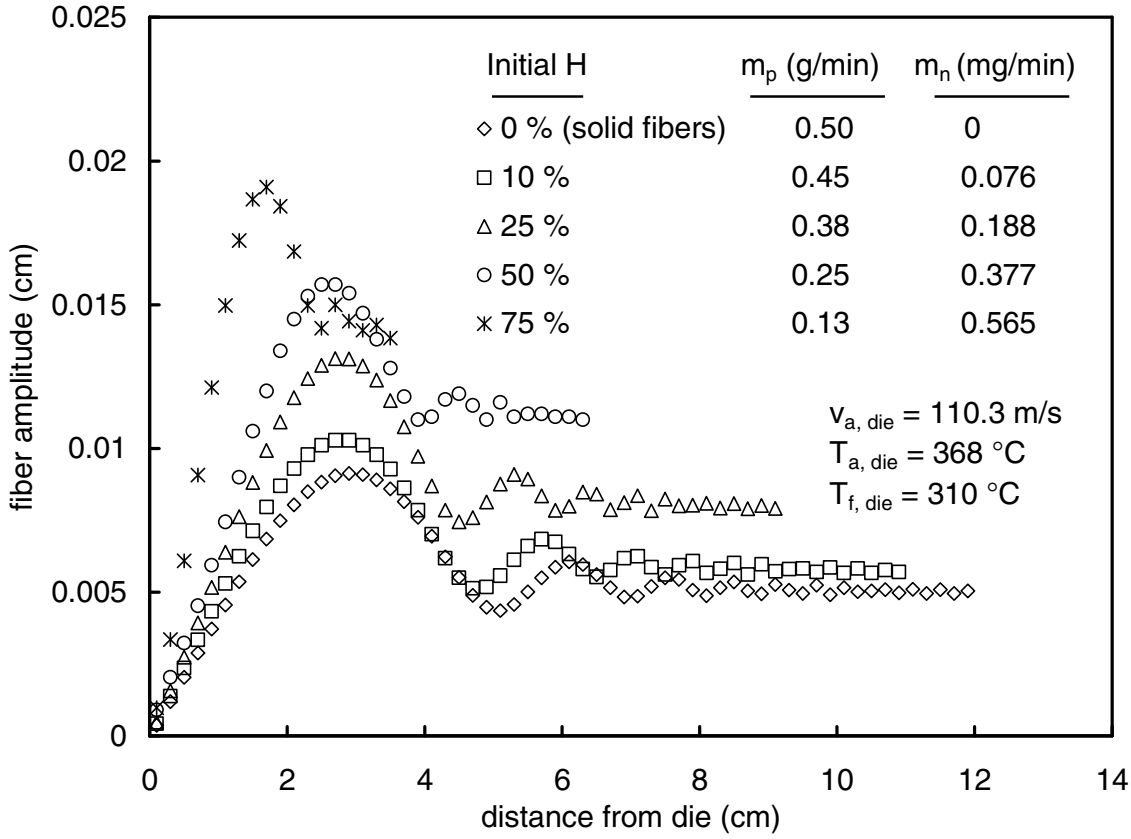

Figure 9. Effect of initial hollowness on the fiber vibration amplitude as predicted by the 3D model.

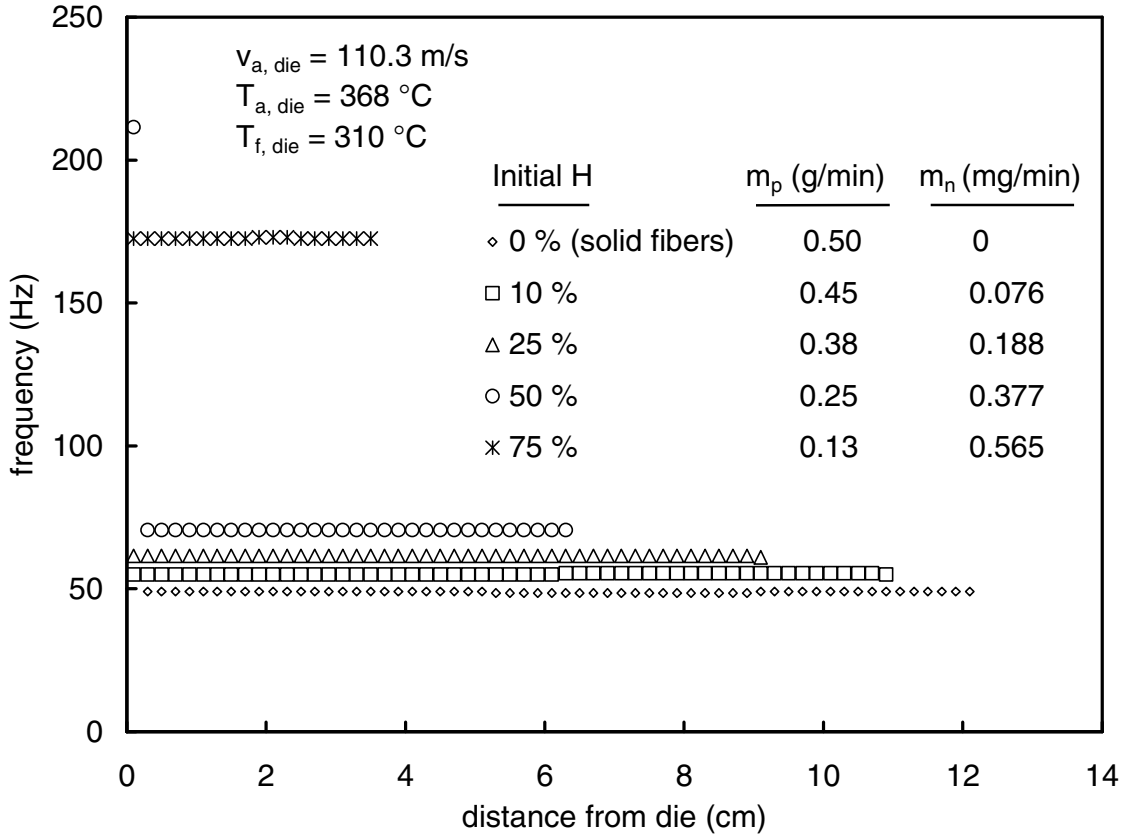

Figure 10. Effect of initial hollowness on the fiber vibration frequency as predicted by the 3D model.

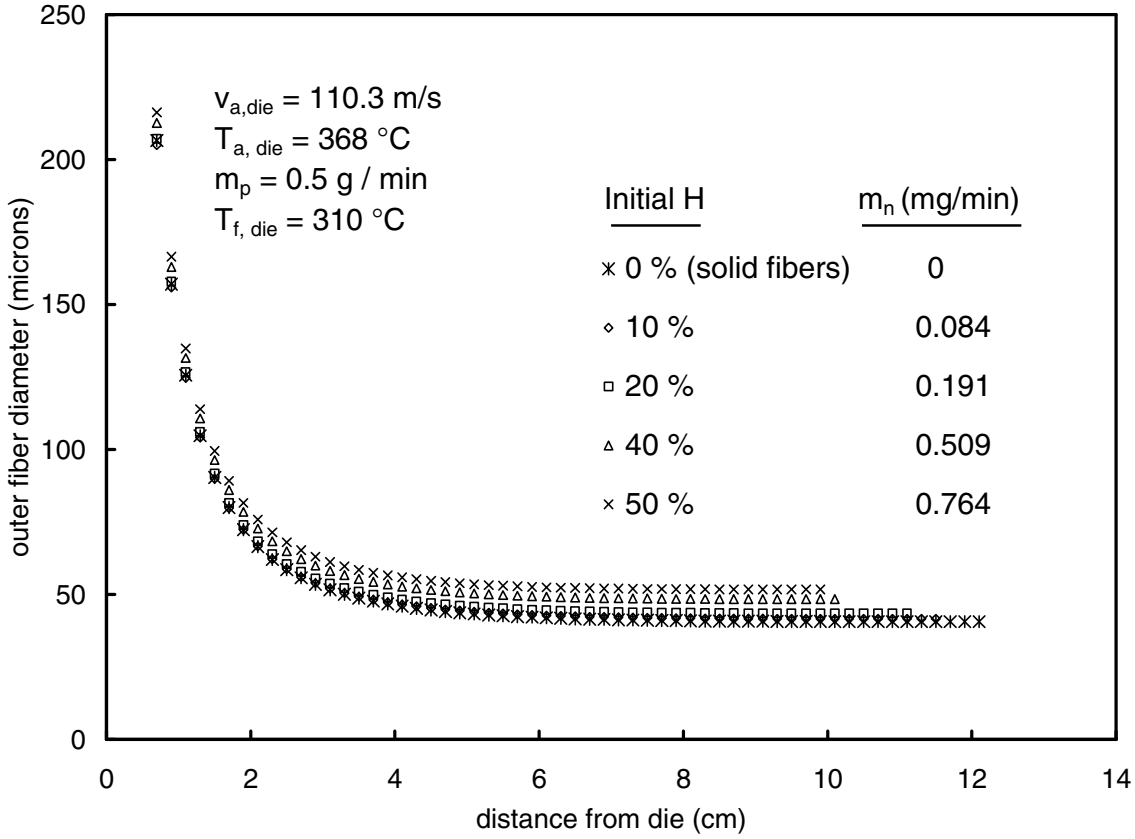

Figure 11. Effect of initial hollowness on the outer fiber diameter profile when the mass flowrate of the polymer is kept constant.

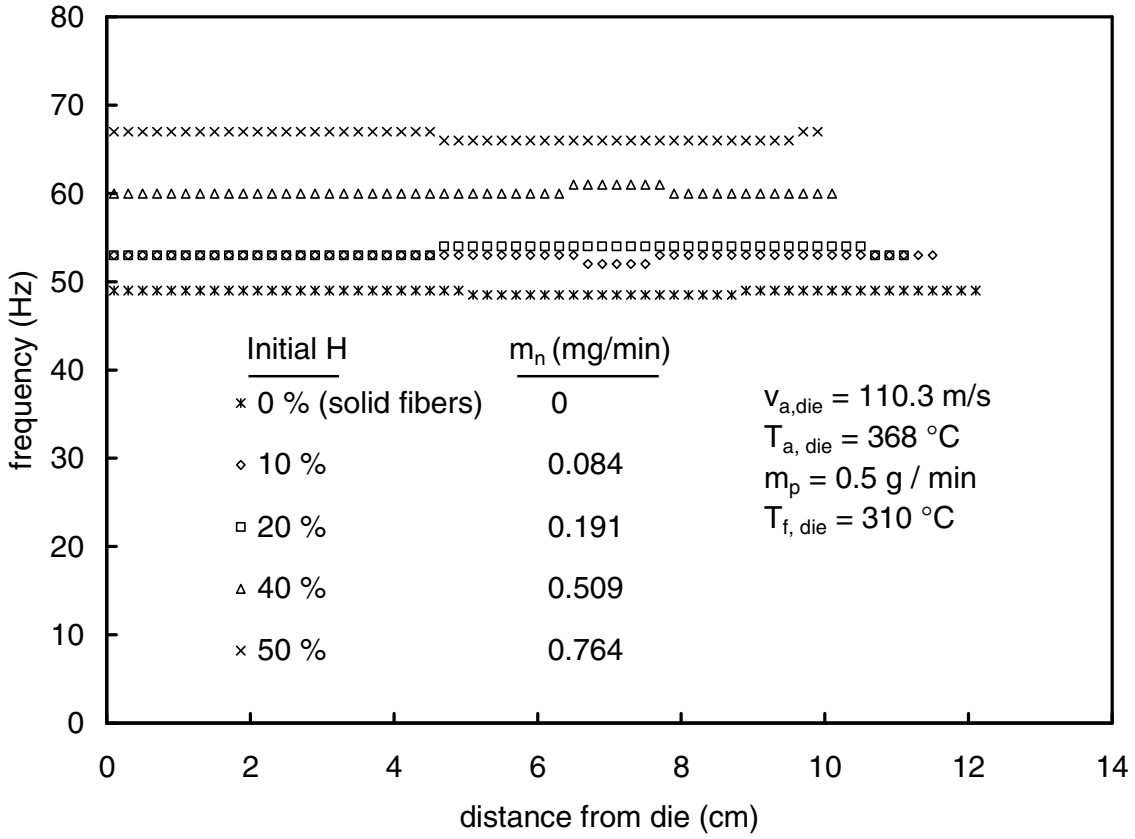

Figure 12. Effect of initial hollowness on the fiber vibration frequency when the mass flowrate of the polymer is kept constant.

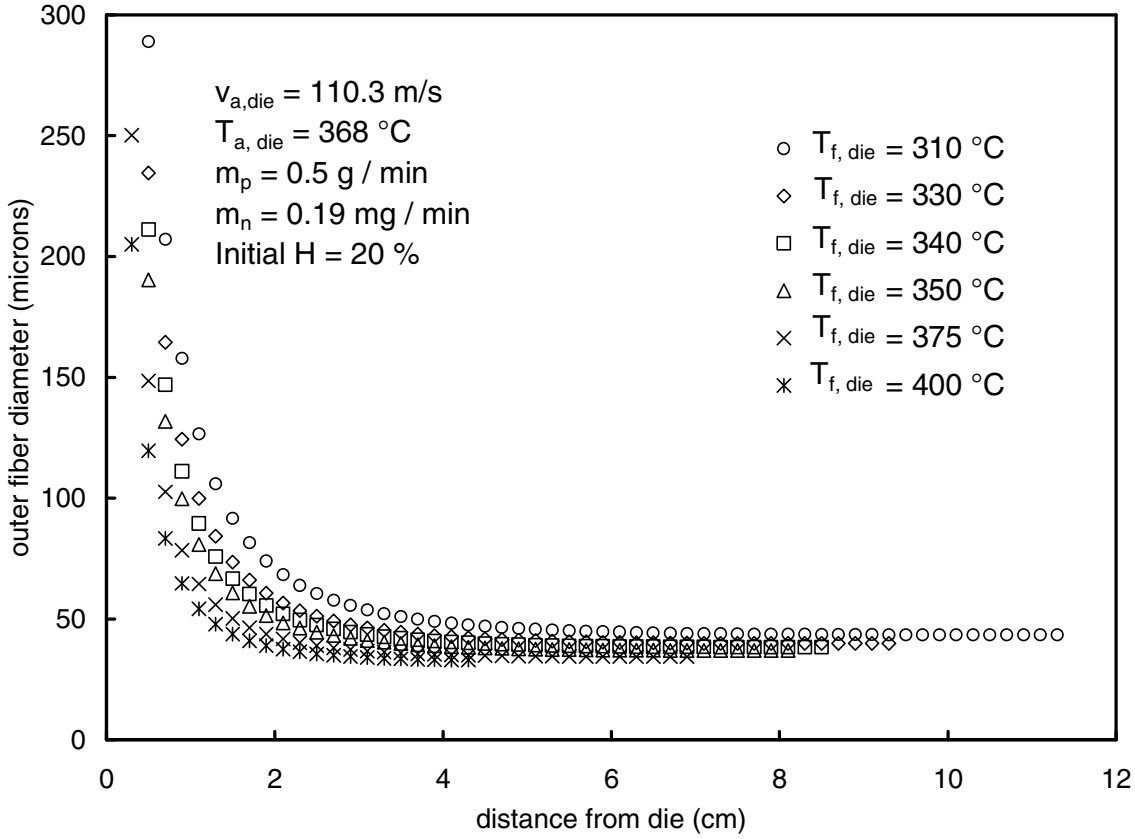

Figure 13. Effect of die temperature on the outer fiber diameter profile for an initial hollowness of 20%. The mass flowrate of the polymer is kept constant at 0.5 g/min.

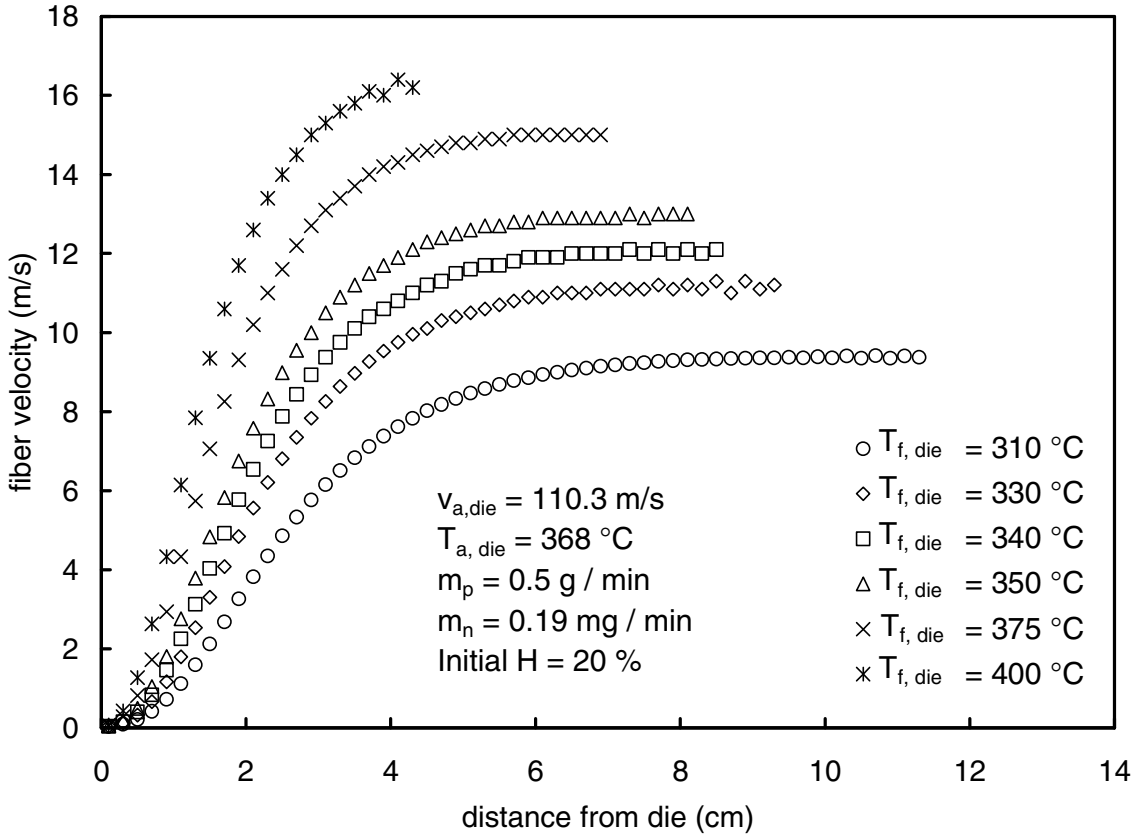

Figure 14. Effect of die temperature on the fiber velocity profile for an initial hollowness of 20%. The mass flowrate of the polymer is kept constant at 0.5 g/min.

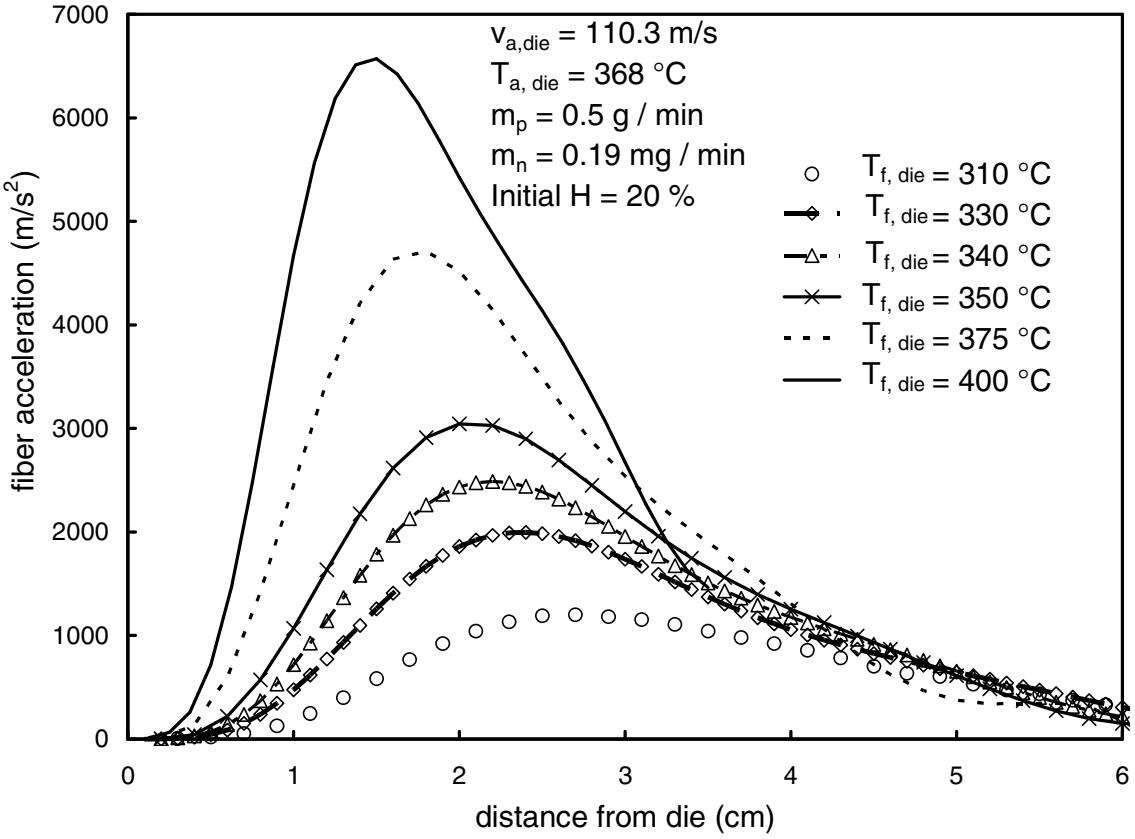

Figure 15. Effect of die temperature on the fiber acceleration along the threadline for an initial hollowness of 20%. The mass flowrate of the polymer is kept constant at 0.5 g/min.

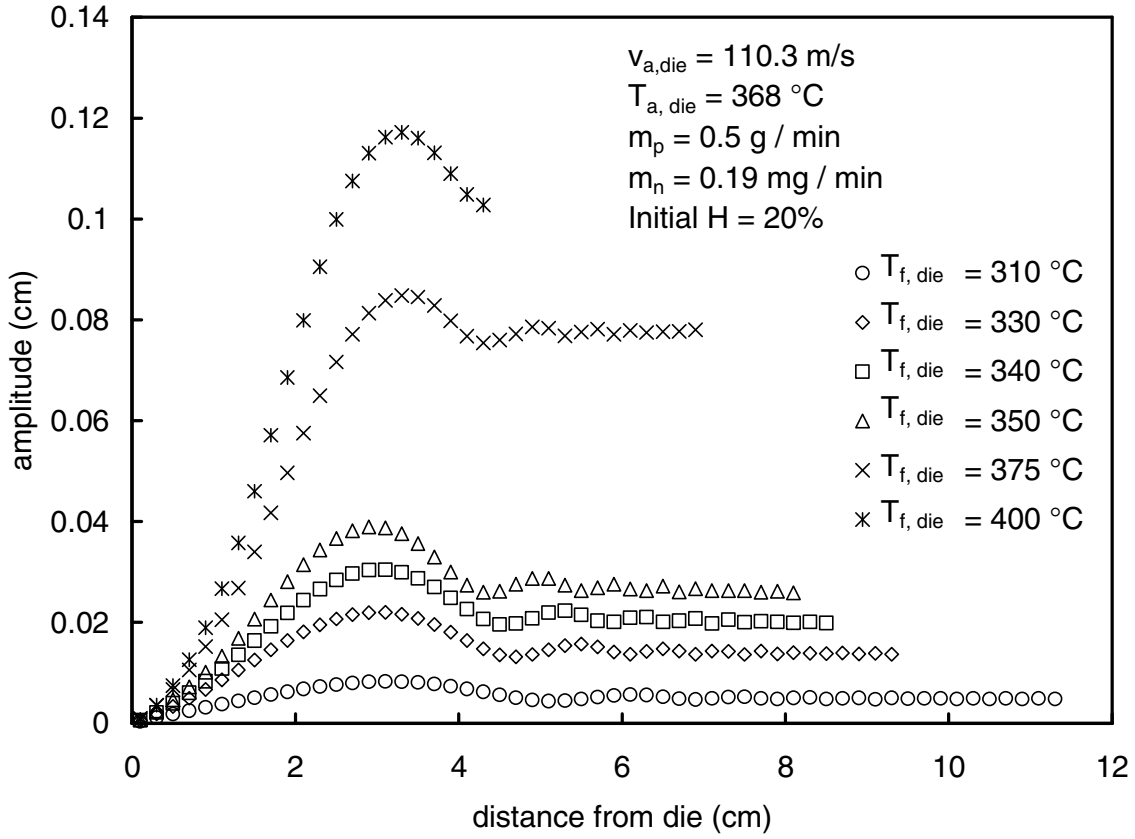

Figure 16. Effect of die temperature on the fiber vibration amplitude for an initial hollowness of 20%. The mass flowrate of the polymer is kept constant at 0.5 g/min.

CHAPTER 4

USING SWIRL DIES TO SPIN SOLID AND HOLLOW FIBERS

The content of this chapter has been submitted as a journal article to *Ind. Eng. Chem. Res.*

ABSTRACT

A swirl die was used to produce both solid and hollow fibers from polypropylene. In a swirl die, the molten polymer stream is attenuated and directed (swirled) by a concentric ring of air jets. In our experiments, the ring contained six air jets. The effects of air flowrate, polymer flowrate, air temperature, and polymer temperature were examined. The fiber diameter, swirl pattern diameter, and swirl frequency were measured. To spin hollow fibers, a lumen fluid (nitrogen) was injected into the polymer as the polymer exited the spinning die. The effect of fiber hollowness on the die operation and resulting swirled fiber were determined.

4.1 Introduction

The swirl die is used in adhesive applications for accurate spraying of adhesive on a target or substrate.[1] For example, as one of the steps in the manufacture of baby diapers, adhesive is used to bond a stretched elastic strand with a disposable nonwoven mat. There is an economic driving force to reduce operating costs in the nonwovens industry while increasing the quality of the product. Improvements in existing technologies for hot melt adhesive applications have resulted in lower variability in the final product, enhanced product quality, and savings in raw material. Since the elastic strand/substrate

is not in direct contact with the swirl nozzle, the swirl deposition technique is a non-contact adhesive coating method. The air jet bores in the swirl die are aligned in such a way so as to direct the hot air tangential to the hot melt adhesive and impart a tightly controlled helical motion to the adhesive. Bond strength, laydown accuracy, line speeds, etc. are factors which must be taken into account in order to optimize the deposition process.

A swirl die is a type of melt blowing nozzle. The more commonly recognized form of melt blowing is where hot gas streams rapidly attenuate molten polymer strands to form fine fibers (see Shambaugh[2]). Subsequently, these fibers are used in filters, sorbent media, and a myriad of other uses. However, fine fibers are not the goal of an adhesive swirl die. Rather, the goal is to achieve controlled deposition of the hot melt adhesive on the target (which may be a nonwoven mat or an elastic strand). A number of publications[3-6] describe a mathematical model of the melt blowing process using conventional melt blowing dies such as annular and slot dies. Studies on the fiber motion below such conventional dies have shown that the fiber motion is quite random.[7] In contrast, the fiber motion below the swirl die is regular and controlled, and this factor is essential for minimizing adhesive usage. Ziecker et al.[1] designed a spray gun assembly where the swirl die with an outset nosepiece was used for spraying the hot melt adhesive. These authors emphasized that the spraying of continuous filaments results in improved bond strength and less adhesive usage compared to a bonding technique using adhesive droplets.

Figure 1 shows a schematic of one of the swirl dies used in our study. This die has a 2.1 mm diameter polymer orifice at the center. In a regular pattern around the center are 6 air jet holes. Each air jet hole has a diameter of 0.46 mm and the diameter of the circle passing through the centers of these 6 air jet holes is 4.77 mm. Each air hole is canted at 60 degrees relative to the die face (see side view) and 10 degrees relative to the center hole of the die (see bottom view). The hot air exiting from the air holes causes a spiral (helical) motion to the adhesive; the width of this helical pattern can be controlled by changing the die operation variables. Figure 2 shows a high-speed photograph of a fiber exiting from the swirl die shown in Figure 1. The helical pattern of the fiber is evident from the photograph; this motion is characteristic of fibers formed using swirl dies.

Generally, hollow fibers are prepared by wet spinning, dry spinning or melt spinning.[8,9] Hollow fibers made from these processes find wide applications in hemodialysis and in the manufacture of insulated clothing. Recently, Marla et al.[10] modeled the melt blowing of hollow fibers spun with an annular die configuration. Based on the results of that model, we propose a novel method for the manufacture of hollow fibers using a swirl die. According to the predictions of the Marla et al.,[10] hollow fibers have higher frequencies of vibration than solid fibers (when both are spun from a conventional melt blowing die). Our supposition is that hollow fibers spun from a swirl die will also have higher frequencies of vibration (versus solid fibers spun from a swirl die). If this is so, then the spinning of hollow fibers with swirl dies may result in a method of substantially increasing line speeds in the adhesive deposition process. We will study the operating variables that affect line speeds and determine the processing

limits for accurate deposition. In addition, we will study the fiber motion below swirl dies under different operating conditions and compare this motion with fiber motion below conventional melt blowing dies.

4.2 Experimental Details

The experimental setup was similar to that used by Marla and Shambaugh[6] with the exception that, instead of using a slot die, a swirl die was used. The air was controlled within ± 0.2 slpm by means of a thermal mass flowmeter with a maximum rating of 15 slpm. The collection screen was placed 35 cm below the die and the diameter of the fibers collected on this screen were measured off-line using an optical microscope. The other property of interest was the swirl frequency (also known as loop frequency) that is defined as the number of loops deposited per second. In order to measure the swirl frequency, the collection screen was replaced with a moving collection belt. This belt, which was fabricated from heavy paper, moved between two drums, each of which was driven by an identically rated permanent-magnet DC gear-motor. The RPM of each drum was controlled by a silicon controller rectifier (SCR); the drum speeds were set equal so that the belt moved with a constant speed. The belt was 12 cm wide, the drums were 6.5 cm in diameter, and the axis-to-axis distance between the drums was 200 cm. The drum speed was varied from 220 to 340 rpm, which corresponds to a surface (belt) speed of 44.9 to 69.3 m/min. Typically, an 8 meter length of paper belt was used; this belt was unwound from one drum while being wrapped upon the second drum (see Fig. 3a). Each of the drum assemblies was placed on a stand with adjustable height. By raising or

lowering the drums, the swirl frequency and swirl quality could be measured at any position below the spinneret. After the spinning operation was stabilized, the belt was started and the fibers were deposited on the moving belt, and then the belt was stopped when the end of the belt was reached. An example of the resulting laydown pattern is shown in Figure 3b. To quantify the laydown pattern, the number of loops was counted over a length of 1 meter. Measurements were made near the beginning of the belt (after the pattern had stabilized), at the middle of the belt, and near the end of the belt (while the pattern was still established). For each spinning condition, fibers were collected on three different belts. Thus, each spinning condition gave 9 measurements of the number of loops per meter. The average of these 9 measurements was multiplied by the speed of the belt to give the swirl frequency according to the following formula:

$$\text{swirl frequency (loops/s)} = \text{number of loops deposited per meter (loops/m)} \times \text{belt speed (m/s)}$$

In order to capture the amplitude of displacement of the swirling fiber, a stroboscope was used in conjunction with a Nikon camera equipped with a 105 mm macro lens and ISO 400 film. The stroboscope was set at 500 fpm (flashes per minute) in a darkened room and the camera shutter was kept open for 30 s. Thus, there was a multi-exposure of 250 pictures of the fiber on a single film frame. The polymer used in the experiments was 88 MFR Fina Dypro® isotactic polypropylene. This polymer had an M_w of 165,000 g/mol and a M_n of 41,500 g/mol. The base conditions for the experiments,

unless otherwise mentioned, were a polymer mass flowrate (m_p) of 2.4 g/min, a die temperature ($T_{f,die}$) of 310°C, an air flowrate of 7.5 slpm, and a die temperature ($T_{a,die}$) of 325°C. Observe that the polymer mass throughput is quite high when compared to conventional melt blowing with an annular or slot die where throughputs of 1 g/min or less (per hole) are common. However, higher mass throughputs are quite common in adhesive applications that make use of swirl dies.

4.3 Results and Discussion

In conventional melt blowing there are these four main operating variables: the mass throughput of the polymer, the air flowrate, the polymer temperature at the die, and the air temperature at the exit of the die. Of concern to researchers (e.g., Bansal and Shambaugh[11]; Marla and Shambaugh[5,6]) is the effect of these variables on the properties of melt blown fibers. Similarly, we examined the effect of these same variables on the operation of a swirl die. Of interest are the fiber diameter, the swirl frequency and the quality of the loops.

Effect of Changing the Mass Throughput of the Polymer

Figure 4 shows the effect of changing the mass throughput of the polymer while keeping all other conditions constant. These results are for the spinning of solid (not hollow) filaments with the die type shown in Fig. 1. The fiber diameter increased from 83 µm to 365 µm when the polymer mass throughput was increased from 1.7 g/min to 4.5 g/min. Over the same range of mass throughput change, the swirl frequency decreased

from 81 loops/s to 28 loops/s. These trends for both the swirl frequency and the fiber diameter are similar to the trends predicted by Marla and Shambaugh[5,6] for both annular and slot melt blowing dies. Any decrease below 1.5 g/min resulted in the loss of the well-defined helical pattern characteristic of the swirl die, and the fiber motion became random. Thus, 1.5 g/min was the lower limit of processing for the set of operating conditions listed on Figure 4.

Effect of Changing the Volumetric Flowrate of Air

Figure 5 shows the effect of changing the volumetric flowrate of air while keeping all other conditions at base values. Increasing the air flowrate from 6.3 to 11.4 slpm resulted in a decrease of the fiber diameter from 207 μm to 97 μm and an increase of the swirl frequency from 24 loops/s to 104 loops/s. These trends parallel the predictions of Marla and Shambaugh[5,6] for both annular and slot dies. Any increase in the air flowrate beyond 12 slpm resulted in the fiber losing its regular and controlled helical motion and assuming a random motion, while any decrease in the air flowrate below 6 slpm resulted in insufficient driving force to induce any swirling motion in the fiber. Hence, for a given set of operating conditions, there appears to be a specific range within which the swirl frequency can be increased by increasing the air flowrate. Operating outside this range will compromise the accuracy of the laydown pattern.

Effect of Changing the Initial Air Temperature and Initial Polymer Temperature

Figure 6 shows the effect of varying the temperature of the air at the exit of the swirl die. For conventional melt blowing dies, the initial air temperature does not have a significant effect on the fiber diameter (see Marla and Shambaugh[5,6]). This seems to be true in the case of the swirl die as well, since the fiber diameter seems to be more or less independent of the initial air temperature. The swirl frequency, however, increased from 43 loops/s to 53 loops/s when the initial air temperature was increased from 225 ˚C to 360 ˚C. This is a much smaller percent change than that shown in Figures 4 and 5.

The effect of initial polymer temperature, $T_{f,die}$, was investigated by running the die at 270˚C, 310˚C, and 330˚C (and keeping the other operating parameters at base conditions). Only for the polymer temperature of 310˚C (the base condition) were good loops produced. Operation at the other temperatures resulted in loss of the swirling motion of the fiber; instead, the laydown pattern was random and resembled the pattern produced by a conventional melt blowing die.

Effect of Threadline distance on the Swirl Frequency

The polymer threadline in melt blowing is a mechanical system. As such, the threadline has a characteristic frequency associated with it for a given set of operating conditions; see Rao and Shambaugh.[4] In fact, this natural frequency can be used to improve melt blowing. For example, in melt blowing with slot dies, the air through the slots can be pulsed at the natural frequency of the system, which causes a reduction in the volume of melt blowing air that is required to achieve a certain fiber size.[12] For the swirl die of our experiments, the swirl frequency was measured as a function of distance below

the die to determine a) the dependence of swirl frequency on the threadline distance and, b) the quality of the loops at different locations below the die. The conveyor belt was placed at 15, 20, 25, 30 and 45 cm below the die, and the swirl frequency was measure by counting loops on the collection belt. The results, which are plotted on Figure 7, show that the swirl frequency is almost constant along the threadline. The quality of the loops was also analyzed at these different locations; the loops in all cases were intact and showed no signs of decay even at 45 cm below the die. Thus, the swirl motion is highly regular and persists for a fairly large distance below the die.

High speed photography can be used to observe the motion of the fiber in swirl die spinning. Figure 8a is a multiple exposure photograph of the fiber below a swirl die; the operating conditions are listed on the figure. This picture has 250 flash exposures on a single film frame. The camera and film used were the same as described above in the experimental details section. Now, in spiral motion, the fiber spends most of the time in a hollow cone below the die. Hence, the multiple images of this cone (Figure 8a) show a concentration of fiber exposures at the edges of the cone. In contrast, Figure 8b shows a multiple image of the fiber motion below a conventional slot die. For this die (as well as for an annular die), the fiber moves in the space defined by a solid cone. Hence, the multiple images fill a solid cone with the apex at the polymer orifice. The boundaries of this cone represent the maximum amplitude of fiber displacement from the centerline position. The photographs in Figure 8 were taken with the technique described by Chhabra and Shambaugh.[13]

For Figure 8a the individual fiber positions were examined using the image analysis software ImageJ. From these measurements, the average cone diameter and the variance in the cone diameter are plotted on Figure 9. Because the variance is an order of magnitude less than the cone diameter, the spiral nature of the laydown pattern is maintained (see Figure 3b). For Figure 8b, the solid cone -- versus hollow cone -- motion of fibers results in a uniform laydown pattern. This is, of course, what is desirable when producing continuous (no gaps in the fabric) melt blown sheets.

When swirl nozzles are used for adhesive deposition, it is desirable to increase line speed without losing the accuracy of the adhesive hitting the target or the substrate.[14] At higher line speeds, the tightly controlled laydown pattern of the adhesive must be maintained, and an increase in spiral rotational frequency is desirable. Bond strength is also an important factor that must be taken into consideration, and there are rules of thumb that can be followed to optimize the bond strength with the substrate.[15,16] Chief among these rules are that (a) larger fibers form stronger bonds with the substrate, and (b) fiber crossings serve to strengthen the bonds with the substrate. In our work, reducing the mass throughput of the polymer and increasing the air flowrate resulted in an increase in the swirl frequency (Figures 4 and 5). However, the fiber diameter also decreased on account of these changes, which might negatively affect the bonding strength according to the rules for optimum bonding. Thus, the challenge is to increase the swirl frequency while keeping the fiber diameter large enough to ensure a strong bond with the substrate.

4.4 Hollow Fibers Spun with Swirl Dies

Marla et al.[10] modified their 3D melt blowing model for solid fibers[5] and simulated the manufacture of hollow fibers in the melt blowing process using an annular die configuration. They modeled the effect of hollowness on the fiber properties in the melt blowing process and drew several conclusions based on the predictions of the model. One of their results, which is most relevant to the problem at hand, was that, when hollowness was induced in the fibers, the hollowness caused an increase in the fiber vibration frequency and an increase in the outer fiber diameter. Now, as Figures 4, 5, and 6 show, the operation of a swirl die demonstrates the same trends as conventional melt blowing dies in response to changes in the four primary operating variables in melt blowing. With this similar behavior established, will swirl dies respond to hollowness in a manner similar to the predicted behavior (as described in Marla et al.[10]) for spinning hollow fibers with an annular die? If so, then what are the processing limits? We have tried to address these questions in our work.

In order to spin hollow fibers from a swirl die, the swirl die was modified such that a lumen fluid tube was inserted concentrically within the polymer orifice (i.e., a tube-in-orifice arrangement). This modified die is shown in Figure 10. The lumen tube was supplied with nitrogen gas from a cylinder held at 22 psi and the lumen fluid flowrate was controlled by means of a flowmeter with a range of 0 to 5.6 ml/min. The rest of the experimental setup was the same as described earlier. There are three fluids involved in the operation of the die shown in Figure 10: the lumen fluid (nitrogen), the polymer, and the air that is fed to the outer six holes.

Hollowness is defined by the square of the ratio of the inner to outer diameter of the fiber. Thus, the percent hollowness is

$$\% \text{ hollowness} = H = \left(\frac{D}{d}\right)^2 \text{ x } 100$$

The percent hollowness was measured by taking a bundle of fibers collected on the screen, cutting the fibers with a microtome, measuring the inner and outer diameter under an optical microscope, and then applying the above formula. This technique was developed by De Rovere and Shambaugh[9] for calculating the hollowness of hollow fibers made from the spunbonding process. A photomicrograph of a cross section of some of our hollow fibers is shown in Figure 11a. For comparison, a photomicrograph of solid fibers is shown in Figure 11b.

Effect of Lumen Gas Flow Rate when Polymer Mass Rate is Constant

The lumen fluid flowrate was increased so as to increase the hollowness in the fibers while keeping the polymer mass throughput constant (the operating temperatures and air flowrate were also held constant). Figure 12 shows the results of experiments conducted with polymer mass throughputs of 2.14 g/min and 2.75 g/min. As expected, the outer fiber diameter increased as hollowness increased. For the 2.14 g/min case, the outer fiber diameter increased from 129 µm to 200 µm as the hollowness was increased from 0 % (solid) to 50 %. Similarly, for the 2.75 g/min case the outer fiber diameter increased from 157 µm to 270 µm when the hollowness was increased from 0 % to 49 %. Marla et al.[10] obtained similar results for their modeling work on hollow fibers produced

with an annular die in the melt blowing process. The results shown in Figure 12 are also similar to what occurs during the melt spinning or spunbonding of hollow fibers.[17] These results are fairly intuitive in that the lumen fluid inflates the polymer and causes an outer fiber diameter that increases with increased lumen fluid flowrate.

Figure 13 shows the effect of hollowness on the swirl frequency for the same conditions as in Figure 12. For the 2.14 g/min case, although the outer fiber diameter increases substantially with percentage hollowness (as shown in Fig. 12), the swirl frequency remains relatively unchanged. In fact, there is only a 2.9 % variation in the swirl frequency when the hollowness is increased from 0 % (solid fibers) to 50 % hollow fibers. The 2.75 g/min case also shows that hollowness has little effect on frequency: the lowest frequency (at 20% hollowness) is only 1.34 % lower than the highest frequency (at 0 %). However, as shown in Fig. 12, the outer fiber diameter increases by 72 % when the % hollowness is raised from 0 to 49 %. This result can have a significant impact in adhesive applications since larger fiber diameters are obtained without reduction in the swirl frequency.

Hollowness values above 50 % were not shown in Figures 11 and 12. The reason for this is that, under the conditions used to produce the data in these figures, good helical loops could not be produced at high levels of hollowness. Figure 14 shows a representative plot of the effect of increasing the lumen fluid flowrate on the percent hollowness for a constant polymer mass throughput of 2.75 g/min. As the hollowness was increased up to 40 %, the swirl frequency remained almost constant and the quality of the loops or the helical pattern of the fiber motion was intact. For optimizing the deposition

process – by either increasing the line speed and/or increasing the fiber diameter – the helical pattern of the fiber must be maintained. For the conditions used to produce Fig. 14, at a hollowness of 40 % the fiber begins to lose its helical motion and starts becoming more random. Finally, beyond a hollowness of 50 % there is a breakup of the fiber stream and the polymer spatters on the collection screen. Microscopic analysis of these polymer segments shows a very random diameter distribution and the fibers are quite large (i.e., they show little attenuation). Thus, there is a processing limit on how much hollowness can be introduced into the fibers for our operating conditions. Figure 14 shows the results for a 2.75 g/min polymer rate; similar results were observed for a polymer rate of 2.14 g/min.

Photographs of the fiber below the die can be used to illustrate the transition from highly ordered flow to random motion. Figure 15a is a multi-exposure picture of the fiber motion for a hollowness of 30 %. Similar to Figure 8a (which was for solid fiber spinning), Figure 15a shows that the motion of the fibers is contained in a hollow cone. Loops of these hollow fibers were collected on the belt; the loops were of high quality and similar to those obtained for solid fibers. Figure 15b shows the fiber motion for a hollowness of 50 %; this figure shows a strong resemblance to Figure 8b, a figure which illustrates the characteristic, solid cone, random fiber motion below a slot die. Hence, for the operating conditions used in processing our resin, optimum spiral deposition would be obtained at 30-40 % hollowness. Running at higher hollowness would result in poor spiral deposition.

Effect of Hollowness on the Swirl Frequency for a fixed Outer Fiber Diameter

In order to separate the effect of lumen fluid flowrate on swirl frequency and outer fiber diameter, experiments were conducted where the outer fiber diameter was kept constant while the lumen fluid flowrate and the polymer mass throughput were varied in order to increase the hollowness in the fibers. Figure 16 shows one such run where the outer fiber diameter was fixed at 190 μm and the hollowness was increased from solid fibers (0 % hollowness) to 10, 25 and 35 % hollowness. There appears to be little change in the swirl frequency for a hollowness increase from 0 to 10 %. However, as the hollowness is increased beyond 10 %, the swirl frequency increases. For a hollowness of 35 %, the swirl frequency increases by 55 % versus the 0 % (solid) filaments. Now, for the same outer diameter, less polymer is needed to make a hollow fiber and, hence, adhesive usage is reduced. (This assumes, of course, that bond strength is not seriously compromised.) Also, the line speed or swirl frequency can be significantly increased by inducing hollowness in the fibers. Finally, this technique does not compromise the quality of the loops formed. Here again, there is a processing limit on the amount of hollowness that can be induced in the fibers. Any increase in the hollowness beyond 40 % resulted in the deterioration of the helical loops formed. Table 1 gives further details about Fig. 16, and the table summarizes the results for several other runs where a different value of outer fiber diameter was kept constant.

4.5 Conclusions

The operating ranges for the successful operation of a swirl die were established. Within these ranges, the swirl die can produce helical loops of fiber that, when laid down upon a collection screen, produce an overlapping pattern of fibers. The fiber diameter, swirl diameter, and swirl frequency were measured as a function of operating conditions.

Both solid and hollow fibers were spun with the swirl die. Spinning hollow fibers has the advantages of less material (polymer) required as well as higher spiral frequency. Higher frequency allows the use of higher line speeds when using swirl dies for adhesive application.

Acknowledgements

This work was supported by an NSF GOALI grant (DMII-0245324). The swirl dies were provided through the generous assistance of the Nordson Corporation. The support of 3M and Procter & Gamble is also gratefully acknowledged.

References

(1) Ziecker, R. A.; Boger, B. B.; Smyrna, L. Adhesive Spray Gun and Nozzle Attachment. US Patent 4,785,996, Nov. 22, **1988**.

(2) Shambaugh, R. L. A Macroscopic View of the Melt Blowing Process for Producing Microfibers. *Ind. Eng. Chem.* **1988,** *27*(12), 2363-2372.

(3) Uyttendaele, M. A. J.; Shambaugh, R. L. Melt Blowing: General Equation Development and Experimental Verification. *AIChE J.* **1990,** *36*(2), 175-186.

(4) Rao, R. S.; Shambaugh, R. L. Vibration and Stability in the Melt Blowing Process. *Ind. Eng. Chem.* **1993,** *32*(12), 3100-3111.

(5) Marla, V. T.; Shambaugh, R. L. Three-Dimensional Model of the Melt Blowing Process. *Ind. Eng. Chem.* **2003,** *42*(26), 6993-7005.

(6) Marla, V. T.; Shambaugh, R. L. Modeling of the Melt Blowing Performance of Slot Dies. *Ind. Eng. Chem. Res.* **2004**, *43*(11), 2789-2797.

(7) Chhabra, R. An Experimental Study of Fiber Motion and Nonwoven Webs in Melt Blowing. Ph.D. Dissertation, University of Oklahoma, Norman, OK. 1997.

(8) Baum, B.; Holley, W.; White, R. A. Hollow Fibres in Reverse Osmosis, Dialysis, and Ultrafiltration. In *Membrane Separation Processes*; Meares, P., Ed.; Elsevier: New York, 1976; pp 187-227.

(9) De Rovere, A.; Shambaugh, R. L. Melt-Spun Hollow Fibers for Use in Nonwoven Structures. *Ind. Eng. Chem. Res.* **2001,** *40*(1), 176-187.

(10) Marla, V. T.; Shambaugh, R. L.; Papavassiliou, D. V. Modeling the Melt Blowing of Hollow Fibers. *Ind. Eng. Chem. Res.*, in press.

(11) Bansal, V.; Shambaugh, R. L. On-line Determination of Diameter and Temperature during Melt Blowing of Polypropylene. *Ind. Eng. Chem. Res.* **1998,** *37*(5), 1799-1806.

(12) Tyagi, M. K.; Shambaugh, R. L. Use of Oscillating Jets in Fiber Processing. *Ind. Eng. Chem.* **1995,** *34*(2), 656-660.

(13) Chhabra, R.; Shambaugh, R. L. Experimental Measurements of Fiber Threadline Vibrations in the Melt-Blowing Process. *Ind. Eng. Chem. Res.* **1996,** 35(11), 4366-4374.

(14) Saidman, L. *Hitting the Target: Accurate Adhesive Application at Increasing Line Speeds*, Proceedings of International Nonwovens Technical Conference, Baltimore, MD, Sept 15-18, 2003.

(15) Ramspeck, A. *Elasticized structures: Advancements in Adhesive Bonding for Nonwoven Disposables*, Proceedings of International Nonwovens Technical Conference, Atlanta, GA, Sept 24-26, 2002.

(16) Saidman, L. Rules for Optimum Bonding: Advancements in Fiber Application Technology Minimize Waste and Refine Product Features. *Adhes. Age*. **2002,** *45*(2), 24-28.

(17) De Rovere, A.; Shambaugh, R. L. Melt-Spun Hollow Fibers: Modeling and Experiments. *Polym. Eng. Sci.* **2001,** *41*(7), 1206-1219.

Expt number	Target Diameter µm (± 15%)	m_p g/min	m_n ml/min	Airflow slpm	Swirl Frequency (loops/s)	% hollowness	% increase
1	250	4.04	0	7.65	35.14	0	-
	250	3.25	0.64	7.65	35.14	15	0
	250	2.84	1.86	7.65	42.16	37	20
2	190	3.4	0	7.5	35.13	0	0
	190	3	0.37	7.5	35.13	10	-
	190	2.65	0.98	7.5	42.16	25	20
	190	2.17	1.31	7.5	54.46	35	55
3	170	2.75	0	7.5	44.19	0	-
	170	2.53	0.28	7.5	46.11	9	4.17
	170	2.05	2.29	7.5	61.49	50	37.5
4	150	1.82	0	6	35.13	0	-
	150	1.66	0.41	6	38.65	18	10
	150	1.41	1.24	6	47.43	44	35

Table 1. Summary of results of experiments where the outer fiber diameter was kept constant and the hollowness in the fibers was increased. $T_{a,die}$ and $T_{f,die}$ were kept at 325 ˚C and 310 ˚C, respectively.

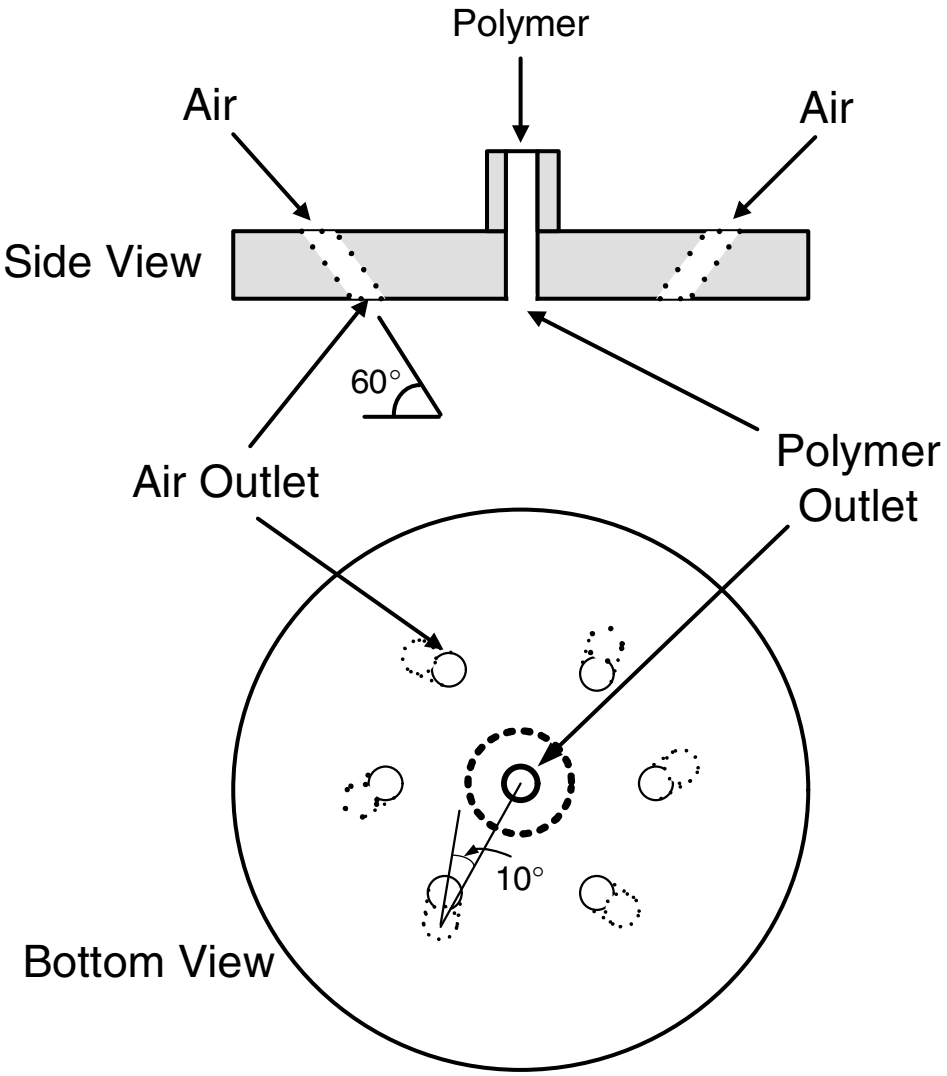

Figure 1. A swirl nozzle with the polymer orifice flush with the discharge plate. This nozzle has six air inlets. (This swirl nozzle produces solid, not hollow, fibers.) The air holes are 0.46 mm in diameter. The diameter the air hole pattern is 4.77 mm. Each air hole is canted at 60 degrees relative to the die face and 10 degrees relative to the center hole of the die (the angles are shown on the figure). The polymer capillary is 2.1 mm in diameter. This nozzle was furnished by the Nordson Corporation.

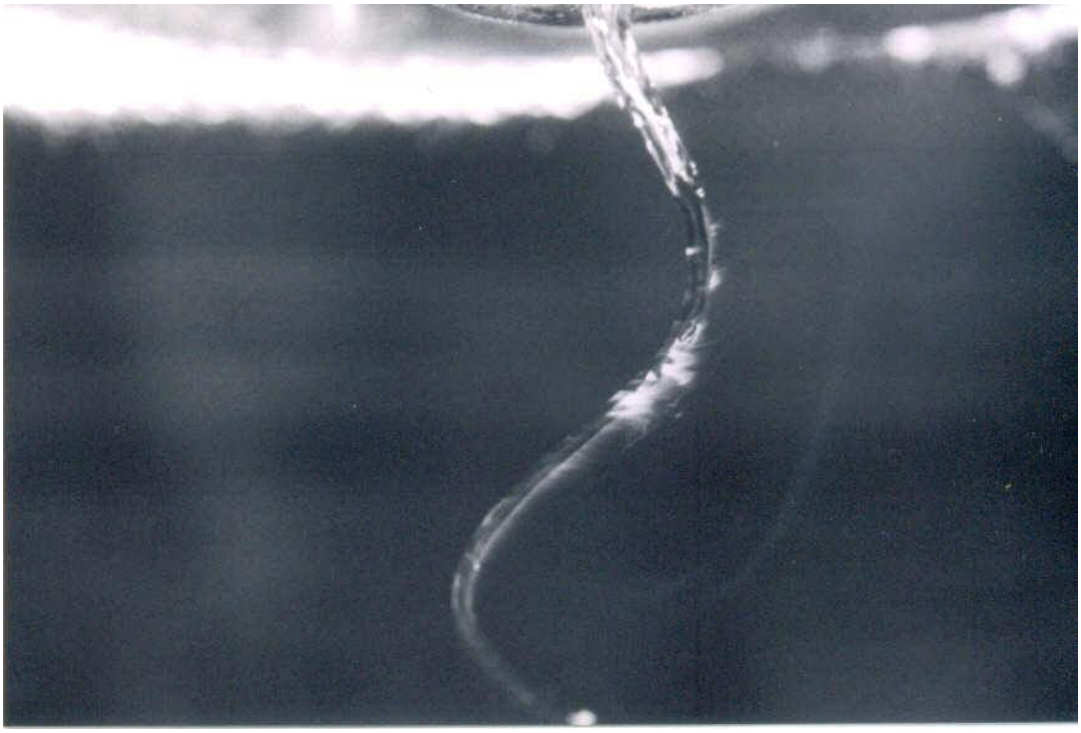

Figure 2. High-speed flash photograph of molten polymer exiting from a swirl die of the type shown in Fig. 1. The field of view for this photograph was 31.2 mm x 46.8 mm. This photo was taken with a Nikon 35 mm camera equipped with a macro lens. The polymer rate was 2.4 g/min, the air rate was 7.5 liter/min, the polymer temperature was 310 ˚C , and the air temperature was 325 ˚C. The polymer was 88 MFR Fina Dypro® isotactic polypropylene.

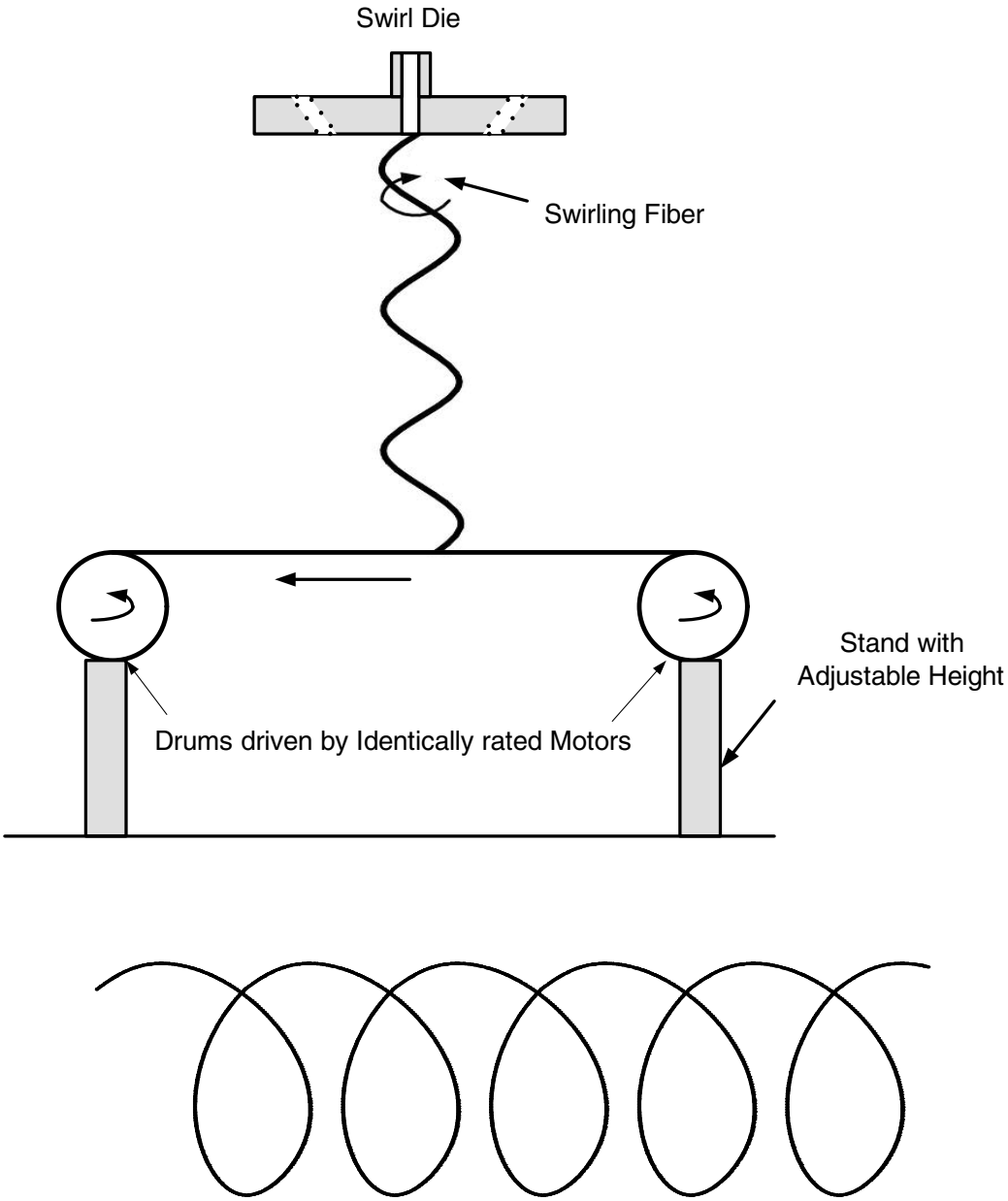

Figure 3. The swirl die with collector belt used to collect the fibers and measure the swirl frequency. (a) side view of apparatus (top). (b) top view of the deposition pattern of the fiber on the belt (bottom). The drums were 6.5 cm in diameter and were placed 200 cm apart. The belt was fabricated from heavyweight paper. In a typical run, about 8 meters of belt was fed from the feed roll to the windup roll.

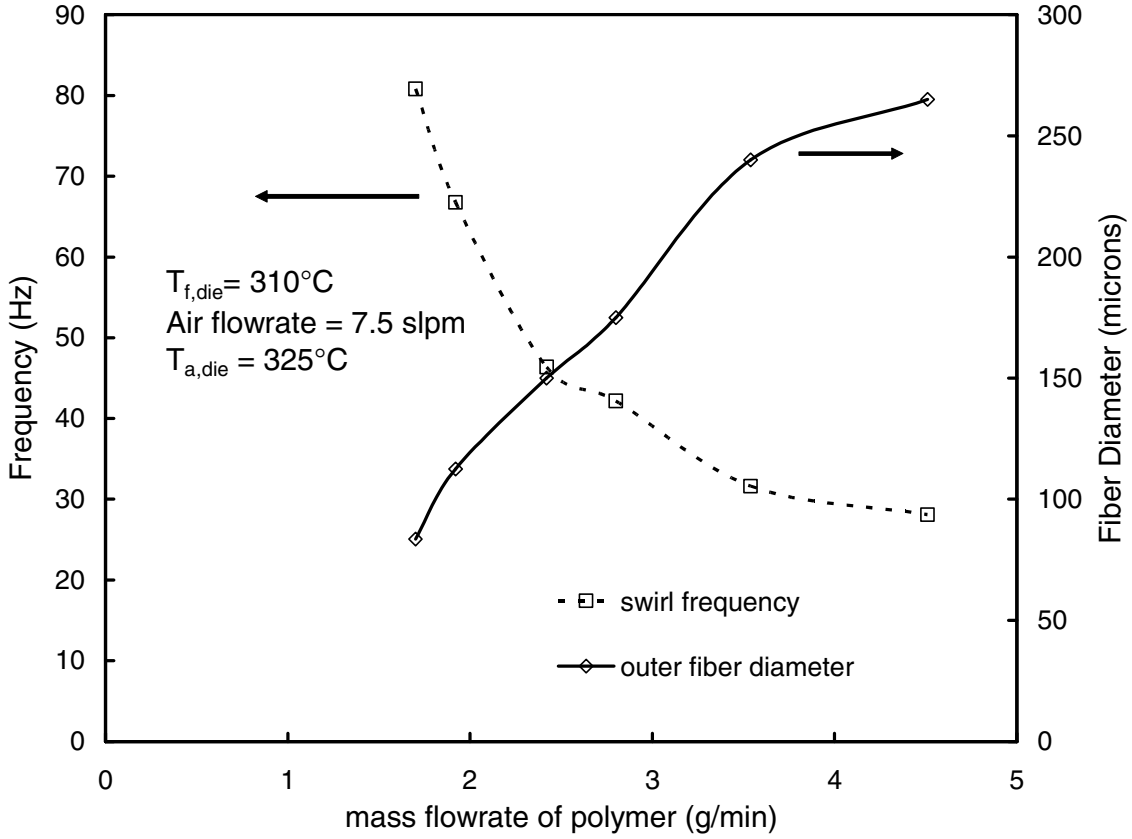

Figure 4. The effect of polymer flowrate on the final fiber diameter and swirl frequency. These results were for solid fibers produced with the type of die shown in Fig. 1.

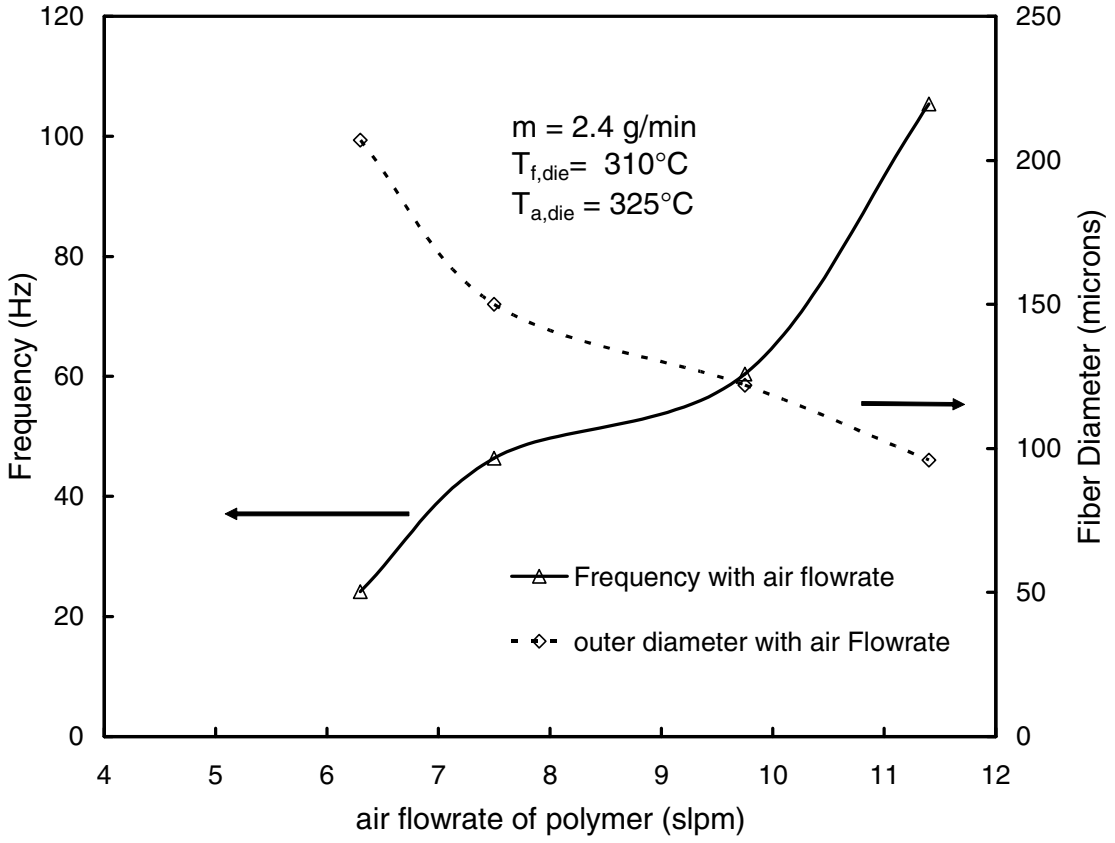

Figure 5. The effect of air flowrate on the final fiber diameter and swirl frequency. These results are for solid fibers.

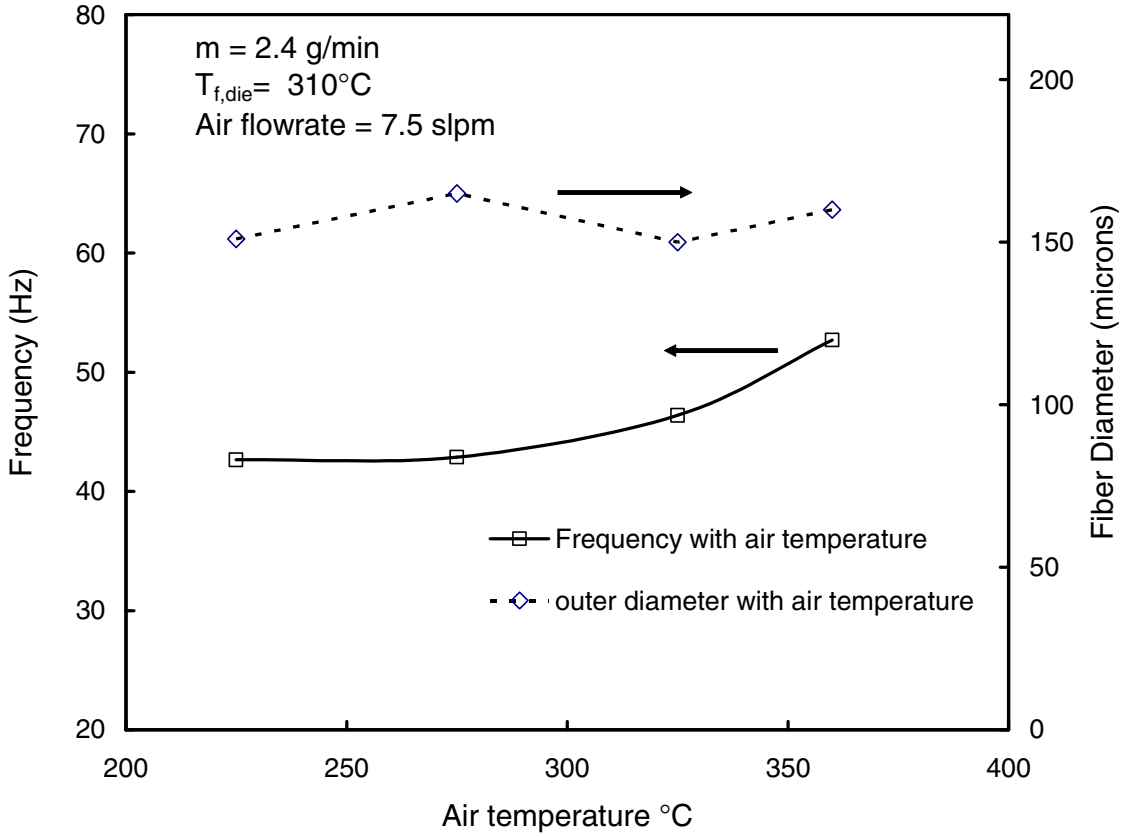

Figure 6. Effect of changing the air temperature (at the die) on the final fiber diameter and swirl frequency. These results are for solid fibers.

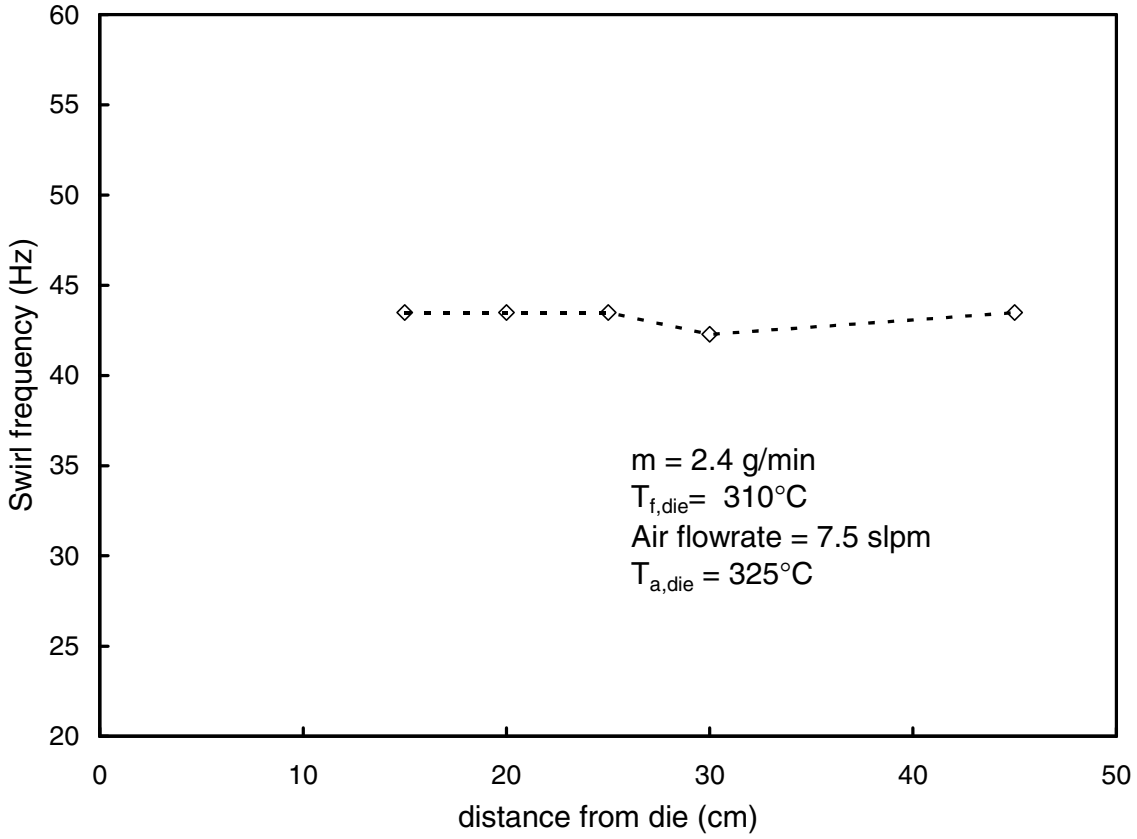

Figure 7. Effect of threadline distance on the swirl frequency.

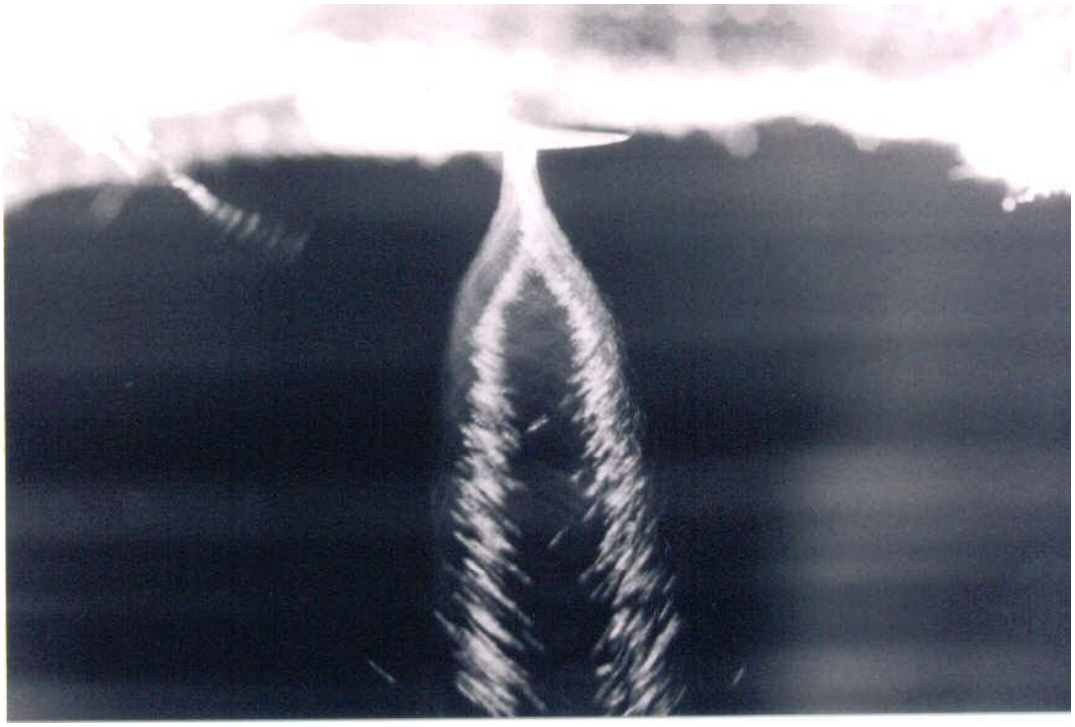

Figure 8a. Multiple-image photograph of the fiber exiting from a swirl die of the type shown in Fig. 1. The operating conditions for the die were mp = 2.4 g/min, $T_{f,die}$ = 310 ˚C, $T_{a,die}$ = 325 ˚C, and air flowrate = 7.5 slpm. For this photograph, the room was darkened, the exposure time set at 30 seconds, and a single film frame was exposed with 250 flashes of a strobe light (i.e., the strobe rate was 500 flashes per minute).

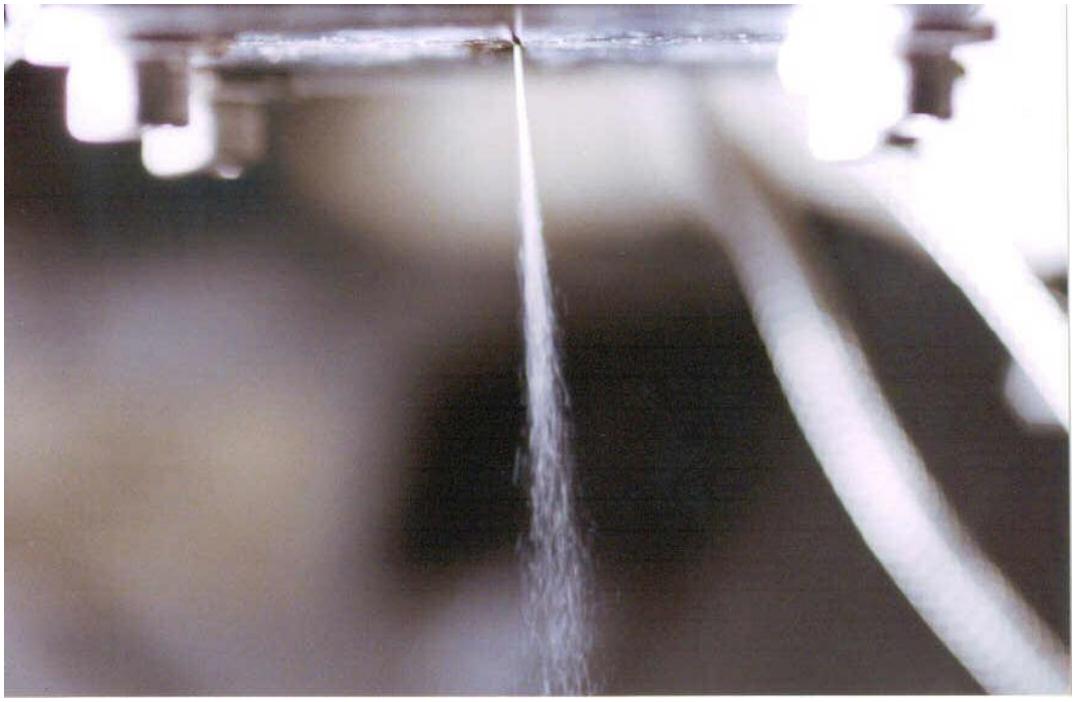

Figure 8b. Multiple image photograph of a fiber exiting from a slot die. The photographic technique is described in Chhabra and Shambaugh.[13] The slot die used in this image was described by Marla and Shambaugh (2004). The die operating conditions were m_p = 0.5 g/min, $T_{f,die}$ = 310 ˚C, $T_{a,die}$ = 310 ˚C and air flowrate = 125 slpm. The photograph was taken with the same technique described in the caption for Fig. 2. The strobe rate was 560 frames per minute, and the exposure time was 30 seconds, which resulted in 280 exposures on this single film frame. The die slot length was 7.46 cm, the air gap was 0.65 mm , and the die had a single polymer orifice.

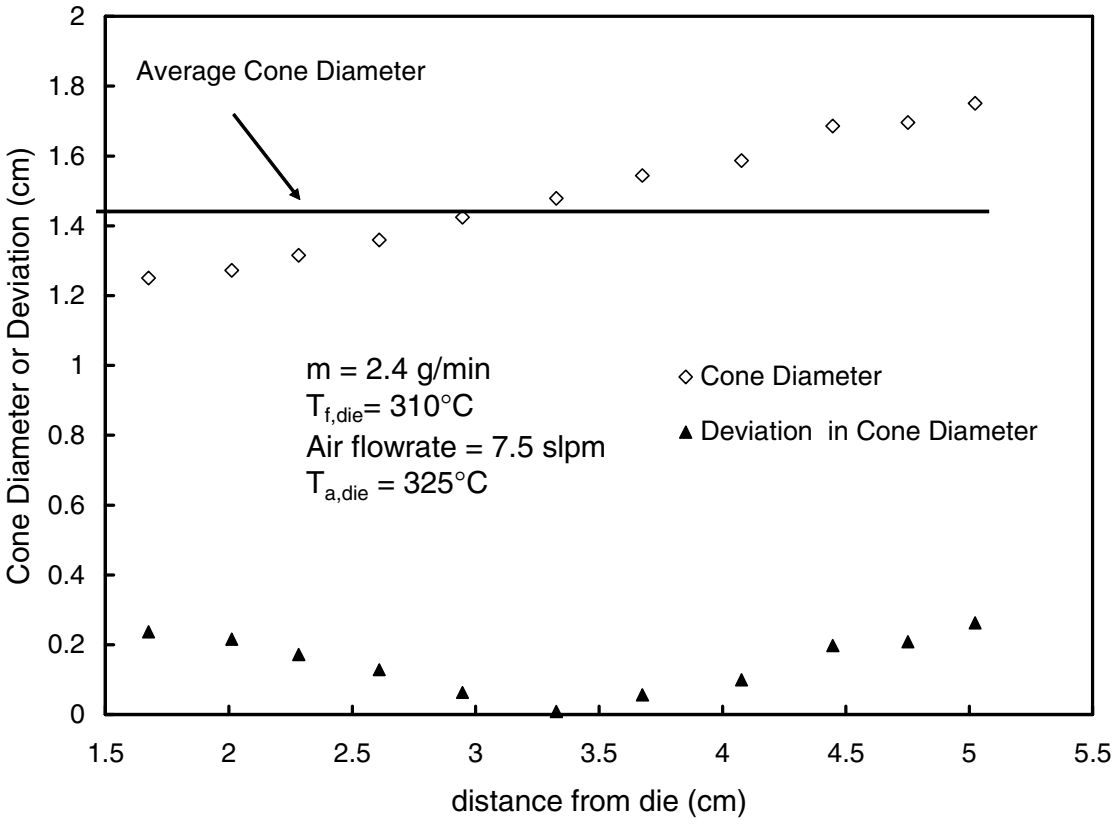

Figure 9. A comparison of cone diameter and cone variance for the fiber motion shown in Fig. 8a.

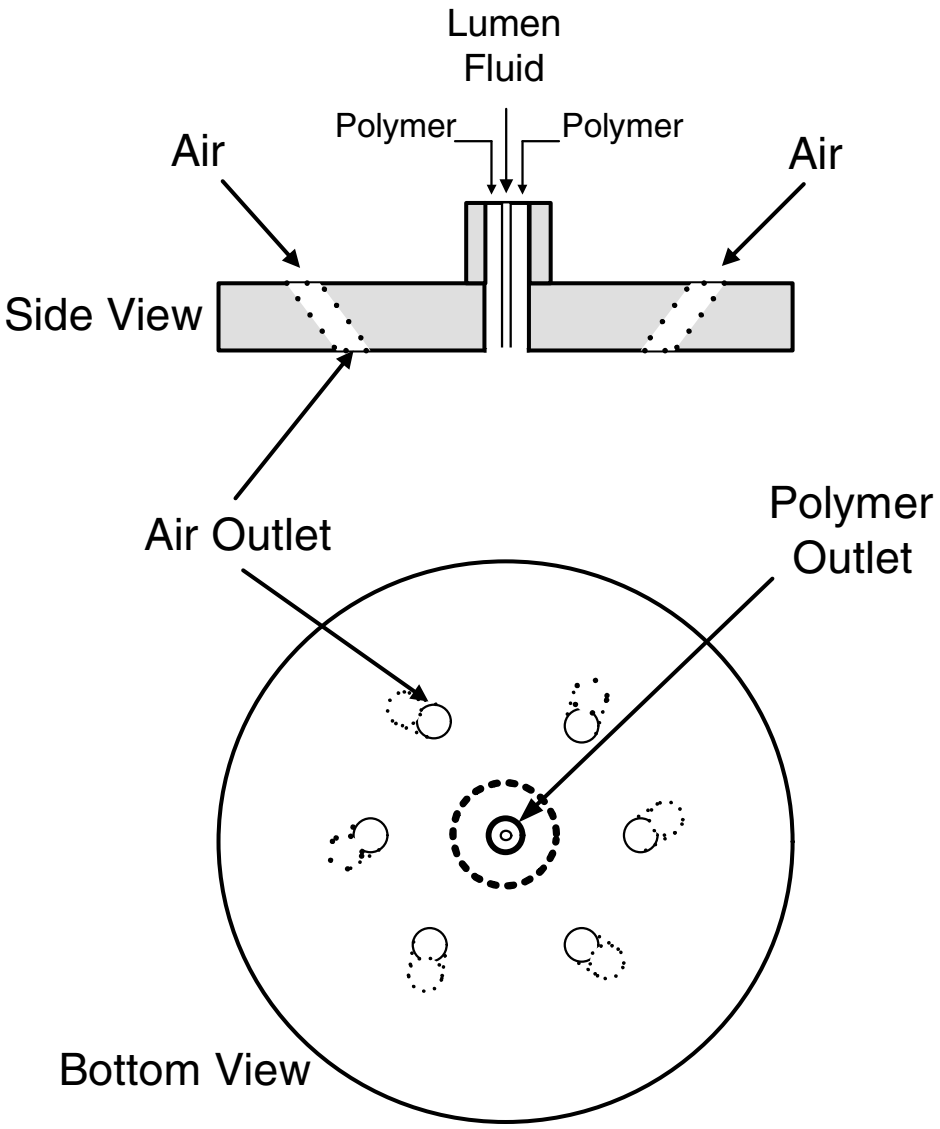

Figure 10. The modified swirl die used to produce hollow fibers. The air hole configuration is the same as in Fig. 1. The lumen tube has an inside diameter of 0.575 mm and an outside diameter of 1.2 mm. The annular polymer capillary has an outside diameter of 2.1 mm. This nozzle was furnished by the Nordson Corporation.

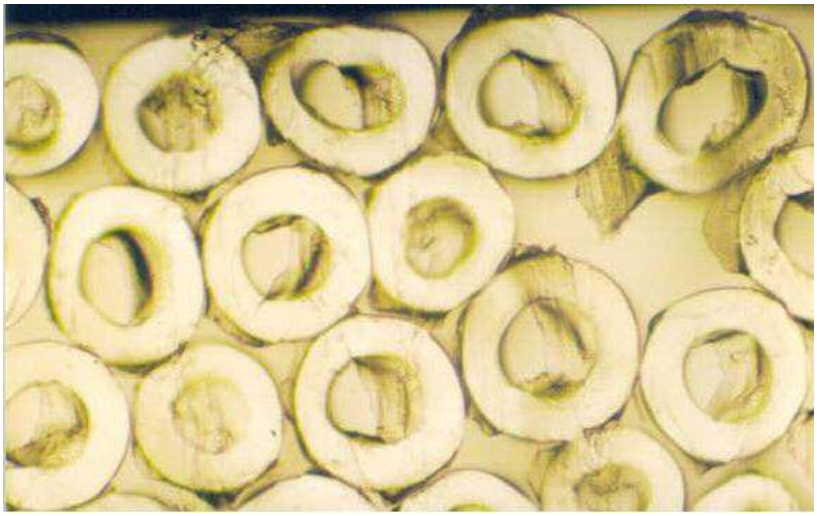

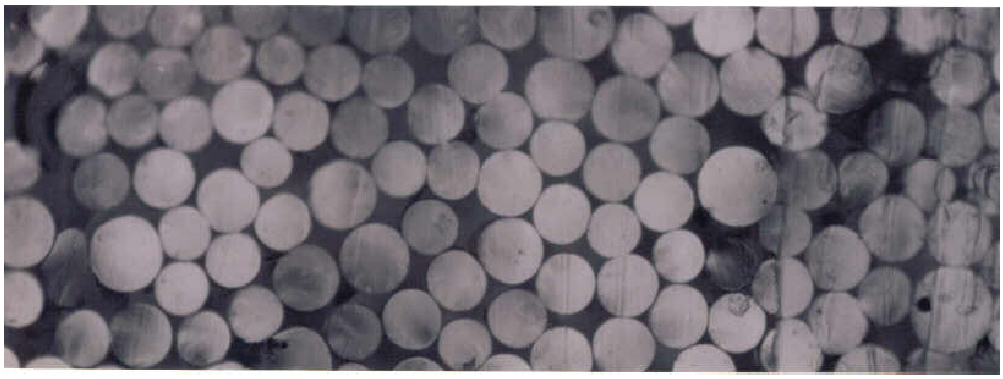

Figure 11. (a) Photomicrograph of 30 % hollow fibers manufactured using the modified swirl die assembly shown in Figure 10. The average outer diameter was 190 µm; and the inner diameter was 104 µm. (b) A photomicrograph of solid fibers made with the swirl die assembly shown in Fig. 1. The diameter of these fibers is 60 µm. A microscope magnification of 100 X was used to take these pictures.

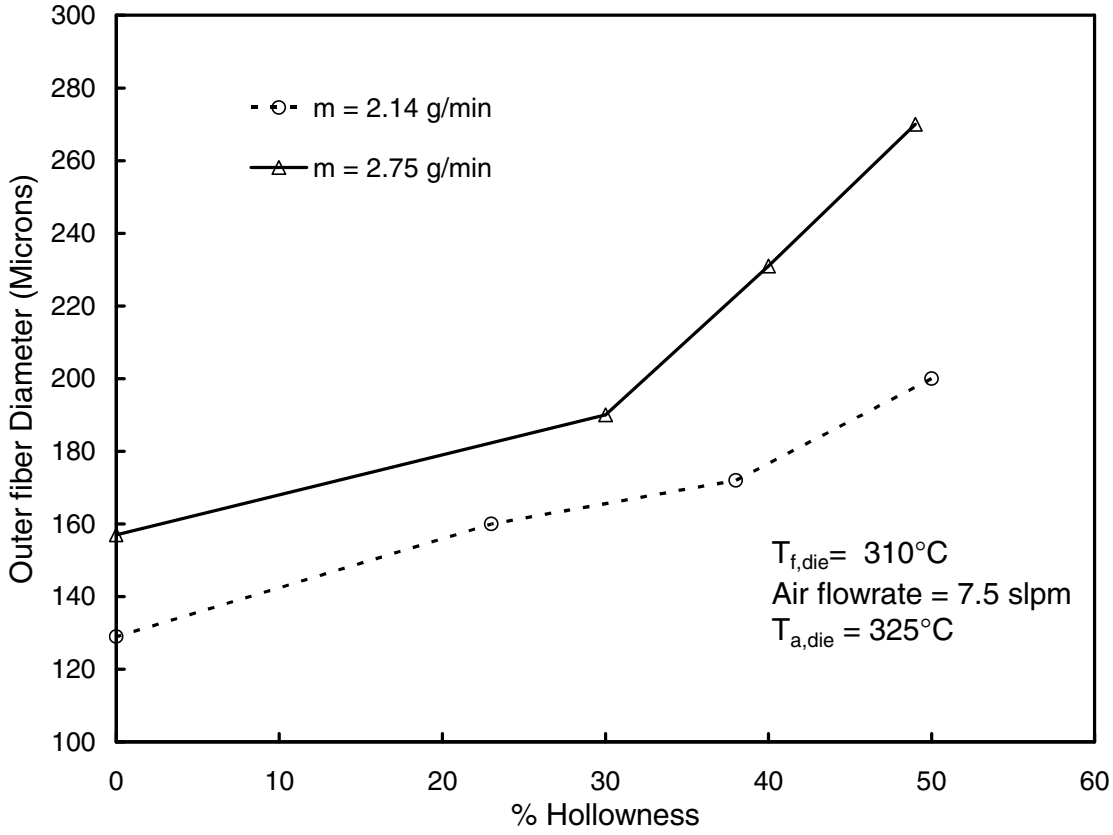

Figure 12. Effect of hollowness on the outer fiber diameter when the mass flowrate of the polymer was kept constant. These data were produced using the die shown in Fig. 10. The collection belt was placed 35 cm below the die. Each data point is the average of 10 measurements, and the maximum standard deviation of these measurements is 15 %.

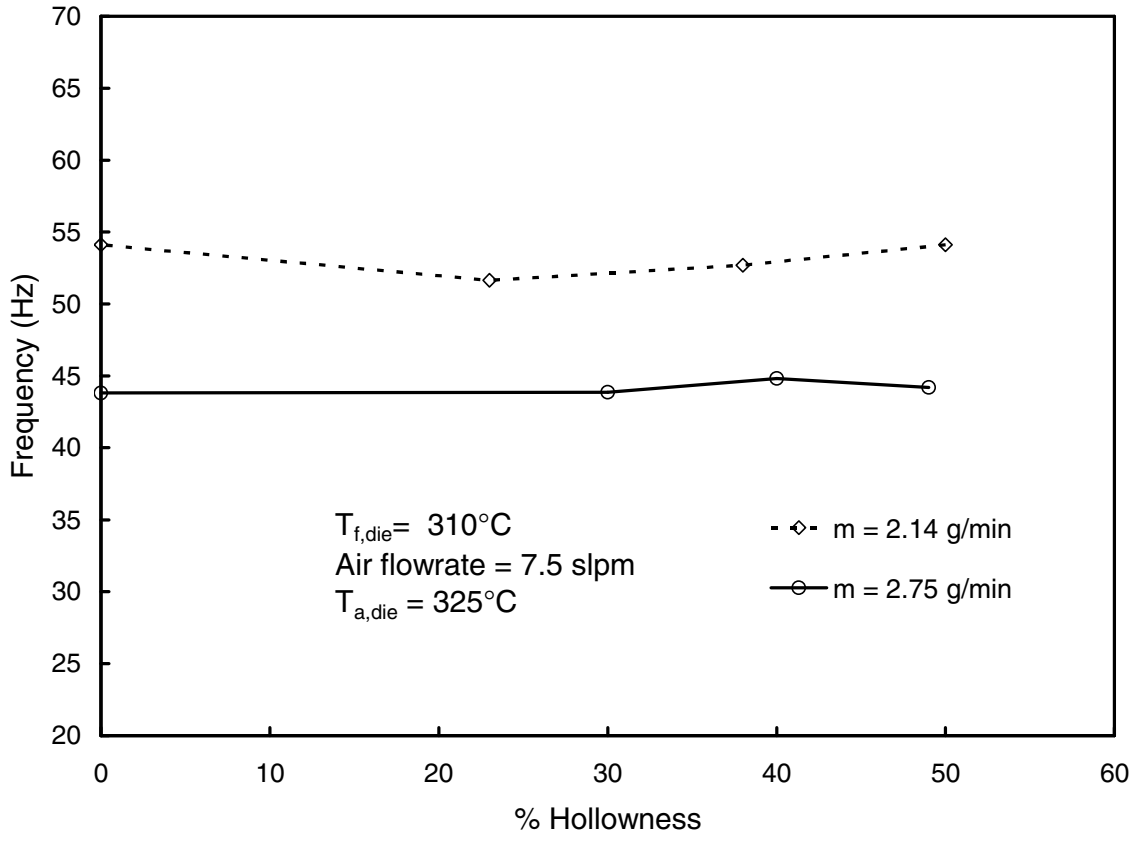

Figure 13. Effect of hollowness on the swirl frequency when the mass flowrate of the polymer was kept constant. The operating conditions are the same as in Figure 12. Each data point is based on 9 replicate measurements and the maximum standard deviation is 4 %.

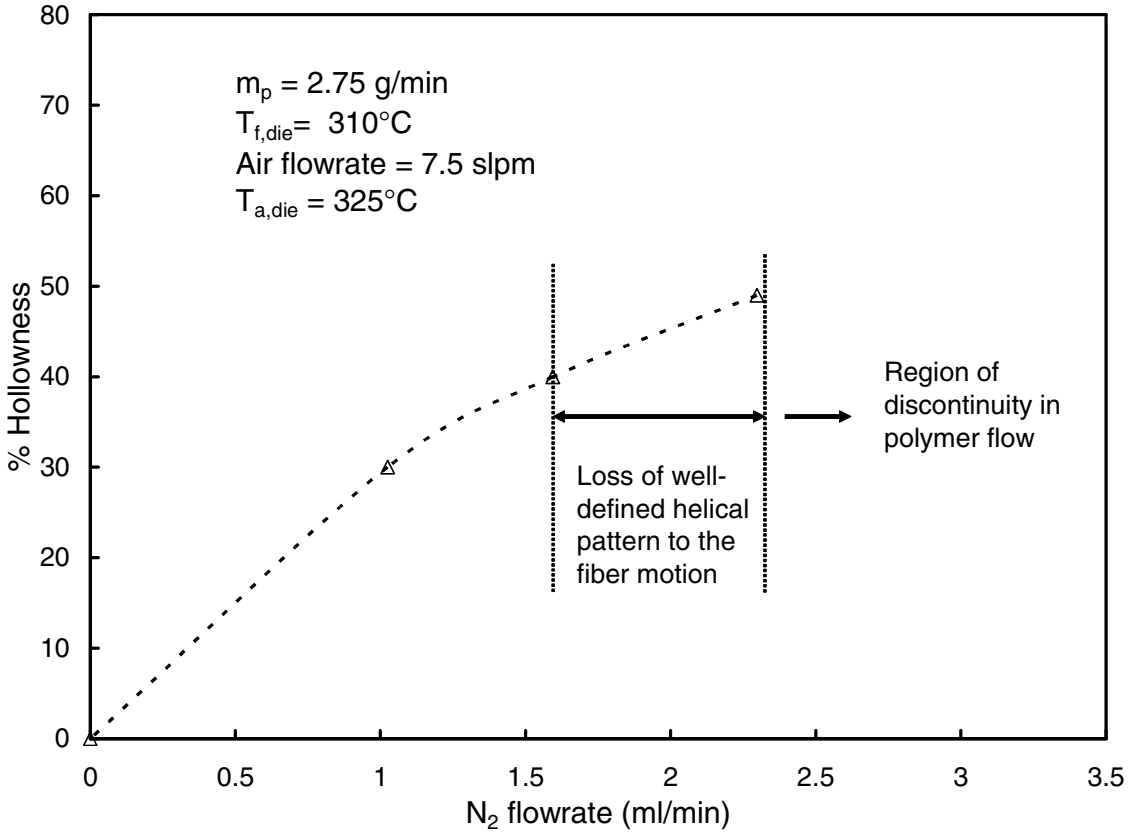

Figure 14. Effect of increasing the lumen fluid flowrate on the % hollowness for a polymer mass flowrate of 2.75 g/min.

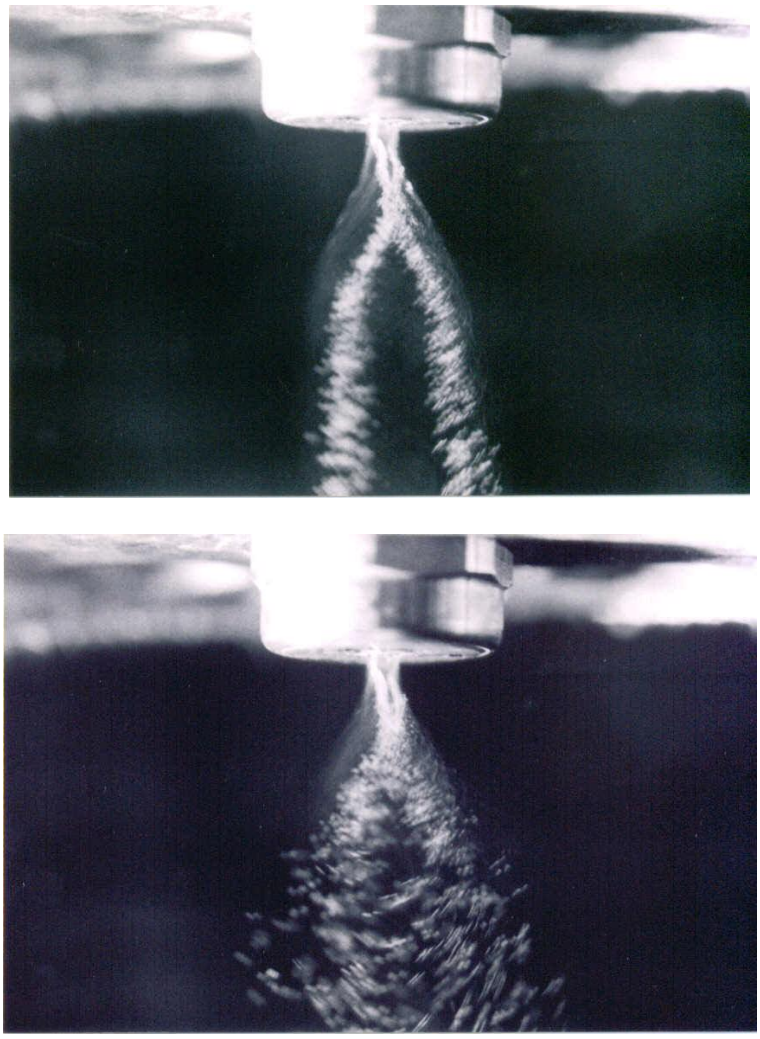

Figure 15. Multiple-image photograph of hollow fibers exiting from the swirl die for (a) 30 % hollowness (top), and (b) 50 % hollowness (bottom). The die operating conditions are the same as shown in Figure 14. The photographic conditions were the same as listed on Figure 8a.

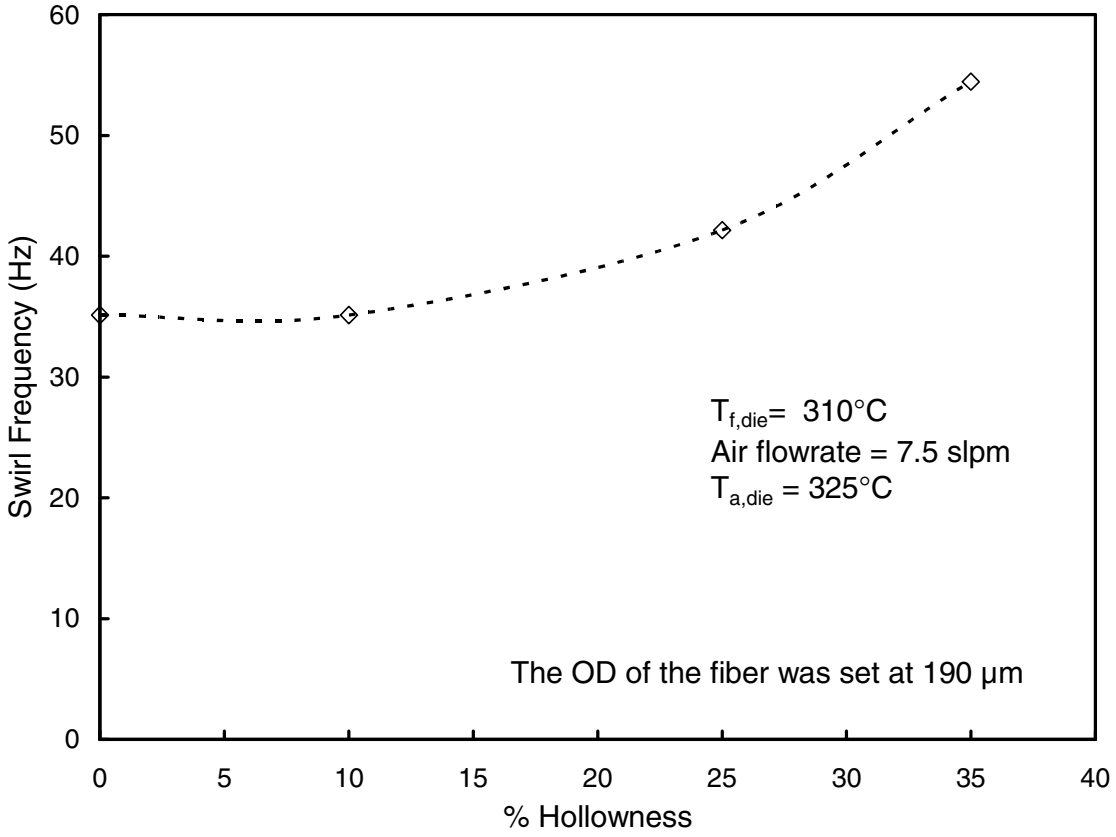

Figure 16. Effect of hollowness on the swirl frequency when the outer fiber diameter was kept constant at 190 µm.

CHAPTER 5

CALIBRATION OF AN INFRARED CAMERA FOR ACCURATE DETERMINATION OF THE TEMPERATURE OF POLYMER FILAMENTS

A revised version of this Chapter will be submitted as a journal article. This chapter will be referred to as Marla et al. 2005a in subsequent chapters.

5.1 Introduction

Determination and prediction of the temperature of fine polymer filaments is important in many commercial processes such as Melt Spinning, Melt Blowing etc. There are two main techniques for measuring the polymer temperature - a contact technique and a non-contact technique. The contact technique involves use of fine thermocouple probes for measuring temperature. However this technique has a limitation: In continuous fiber-making processes, using this technique would mean disturbing the flow.[1] Infrared thermography is a non-contact technique to measure the temperature and the underlying principle is conversion of the radiant energy received by the detector elements of an Infrared (IR) camera from the target into the target temperature. The radiant energy depends on the emissivity of the target, and from Kirschoff's law it follows that good absorbers are good emitters. Modern Infrared cameras have come a long way from the traditional versions that used liquid nitrogen for cooling the thermal sensors. Modern Infrared cameras use a grid of uncooled microbolometers as thermal radiation detectors, and the typical size of the array is 320 x 240 elements. This is a limitation of the IR

camera, because a target that has the same size or smaller than the element/pixel size will not give the same response as a larger target of the same material at the same temperature.[2] Also, in order to accurately determine the target temperature, the emissivity of the target must be known. Emissivity varies with several factors such as the material composition, surface roughness, material geometry, angle of vision and temperature.

The emissivity of polymers in the form of powder or thin films has been investigated by several researchers. A common assumption made while using infrared thermography is that the polymer is opaque (transmittance is zero). Hence an indirect method for evaluating the emissivity (e) involves measuring the reflectance (r) and then using the formula e = 1-r. Richmond[3] gave a detailed description on the measurement techniques for the reflectance of a material. Hansel and Lee[4] devised a simple technique for determining the emissivity of polymers in powdery form at high temperature and demonstrated this technique using polystyrene. Fujikura[5] measured the emissivity of several polymeric thin films as a function of film thickness. Cao et al.[6] determined the emissivity of thin polyethylene films as a function of both temperature and film thickness. Gay[7] determined the emissivity of polyimide-coated aluminum plate as a function of temperature. There are also bibliographic sources that tabulate the emissivity of surfaces of several materials.[8] However, to the best of our knowledge there is no detailed study on the emissivity of fine polymeric filaments of circular cross-section. Without accurate estimation of the emissivity of the material, an infrared image of an object may be of little or no use. Hence, effective use of the IR camera for obtaining quantitative data requires a careful calibration procedure where the spatial resolution of

the thermal imaging system is taken into account. The spatial resolution may be defined as the ability of the thermal imaging radiometer to accurately measure the temperature of objects whose size is of the same order as the detector element. Most IR camera manufacturers provide a slit response function curve which characterizes the thermal imaging system by the relative response to a vertical slit target of various widths.[9] This curve helps quantifying the error in the measurement of target temperature as a function of the size of the target. However, no information is provided on the technique used to generate such correction factors or the geometry of the object. The object of this work is to describe a simple technique one could use to calibrate the IR camera and thereby use it effectively for accurate measurement of the temperature of small targets of circular cross-section. For facilitating easy reading of this work, a review of basic terms used in Thermography is given in the next section.

5.2 Basic Thermography Terms and Technical Specifications of the IR Camera

The IR camera used in the present study was ThermaCAM® S60 manufactured by FLIR Systems. The spectral range for this camera is 7.5-13 μm (longwave). Thermal imaging radiometers with 3-5 μm (shortwave) or 3-14 μm (broadband) spectral response are also commercially available. The IR image displayed has a resolution of 640 x 480 pixels while the actual number of thermal detector sensors or elements is 320 x 240. The other prominent features of this IR camera can be found on the manufacturer's website and the camera's user manual.[10] The IR lens on this camera has a field of view (FOV) of 24˚ x 18˚ with a minimum focus distance of 0.3 m or 11.81 inches. Thus the horizontal

field of view (HFOV) at this minimum focus distance is 5.02 inches while the vertical field of view (VFOV) is 3.77 inches. The instantaneous field of view (IFOV) at a certain distance from the target is defined as the ratio of the HFOV at that distance to the number of thermal detector elements in the horizontal direction (320 elements or pixels). Alternatively it is the ratio of the VFOV to the number of detector elements in the vertical direction (240 elements or pixels). These terms are explained in Figure 1. As can be seen, the HFOV, VFOV and the IFOV increase as the distance from the IR lens to the target (L) increases. Also, the response of the IR camera would be maximum when the IFOV is minimum, or, when the IR camera is closest to the target. Mathematically, these quantities can be calculated as

$$\text{HFOV} = 2 \times L \times \text{TAN}(12) \quad (1)$$

$$\text{VFOV} = 2 \times L \times \text{TAN}(9) \quad (2)$$

$$\text{IFOV} = \frac{\text{HVOF}}{320} \text{ or } \frac{\text{VFOF}}{240} \quad (3)$$

where the quantities in the parentheses for the trigonometric relationship is evaluated in degrees and L is the distance from the IR camera to the target. Table 1 shows the HFOV, VFOV and the IFOV for several working distances.

The camera also came with a 100 µm close-up lens for which the minimum focus distance is 80 mm while the maximum working distance is 110 mm. The IFOV for the minimum and maximum focus distance is approximately 80 µm and 108 µm respectively. The close-up lens fits on the 24˚ lens of the IR camera and has certain advantages over the 24˚ lens. Since it has a very narrow range of working distances (80-110 mm), the detector receives radiant energy only from the object under consideration

and the user need not worry about radiation from other objects which would contaminate the target signal. Secondly, since the IFOV of the close-up lens is so small compared to the 24˚ lens, the signal from very small targets would be far stronger than with the 24˚ lens. However, the close-up lens is susceptible to damage very easily if proper precautions are not taken. For example, since the working distance is so small, a tiny vibration or jerk can cause it to come in contact with the high-temperature target and irreparably damage it.

5.3 Experimental Setup

Figure 2a shows the schematic of the test unit that was built to calibrate the IR camera. Compressed air regulated at 70 psi was passed through a thermal mass flow meter that was adjusted for 50 slpm of air at standard conditions of 21 ˚C and 1 atmosphere pressure. The air then passed through a reservoir heated by two 750 W cartridge heaters. Line 2 was heated a 420 W tape heater and finally line 3 was heated by another 420 W tape heater. All the heating lines were wrapped in two layers of insulation – an inner layer of fiberglass foam insulation, which was in contact with the 3/8" stainless steel pipe, and an outer layer of fiberglass cloth tightly wrapped around the inner layer. Thermocouples were placed in each of these lines and the temperatures were controlled to obtain the desired temperature at the discharge of the pipe. Line 4, from which the air exited, had an ID of 0.493" and an OD of 0.675". The pipe material was SS 304 with a length of 30" resulting to a L/D of 60. The air exiting from the pipe at 50 slpm had a

Reynolds number of 4300-4600 depending on the temperature of the air at the discharge. The cylindrical coordinate system was chosen, and is also shown in Figure 2a.

Mean air velocity measurements below the pipe discharge were taken using a conventional Pitot tube that had an outer diameter of 0.7 mm and an inner diameter of 0.4 mm. A two way valve enabled us to measure the stagnation pressure from two instruments – an Ashcroft® digital industrial pressure gauge (model 2074; range 0-30 psi with 0.25 % accuracy) supplied by Cole Parmer and a Dwyer model 25 liquid manometer. The model 25 manometer had a range of 1.27 to 76.2 mm of water. The Pitot tube was attached to a three-dimensional manual traverse that could position the Pitot tube precisely within the flow field. The traverse had 0.001" resolution (or 25.4 μm resolution), which is particularly useful in flow fields with steep velocity gradients. The air temperature measurements below the pipe discharge were made using a J-type 0.01" diameter thermocouple connected to an Omega® microprocessor thermometer (model HH21) that digitally displayed the measured temperature.

Polymer fibers of different diameters (0.1 mm – 2 mm) were prepared in our laboratory using an extruder and gear pump assembly, the details of which can be found in Marla and Shambaugh.[11] It is important to note that these fibers have circular cross-sections. The diameter of the fibers was measured using an optical microscope. The polymer used in most of the experiments was 88 MFR Fina Dypro® isotactic polypropylene. This polymer had a M_w of 165,000 g/mol and a M_n of 41,500 g/mol. Some experiments with fibers made of Polybutylene were also performed. This resin was Grade 0400 manufactured by Basell Polyolefins and had a MFR of 20. The fiber was held

8 mm below the exit of the pipe and was oriented horizontally by means of a special device attached to the traverse unit as shown in Figure 2b. Using the traverse, the fiber was positioned exactly below the center of the discharge tube. The IR camera was placed at different distances from the polymer fibers and the real-time IR image of the fiber could be seen either on a 4" LCD screen attached to the IR camera or on a monitor by means of a firewire (IEEE 1394) cable connecting the IR camera with a PC.

5.4 Results and Discussion

While the air flowrate was kept constant at 50 slpm, the heaters in Lines 1, 2 and 3 were adjusted to obtain temperatures of 105 ˚C, 121 ˚C and 141 ˚C at 8 mm below the discharge. The highest temperature chosen was 141 ˚C because the melting point of the polypropylene fibers is 165 ˚C and temperatures near or above this melting point would cause dimensional changes, stretching etc. thereby changing the geometry of the fibers. For a discharge temperature of 141 ˚C, the radial velocity and temperature profile of air at z = 8 mm is shown in Figures 3a and 3b respectively. It can be seen that the air flowfield at z = 8 mm displays a flat velocity and temperature profile in the region around the z-axis. Hence, one can safely make the assumption that a fine polymer filament placed at this location would assume the same temperature as the air, since there are no heat losses from the portion of the polymer filament near the z-axis. Velocity and temperature profiles for several other downstream locations are also shown for comparison. The flat-topped profile gradually changes into a bell-shaped profile as z increases and this type of behavior is typical for round jets.

The fiber temperature recorded from the IR measurements was the maximum temperature displayed by a line that was drawn perpendicular to the fiber on its IR image such that this line coincided with the z-axis. From this point onwards, unless otherwise mentioned all measurements of fiber temperature were made at this location. Using the close-up lens, the temperature of a 1.9 mm fiber placed in the flowfield with a discharge temperature of 141˚C was measured. Since the fiber must attain the temperature of 141 ˚C, the emissivity of the fiber was adjusted (the IR camera had adjustable emissivity) until the maximum temperature recorded was 141 ˚C. The emissivity was found to be 0.82. This procedure was repeated for discharge temperatures of 105 ˚C and 121 ˚C and the emissivity was found to be the same. A 1.9 mm fiber, when viewed with the close-up lens, occupies 19 detector elements (or pixels) on the IR image and hence it is quite obvious that the response would be 100 %. Next, a 1.33 mm fiber was placed in the flowfield and it was observed that under an emissivity of 0.82, the recorded temperatures were 138 ˚C, 118 ˚C and 101 ˚C for discharge temperatures of 141 ˚C, 121 ˚C and 105 ˚C respectively. A 1.33 mm fiber, when viewed with a close-up lens occupies around 13 pixels, and hence one would expect that the response would be 100 % and the recorded temperature would be the same as for a 1.9 mm fiber. Using the close-up lens and assuming an emissivity of 0.82, the temperature of fibers of different diameters was recorded.

The close-up lens from the IR camera was removed and measurements were made with the 24˚ lens. Starting from the minimum focus distance of 11.81”, temperature measurements of the fibers were made at several target distances with a maximum

distance of 120". This data is plotted in Figure 4. The ordinate is the ratio of the recorded fiber temperature in Celsius assuming an emissivity of 0.82 to the actual temperature in Celsius (depending on the heater settings, this would be one of 141 ˚C, 121 ˚C or 105 ˚C). The abscissa is the ratio of the instantaneous field of view (IFOV) to the fiber diameter. As explained in equations 1-3, the IFOV increases with target distance. The ordinate in Figure 4 can be construed as the signal strength and this decreases with increasing target distance. Also, for a fiber of certain diameter, the signal strength is almost independent of temperature and this trend is seen in all of the fibers. It can also be seen that the signal strength shows signs of diameter dependence as the curves for different fiber diameters do not overlap. Now, at the same abscissa, it seems reasonable to expect that a fiber of diameter 0.86 mm would occupy the same area of the IR image as a fiber of 0.69 mm or 0.48 mm or any other diameter. Hence it would seem logical that the signal strength at the same abscissa would be the same considering the way the normalization has been performed. This was not observed, however, suggesting that there is some inherent diameter-dependent property of the fiber causing this phenomenon.

We can address the above issue by introducing an "apparent emissivity" that depends on the diameter of the fiber. We assume that the signal strength as observed from the close-up lens of the IR camera is always 100 %, since the fiber occupies more than one pixel or thermal sensor element. We adjust the emissivity of the fiber until the observed temperature is the same as what would be for a 1.9 mm fiber. For example, adjusting the emissivity of the 1.33 mm fiber to 0.78 gave the measured temperature to be 141 ˚C, 121 ˚C or 105 ˚C for the respective discharge temperatures. Furthermore, we

observed that the "apparent emissivity" was independent of the discharge temperature. Figures 5a and 5b show the apparent emissivity as a function of fiber diameter for polypropylene (PP) and polybutylene (PB) fibers, respectively. Both Figures show the same trend - the apparent emissivity increases with increasing fiber diameter and finally reaches an asymptotic value of 0.82 and 0.85 for PP and PB fibers, respectively. Golzar et al.[1] used a similar approach for Polyethyletherketone (PEEK) fibers and observed the same trend. In addition, Fujikura[5] observed the same trend while measuring the emissivity of polymer films of different thicknesses.

Using these values of apparent emissivity, the measurements were made with the 24˚ lens for the same target distances as Figure 4 and the results are plotted in Figure 6. The apparent emissivity approach makes the resultant plot independent of fiber diameter and Figure 7 shows a power law fit to the entire data. Using Figure 7, the four-step procedure to estimate the true temperature of the polymer filament is outlined below:

1. Determine the diameter of the polymer fiber and adjust the apparent emissivity using Figure 5. Insert this value in the settings of the IR camera.
2. Determine the distance between the target and the IR camera and using equation 3, determine the IFOV.
3. Using the power law fit in Figure 7, find the ordinate corresponding to the abscissa (where the abscissa is equal to the ratio of IFOV to the fiber diameter)
4. Measure the temperature of the target from the same distance using the IR camera and divide this value by the ordinate obtained in step 3 to obtain the true temperature of the polymer.

As an example consider a PP fiber of 0.475 mm diameter with the IR camera at a distance of 40" from the fiber. The HFOV, VFOV and the IFOV for this setting are 17.01", 12.67" and 1.35 mm respectively. The apparent emissivity determined from Figure 5a for this fiber diameter is 0.63. The ratio of IFOV to the fiber diameter is 2.84 and using this as the abscissa in the power law expression in Figure 7, the ordinate is 0.53. Hence the temperature of the fiber using an apparent emissivity of 0.63 in the IR camera is divided by 0.53 to obtain the true temperature of the polymer. This calibration curve makes it possible to use the IR camera far from the target in situations where it is not safe to get too close to the target. The advantage of this calibration curve is that there is no significant loss in accuracy in the measurement of small targets even at large distances. It should be noted that while this curve is primarily for PP and PB fibers in the range of 100 μm to 2 mm, this technique can be adapted for any other polymeric material.

5.5 Conclusions

Effective use of an IR camera requires careful estimation of target emissivity and knowledge of the surrounding conditions such as humidity and ambient temperature. There are errors in the temperature measurement when the target dimensions are of the same order as that of each element of the thermal sensor. A simple procedure was described to calibrate an IR camera enabling the user to obtain accurate temperature measurements of polymer fibers of diameter in the range 100 μm – 2 mm at different

target distances. It was found that by introducing an apparent emissivity which varied as a function of the fiber diameter, a universal response curve of signal strength as a function of both fiber diameter and target distance was obtained. Fibers made of both polypropylene and polybutylene and of different diameters clustered very well on this curve and a power law was fitted to the entire data. A four-step procedure was proposed to accurately determine the temperature of polymer fibers of known diameter at any working distance. This approach can be used for measurement of filament temperature in continuous fiber-making processes such as melt spinning and melt blowing.

Acknowledgements

This work was supported by an NSF GOALI grant (DMII-0245324). The support of 3M and Procter & Gamble is also gratefully acknowledged.

References

1. Golzar, M.; Beyreuther, R.; Brunig, H.; Tandler, B.; Vogel, R. Online Temperature Measurement and Simultaneous Diameter Estimation of Fibers by Thermography of the Spinline in the Melt Spinning Process. *Adv. Polym. Tech*. **2004,** *23*(3), 176-185.
2. Garber, W. C.; Seffrin, J. R. IRINFO Web Page. http://www.irinfo.org/Articles/article_10_20_2002_applying_distance.html (Accessed May 2005), Applying Distance to Spot Ratio Values to Infrared Imagers for Accurate Temperature Measurement.
3. Richmond, J. C. Measurement of Thermal Radiation Properties of Materials. *High Temp.-High Pres*. **1978,** *11*(4), 355-381.
4. Hansel, J. G.; Lee, S. Y. Technique for Measuring the Emittance of Polymers at Elevated Temperatures. *Appl. Spectrosc.* **1967,** *21*(4), 261-262.
5. Fujikura, Y. Emissivity of Polymers. *Yamagata Daigaku Kiyo, Kogaku*. **1999,** *25*(2), 55-68.
6. Cao, B.; Sweeney, P.; Campbell, G. A. *Infrared Characteristics of Thin Polymer Film: Temperature Measurement of Polyethylene*, Annual Technical Conference - Society of Plastics Engineers, New York, May 1-4, 1989.
7. Gay, F. P. Polymer Emissivity. *J. Polym. Sci*. **1973,** *11*, 2227-2235.
8. Singham, J. R. Tables of Emissivity of Surfaces. *Int. J. Heat Mass Transfer*. **1962,** *5*(1-2), 67-76.
9. Inframetrics Inc. *Model 600L Operator's Manual*, North Billerica, MA, 1989.
10. FLIR Systems. *ThermaCAM® S60 Operator's Manual*, Boston, MA, 2004.

11. Marla, V. T.; Shambaugh, R. L. Modeling of the Melt Blowing Performance of Slot Dies. *Ind. Eng. Chem. Res*. **2004,** *43*(11), 2789-2797.

12. Fujikura, Y.; Suzuki, T.; Matsumoto, M. Emissivity of Chlorinated Polyethylene. *J. Appl. Polym. Sci*. **1982,** *27*(4), 1293-1300.

L (inches)	L (cm)	VFOV (inches)	VFOV (cm)	HFOV (inches)	HFOV (cm)	IFOV (inches)	IFOV (mm)
12	30.48	3.802	9.656	5.102	12.959	0.016	0.405
14	35.56	4.435	11.266	5.952	15.119	0.019	0.472
16	40.64	5.069	12.875	6.803	17.279	0.021	0.540
18	45.72	5.703	14.485	7.653	19.439	0.024	0.607
20	50.8	6.336	16.094	8.503	21.599	0.027	0.675
22	55.88	6.970	17.703	9.354	23.758	0.029	0.742
24	60.96	7.603	19.313	10.204	25.918	0.032	0.810
26	66.04	8.237	20.922	11.054	28.078	0.035	0.877
28	71.12	8.871	22.532	11.905	30.238	0.037	0.945
30	76.2	9.504	24.141	12.755	32.398	0.040	1.012
32	81.28	10.138	25.750	13.605	34.558	0.043	1.080
34	86.36	10.772	27.360	14.456	36.718	0.045	1.147
36	91.44	11.405	28.969	15.306	38.878	0.048	1.215
38	96.52	12.039	30.579	16.156	41.037	0.050	1.282
40	101.6	12.672	32.188	17.007	43.197	0.053	1.350
42	106.68	13.306	33.797	17.857	45.357	0.056	1.417
44	111.76	13.940	35.407	18.707	47.517	0.058	1.485
46	116.84	14.573	37.016	19.558	49.677	0.061	1.552
48	121.92	15.207	38.626	20.408	51.837	0.064	1.620
50	127	15.841	40.235	21.258	53.997	0.066	1.687
52	132.08	16.474	41.844	22.109	56.156	0.069	1.755
54	137.16	17.108	43.454	22.959	58.316	0.072	1.822
56	142.24	17.741	45.063	23.810	60.476	0.074	1.890
58	147.32	18.375	46.673	24.660	62.636	0.077	1.957
64	162.56	20.276	51.501	27.211	69.116	0.085	2.160
66	167.64	20.910	53.110	28.061	71.275	0.088	2.227
68	172.72	21.543	54.720	28.912	73.435	0.090	2.295
70	177.8	22.177	56.329	29.762	75.595	0.093	2.362

Table 1. HFOV, VFOV and IFOV for various target distances (L) for the 24˚ IR lens

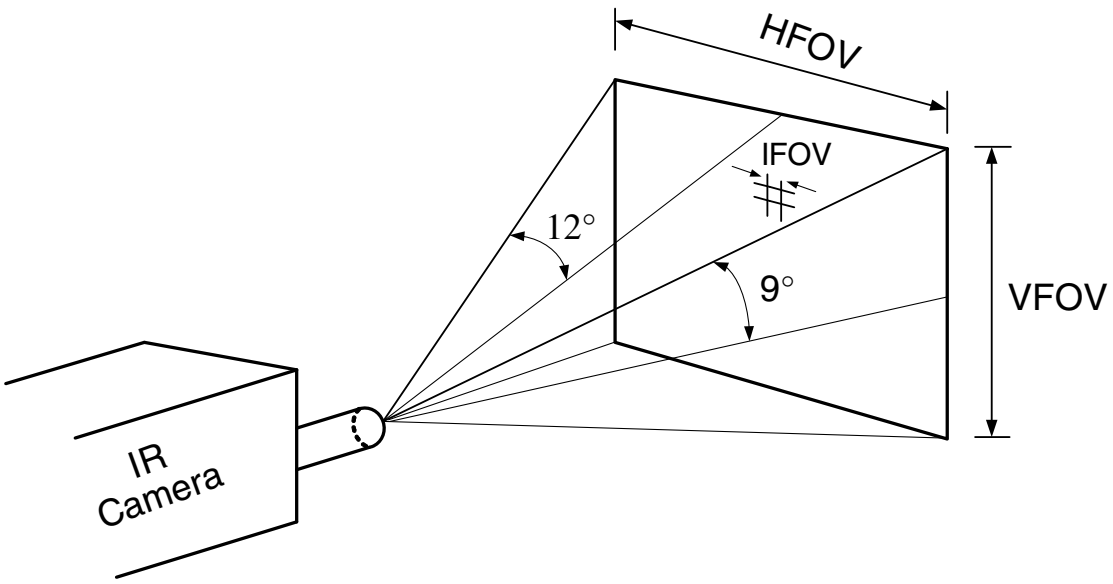

Figure 1. Horizontal field of view (HFOV), vertical field of view (VFOV) and instantaneous field of view (IFOV) for the 24 ˚ IR lens. L is the distance from the front of the lens to the target.

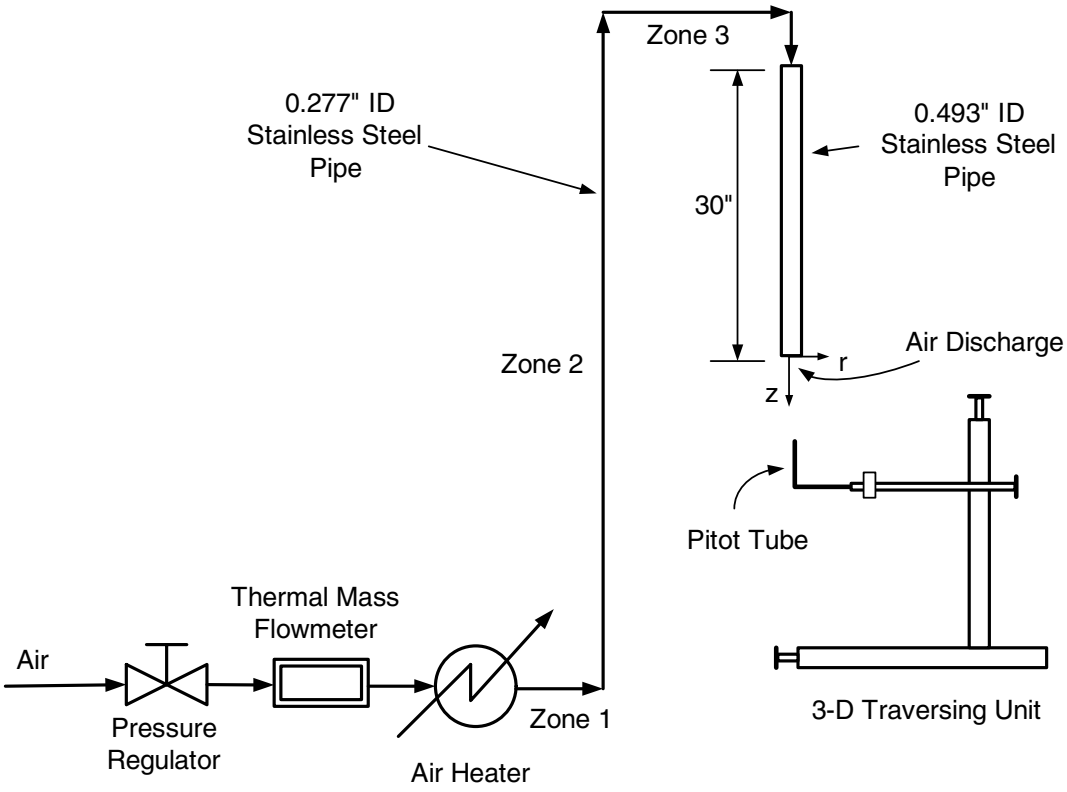

Figure 2a. Test unit built for calibration of the IR camera. The r and z directions (for the cylindrical coordinate system) are also shown in the Figure. The z axis coincides with the longitudinal axis of the stainless steel discharge pipe.

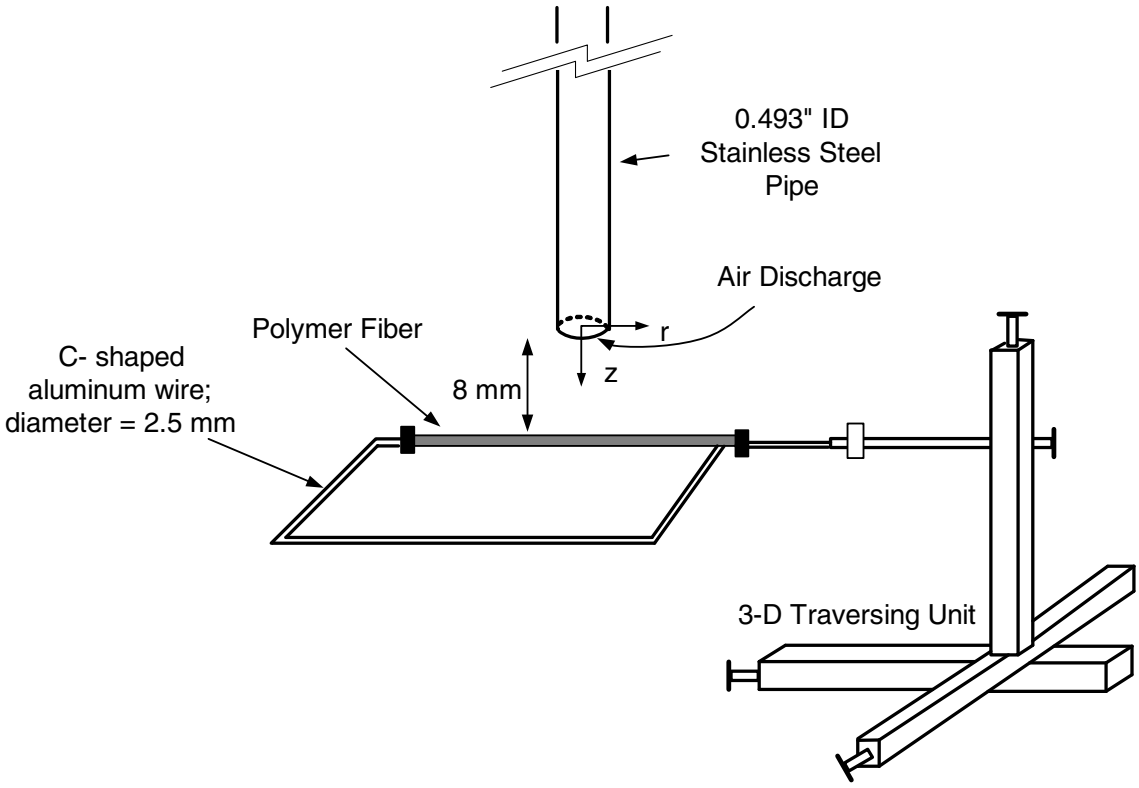

Figure 2b. Aluminum holder used to hold the fiber horizontally in the flowfield

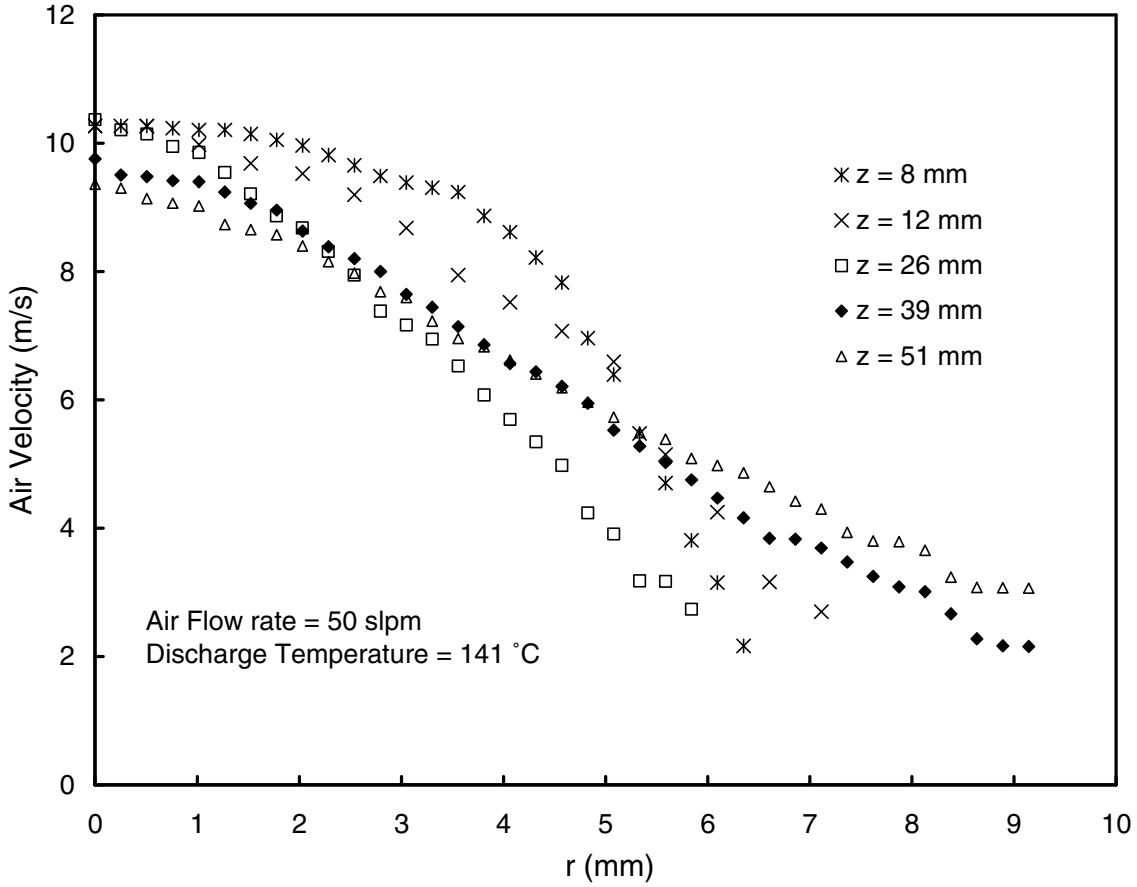

Figure 3a. Velocity profile of air at different downstream (z) locations as a function of radial distance (r).

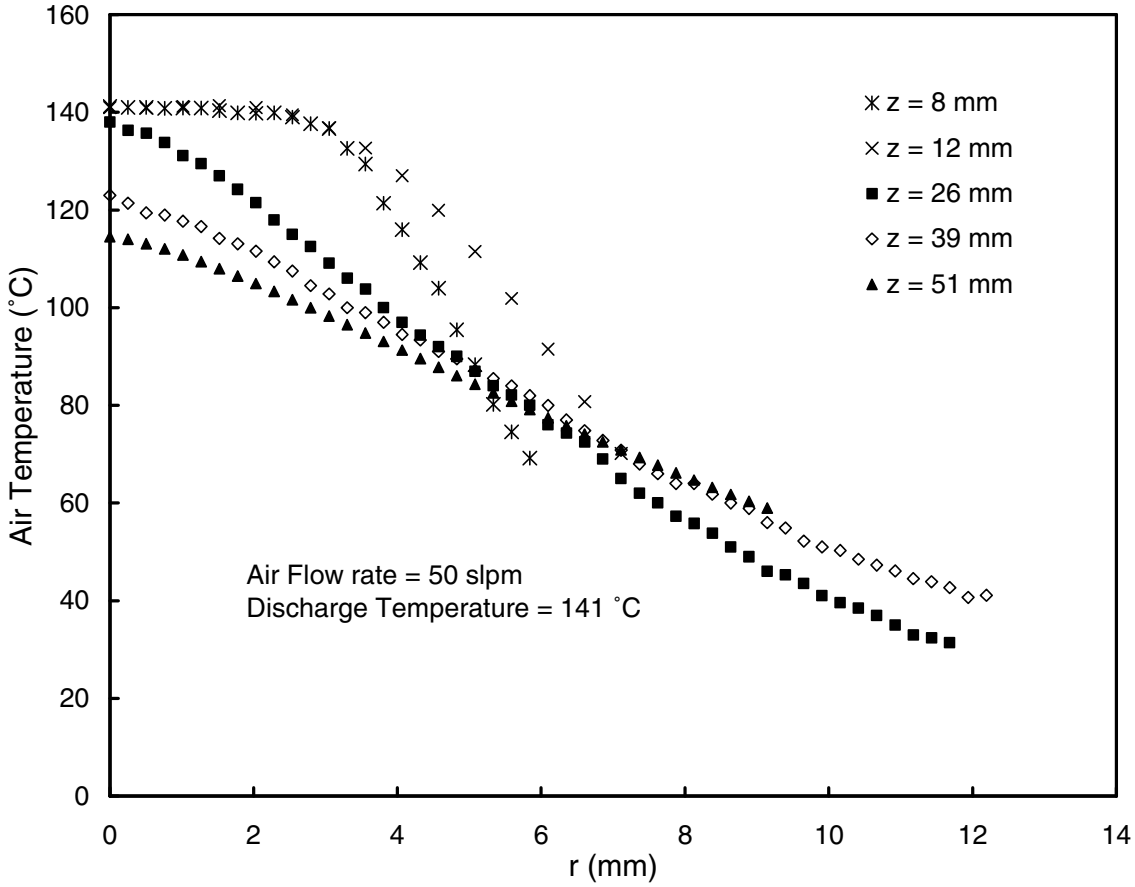

Figure 3b. Temperature profile of air at different downstream (z) locations as a function of radial distance (r).

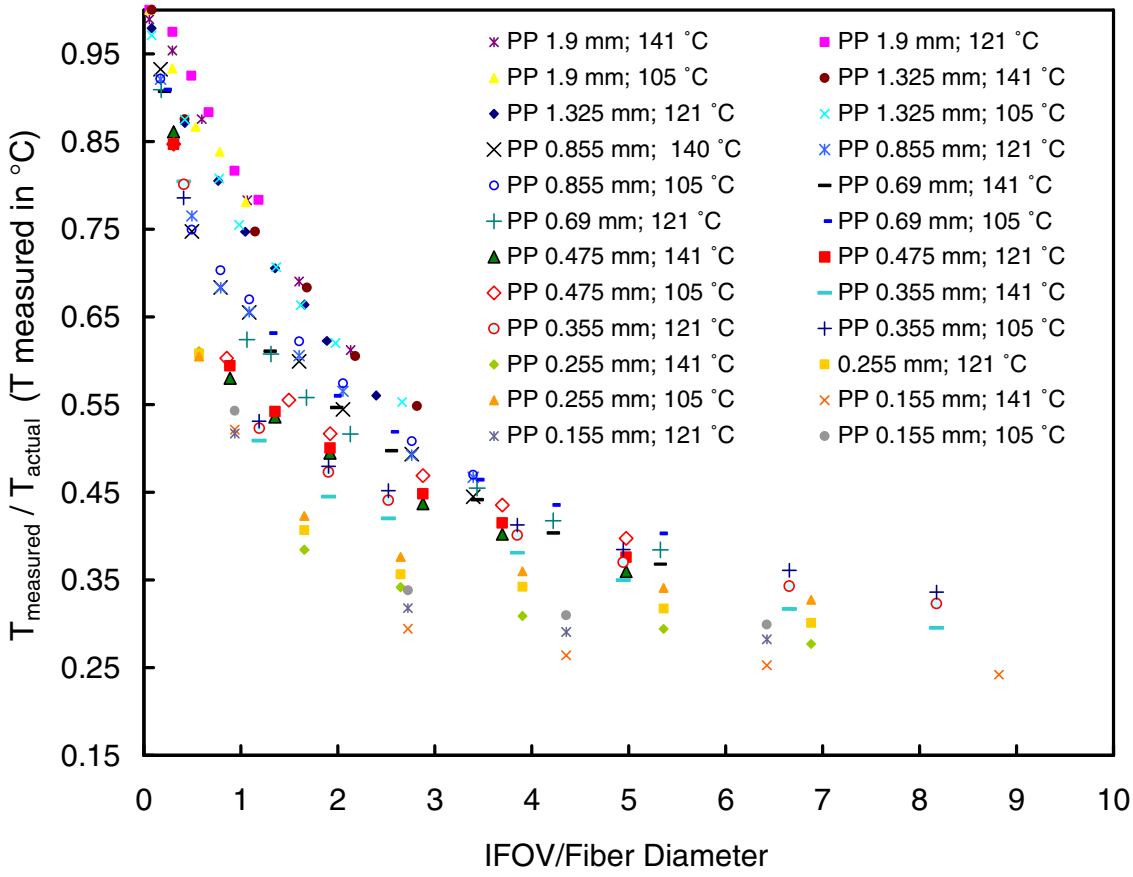

Figure 4. The variation of signal strength with the ratio of IFOV to fiber diameter. The signal strength in this figure is defined as the measured temperature of the fiber using an emissivity of 0.82 in the IR camera to the actual fiber temperature (in Celsius). The IFOV on the abscissa is normalized by the fiber diameter. The data for the three discharge temperatures of 105 ˚C, 121 ˚C and 141 ˚C and for several fiber diameters are plotted.

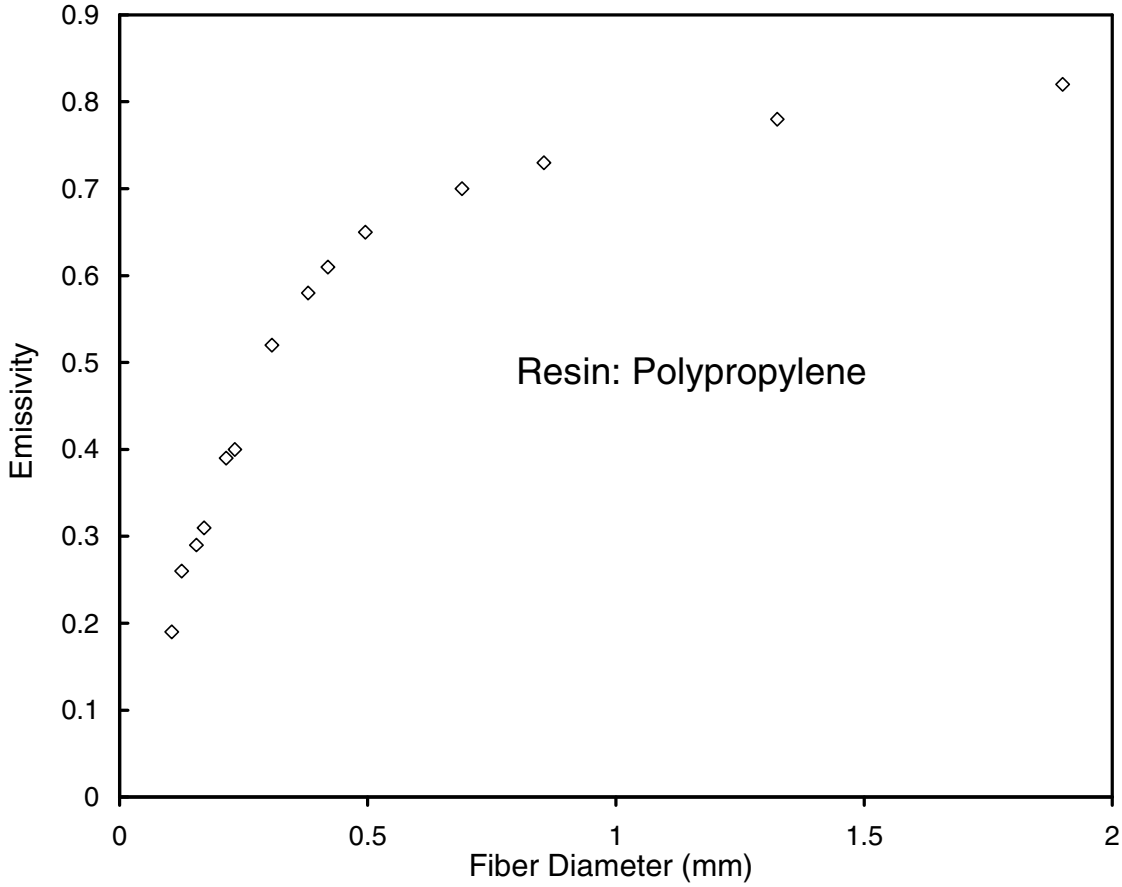

Figure 5a. Apparent emissivity of polypropylene (PP) fibers as a function of fiber diameter. The plotted values were found to be independent of discharge temperature. The close-up lens was used for these measurements.

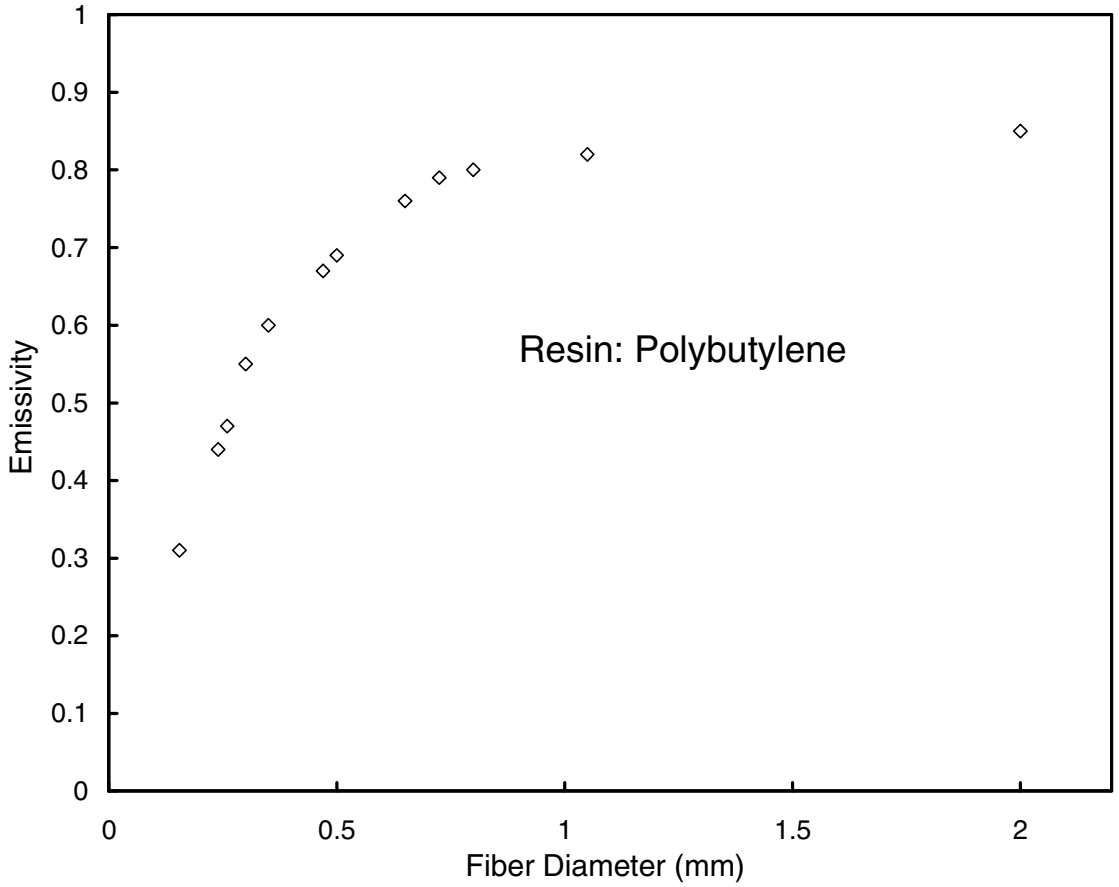

Figure 5b. Apparent emissivity of polybutylene (PB) fibers as a function of fiber diameter. The plotted values are independent of discharge temperature. The close-up lens was used for these measurements.

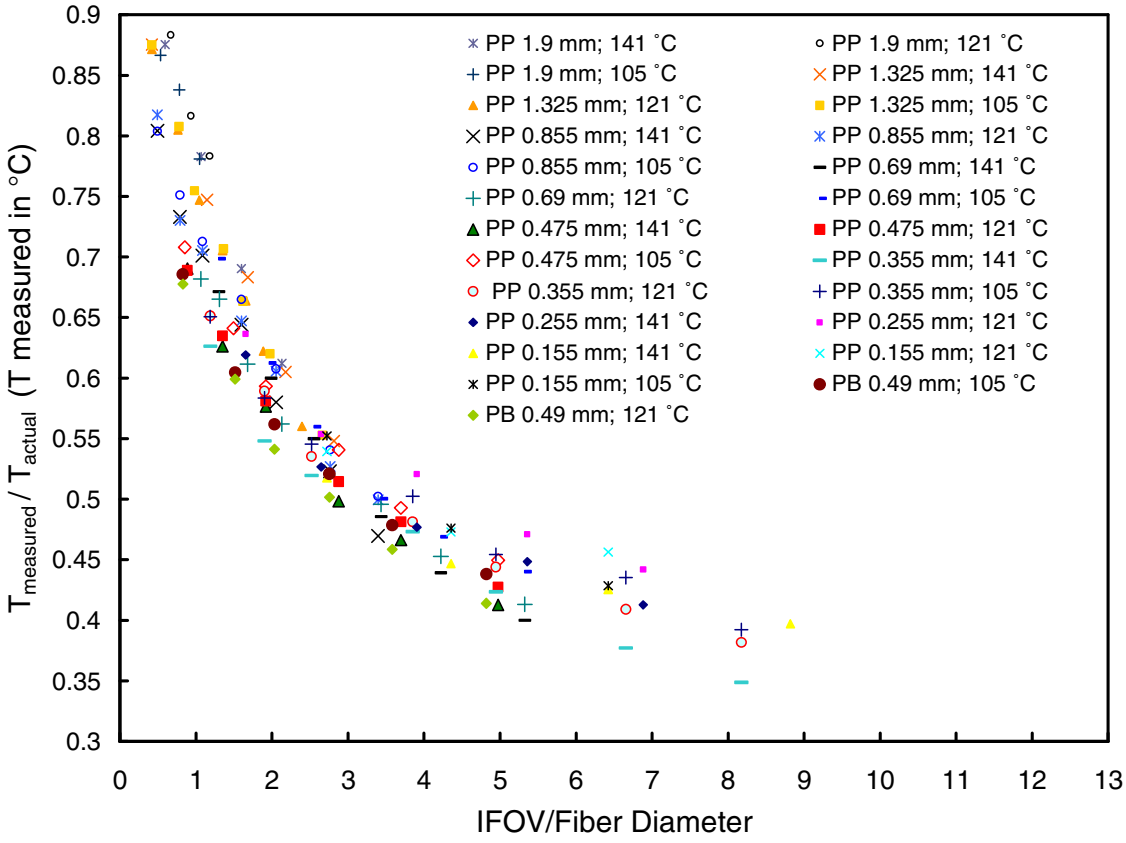

Figure 6. The variation of signal strength with the ratio of IFOV to fiber diameter. The apparent emissivity for each fiber was determined using Figures 5a and 5b and this value was inserted in the IR camera. The signal strength in this figure is defined as the measured temperature of the fiber using this apparent emissivity in the IR camera to the actual fiber temperature (in Celsius). The IFOV on the abscissa is normalized by the fiber diameter. The data for the three discharge temperatures of 105 ˚C, 121 ˚C and 141 ˚C and for several fiber diameters are plotted.

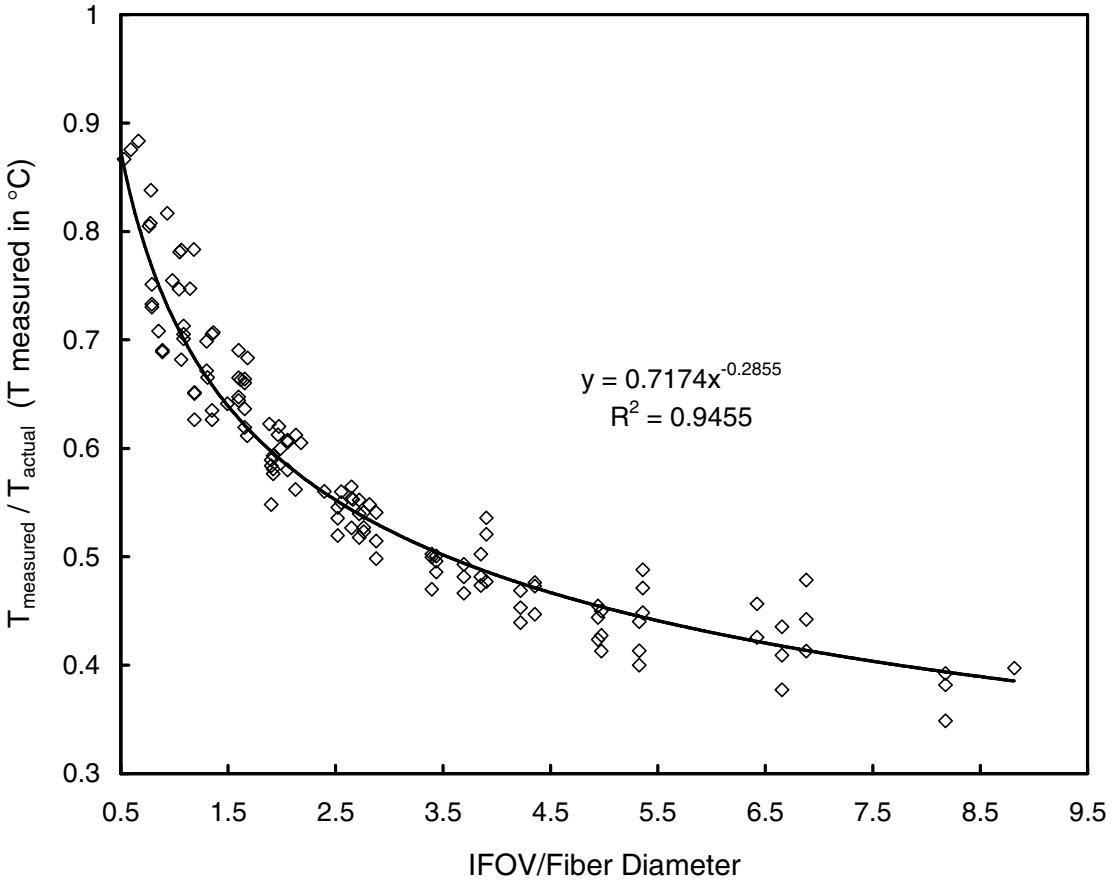

Figure 7. Power law fit to the entire data in Figure 6.

CHAPTER 6

UNSTEADY STATE HEAT TRANSFER FROM POLYMER FILAMENTS TO AIR IN NORMAL AND PARALLEL FLOW

A revised version of this Chapter will be submitted as a journal article. This chapter will be referred to as Marla et al. 2005b in subsequent chapters.

6.1 Introduction

Forced convection is the dominant mode of heat transfer in commercial fiber-making processes such as melt spinning and melt blowing. Melt Spinning is a process in which molten polymer is forced out of a tiny orifice and is wound on a godet placed some distance away from the orifice. In melt blowing, high velocity streams of hot air impact molten polymer emerging from an orifice. The force of the air attenuates the molten polymer to form micron or sub-micron size fibers. Temperature gradients on the order of 1000 ˚C/m are quite common in these processes.[1] Melt spinning involves cooling of a molten polymer moving through stationary air (sometimes cooling air is supplied normal to the fiber axis) while in melt blowing, close to the die, the air velocity vector is almost parallel to the fiber axis. Hence, in both processes, heat transfer occurs from a polymer filament to an air stream that flows parallel to the polymer.

While the problem of heat transfer in flow normal to cylinders and for cylinders inclined at an angle to the air stream is fairly well investigated,[2,3] there are few studies on heat transfer from cylinders oriented parallel to the air stream. Some of the earliest work in heat transfer from thin wires to air in parallel flow was done by Mueller.[4] However, the

measurements were made on a fine wire inside a vertical tube, and the Nusselt number showed dependence on the diameter of the vertical tube. Sano and Nishikawa[5,6] also measured the heat transfer coefficient of a fine wire with air flowing parallel to it. They used wires of different diameters placed in tubes of different diameters and found no effect of the tube diameter on the heat transfer correlation. They attributed the scatter in Mueller's data on the effect of additional turbulence of air flow at the inlet of the tube. The authors also observed that the Nusselt number was independent of wire lengths and wire velocities. Kase and Matsuo[7] placed a heated wire in a stream of air, measured its cooling and converted the data into a correlation between the Nusselt and Reynolds numbers. Their data compared well with the results of Sano and Nishikawa[5] and Kase and Matsuo[7] used this correlation in their mathematical analysis of the melt spinning process. For all of the above work, the range of Reynolds number over which the heat transfer coefficient was measured was 3-120.

In melt spinning and melt blowing, the fiber exhibits lateral vibrations complicating the prediction of the heat transfer coefficient. Kase and Matsuo[7] introduced a multiplying factor (1+K) in the Nusselt number to account for the transverse velocity of cooling air and fiber vibrations in the melt spinning process. The correlation of Kase and Matsuo is the most commonly used heat transfer correlation when modeling the fiber motion in both melt spinning and melt blowing process. While Kase and Matsuo reported that the value of K was solely dependent on the ratio of transverse air velocity to the relative air velocity parallel to the fiber, Lamonte and Han[8] argued that K was an

adjustable constant in the heat transfer correlation that also depended on the polymer used in the process.

The effect of vibration on heat transfer from wires to air in both forced and free convection has been reported by several researchers.[9-11] The study of Lemlich[9] on free convection showed that the heat transfer coefficient increased both with the amplitude and frequency of vibration. Lemlich observed a quadrupling of the rate of heat transfer when vibrations were introduced. Martinelli and Boelter[12] observed a five-fold increase in heat transfer rate over free convection for a ¾" cylinder vibrating in water at a frequency of 40 Hz and an amplitude of 2.54 mm. Anantanarayanan and Ramachandran[10] studied the effect of vibrations on forced convection for wires in free-shear flow. They developed a correlation for forced convection when the wire was stationary and the range of Reynolds number investigated was 198-585. The authors used discharge velocities in the range of 10 m/s to 19 m/s and used an electrically heated 457 μm nichrome wire stretched between 2 supports 58" wide as the test wire. An exciter was used to vibrate the wire to amplitudes in the range of 3-20 mm and frequencies in the range of 75-120 Hz. The authors observed an increase in heat transfer coefficient with both amplitude and frequency and the maximum increase observed over the stationary wire was 130 %. Gupta and Agrawal[11] used an experimental setup that was similar to the one used in the above study but obtained different results. The range of Reynolds number investigated was between 59-9600, thereby spanning the range of Mueller's study[4] (i.e., 3-120) and also that of Anantanarayanan and Ramachandran[10] (i.e., 198-585). In both cases, Gupta and Agrawal[11] reported higher Nusselt numbers for the stationary wire in forced

convection (no vibrations). For the case of the wire under vibration, the authors observed an increase of 300 % in the heat transfer coefficient. The amplitude of vibration for their study was 3-12 mm and the frequency was 8-34 Hz.

Figure 1 shows a Nusselt number (Nu) versus Reynolds number (Re) plot for heat transfer from wires to air in parallel flow based on the different studies discussed above and their applicable range of Reynolds numbers. The figure also shows the curve for cross flow. It should be noted that the correlations are for the case where the wire is under no vibration. The filament diameter was used as the characteristic length scale in calculating the Nusselt and Reynolds number.

Clearly, there is no strong agreement in the data obtained from different studies. While it may be argued that if the experimental setup is different from one study to another, a direct comparison may be difficult, the setup of Anantanarayanan and Ramachandran[10] was similar to that of Gupta and Agrawal[11] and yet they obtained different results. As mentioned earlier, the correlation of Kase and Matsuo[7] is most commonly used while modeling the melt spinning and the melt blowing process. However, this correlation was unable to accurately predict the temperature profile of polypropylene filaments in both of the above mentioned processes. Furthermore, it severely overpredicts the temperature when compared with experimental data.[13,14] In melt spinning, in some cases, the difference in experimental and predicted temperature was 60 $^{\circ}$C,[13] while in melt blowing the difference was found to be >100 $^{\circ}$C.[14]

In view of the above, it becomes clear that the heat transfer correlation needs to be revised in order to predict the fiber temperature profile with more accuracy than that

obtained using the correlation of Kase and Matsuo. It would then be obvious that the heat transfer coefficient determined from an experimental setup that simulates the melt spinning/melt blowing process as closely as possible, would be much more accurate than correlations developed from other experimental setups.

All of the heat transfer studies discussed above were performed using an electrically heated wire. The present study makes use of an unsteady state heat transfer approach to compute the heat transfer coefficient from polymer fibers first in normal flow and then in parallel flow. Also, unlike some studies that used a thermocouple wrapped around the test wire,[10,11] which could alter the flow field, the temperature measurements in the present study are made using an Infrared (IR) camera (which is a non-contact technique of temperature measurement). A description of the IR camera used in the experiments and the test station that was built to determine the heat transfer coefficient is described in the next section.

6.2 IR Camera Details and Experimental Setup

The IR camera used in the present study was ThermaCAM® S60 manufactured by FLIR Systems. The spectral range for this camera is 7.5-13 μm (longwave).The IR image displayed had a resolution of 640 x 480 pixels while the actual number of thermal detector sensors or elements is 320 x 240. The other prominent features of this IR camera can be found on the manufacturer's website and the camera's user manual.[15] The IR lens on this camera has a field of view (FOV) of 24˚ x 18˚ with a minimum focus distance of 0.3 m or 11.81 inches. The camera also came with a 100 μm close-up lens for which the

minimum focus distance is 80 mm while the maximum working distance is 110 mm. The close-up lens fits on the 24˚ lens of the IR camera and has certain advantages over the 24˚ lens in that it can measure the temperature of small targets with greater accuracy. Unless otherwise mentioned, all temperature measurements in the present study were made with the 100 μm close-up lens. The IR camera has the capability to record 60 temperature measurements/s and a real-time plot of these measurements can be seen on the monitor of a PC that is connected to the IR camera by means of an IEEE 1394 (firewire) connection.

Figure 2a shows the schematic of the test unit that was built to determine the heat transfer coefficient. Champagne et al.[16] used a similar setup for measuring the heat transfer coefficient from cylinders at angles of 30˚ to 90˚ to the flow and for Reynolds number in the range of 5-30. Compressed air regulated at 70 psi was passed through a thermal mass flow meter and was adjusted for the desired flow rate in slpm of air (at standard conditions of 21 ˚C and 1 atmosphere pressure). The air then passed through a reservoir heated by two 750 W cartridge heaters. Line 2 was heated by a 420 W tape heater and finally line 3 was heated by another 420 W tape heater. All the heating lines were wrapped in two layers of insulation – an inner layer of fiberglass foam insulation, which was in contact with the 3/8" stainless steel pipe, and an outer layer of fiberglass cloth tightly wrapped around the inner layer. Thermocouples were placed in each of these lines and the temperatures were controlled to obtain the desired temperature at the discharge of the pipe. Line 4, from which the air exited, had an ID of 0.493" and an OD of 0.675". The pipe material was SS 304 with a length of 30" resulting to a L/D of 60. A cylindrical coordinate system was chosen for the analysis, as shown in Figure 2a.

Mean air velocity measurements below the pipe discharge were taken using a conventional Pitot tube that had an outer diameter of 0.7 mm and an inner diameter of 0.4 mm. A two way valve enabled us to measure the stagnation pressure from two instruments – an Ashcroft® digital industrial pressure gauge (model 2074; range 0-30 psi with 0.25 % accuracy) supplied by Cole Parmer and a Dwyer model 25 liquid manometer. The model 25 manometer had a range of 1.27 to 76.2 mm of water. The Pitot tube was attached to a three-dimensional manual traverse that could position the Pitot tube precisely within the flow field. The traverse had 0.001" resolution (or 25.4 μm resolution), which is particularly useful in flow fields with steep velocity gradients. The air temperature measurements below the pipe discharge were made using a J-type 0.01" diameter thermocouple connected to an Omega® microprocessor thermometer (model HH21) that digitally displayed the measured temperature.

Polymer fibers of different diameters (0.1 mm – 2 mm) were prepared in our laboratory using an extruder and gear pump assembly, the details of which can be found in Marla and Shambaugh.[17] It is important to note that these fibers have circular cross-sections. The diameter of the fibers was measured using an optical microscope. The polymer used in most of the experiments was 88 MFR Fina Dypro® isotactic polypropylene. This polymer had a M_w of 165,000 g/mol and a M_n of 41,500 g/mol. Some experiments with fibers made of Polybutylene were also performed. This resin was Grade 0400 manufactured by Basell Polyolefins and had a MFR of 20. For the case for air cross flow over the fiber, the fiber was held horizontally below the pipe discharge using a fiber holder as shown in Figure 2b. For the case of air flow parallel to the fiber,

the fiber was oriented vertically and attached to the traverse in the same manner as the pitot tube. Other details on the experimental setup and the determination of polymer emissivity can found in Marla et al.[18]

6.3 Working Principle and Experimental Scheme

6.3.1 Cross Flow

For a discharge temperature of 141 ˚C and for an air flow rate of 50 slpm, the radial velocity and temperature profile of air at different z locations is shown in Figures 3a and 3b, respectively. It can be seen that the air flow field at z = 8 mm displays a flat velocity and temperature profile in the region around the z-axis. Hence, for all other flow rates of air, one can safely make the assumption that a fine polymer filament placed at this location (i.e., along the r-axis) would assume the same temperature as the air, since there are no heat losses from the portion of the polymer filament near the z-axis. Velocity and temperature profiles for several other downstream locations are also shown for comparison. The flat-topped profile gradually changes into a bell-shaped profile as z increases; this type of behavior is typical for round jets. The validity of the assumption can be seen in Figure 4, which shows an IR image of a 0.855 mm diameter polypropylene fiber in cross flow 8 mm below the pipe discharge for the flow conditions described above. The temperature profile along the length of the fiber clearly shows that the temperature gradient over a small length in the central portion of the fiber was zero. The air flow rate was varied to obtain centerline discharge velocities in the range of 3-15 m/s and pipe discharge temperatures in the range of 90-141 ˚C. The region of zero

temperature gradient was observed over all the values of air flow rates and pipe discharge temperatures used in the experiments.

For cross flow, the determination of the heat transfer coefficient is based on measuring the heating rate of the polymer fiber as it is suddenly introduced in the flow field at z = 8 mm and writing an energy balance for an element of length Δr straddling the z axis and over which the fiber temperature is uniform. The energy balance reduces to

$$V\rho C_p \frac{dT_f(t)}{dt} = h(t)A\left[T_{air} - T_f(t)\right] \quad (1)$$

where

V = volume of the fiber element of length Δr (m^3)

ρ = density of the polymer (kg/m^3)

C_p = specific heat of the polymer ($J/kg \cdot K$)

$h(t)$ = instantaneous heat transfer coefficient ($W/m^2 \cdot K$)

A = area of heat transfer over a length Δr (m^2)

T_{air} = temperature of the air as determined from the thermocouple (˚C)

$T_f(t)$ = instantaneous fiber temperature as determined from the IR camera (˚C)

t = time (s)

Simplifying eq 1, we get

$$h(t) = \frac{\rho C_p d_f \frac{dT_f(t)}{dt}}{4\left[T_{air} - T_f(t)\right]} \quad (2)$$

where

d_f = fiber diameter (m)

The procedure for determining the heat transfer coefficient in cross flow to air is described in a stepwise manner below

1. The traverse was adjusted so that the fiber is centered and the z axis intersects the axis of the fiber exactly 8 mm below the pipe discharge. This is the initial position of the traverse unit and a steel bolt is placed to mark this position. A steel plate was placed adjacent to the traverse stand and acts as a guide to move the entire traverse unit in a straight line.
2. The IR camera with the 100 μm close-up lens was focused so that the region of the fiber with the uniform temperature was in sharp focus.
3. The entire traverse stand was moved out of the flow field in a straight line using the steel plate as the guide.
4. After a couple of minutes (to allow the fiber to cool down) the traverse unit was brought back to its initial position (using the steel plate and bolt as a guide) and the IR camera started recording and plotting the heating of the fiber at the rate of 60 measurements/s in real-time mode. The plot could be seen on the monitor of a PC which is connected to the IR camera by means of a IEEE 1394 connection.
5. A representative plot of the heating of a 0.49 mm diameter polypropylene fiber as a function of time is shown in Figure 5. The fiber quickly reached the air temperature and its temperature remained constant thereafter.
6. The curve was fitted to a 5^{th} order polynomial and the instantaneous heating rate $\frac{dT_f(t)}{dt}$ was computed.

7. Using eq 2, the instantaneous heat transfer coefficient, h(t), was calculated and is shown in Figure 6.

8. The time-averaged heat transfer coefficient was calculated as $\bar{h} = \frac{1}{T}\int_0^T h(t)\,dt$, where T is taken as the time when the temperature difference between the air and the fiber becomes less that 20 ˚C and t = 0 corresponds to when the fiber is just brought into the flow field and into the focus of the IR camera . Figure 5 shows the location of T for the conditions shown in the figure.

The advantage of using the 100 µm close-up lens is that it has a very small depth of field and the temperature of a target will show a maximum only when it is in sharp focus. It should be noted that if the fiber is out of focus when viewed from the IR camera, the camera displays a temperature lower than what it would be if in focus. Each run was repeated and the results were found to be very reproducible. The runs for cross flow were done with both polypropylene and polybutylene fibers. While the highest pipe discharge temperature with the polypropylene fibers was 141 ˚C, the highest discharge temperature for polybutylene fibers was 105 ˚C. This was because the melting point of polypropylene is 165 ˚C while that for polybutylene is 125 ˚C. Discharge temperatures near or above the melting point of a polymer would cause dimensional changes, such as stretching, thereby changing the geometry of the fibers.

6.3.2 Parallel Flow

For the case where the fiber is parallel to the air flow, the fiber was oriented along the z axis and attached to the traverse such that the tip of the fiber was 3 mm away from the pipe discharge. The procedure for determining $\bar{h}$ was exactly the same as that for cross flow with the exception that the measurements were made at z = 7 mm and z = 10 mm and the average of the two readings was reported. It was found that the $\bar{h}$ determined from these 2 locations did not vary by more than 10 %.

6.4 Results and Discussion

Figure 7 shows the instantaneous temperature of five polypropylene fibers of different diameter under the same flow conditions in cross flow arrangement. The rate of heating increases as the fiber diameter decreases and this is quite an intuitive result. The smaller the fiber, the less power required to heat it to a desired temperature and, consequently, the faster that it will rise to the final temperature. The time-averaged heat transfer coefficient, $\bar{h}$, increased as the fiber diameter decreased. Similar results were obtained with polybutylene fibers. The entire data obtained from the cross flow runs was converted into a Nu-Re plot and is shown in Figure 8. The data for both PP and PB fibers agree very well with the cross flow correlation of McAdams.[2] The standard deviation in the heat transfer coefficient for a fixed Reynolds number is defined as $\sqrt{\frac{\int_0^T (h(t)-\bar{h})^2 dt}{T}}$.

The standard deviation is shown on the plot for each data point and is less than 10 % in most cases.

Figure 9 shows the heating rate for 3 different polypropylene fibers in parallel flow. The same trends as that in cross flow were obtained. It can also be noted that the temperature gradients are not as steep as in cross flow. Figure 10 shows the heating rate for a 0.68 mm PP fiber at different z locations for the conditions shown in the figure. It was observed that the heating rate did not change significantly over a 1.9 cm length of the fiber. Using a pitot tube and thermocouple probe it was also seen that the centerline air velocity and air temperature did not change significantly over this length.

Figure 11 shows the Nu-Re plot of the data obtained from the parallel flow runs. Also shown on the graph are the correlations obtained from other studies over the range of applicable Reynolds number. The present data lie in between the data of Gupta and Agrawal[11] and those of the rest of the authors. The varied results obtained raise the question of how the boundary layer is modified by the wire in the experimental setup of each study. In the present study, one end of the fiber is attached to the traverse, but the other end is free and 3 mm away from the pipe discharge. It was observed that the fiber displayed some vibration as it was suddenly brought in the flow field and heated by the streams of hot air. If the vibration of the fiber causes changes in the pattern of the boundary layer so as to cause turbulence and promote mixing, then the heat transfer coefficient will increase. As described earlier, the effect of vibration on a wire is an increase in the rate of heat transfer in both forced and free convection.[9-12] Fiber vibrations

are present in the melt spinning process and are very pronounced in the melt blowing process.

The polymers used in the present study are the same as those used in our laboratory for the melt spinning and melt blowing processes. Since the experimental study was designed to simulate these processes closely, the heat transfer correlation from the present study should yield a better temperature profile when used in a melt spinning/melt blowing model compared to that obtained from the Kase and Matsuo[7] correlation. Kase and Matsuo vibrated a 0.2 mm wire at an amplitude of 0.2 cm and a frequency of 4 Hz under a parallel flow of air at 20 cm/s and found the increase in heat transfer to be 30 % or K = 0.3. It was interesting to observe that the ratio of the heat transfer coefficient from the present study to that of Kase and Matsuo (without vibration) was between 1.15 and 1.5 or an increase ranging from 15 % to 50 %. It may be noted that the above values span the 30 % increase due to vibration as reported by Kase and Matsuo. For melt spinning, where the Reynolds numbers are less than 150, a correlation for the data obtained from the present study is

$$Nu = 1.4 + 0.0141\ Re,\ 24<Re < 150 \qquad (3)$$

A correlation based on the present study, which is applicable for Reynolds numbers between 150 and 923, can be given as

$$Nu = 0.3575\ Re^{0.46} \qquad (4)$$

Table 1 summarizes the various correlations and the Reynolds number over which they are applicable.

6.5 Conclusions

An unsteady state approach was used to determine the heat transfer coefficient for polymer filaments normal and parallel to an air stream. The time-averaged heat transfer coefficient for the case of a fiber in cross flow with a hot air stream compared well with the well-established McAdams[2] correlation. For heat transfer from fibers to air in parallel flow, the calculated Nusselt number was higher than that of Kase and Matsuo[7] but less than that obtained by Gupta and Agrawal.[11] The correlation of Kase and Matsuo for the case of a vibrating wire yielded a heat transfer coefficient that was 30 % higher than that for a non-vibrating wire. The Nusselt numbers obtained from the present study were 15-50 % higher than the correlation of Kase and Matsuo for a non-vibrating wire. Since the fiber displayed some vibratory motion as it was suddenly introduced in the flow field, the results of the present study find agreement with the correlation of Kase and Matsuo for a vibrating wire. The next step would be to insert the heat transfer correlation obtained from the present study in mathematical models for the melt spinning and melt blowing processes and compare the predicted temperature profiles with on-line measurements of fiber temperature in these two processes. Such an investigation is currently underway.

Acknowledgements

This work was supported by an NSF GOALI grant (DMII-0245324). The support of 3M and Procter & Gamble is also gratefully acknowledged.

References

1. Uyttendaele, M. A. J.; Shambaugh, R. L. Melt Blowing: General Equation Development and Experimental Verification. *AIChE J.* **1990,** 36(2), 175-186.
2. McAdams, W. H. *Heat Transmission*, 3rd ed.; Kirkpatrick S. D., Ed; McGraw-Hill Series in Chemical Engineering; McGraw-Hill Book Company, Inc.: New York, NY, 1954; pp 258-260
3. Morgan, V. T. *Advances in Heat Transfer*; Academic Press: New York, NY, 1975; Vol.11, pp 239-243.
4. Mueller, A. C. Heat Transfer from Wires to Air in Parallel Flow. *Trans. Am. Inst. Chem. Eng.* **1942,** 38, 613-627.
5. Sano, Y.; Nishikawa, S. Heat Transfer Coefficient of Five Wires in Air Flow. *Kagaku Kogaku.* **1964,** *2*(2), 199-202.
6. Sano, Y.; Nishikawa, S. Effect of Turbulence on the Heat Transfer of Fine Wire in Turbulence Flow. *Kagaku Kogaku.* **1965,** *29*(4), 251-252.
7. Kase, S.; Matsuo, T. Studies on Melt Spinning. I. Fundamental Equations on the Dynamics of Melt Spinning. *J. Polym. Sci., Part A*. **1965,** *3*, 2511-2554.
8. Han, C. D.; Lamonte, R. R. Studies on Melt Spinning, I. Effect of Molecular Structure and Molecular Weight Distribution on Elongational Viscosity. *Trans. Soc. Rheol.* **1972,** 16(3), 447-472.
9. Lemlich, R. Effect of Vibration on Natural Convective Heat Transfer. *Ind. Eng. Chem*. **1955,** *47*(6), 1175-1180.

10. Anantanarayanan, R.; Ramachandran, A. Effect of Vibration on Heat Transfer From a Wire to Air in Parallel Flow. *Trans. Am. Soc. Mech. Eng*. **1958,** *80*, 1426-1432.

11. Gupta, C. P.; Agrawal, D. D. Heat Transfer From a Vibrating Wire to Air in Parallel Flow. *J. Inst. Eng.* **1968,** *48*(9), 557-579.

12. Martinelli, R.; Boelter, L. M.; Weinberg, E. P.; Yahakis. Heat Transfer to a Fluid Flowing Periodically at Low Frequencies in a Vertical Tube. *Trans. Am. Soc. Mech. Eng*. **1943,** *65*, 789-1432.

13. De Rovere, A.; Shambaugh, R. L. Melt-Spun Hollow Fibers: Modeling and Experiments. *Polym. Eng. Sci.* **2001,** *41*(7), 1206-1219.

14. Bansal, V.; Shambaugh, R. L. On-line Determination of Diameter and Temperature during Melt Blowing of Polypropylene. *Ind. Eng. Chem. Res.* **1998,** *37*(5), 1799-1806.

15. FLIR Systems. *ThermaCAM® S60 Operator's Manual*, Boston, MA, 2004.

16. Champagne, F. H.; Sleicher, C. A.; Wehrmann, O. H. Turbulence measurements with inclined hot-wires Part 1. Heat transfer experiments with inclined hot-wire. *J. Fluid. Mech.* **1967,** *28*(1), 153-175.

17. Marla, V. T.; Shambaugh, R. L. Modeling of the Melt Blowing Performance of Slot Dies. *Ind. Eng. Chem. Res*. **2004,** *43*(11), 2789-2797.

18. Marla, V. T.; Shambaugh, R. L.; Papavassiliou, D. V. Calibration of an Infrared Camera for Accurate Determination of the Temperature of Polymer Filaments. To be Submitted. (2005a)

Authors	Correlation	Re range
Anantanarayanan and Coworkers (1958)	$Nu = 0.0522\ Re^{0.729}$	198-585
Sano and Nishikawa (1964)	$Nu = 0.32 + 0.155\ Re^{0.5}$	1-100
Kase and Matsuo (1965)	$Nu = 0.42\ Re^{0.334}$	0.5-50
Gupta and Agrawal (1968)	$Nu = 1.2\ Re^{0.249}$ $Nu = 0.068\ Re^{0.762}$	$59 \leq Re \leq 200$ $200 < Re < 9600$
Present Study	$Nu = 1.4 + 0.0141\ Re$ $Nu = 0.3575\ Re^{0.46}$	$24 \leq Re \leq 150$ $150 < Re < 923$

Table 1. Comparison of correlations from different studies for heat transfer from wires to air in parallel flow. The range of Reynolds numbers over which the correlations are valid is also shown

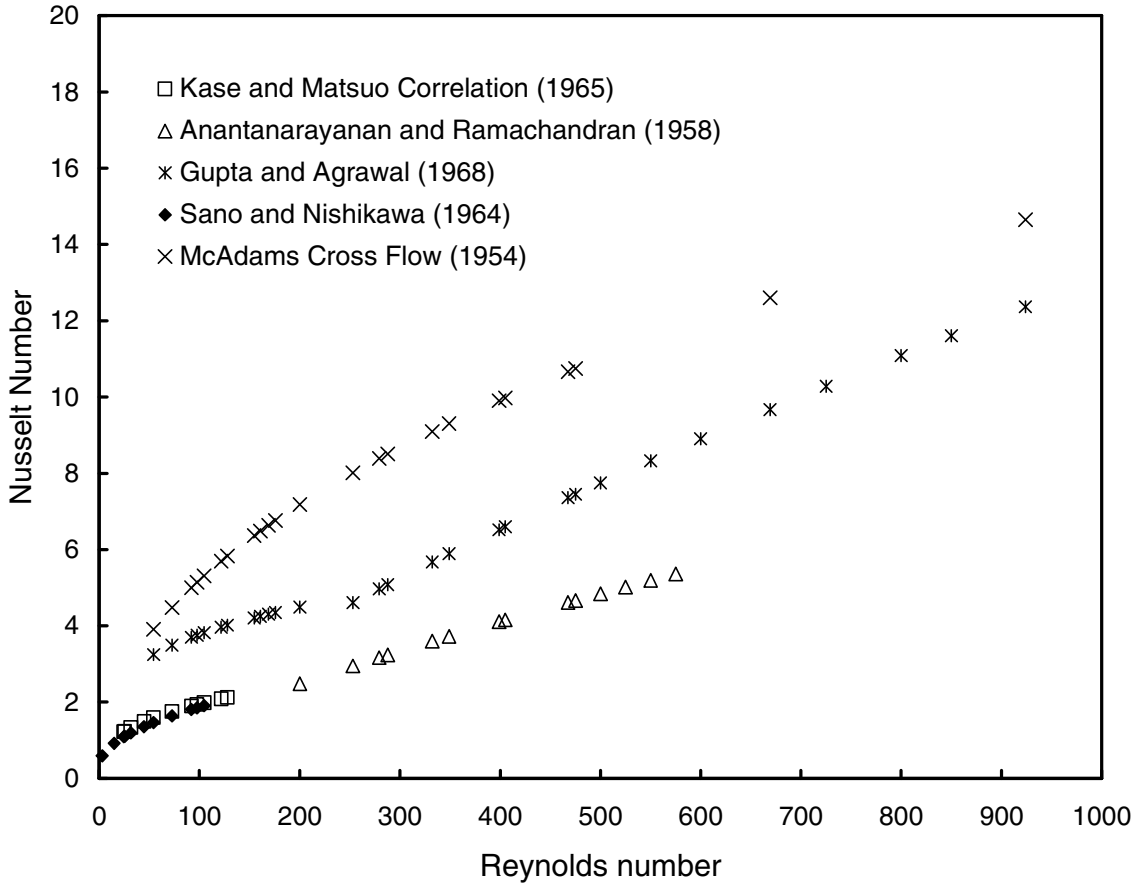

Figure 1. Effect of Reynolds number on the Nusselt number for the case of air flowing parallel to a fine wire. The data is based on correlations obtained from different studies. For comparison, the effect of Reynolds number on the Nusselt number for the case where the air flows normal to the wire is also shown.

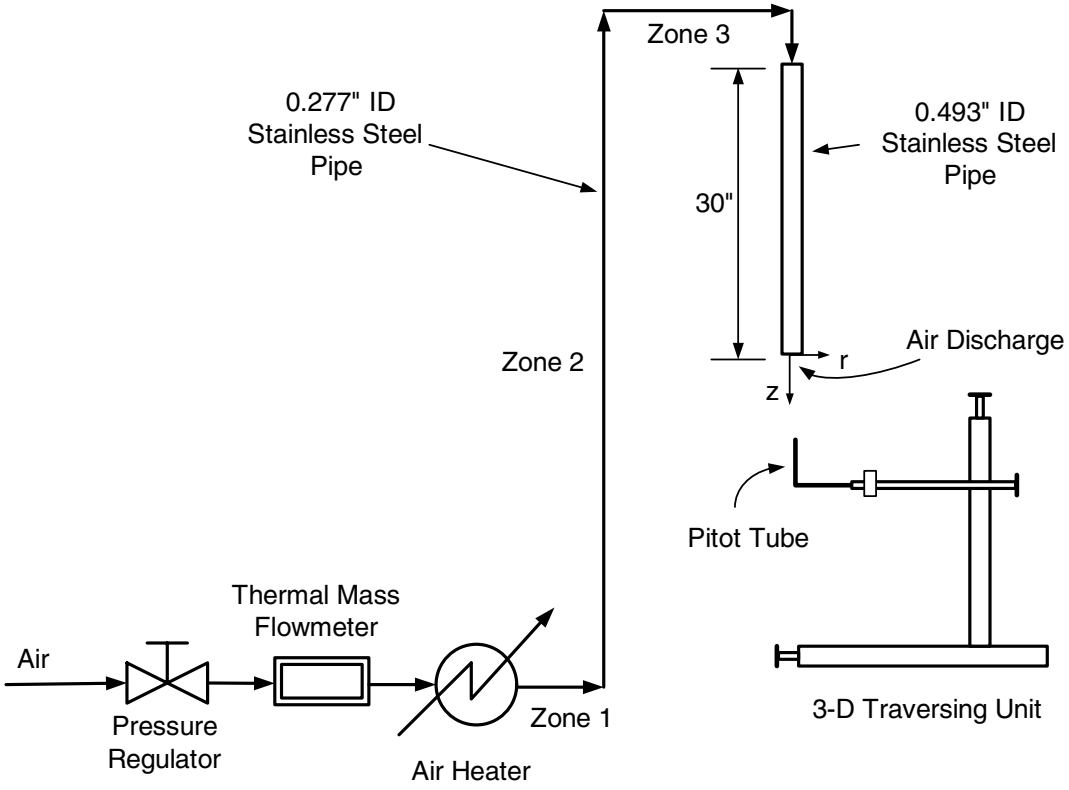

Figure 2a. Test unit built for calibration of the IR camera. The r and z directions (for the cylindrical coordinate system) are also shown in the Figure. The z axis coincides with the longitudinal axis of the stainless steel discharge pipe.

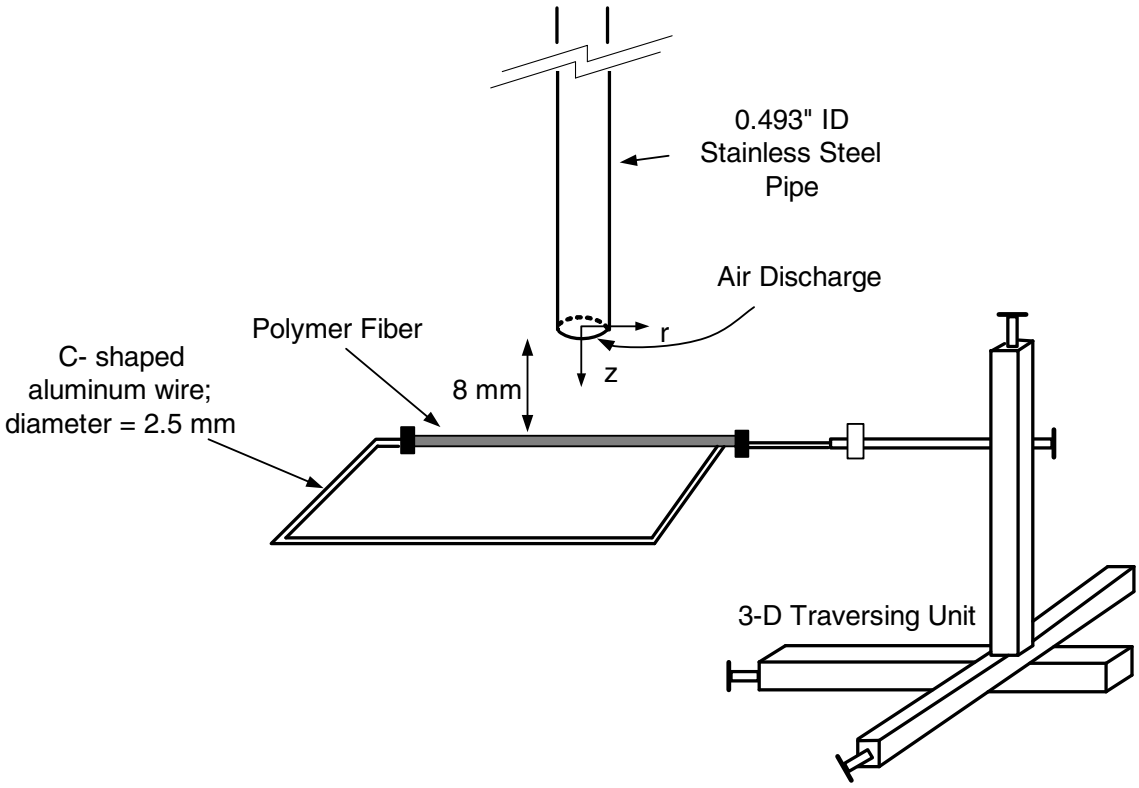

Figure 2b. Aluminum holder used to hold the fiber horizontally in the flow field.

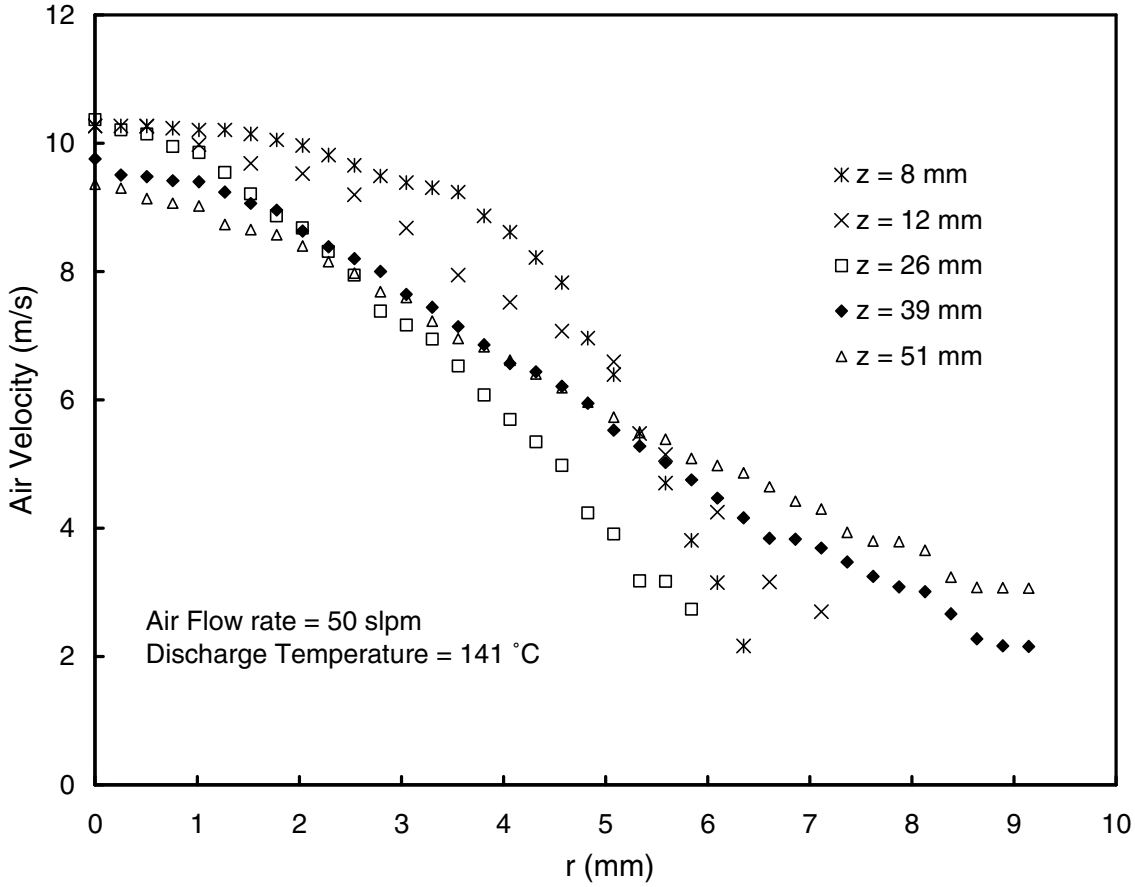

Figure 3a. Velocity profile of air at different downstream (z) locations as a function of radial distance (r) for a centerline discharge velocity of 10.1 m/s and a temperature of 141 ˚C.

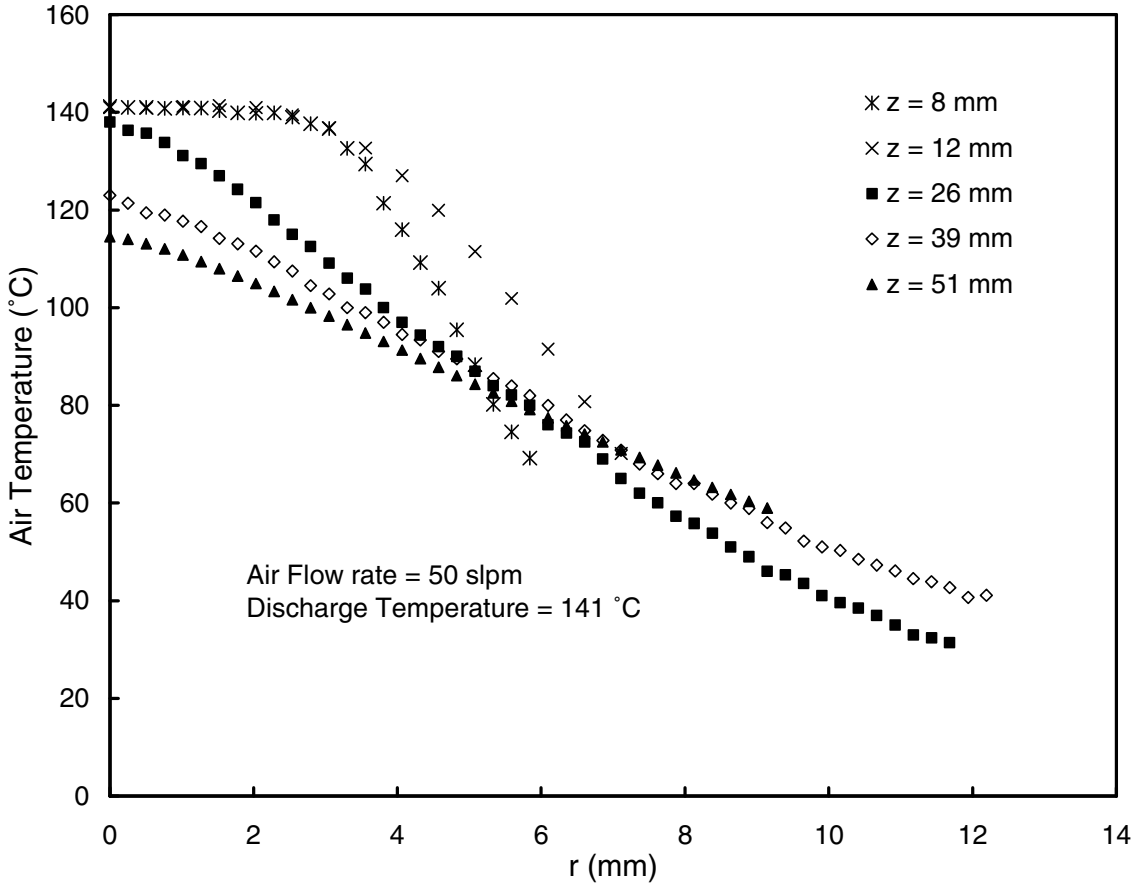

Figure 3b. Temperature profile of air at different downstream (z) locations as a function of radial distance (r) for a centerline discharge velocity of 10.1 m/s and a temperature of 141 ˚C.

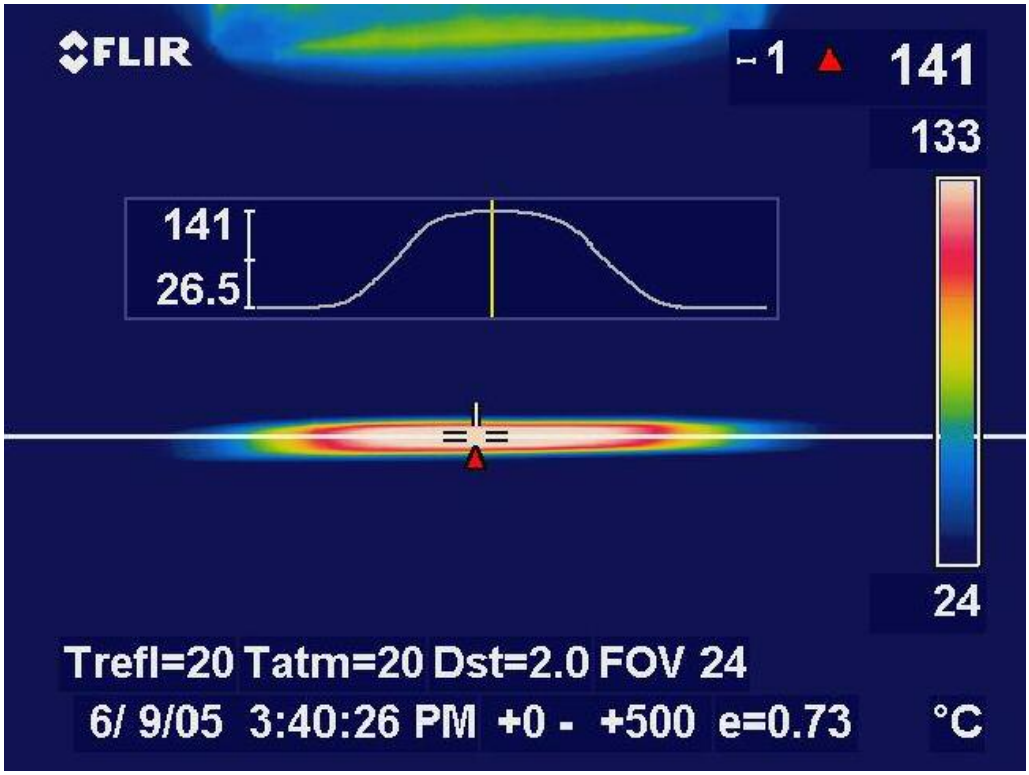

Figure 4. Infrared image of a polypropylene fiber held in cross flow 8 mm below the pipe discharge. The air velocity and temperature at this point were 10.1 m/s and 141 ˚C respectively. The fiber temperature profile along the horizontal line drawn along the length of the fiber is also shown. The z axis coincides with the longitudinal axis of the pipe while the length of the fiber is along the r-direction.

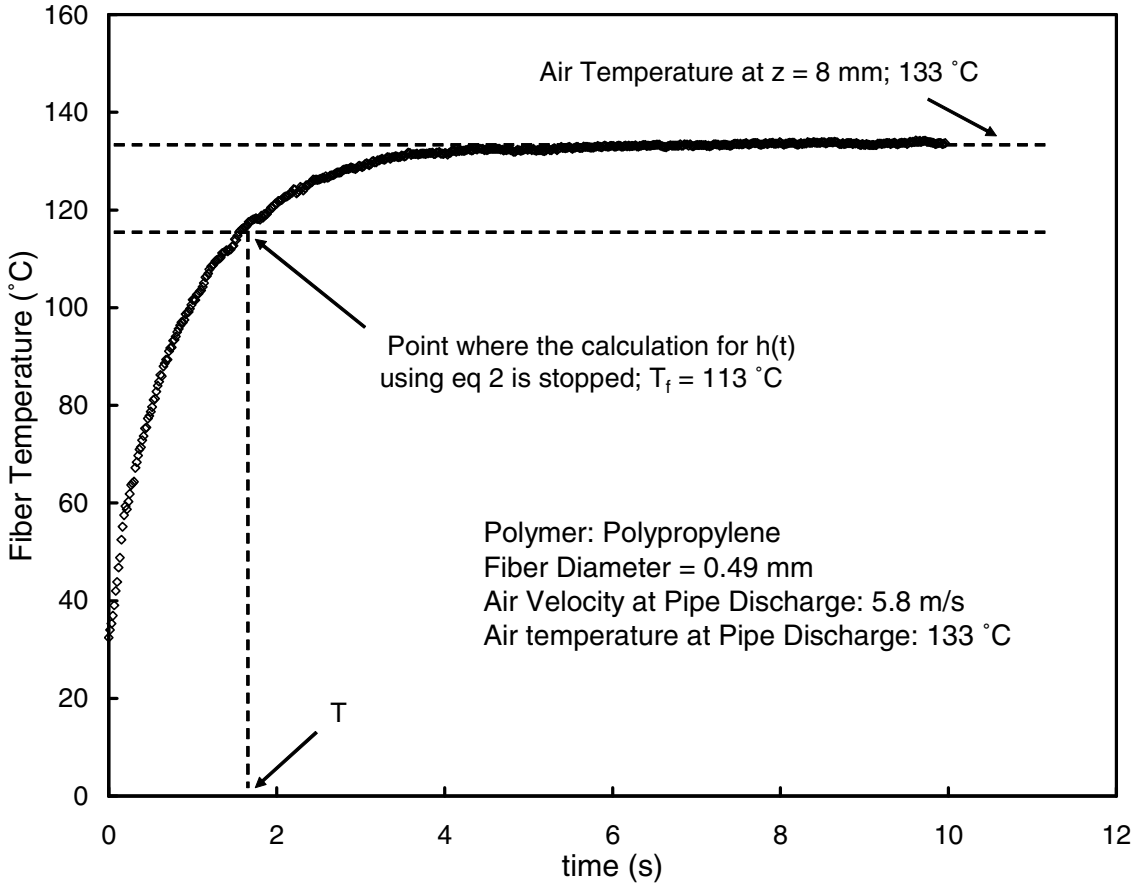

Figure 5. Heating of a polypropylene fiber under a stream of hot air. The air velocity and temperature at the pipe discharge are shown on the figure. The time at which the difference between the air and fiber temperature becomes less than 20 ˚C, T, is also shown.

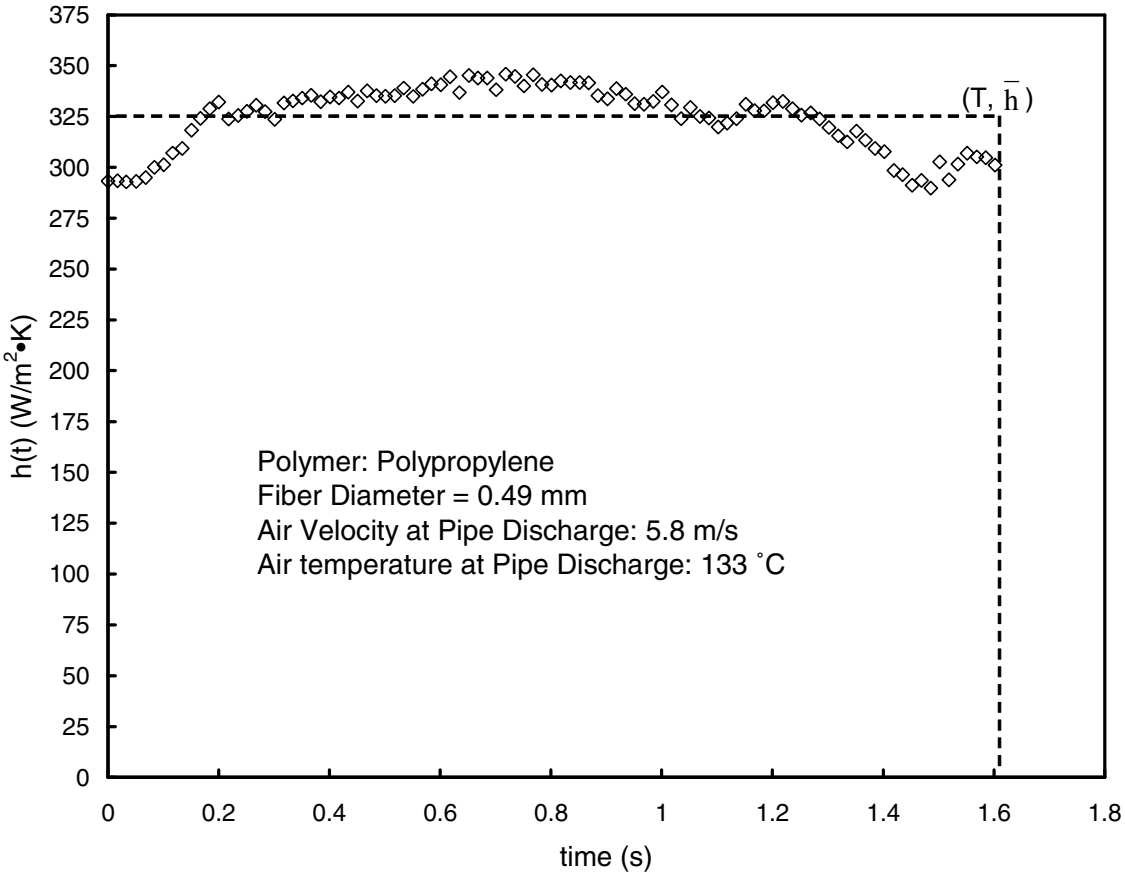

Figure 6. Instantaneous heat transfer coefficient calculated for a polypropylene fiber held normal to the air flow from the pipe. The flow conditions were the same as in Figure 5. The time-averaged heat transfer coefficient, $\bar{h}$, and T are shown on the figure.

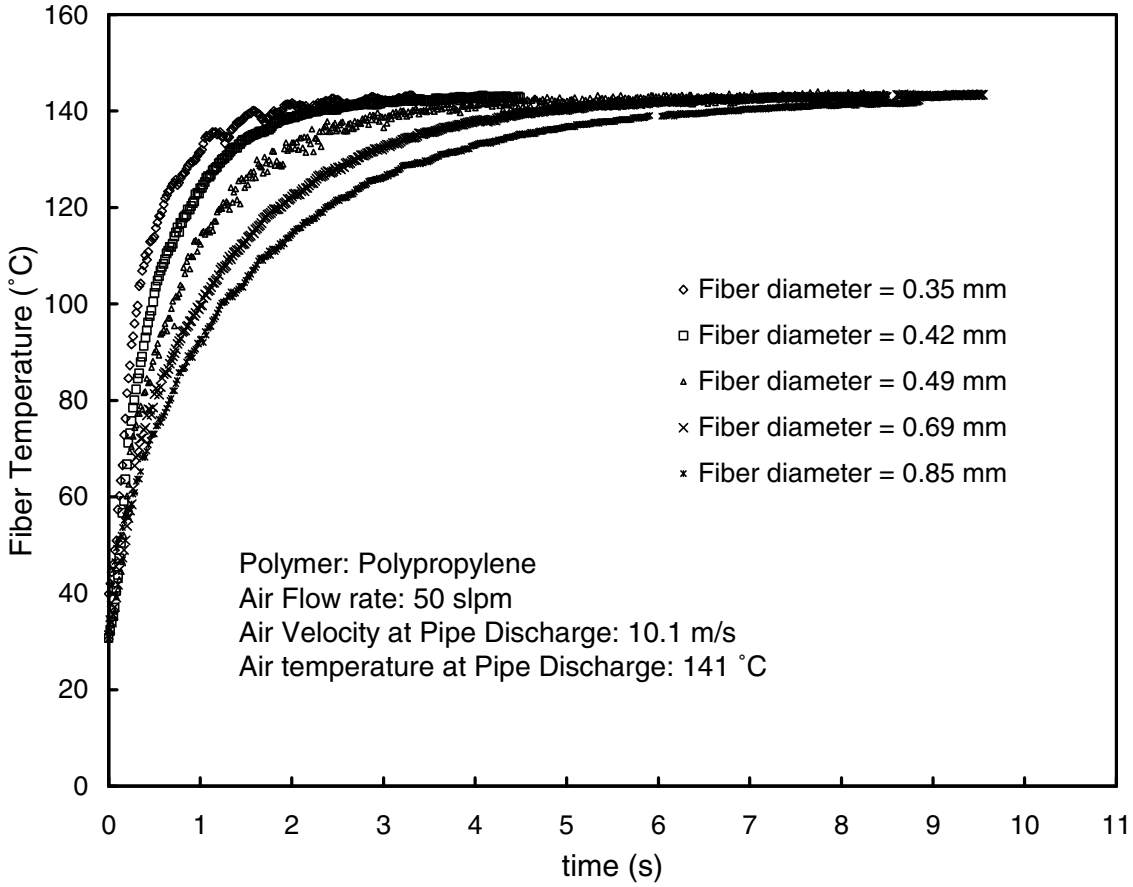

Figure 7. Instantaneous temperature profiles of 5 polypropylene fibers of different diameters for the conditions shown in the Figure. The fiber was held normal to the air stream (cross flow).

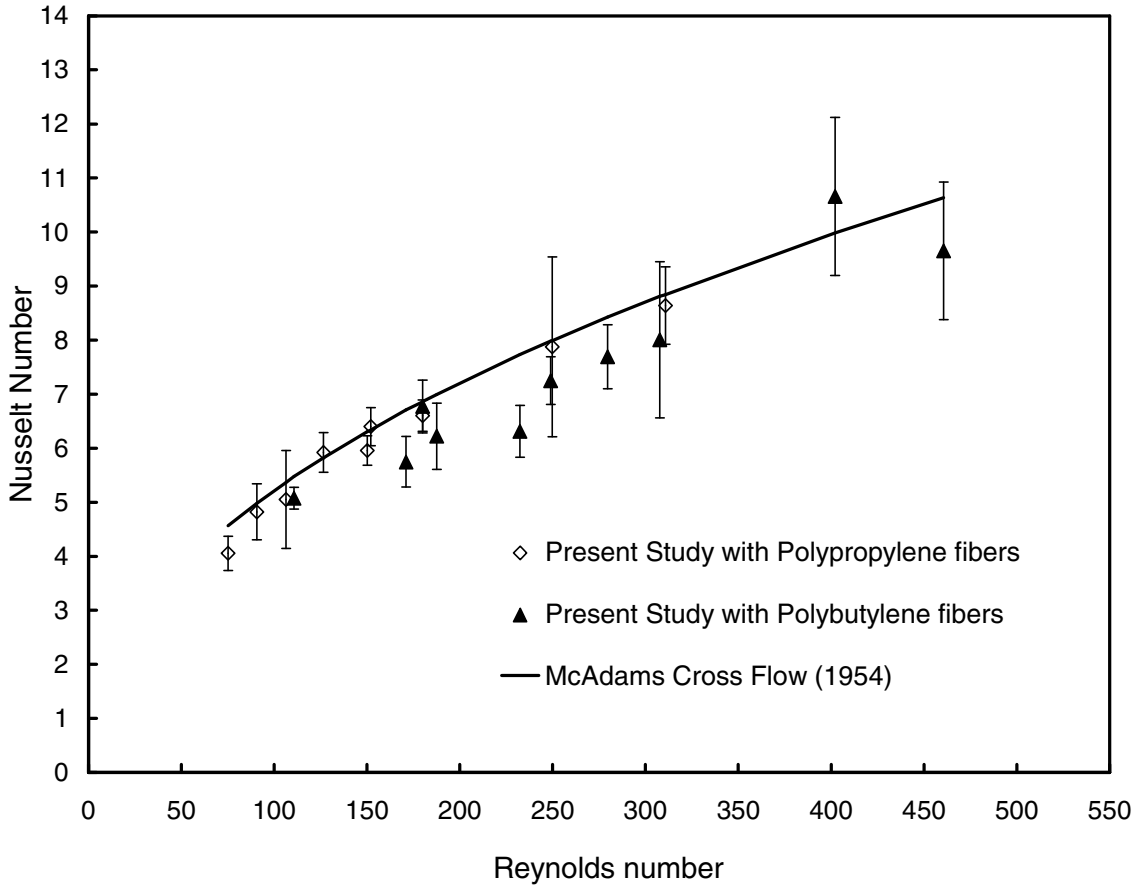

Figure 8. Effect of Reynolds number on the Nusselt number obtained from the present study for the case where the air flows normal to the fiber axis. Data obtained from both polypropylene and polybutylene fibers are plotted. For comparison, the correlation of McAdams (1954) is also shown.

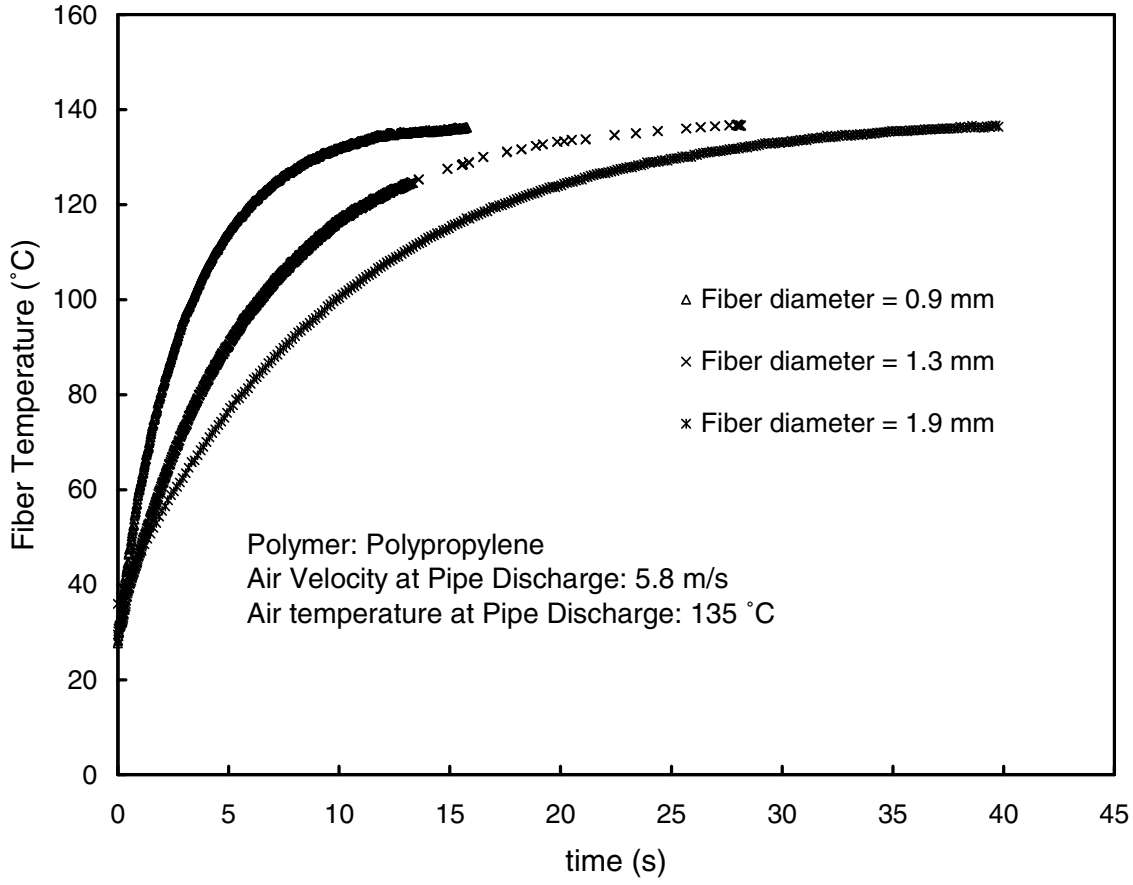

Figure 9. Instantaneous temperature profiles of 3 polypropylene fibers of different diameters for the conditions shown in the Figure. The fiber was held parallel to the air stream.

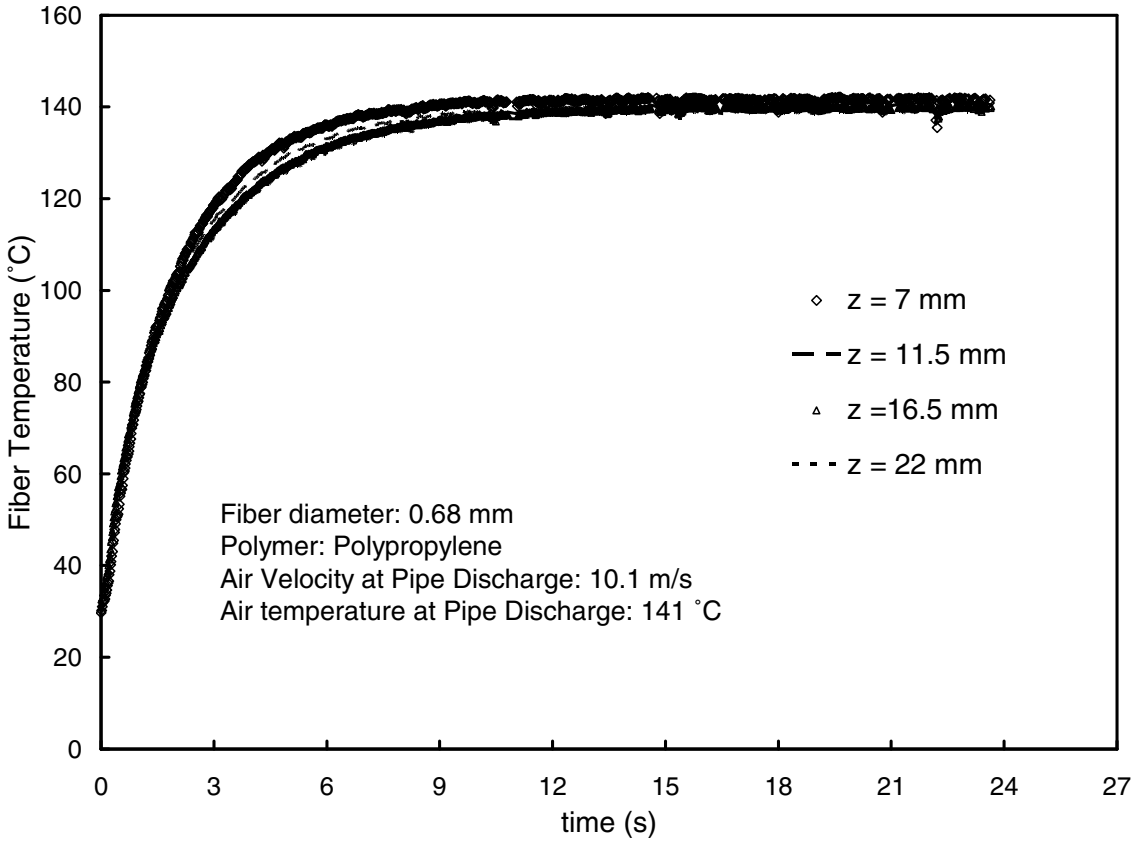

Figure 10. Instantaneous temperature profile at different z locations for a polypropylene fiber having a diameter of 0.68 mm. The fiber was held parallel to the air stream. The distance from the tip of the fiber to the pipe discharge was 3 mm. Hence z = 22 mm corresponds to 19 mm from the tip of the fiber. The air velocity and temperature remain almost constant along this length and the values are shown on the figure.

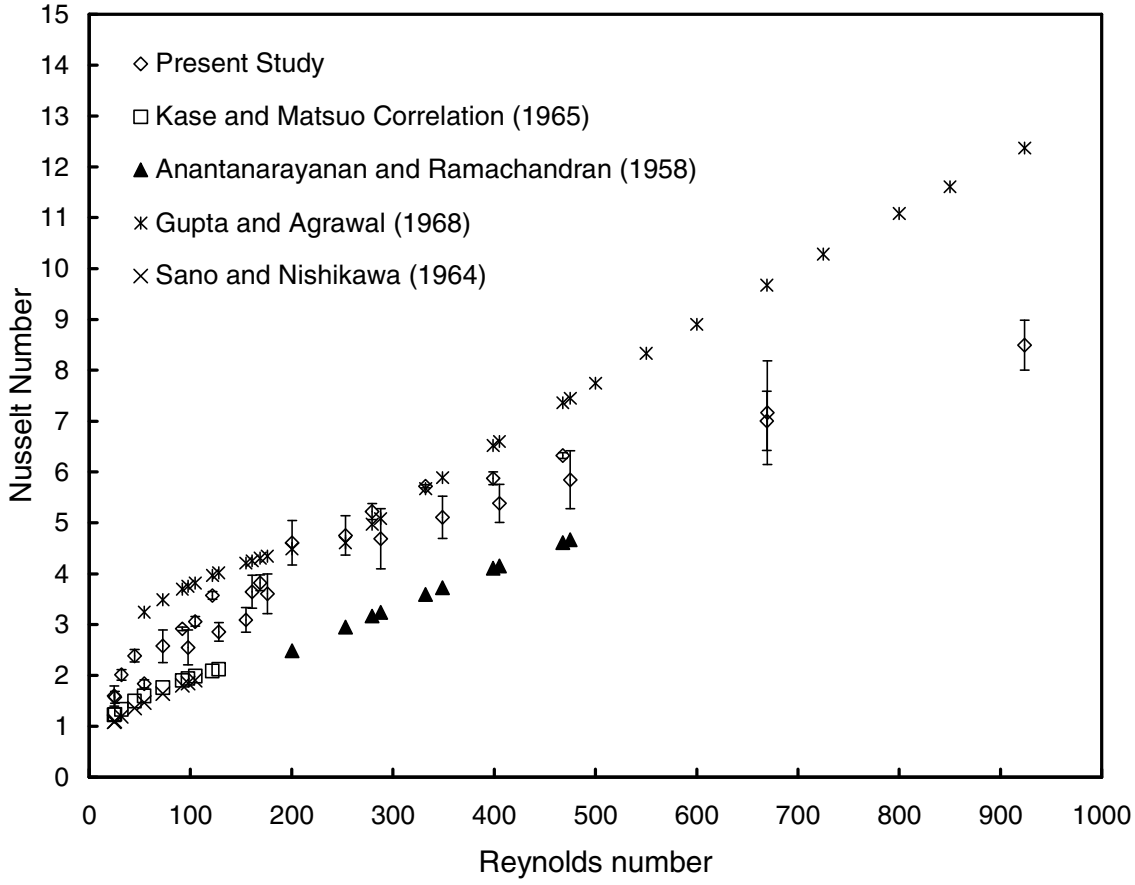

Figure 11. Effect of Reynolds number on the Nusselt number obtained from the present study for the case of air flowing parallel to the fiber axis. The correlations from other studies in the range of applicable Reynolds numbers are also shown on the figure.

CHAPTER 7

ON-LINE MEASUREMENT OF FIBER DIAMETER AND TEMPERATURE IN THE MELT SPINNING AND MELT BLOWING PROCESS

A revised version of this Chapter will be submitted as a journal article.

7.1 Introduction

Melt Spinning and Melt Blowing are widely used commercial processes for the manufacture of fibers and nonwovens, respectively. Experimental measurements of fiber properties along the spinline help in understanding the process of fiber formation and also serve as a valuable dataset for comparing the predictions from mathematical models. Although the fiber motion in melt blowing is severe compared to melt spinning, the two processes are not too dissimilar and similar techniques have been used for measuring the fiber properties along the spinline. A good overview of the melt blowing process is given by Shambaugh.[1]

Several studies in the past have focused on the on-line measurement of fiber diameter, fiber temperature, birefringence and fiber velocity along the spinline. More recently, on-line X-ray characterization of the fiber in melt spinning was conducted to monitor structural changes along the threadline.[2] While the fiber velocity has been measured using primarily Laser Doppler Velocimetry,[3,4] and the birefringence using a polarizing microscope[5-7] or crossed polarizers,[8] several methods have been used for measuring the fiber diameter and a brief review of these methods is in order.

Lu and Spruiell[5] used a polarizing microscope which was mounted sideways such that the running fiber could be seen through the eyepiece of the microscope. By using a calibrated micrometer eyepiece, the fiber diameter could be measured. Bheda and Spruiell[9] measured the fiber diameter in melt spinning using a Zimmer diameter monitor based on the principle of electrooptic back illumination. Their setup permitted several measurements at each spinline position and a statistical analysis was conducted to determine the average diameter. A similar setup for measuring the fiber diameter profile was used by several other research groups.[10,11] Haberkorn et al.[12] used a forward laser light scattering (LLS) technique to determine the fiber diameter along the spinline. The fiber diameter was determined from the distance between the interference maxima on the diffraction pattern which was recorded on a charged-couple device or CCD camera. Wallen et al.[13] used small angle light scattering to study the fiber diameter and orientation in the melt blowing process. Bansal and Shambaugh[6,7] used high-speed macro photography for measuring the fiber diameter in both the melt spinning and melt blowing process. Oh et al.[14] obtained the diameter profile for solid and hollow fibers in the melt spinning process by making on-line measurements using a special capturing device, which trapped and froze the filament. The captured filaments were cut with a microtome and the inner and outer fiber diameters were measured with a microscope. Bresee and Qureshi[15] used a pulsed laser in conjunction with a rapid framing rate camera to acquire the fiber diameter in the melt blowing process. Zhao and Wadsworth[16] used a 51 cm long rigid mechanical arm to collect the fiber at different locations along the melt blowing spinline and analyzed the collected fibers using an optical microscope and an image

analyzing software. Recently, Golzar et al.[17] used an Infrared Camera to measure the fiber diameter in the melt spinning process. However, due to the resolution of the Infrared camera, diameter measurements below 25 μm were not possible. Moore et al.[18] used an ensemble laser diffraction (ELD) technique to determine the fiber diameter distribution at any location below a melt blowing die.

Compared to the numerous techniques used for determining the fiber diameter profile, the fiber temperature profile has been measured mostly using an Infrared (IR) Camera. An IR camera allows for non-contact measurement of the fiber temperature. However, the technical specifications or capabilities in commercially available IR cameras can be different from one another in relation to their spectral range, the type of thermal sensors and their spatial resolution. For example, Lu and Spruiell[5] used a Barnes Infrared Microscope to measure the temperature of the filament in the melt spinning process. While the resolution of the IR microscope would be far superior to other IR cameras, the accuracy of temperature measurement also depends on the accuracy with which the emissivity is estimated. The authors used a null-balance technique where the temperature of the filament was compared with that of a small heater at a known temperature. The radiation from the filament was compared with that of the heater and the filament temperature was assumed to be the same as the heater temperature at the point where the filament radiation did not disturb that of the heater. However, it would seem that this technique could be applied only if the emissivity of the heater was the same as that of the filament. Alternatively, unless the authors made use of a localized emissivity (different emissivity setting for different regions in the field of view of the IR

camera) while viewing the image on the IR screen, the measurements may not have been accurate. In addition, since the IR microscope has a depth of field on the order of a few microns, it would be difficult to use this technique in melt blowing where the fiber motion is severe. Bresee and Ko[19] used a digital IR thermometer with adjustable emissivity for temperature measurements of fibers in melt blowing. They inserted a probe into the fiber stream and measured the temperature of the fiber as they collected on the probe surface. However, since this technique requires insertion of a probe in the polymer stream, it cannot be applied to melt spinning. Bansal and Shambaugh[6,7] and De Rovere and Shambaugh[20] used a slit response factor or SRF curve to account for the spatial resolution of their IR camera while measuring the temperature of fibers in the melt spinning and melt blowing process. This was to account for the errors involved in measuring the temperature of fine fibers. Errors in measurement can also be attributable to incorrect estimation of object emissivity. Marla et al.[21] described a procedure by way of which one could quantify the errors involved during temperature measurements of fine filaments. Several studies use emissivity values provided by the manufacturers of their IR camera or from other references. However, emissivity has been known to be a function of thickness in case of thin polymer films,[22] diameter in case of cylindrical objects,[21] and also on the angle of vision among several other factors.

Both melt spinning and melt blowing involve heat transfer from a polymer filament to an air stream that flows parallel to the polymer. While there are several correlations for heat transfer from wires to air in parallel flow,[23-25] the heat transfer correlation of Kase and Matsuo[26] is commonly used in mathematical models for melt spinning and melt

blowing. However, when it is used in melt blowing models, it severely overpredicts the temperature when compared with experimental data. In melt spinning, in some cases, the difference between experimental and predicted temperature was 60 ˚C,[20] while in melt blowing the difference was found to be >100 ˚C.[7] With the intent of developing a better heat transfer coefficient correlation, we began an experimental campaign which started with the development of a slit response factor or SRF curve for our Infrared Camera[21] for accurate determination of the temperature of fine polymer filaments. We then used an unsteady state approach to determine the heat transfer coefficient for polymer filaments parallel to an air stream.[27] The correlation that was developed from the above experimental study was

$$Nu = 1.4 + 0.0141\ Re,\ 24 \leq Re \leq 150 \quad (1)$$

$$Nu = 0.3575\ Re^{0.46},\ 150 < Re < 923 \quad (2)$$

As a comparison, the correlation of Kase and Matsuo[26] is given below

$$Nu = 0.42\ Re^{0.334} \quad (3)$$

In this paper, we evaluate the performance of the newly developed correlation by employing it in the models for melt spinning and melt blowing and comparing the predicted temperature profile with on-line temperature measurements.

7.2 Details of Experimental Setup

7.2.1 Melt Blowing

Figure 1 shows the experimental setup for measurement of the fiber diameter and temperature in the melt blowing process. The setup was identical to that used by Marla

and Shambaugh.[28] A Brabender extruder of 19.1 mm (0.75 in.) diameter and 381 mm length was used to melt and pressurize the polymer. The barrel had a 20:1 *L*/*D* ratio and a 3:1 compression ratio. The polymer exiting from the extruder was then fed to a modified Zenith pump, which pumps controlled quantities of molten polymer through a single-hole melt blowing slot die. The polymer capillary had an inside diameter of 0.420 mm. The two air slots were set flush with the nosepiece, and the slot widths were 0.65 mm. Each slot had a length of 74.6 mm (2.94 in.). The die assembly was heated with two 250 W cartridge heaters. A thermal mass flow meter was used to measure the air flow rate, which was maintained at either 100 or 125 slpm (at standard conditions of 21°C and atmospheric pressure). The centerline air velocity and temperature below the die was determined using a pitot tube and thermocouple probe respectively. The details of these equipments can be found in Marla et al.[21] The fiber diameter profile was obtained using high-speed flash photography the details of which can be found in Bansal and Shambaugh.[7] The camera used was a Nikon N90S equipped with a 105-mm Nikon macro lens and the illumination was provided by a Sunpak Auto 622 flash. The polymer used in the experiments was 88 MFR Fina Dypro isotactic polypropylene. The polymer had an M_w of 165 000 g/mol and an M_n of 41 500 g/mol.

The temperature of the polymer filaments was determined using an Infrared Camera. The IR camera used in the present study was ThermaCAM® S60 manufactured by FLIR Systems. The spectral range for this camera is 7.5-13 μm (longwave).The IR image displayed had a resolution of 640 x 480 pixels while the actual number of thermal detector sensors or elements is 320 x 240. The other prominent features of this IR camera

can be found on the manufacturer's website and the camera's user manual.[29] The IR lens on this camera has a field of view (FOV) of 24˚ x 18˚ with a minimum focus distance of 0.3 m or 11.81 inches. The camera also came with a 100 µm close-up lens for which the minimum focus distance is 80 mm while the maximum working distance is 110 mm. The close-up lens fits on the 24˚ lens of the IR camera and has certain advantages over the 24˚ lens in that it can measure the temperature of small targets with greater accuracy. Unless otherwise mentioned, all temperature measurements in the present study were made with the 100 µm close-up lens. The IR camera had the capability to record 60 temperature measurements/s and a real-time plot of these measurements could be seen on the monitor of a PC that was connected to the IR camera by means of an IEEE 1394 (firewire) connection. Since the 100 µm close-up lens has a small depth of field and melt-blown fibers exhibit lateral motion, the fiber moves in and out of focus of the IR camera. When the fiber is in focus, the real-time plot displays a spike in the fiber temperature and this was noted down as the fiber temperature. Starting at 1 cm below the die, measurements were made at intervals of 1 cm up to 12 cm below the melt blowing die. Beyond 12 cm, the fiber temperature was measured at 13, 15, 17, 20 and 25 cm below the die. Close to the die, reflections from the die would affect the measured fiber temperature. Hence measurements were made from 1 cm below the die. The variation of emissivity with fiber diameter for both polypropylene and polybutylene, the procedure for using the SRF curve and the operating procedure of the IR camera are described elsewhere.[21] The base conditions for the experiments, unless otherwise specified, were

$m_p = 0.75$ g/min

$T_{f,die}$ = 310 °C

$T_{a,die}$ = 368 °C

Air flow rate = 125 slpm

The effect of mass throughput of the polymer was investigated by increasing it to 1 g/min and 1.25 g/min while keeping all other base conditions constant. The effect of air flow rate was also investigated by changing it to 100 slpm while keeping all the other base conditions constant.

7.2.2 Melt Spinning

For melt spinning, the experimental setup was the same as melt blowing except that the air supply was turned off and a different die was used. A single-hole spinneret was used for the production of fibers. The single-hole spinneret had a diameter of 0.407 mm (0.016 in) and a length 2.97 mm (0.1169 in). In addition to polypropylene, polybutylene fibers were also spun. The polybutylene resin was Grade 0400 manufactured by Basell Polyolefins and had a MFR of 20. The molten polymer exiting the die was drawn by a mechanical take-up roll located 1.4 m below the spinneret. For experiments with both polypropylene (PP) and polybutylene (PB), the spinneret temperature was kept at 200 ^{o}C and the polymer throughput was kept at 1g/min. For polypropylene, the mechanical take-up roll was used at six spinning speeds ranging from 500 m/min to 1750 m/min while polybutylene was spun at speeds of 500 m/min and 1000 m/min. The fiber diameter and temperature were measured in the same way as in melt blowing. Beginning from 3 cm below the die, the temperature measurements were made at 1 cm intervals up to 12 cm

below the die. Beyond 12 cm, the measurements were made at intervals of 2.5 cm up to 20 cm below the die.

7.3 Modeling Details

7.3.1 Melt Spinning

The energy balance over a differential element of size Δy of the fiber at any distance y below the spinneret can be written as

$$m_p C_{p,f} \frac{dT_f}{dy} = -\pi h \; d_y (T_f - T_a) \qquad (4)$$

where

m_p = mass throughput of the polymer (kg/s)

$C_{p,f}$ = specific heat of the polymer (J/kg·K)

d_y = fiber diameter at any distance y below the spinneret (m)

h = convective heat transfer coefficient (W/m^2·K)

T_a = temperature of the ambient air (˚C)

T_f = fiber temperature (˚C)

At very high spinning speeds (in excess of 4000 m/min), the stress in the polypropylene fiber increases and induces crystallization in the fiber.[6] Equation 4 neglects the heat gained by the polymer due to crystallization and for the moderate spinning speeds in our experiments, this is a reasonable assumption. The fiber diameter profile in eq 4 was obtained using high-speed flash photography. The specific heat capacity of both polypropylene and polybutylene do not vary significantly with temperature and can be

assumed to be constant. Then, eq 4 is an ordinary differential equation with the temperature of the fiber, T_f, as the only dependent variable. This ODE can be numerically solved for T_f using the 4^{th} order Runge-Kutta method. By using different correlations for calculating the convective heat transfer coefficient in eq 4, the predicted fiber temperature can be compared with the results from on-line temperature measurements.

7.3.2 Melt Blowing

For melt blowing, the model of Marla and Shambaugh[30] was used and unlike melt spinning where T_f was the only dependent variable, the melt blowing model was solved for the fiber diameter as well. The details of the model can be found in Marla and Shambaugh.[30] The model was solved using both the Kase and Matsuo heat transfer correlation (eq. 3) and the correlation developed by Marla et al.[27]

7.4 Results and Discussion

7.4.1 Melt Spinning

Figure 2 shows representative plots of on-line diameter profiles for polypropylene spun at 500 and 1750 m/min using high-speed flash photography. The fiber attenuated rapidly close to the spinneret and the fibers spun at 1750 m/min attenuated faster than the fibers spun at 500 m/min. The diameter profiles were fit to 4^{th} order polynomials so that they could be inserted in eq 4 as a function of distance from the spinneret, y. Table 1 shows the coefficients of the 4^{th} order polynomial for each spinning speed for both PP and PB. For the correlations in Table 1, y must be in cm and the fiber diameter is obtained in microns.

Figure 3 shows the results from the on-line temperature measurements for PP for six different spinning speeds. The fibers seem to cool faster with increase in spinning speed. Other studies[6,9] showed that the take-up speed did not significantly affect the fiber temperature profile. Bansal and Shambaugh[6] explained their results in the following way: Higher spinning speeds result in finer diameters and since they possess less sensible heat, they cool at a faster rate. However, finer fibers are exposed to the ambient air for less time. These two effects apparently counter each other and hence the fiber temperature showed little dependence on spinning speed. However, our experiments show that the spinning speed does affect the fiber temperature although it is of the order of 10-25 ˚C. For example, at 20 cm below the die, the temperature of the fiber spun at 1750 m/min is 90 ˚C while that spun at 500 m/min is 115 ˚C. Figure 4 shows the results from the on-line temperature measurements for PB for two different spinning speeds and trends parallel that observed for polypropylene

Accurate determination of polymer emissivity is very critical while measuring the filament temperature. Several research groups have shown that the emissivity of thin films increases with film thickness.[22,31] The plot of emissivity versus film thickness shows an initial region of rapid increase of emissivity with film thickness and then an asymptotic behavior. Marla et al.[21] determined the emissivity of polymer filaments of different diameters and observed a trend similar to that of emissivity versus film thickness. If the diameter-dependence of emissivity is not taken into consideration then the measured temperature of the fiber using an IR camera will be incorrect. Marla et al.[21] observed that the emissivity of polypropylene fibers asymptotically approached a value

of 0.82. If this is the emissivity setting used in the IR camera for measurements all along the spinline, then the measured values of fiber temperature would be lower than the true temperature of the fiber. The results for PP spun at six different speeds are shown in Figure 5. The temperature measurements using an emissivity setting of 0.82 are substantially lower than the true temperature of the fiber all along the spinline. At 20 cm below the spinneret, for a spinning speed of 1750 m/min, the uncorrected temperature (with emissivity constant at 0.82) is 49 ˚C while the true temperature (with emissivity as a function of fiber diameter) is 90 ˚C. Also, the difference between the corrected and uncorrected temperature increases along the spinline. This is because the fiber diameter decreases along the threadline and the emissivity of polymer filaments shows strong dependence on emissivity as the diameter decreases.[21] Since emissivity of the target determines its temperature, the error due to an incorrect emissivity setting becomes more pronounced along the spinline.

Figures 6-11 show the predicted temperature profile obtained by solving eq 4 for PP at each spinning speed. The temperature profiles obtained by inserting different heat transfer correlations in eq 4 are shown and the experimental data is also shown for comparison. For each of the spinning speed, the predictions obtained on using the Kase and Matsuo[26] heat transfer correlation were higher compared to experimental data. However, the temperature profile obtained on using the correlation developed by Marla et al.[27] compared favorably with experimental data for each spinning speed. Similar observations were made with PB and the results are plotted in Figures 12 and 13. It may be pointed out that the heat transfer correlation of Marla et al.[27] was developed for the

case of polymer fiber of fixed diameter in a hot stream of air. The transient heating of the fiber was recorded using the same IR camera as in our experiments. Fibers of different diameter were used in their experiments. By writing an energy balance over a differential element, the instantaneous heat transfer coefficient was determined. Using statistical analysis, a time-averaged heat transfer coefficient was determined for each experiment and this was used to calculate the Nusselt number. The experimental setup for determining the heat transfer coefficient was designed with the intention of simulating the melt spinning and melt blowing process as closely as possible. Although the setup of Marla et al.[27] for determining the heat transfer coefficient was for simulating the case of heat transfer from fine filaments to air in parallel flow there is a fundamental difference with the mechanism of heat transfer from fibers in the melt spinning and melt blowing process. The fibers used in the experiments of Marla et al. had a fixed diameter while in both melt spinning and melt blowing, the fiber diameter decreases along the spinline. However, the favorable agreement of the predicted temperature profile (obtained when the correlation of Marla et al. is used in eq 4) with the experimental data seems to suggest that the attenuating fiber follows a mechanism of heat transfer which is similar to that from a fiber of constant diameter. Incidentally, the resins used in our melt spinning and melt blowing experiments were the same resins used by Marla et al. in their experiments for determining the heat transfer coefficient. However, the eqs 1-3 used for calculating the heat transfer coefficient are dimensionless and material-independent.

7.4.2 Melt Blowing

Figure 14 and 15 show the centerline air velocity and temperature respectively below the melt die for the conditions shown on the figure. It should be noted that these measurements were made in the absence of the polymer, i.e., the polymer flow was stopped during these measurements. These measurements are useful in understanding the flow field below melt blowing dies and also serve as boundary conditions in mathematical models for melt blowing.[28,30,32] Several other researchers[33-36] made measurements of the air velocity and temperature below slot dies in different configurations and have developed dimensionless empirical correlations. Recently, computational fluid dynamics (CFD) has been used to investigate the flow fields below melt blowing slot dies.[37-39] The centerline velocity decreases along the threadline with the velocity being slightly higher for the 125 slpm case compared to the 100 slpm case. The centerline air temperature profile shows a similar trend to the air velocity profile. However, the reduction in the air flow rate from 125 slpm to 100 slpm did not seem to affect the air temperature.

Figure 16 shows the fiber diameter profiles for different polymer throughputs while keeping the other conditions same as the base conditions mentioned earlier. The fiber diameter increases at any point below the melt blowing die as the mass throughput of the polymer increases. Also, the die swell increases with increase in the polymer flow rate. Figure 17 shows the diameter predictions from the Marla and Shambaugh[30] model for the base operating conditions. The heat transfer correlation of both Kase and Matsuo[26] and Marla et al.[27] was used in the model. The diameter profile from on-line measurements is

also plotted on the figure. The final diameter obtained when using the different heat transfer correlations in the model is shown in the figure. The choice of heat transfer correlation does not seem to affect the model predictions of fiber diameter profile and there is good agreement between experimental data and model predictions. Uyttendaele and Shambaugh[40] obtained a similar result with an annular melt blowing die. Similar results were obtained for all other operating conditions.

Figure 18 shows the effect of air flow rate on the fiber diameter profile. The air flow rate does not significantly affect the diameter profile and this result parallels the findings from the experimental and modeling work of Marla and Shambaugh with slot dies.[28]

Figure 19 shows the temperature profile obtained from on-line measurements for different polymer throughputs. The fiber temperature profile does seem to indicate that larger fibers cool slower as the fiber temperature at any spinline position shows an increase with the mass throughput of the polymer. At any spinline location, there are two effects which counter one another due to an increase in the mass flow rate of the polymer. With an increase in the polymer flow rate, the thermal inertia ($m \cdot C_{p,f}$) of the fibers increases due to the increase in diameter. However, the increase in polymer mass throughput also causes an increase in the surface area for heat transfer. Our experimental data indicate that the former effect dominates the heat transfer process. Similar results were obtained by Bresee and Ko.[19]

Figures 20-23 show the temperature profile obtained from the Marla and Shambaugh[30] model. The experimental data is also plotted on each figure. In each case,

the model predictions on using the Kase and Matsuo[26] correlation were higher than when the correlation of Marla et al.[27] was used. The centerline air temperature is also plotted on each figure and it can be seen that the fiber remains comparatively hotter all along the threadline. While the agreement of the predicted temperature on using the correlation of Marla et al. was not as good as in melt spinning, the predictions are definitely better compared to when the correlation of Kase and Matsuo was used in the model. For example, in figure 20, at 25 cm below the die, the model predictions based on the heat transfer correlation of the former is 118 ˚C and is 190 ˚C based on the correlation of the latter. At the same location the experimentally measured fiber temperature is 94 ˚C. The reason the model predictions are slightly higher compared to experimental data may be due to the severe transverse vibratory motion of the fiber. It has been shown that for heat transfer from wires to air in parallel flow, vibrations cause an increase in the heat transfer coefficient.[25,41] Although Marla et al.[27] reported that the fiber did exhibit vibrations during their measurement of heat transfer coefficient, they were relatively minor compared to that observed in melt blowing. The severe transverse motion of the fiber may be responsible for the increase in the rate of heat transfer from the polymer to ambient air.

7.5 Conclusions

On-line measurements of fiber diameter and temperature were made in the melt spinning and melt blowing process. In melt spinning, the fibers seemed to cool slightly faster with increase in spinning speed for both PP and PB. An incorrect emissivity setting

in the IR camera while measuring the fiber temperature resulted in an error in temperature measurement, which increased along the spinline. When the heat transfer correlation developed by Marla et al.[27] was used while numerically solving for the fiber temperature, the predictions compared very well with experimental data. In melt blowing, the fiber temperature at any downstream location showed a slight increase with an increase in the mass throughput of the polymer over the range of mass flow rates studied. The predictions of the fiber diameter profile from the melt blowing compared favorably with experimental data obtained from high speed flash photography. The choice of heat transfer correlation did not show a strong affect on the predicted diameter profile obtained from the melt blowing model. The predictions for fiber temperature based on the correlation of Marla et al.[27] compared better with experimental data than the predictions based on the Kase and Matsuo[26] correlation.

Acknowledgements

This work was supported by an NSF GOALI grant (DMII-0245324). The support of 3M and Procter & Gamble is also gratefully acknowledged.

References

(1) Shambaugh, R. L. A Macroscopic View of the Melt Blowing Process for Producing Microfibers. *Ind. Eng. Chem. Res.* **1988,** *27*(12), 2363-2372.

(2) Hsiao, B. S.; Barton, R.; Quintana, J. Simple On-line X-ray Setup to Monitor Structural Changes During Fiber Processing. *J. Appl. Polym. Sci*. **1996,** *62*, 2061-2068.

(3) Wu, T. T.; Shambaugh, R. L. Characterization of the Melt Blowing Process with Laser Doppler Velocimetry. *Ind. Eng. Chem. Res.* **1992,** *31*(1), 379-389.

(4) Takarada, W.; Ito, H.; Kikutani, T.; Okui, N. Studies on High-Speed Melt Spinning of Noncircular Cross-Section Fibers. I. Structural Analysis of As-Spun Fibers. *J. Appl. Polym. Sci.* **2001,** *80*, 1575-1581.

(5) Lu, F. M.; Spruiell, J. E. The Influence of Resin Characteristics on the High Speed Melt Spinning of Isotactic Polypropylene. II. On-Line Studies of Diameter, Birefringence, and Temperature Profiles. *J. Appl. Polym. Sci*. **1987,** *34*, 1541-1556.

(6) Bansal, V.; Shambaugh, R. L. On-line Determination of Density and Crystallinity during Melt Spinning. *Polym. Eng. Sci.* **1996,** *36*(22), 2785-2798.

(7) Bansal, V.; Shambaugh, R. L. On-line Determination of Diameter and Temperature during Melt Blowing of Polypropylene. *Ind. Eng. Chem. Res.* **1998,** *37*(5), 1799-1806.

(8) De Rovere, A. Characterization of Hollow Fiber Properties During the Melt Spinning Process . Ph.D. Dissertation, University of Oklahoma, Norman, OK. 2000

(9) Bheda, J. H.; Spruiell, J. E. Dynamics and Sturcture Development during High Speed Melt Spinning of Nylon 6. I. On-line Experimental Measurements. *J. Appl. Polym. Sci*. **1990,** *39*, 449-463.

(10) Denton, J. S.; Cuculo, J. A.; Tucker, P. A. Computer Simulation of High-Speed Simulation of PET. *J. Appl. Polym. Sci*. **1995,** *57*, 939-951.

(11) Kikutani, T.; Nakao, K.; Takarada, W.; Ito, H. On-line Measurement of Orientation Development in High-Speed Melt Spinning Process. *Polym. Eng. Sci*. **1999,** *39*(12), 2349-2357.

(12) Haberkorn, H.; Hahn, K.; Breur, H.; Dorrer, H. D.; Matthies, P. On the Neck-Like Deformation in High-Speed Spun Polyamides. *J. Appl. Polym. Sci*. **1993,** *47*, 1551-1579.

(13) Wallen, J.; Fellers, J. F..; Bresee, R. R. Small Angle Light Scattering Studies of the Fiber Attenuation Process During Melt Blowing. *Int. Nonwovens. J.* **1995,** *7*(3), 49-50.

(14) Oh, T. H.; Lee, M. S.; Kim, S. Y.; Shim, H. J. Studies on Melt-Spinning Process of Hollow Fibers. *J. Appl. Polym. Sci.* **1997,** *68*, 1209-1217.

(15) Bresee, R. R.; Qureshi, U. A. Fiber Motion Near the Collector During Melt Blowing Part 1: General Considerations. *Int. Nonwovens. J.* **2002,** *11*(2), 27-34.

(16) Zhao, R.; Wadsworth, L. C. Attenuating PP/PET Bicomponent Melt Blown Microfibers. *Polym. Eng. Sci*. **2003,** *43*(2), 463-469.

(17) Golzar, M.; Beyreuther, R.; Brunig, H.; Tandler, B.; Vogel, R. Online Temperature Measurement and Simultaneous Diameter Estimation of Fibers by Thermography of the Spinline in the Melt Spinning Process. *Adv. Polym. Tech*. **2004,** *23*(3), 176-185.

(18) Moore, M, M.; Shambaugh, R. L.; Papavassiliou, D. V. Ensemble Laser Diffraction for Online Measurement of Fiber Diameter Distribution During the Melt Blowing Process. *Int. Nonwovens. J.* **2004,** *13*(2), 42-47.

(19) Bresee, R. R.; Ko, W. C. Fiber Formation During Melt Blowing. *Int. Nonwovens. J.* **2003,** *12*(2), 21-28.

(20) De Rovere, A.; Shambaugh, R. L. Melt-Spun Hollow Fibers: Modeling and Experiments. *Polym. Eng. Sci.* **2001,** *41*(7), 1206-1219.

(21) Marla, V. T.; Shambaugh, R. L.; Papavassiliou, D. V. Calibration of an Infrared Camera for Accurate Determination of the Temperature of Polymer Filaments. To be Submitted for Publication. (2005a)

(22) Fujikura, Y. Emissivity of Polymers. *Yamagata Daigaku Kiyo, Kogaku*. **1999,** *25*(2), 55-68.

(23) Mueller, A. C. Heat Transfer from Wires to Air in Parallel Flow. *Trans. Am. Inst. Chem. Eng.* **1942,** 38, 613-627.

(24) Sano, Y.; Nishikawa, S. Heat Transfer Coefficient of Five Wires in Air Flow. *Kagaku Kogaku.* **1964,** *2*(2), 199-202.

(25) Gupta, C. P.; Agrawal, D. D. Heat Transfer From a Vibrating Wire to Air in Parallel Flow. *J. Inst. Eng.* **1968,** *48*(9), 557-579.

(26) Kase, S.; Matsuo, T. Studies on Melt Spinning. I. Fundamental Equations on the Dynamics of Melt Spinning. *J. Polym. Sci., Part A*. **1965,** *3*, 2511-2554.

(27) Marla, V. T.; Shambaugh, R. L.; Papavassiliou, D. V. Unsteady State Heat Transfer From Polymer Filaments To Air In Normal And Parallel Flow. To be Submitted for Publication. (2005b)

(28) Marla, V. T.; Shambaugh, R. L. Modeling of the Melt Blowing Performance of Slot Dies. *Ind. Eng. Chem. Res.* **2004**, *43*(11), 2789-2797.

(29) FLIR Systems. *ThermaCAM® S60 Operator's Manual*, Boston, MA, 2004.

(30) Marla, V. T.; Shambaugh, R. L. Three-Dimensional Model of the Melt Blowing Process. *Ind. Eng. Chem. Res.* **2003,** *42*(26), 6993-7005.

(31) Cao, B.; Sweeney, P.; Campbell, G. A. *Infrared Characteristics of Thin Polymer Film: Temperature Measurement of Polyethylene*, Annual Technical Conference - Society of Plastics Engineers, New York, May 1-4, 1989.

(32) Rao, R. S.; Shambaugh, R. L. Vibration and Stability in the Melt Blowing Process. *Ind. Eng. Chem. Res.* **1993,** *32*(12), 3100-3111.

(33) Harpham, A. S.; Shambaugh, R. L. Flow Field of Practical Dual Rectangular Jets. *Ind. Eng. Chem. Res.* **1996,** *35*(10), 3776-3781.

(34) Harpham, A. S.; Shambaugh, R. L. Velocity and Temperature Fields of Dual Rectangular Jets. *Ind. Eng. Chem. Res.* **1997,** *36*(9), 3937-3943.

(35) Tate, B. D.; Shambaugh, R. L. Modified Dual Rectangular Jets for Fiber Production. *Ind. Eng. Chem. Res.* **1998,** *37*(9), 3772-3779.

(36) Tate, B. D.; Shambaugh, R. L. Temperature Fields below Melt-Blowing Dies of Various Geometries. *Ind. Eng. Chem. Res.* **2004,** *43*(17), 5405-5410.

(37) Krutka, K. M.; Shambaugh, R. L.; Papavassiliou, D. V. Analysis of a Melt-Blowing Die: Comparison of CFD and Experiments. *Ind. Eng. Chem. Res.* **2002,** *41*(20), 5125-5138.

(38) Krutka, K. M.; Shambaugh, R. L.; Papavassiliou, D. V. Effects of Die Geometry on the Flow Field of the Melt-Blowing Process. *Ind. Eng. Chem. Res.* **2003,** *42*(22), 5541-5553.

(39) Krutka, K. M.; Shambaugh, R. L.; Papavassiliou, D. V. Effects of Temperature and Geometry on the Flow Field of the Melt Blowing Process. *Ind. Eng. Chem. Res.* **2004,** *43*(15), 4199-4210.

(40) Uyttendaele, M. A. J.; Shambaugh, R. L. Melt Blowing: General Equation Development and Experimental Verification. *AIChE J.* **1990,** *36*(2), 175-186.

(41) Anantanarayanan, R.; Ramachandran, A. Effect of Vibration on Heat Transfer From a Wire to Air in Parallel Flow. *Trans. Am. Soc. Mech. Eng*. **1958,** *80*, 1426-1432.

Polymer	Spinning speed (m/min)	Coefficients of the polynomial $ay^4 + by^3 + cy^2 + dy + e$				
		a	b	c	d	e
Polypropylene	500	-1.776×10^{-14}	- 0.143	6.775	- 112.350	878.160
	800	4.867×10^{-3}	0.407	11.509	-145.898	938.57
	1000	2.012×10^{-2}	1.038	19.707	- 179.945	973.064
	1200	1.714×10^{-2}	- 0.914	18.146	- 172.923	942.920
	1500	1.037×10^{-2}	- 0.607	13.674	- 152.677	913.797
	1750	9.644×10^{-3}	- 0.554	12.934	- 150.273	892.569
Polybutylene	500	2.305×10^{-2}	- 1.073	18.297	- 160.111	954.904
	1000	7.152×10^{-3}	0.372	8.286	- 108.846	872.800

Table 1. Coefficients of the 4th order polynomial used to fit the diameter profiles obtained from high speed flash photography in the melt spinning process for each spinning speed

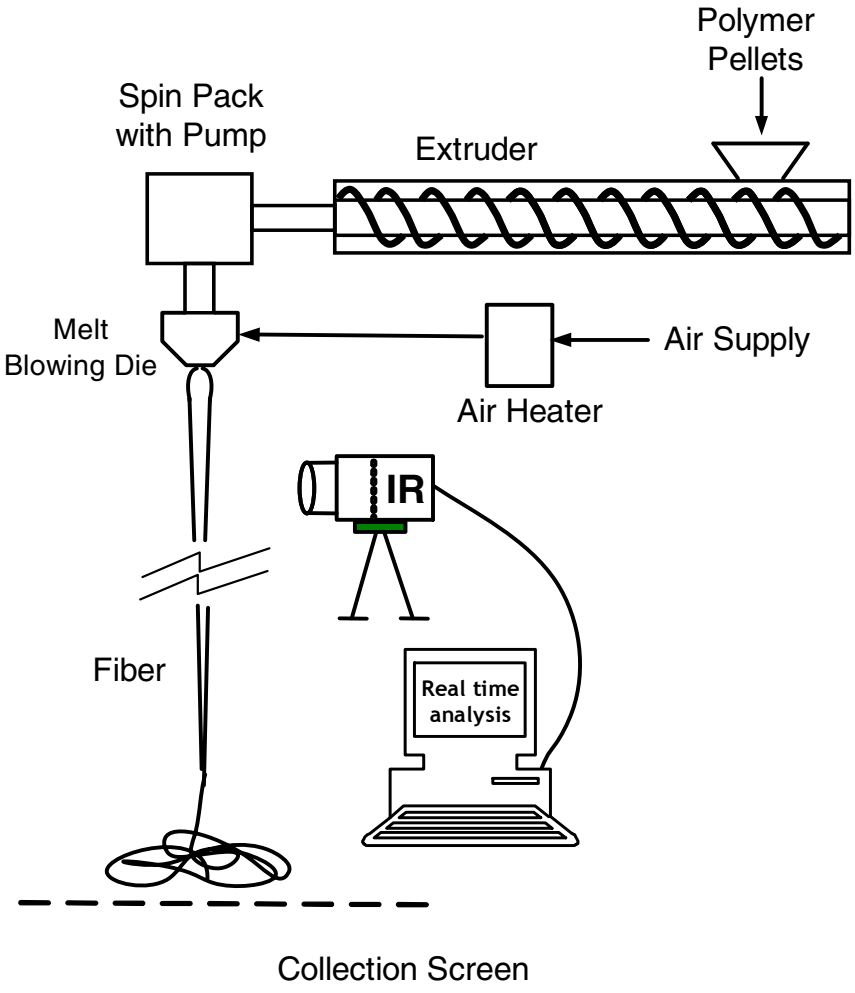

Figure 1. Experimental equipment for melt blowing. For melt spinning, the same equipment was used with the air supply turned off and with a different spinneret.

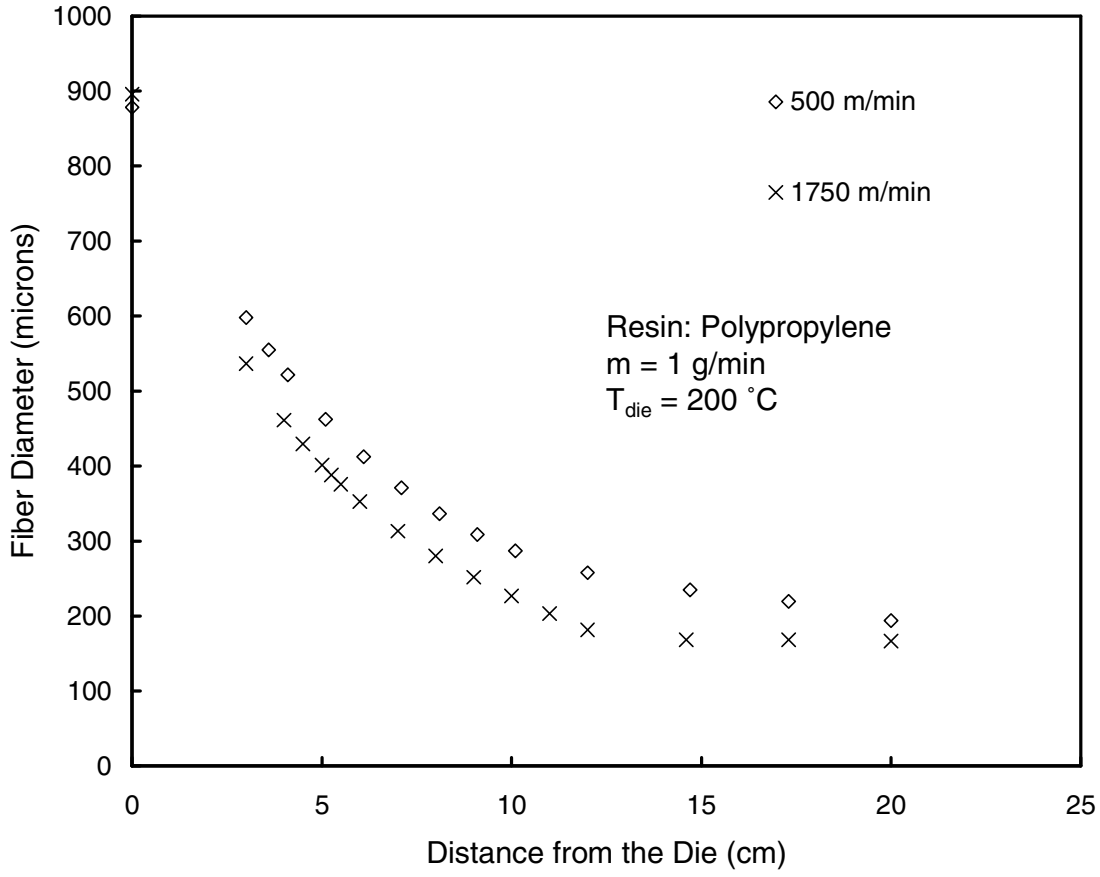

Figure 2. Fiber diameter profile obtained using high-speed photography for PP spun at speeds of 500 m/min and 1750 m/min.

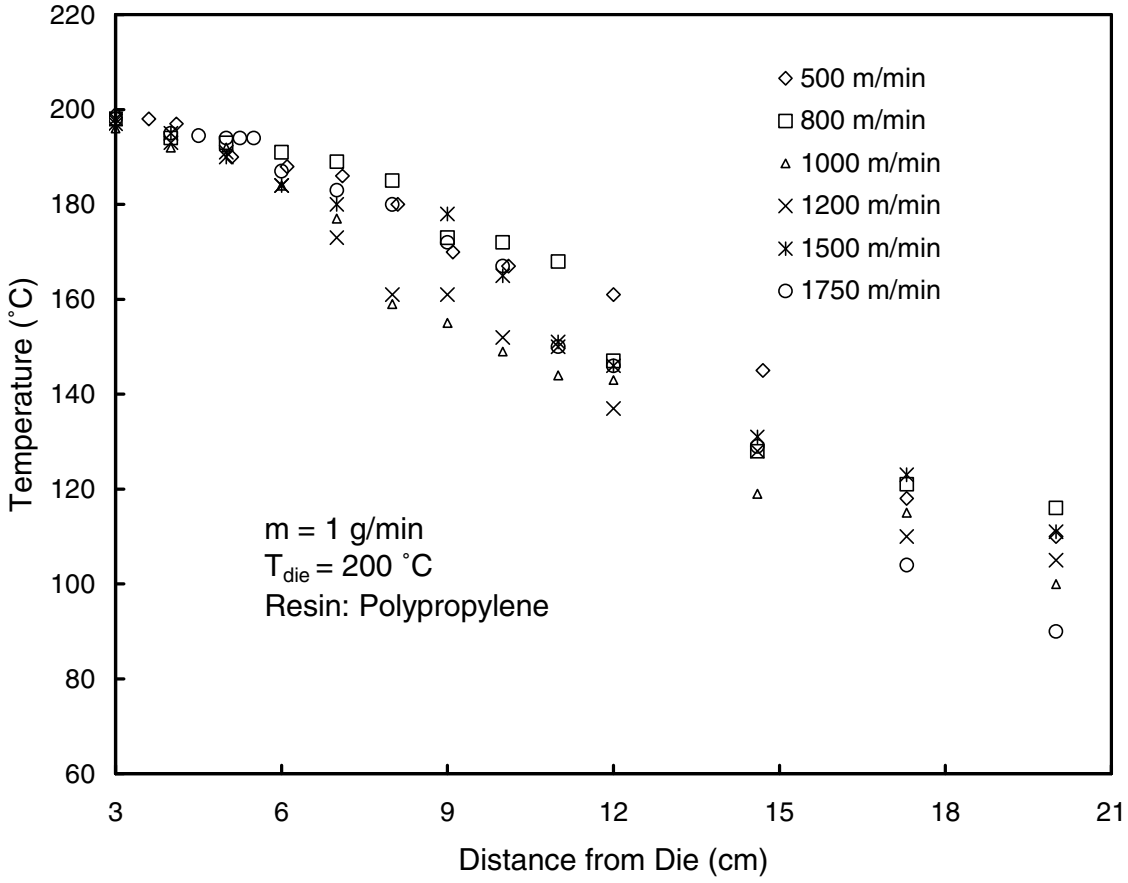

Figure 3. Fiber temperature profile for PP spun at six different speeds from 500 m/min to 1750 m/min. The dependence of PP emissivity on the fiber diameter was accounted for while making the measurements. (See Marla et al.[21])

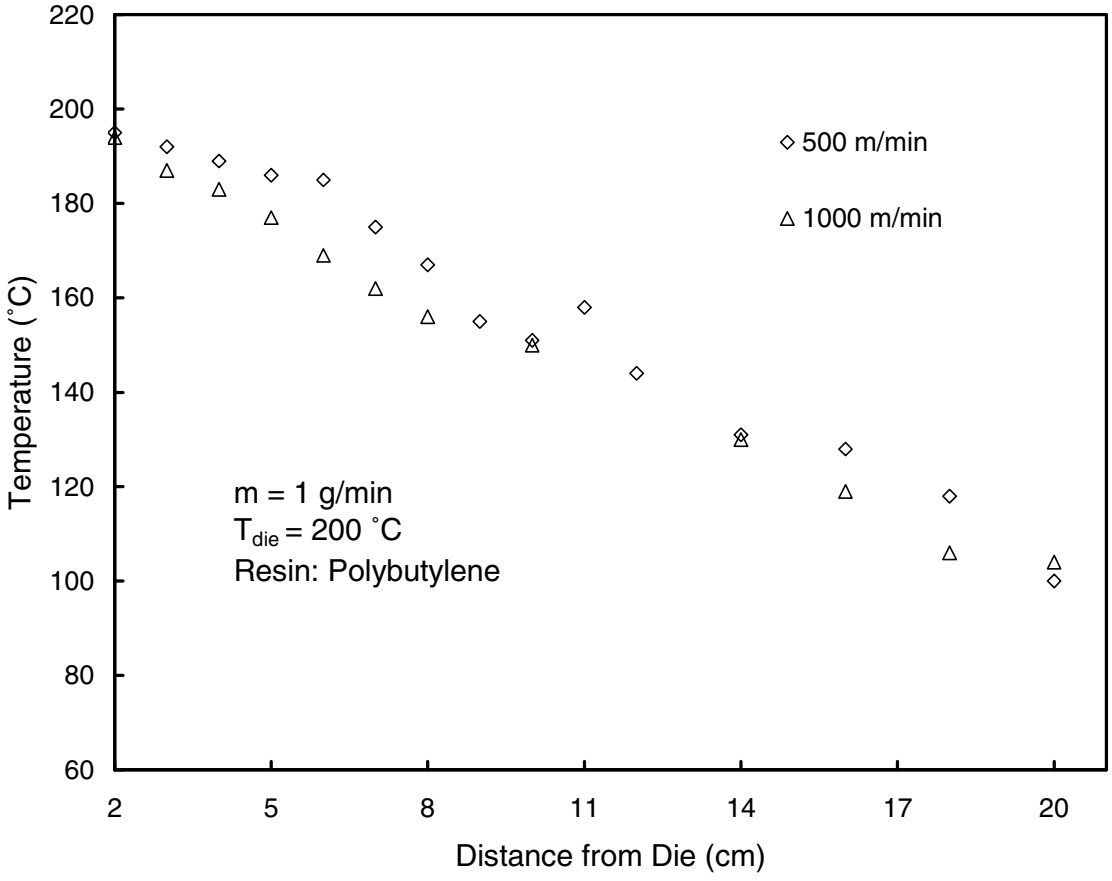

Figure 4. Fiber temperature profile for PB spun at speeds of 500 m/min and 1000 m/min. The dependence of PB emissivity on the fiber diameter was accounted for while making the measurements. (See Marla et al.[21])

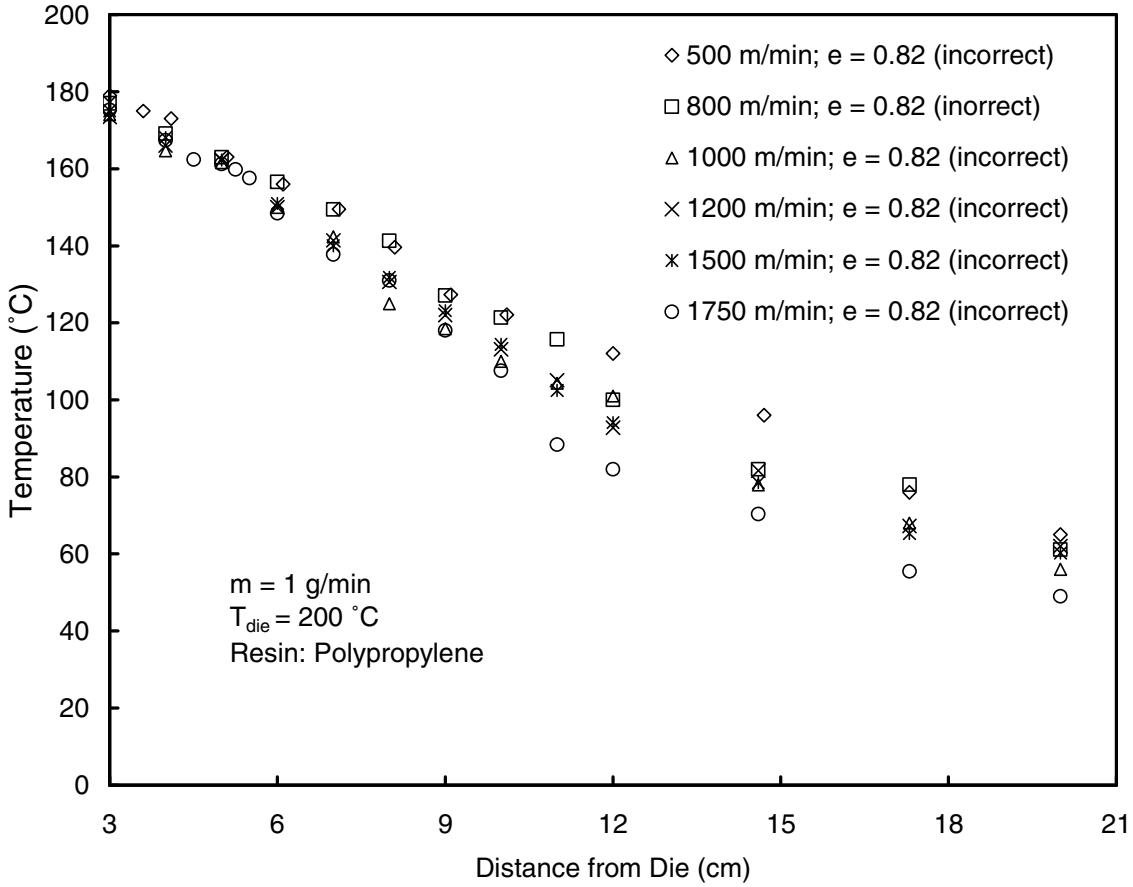

Figure 5. Fiber temperature profile for PP spun at six different spinning speeds from 500 m/min to 1750 m/min. The temperature was measured using a constant emissivity setting of 0.82 (incorrect) in the IR camera. Operating conditions are same as shown in Figure 3.

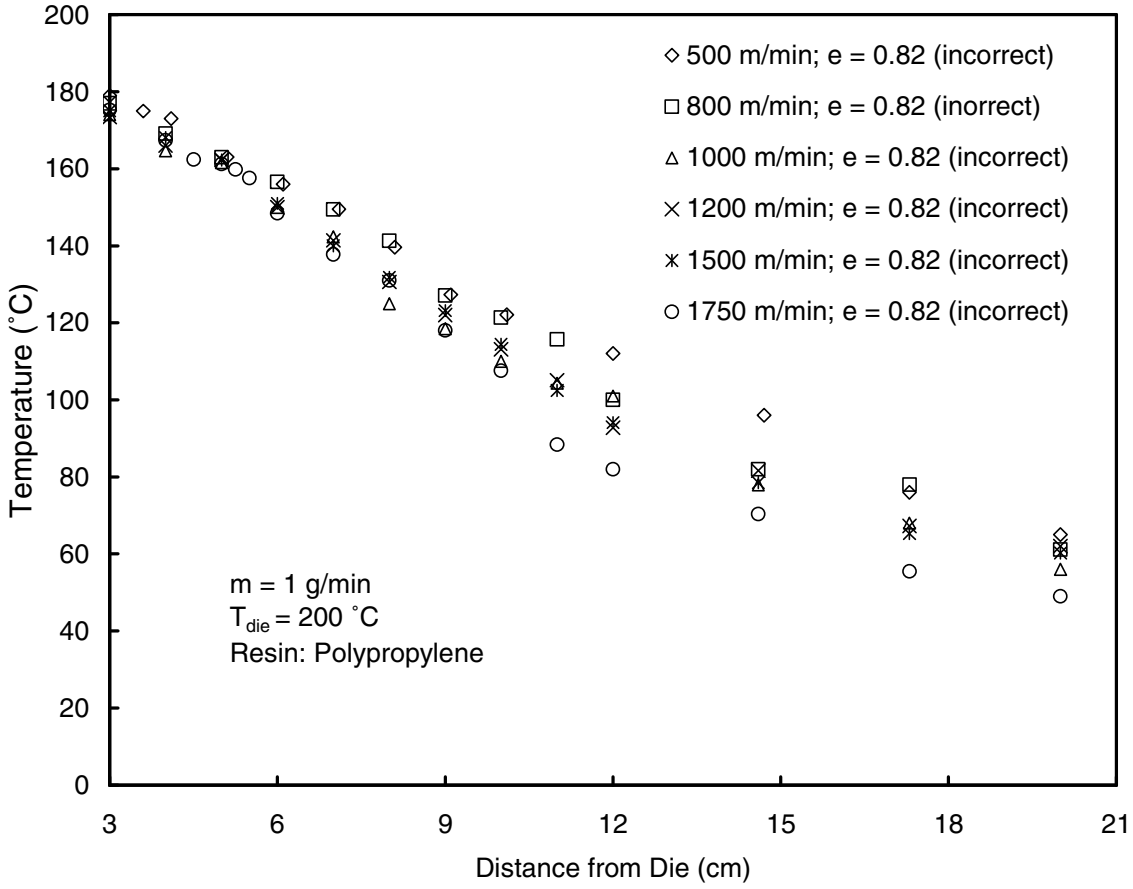

Figure 6. Temperature profile obtained by solving eq 4 for a spinning speed of 500 m/min. The polymer used was Polypropylene. The heat transfer coefficient, h, in eq 4 was calculated using both the Kase and Matsuo correlation and the correlation developed by Marla et al.[27] The experimental data for the same spinning speed is also plotted on the figure.

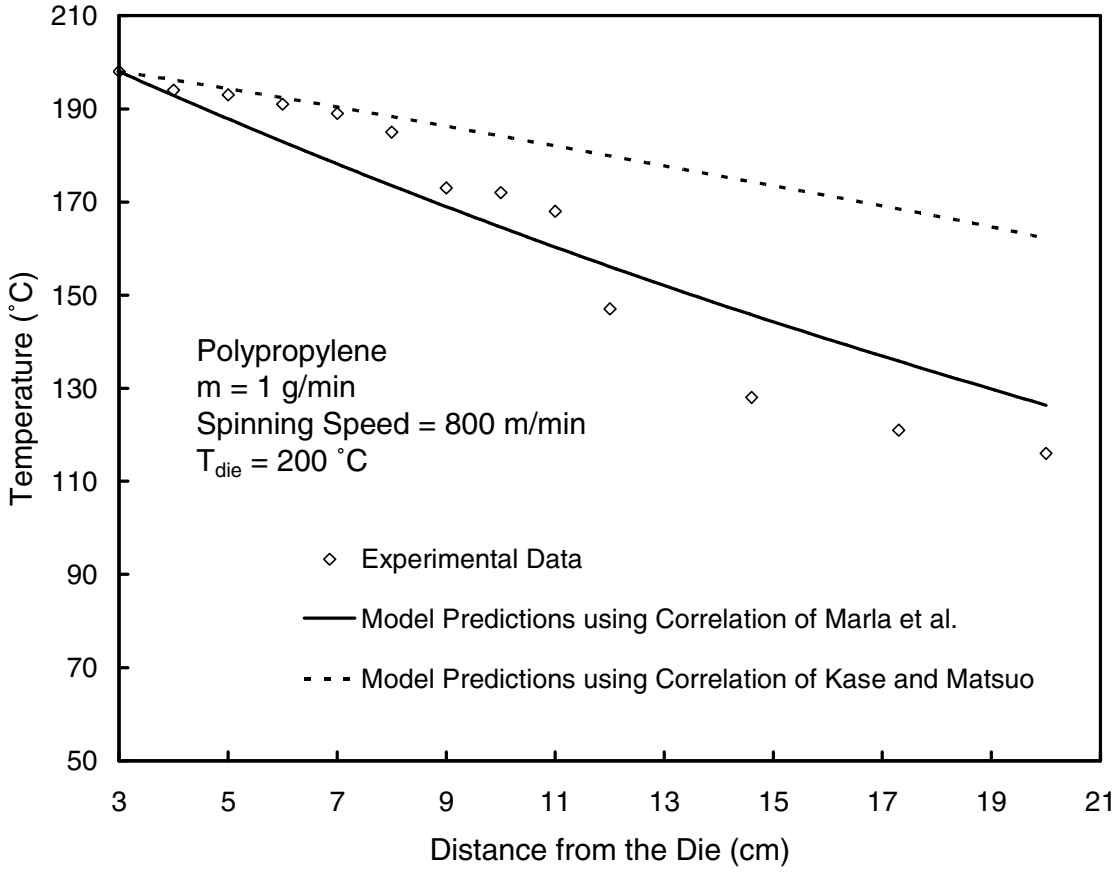

Figure 7. Temperature profile obtained by solving eq 4 for a spinning speed of 800 m/min. The polymer used was Polypropylene. The heat transfer coefficient, h, in eq 4 was calculated using both the Kase and Matsuo correlation and the correlation developed by Marla et al.[27] The experimental data for the same spinning speed is also plotted on the figure.

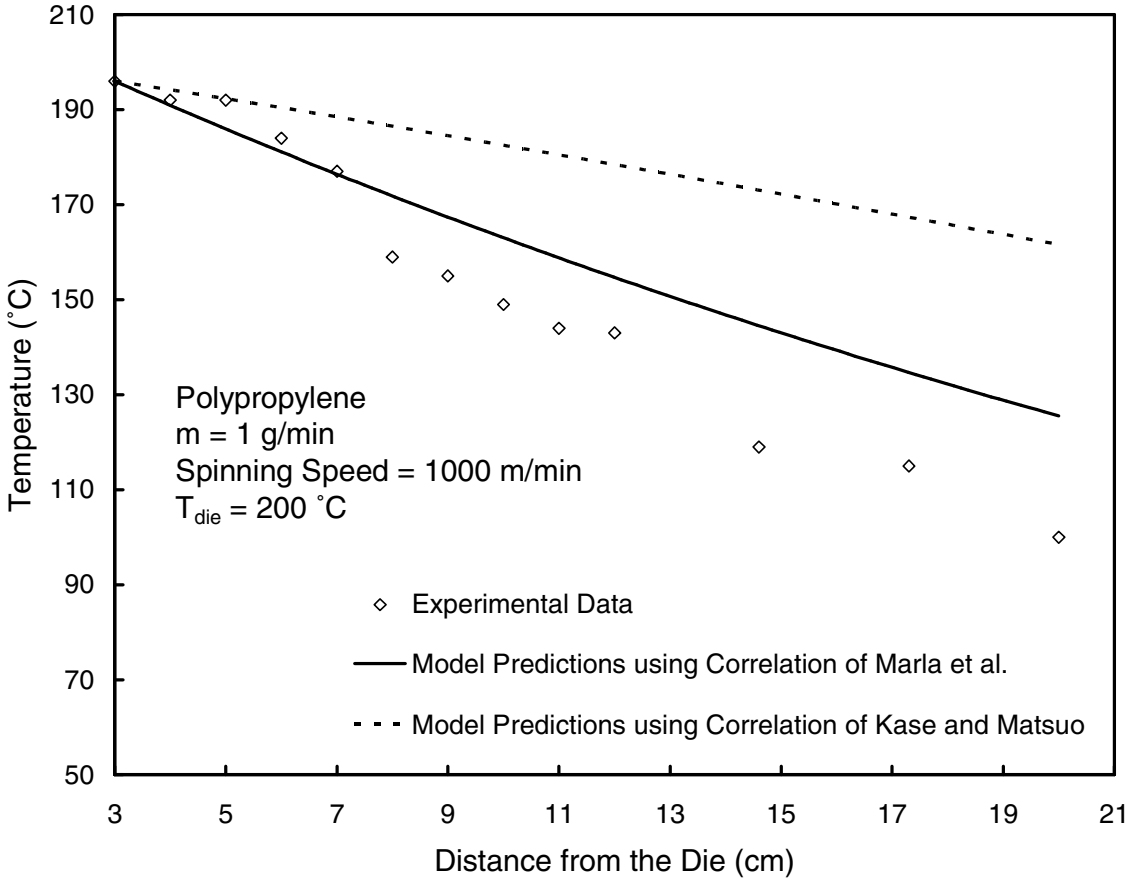

Figure 8. Temperature profile obtained by solving eq 4 for a spinning speed of 1000 m/min. The polymer used was Polypropylene. The heat transfer coefficient, h, in eq 4 was calculated using both the Kase and Matsuo correlation and the correlation developed by Marla et al.[27] The experimental data for the same spinning speed is also plotted on the figure.

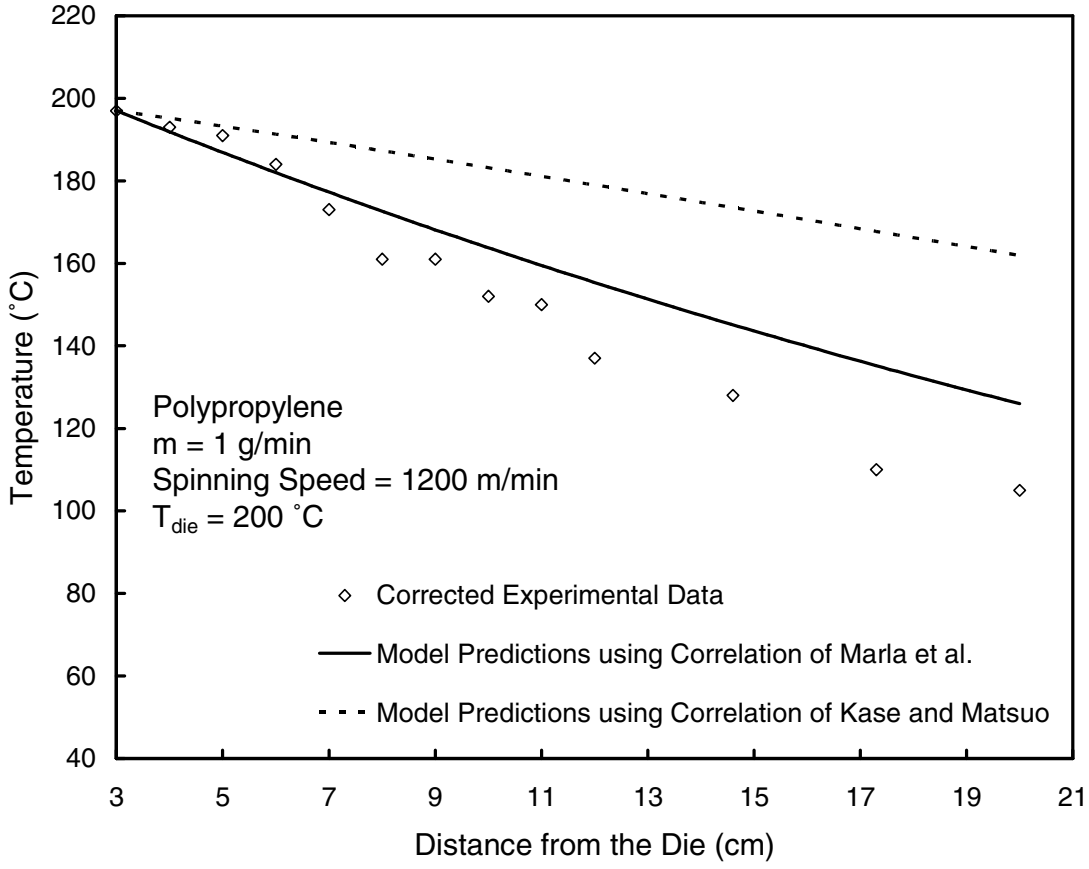

Figure 9. Temperature profile obtained by solving eq 4 for a spinning speed of 1200 m/min. The polymer used was Polypropylene. The heat transfer coefficient, h, in eq 4 was calculated using both the Kase and Matsuo correlation and the correlation developed by Marla et al.[27] The experimental data for the same spinning speed is also plotted on the figure.

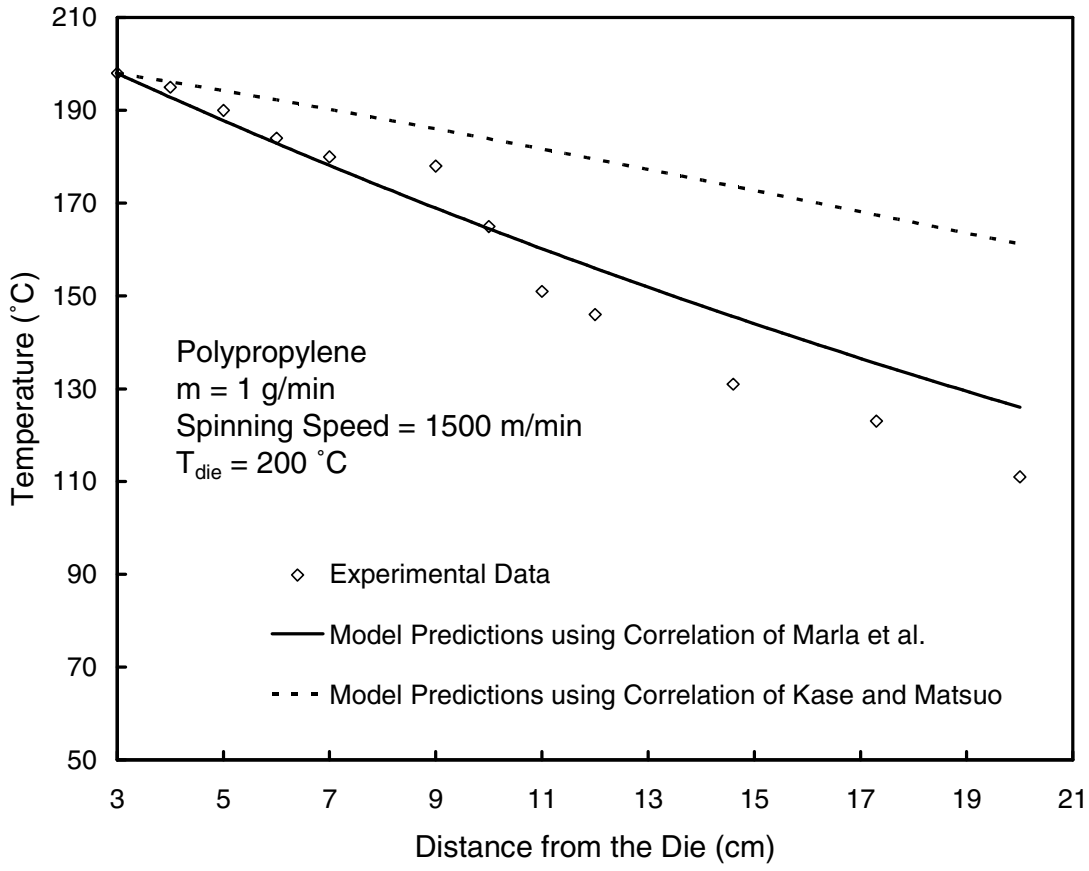

Figure 10. Temperature profile obtained by solving eq 4 for a spinning speed of 1500 m/min. The polymer used was Polypropylene. The heat transfer coefficient, h, in eq 4 was calculated using both the Kase and Matsuo correlation and the correlation developed by Marla et al.[27] The experimental data for the same spinning speed is also plotted on the figure.

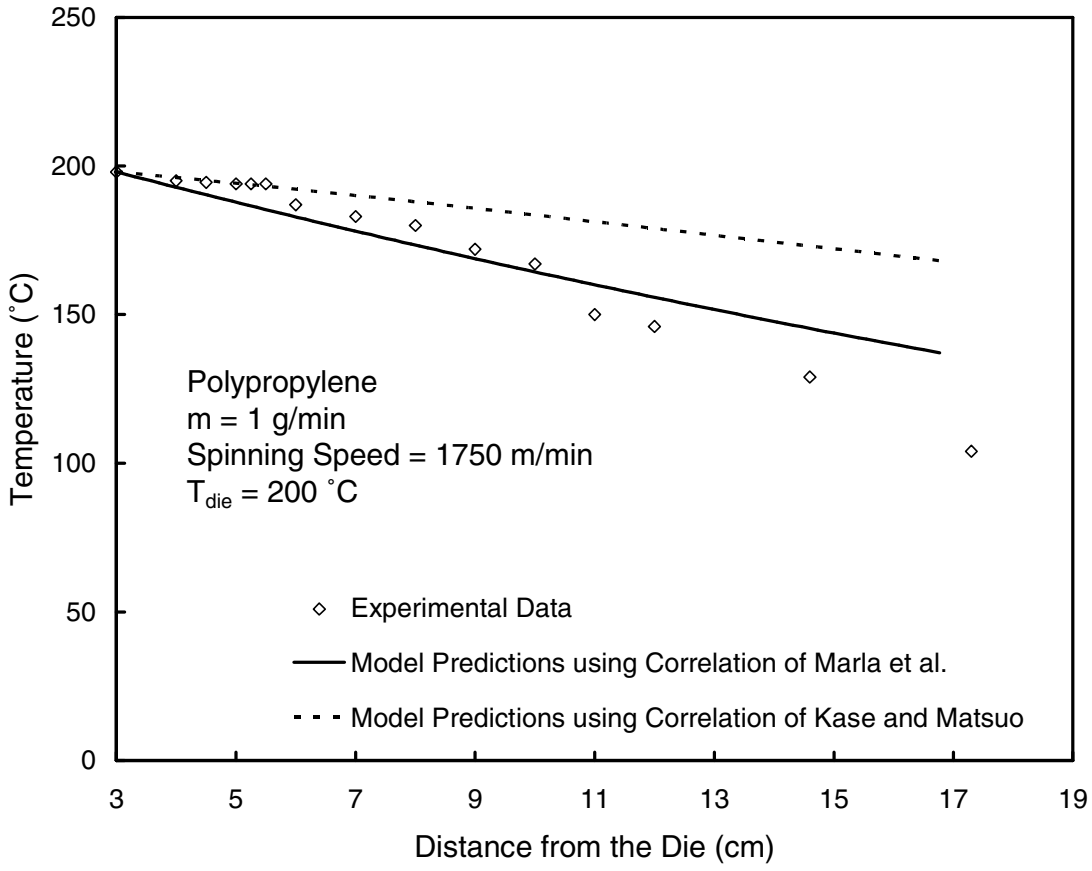

Figure 11. Temperature profile obtained by solving eq 4 for a spinning speed of 1750 m/min. The polymer used was Polypropylene. The heat transfer coefficient, h, in eq 4 was calculated using both the Kase and Matsuo correlation and the correlation developed by Marla et al.[27] The experimental data for the same spinning speed is also plotted on the figure.

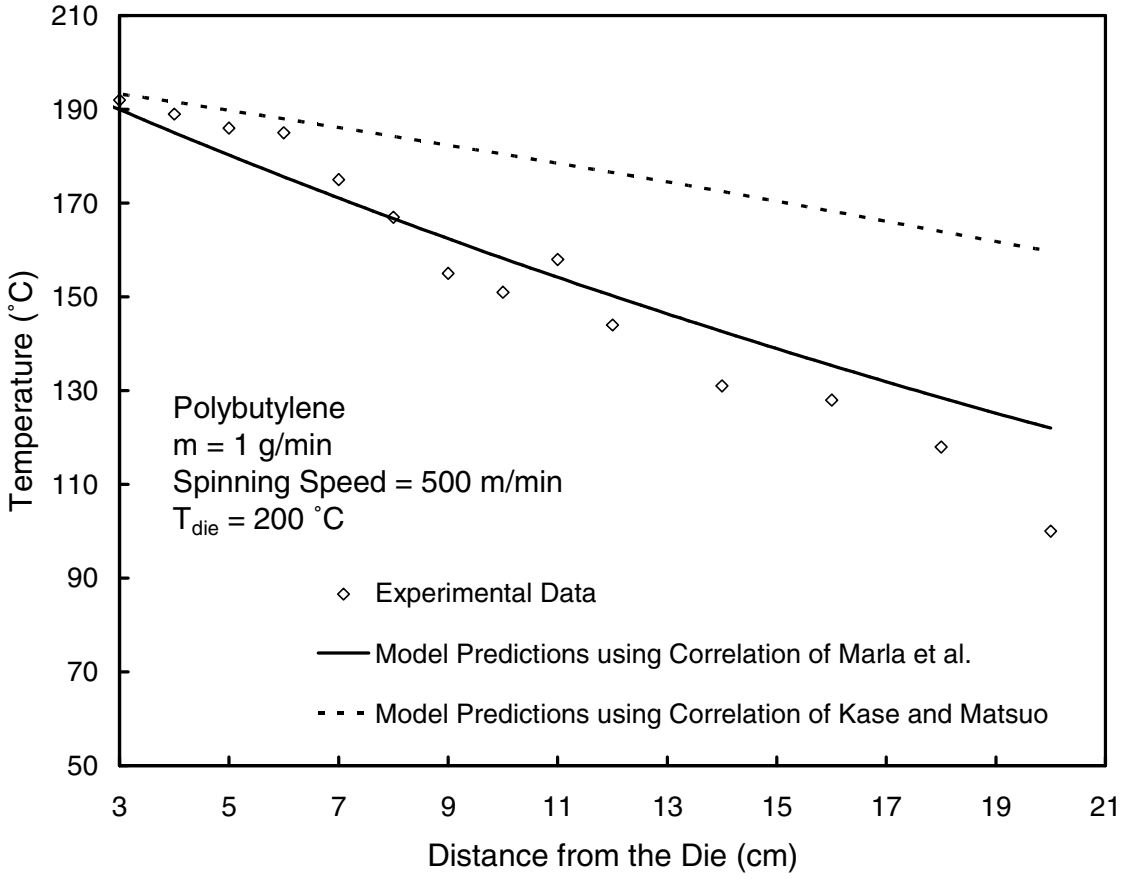

Figure 12. Temperature profile obtained by solving eq 4 for a spinning speed of 500 m/min. The polymer used was Polybutylene. The heat transfer coefficient, h, in eq 4 was calculated using both the Kase and Matsuo correlation and the correlation developed by Marla et al.[27] The experimental data for the same spinning speed is also plotted on the figure.

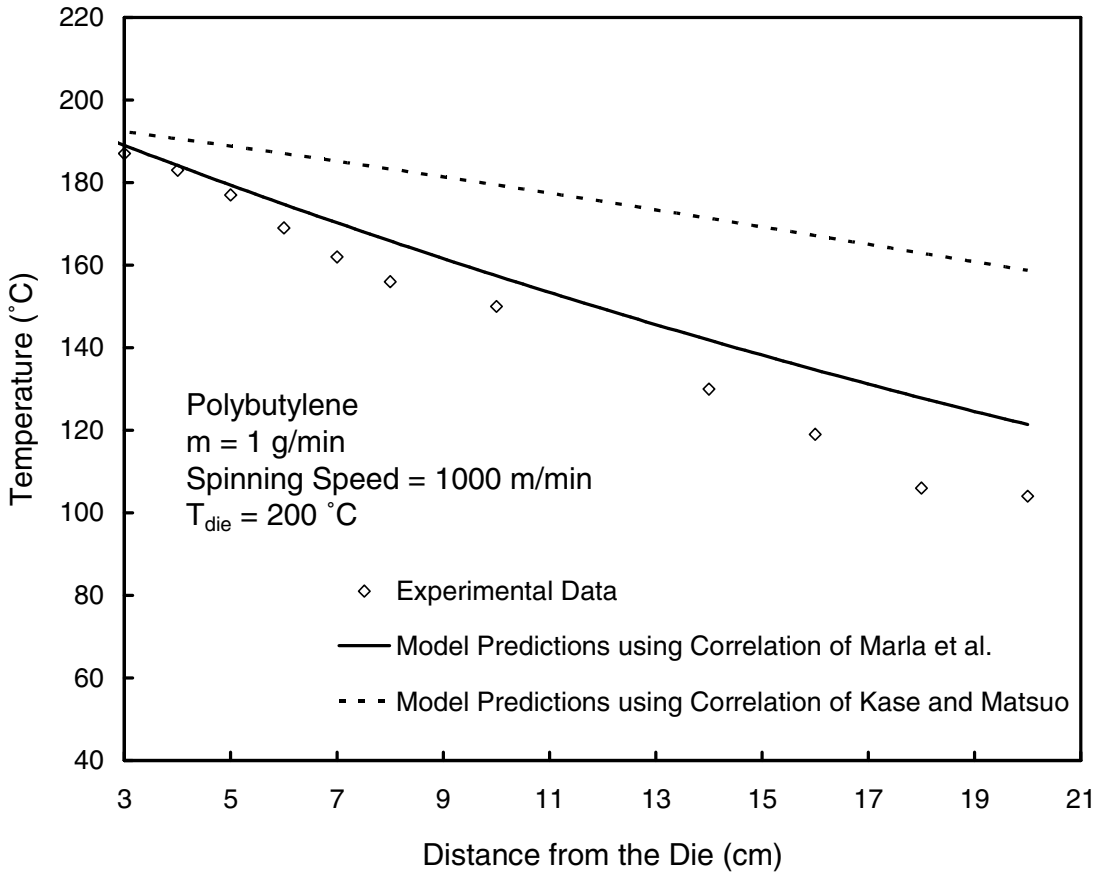

Figure 13. Temperature profile obtained by solving eq 4 for a spinning speed of 1000 m/min. The polymer used was Polybutylene. The heat transfer coefficient, h, in eq 4 was calculated using both the Kase and Matsuo correlation and the correlation developed by Marla et al.[27] The experimental data for the same spinning speed is also plotted on the figure.

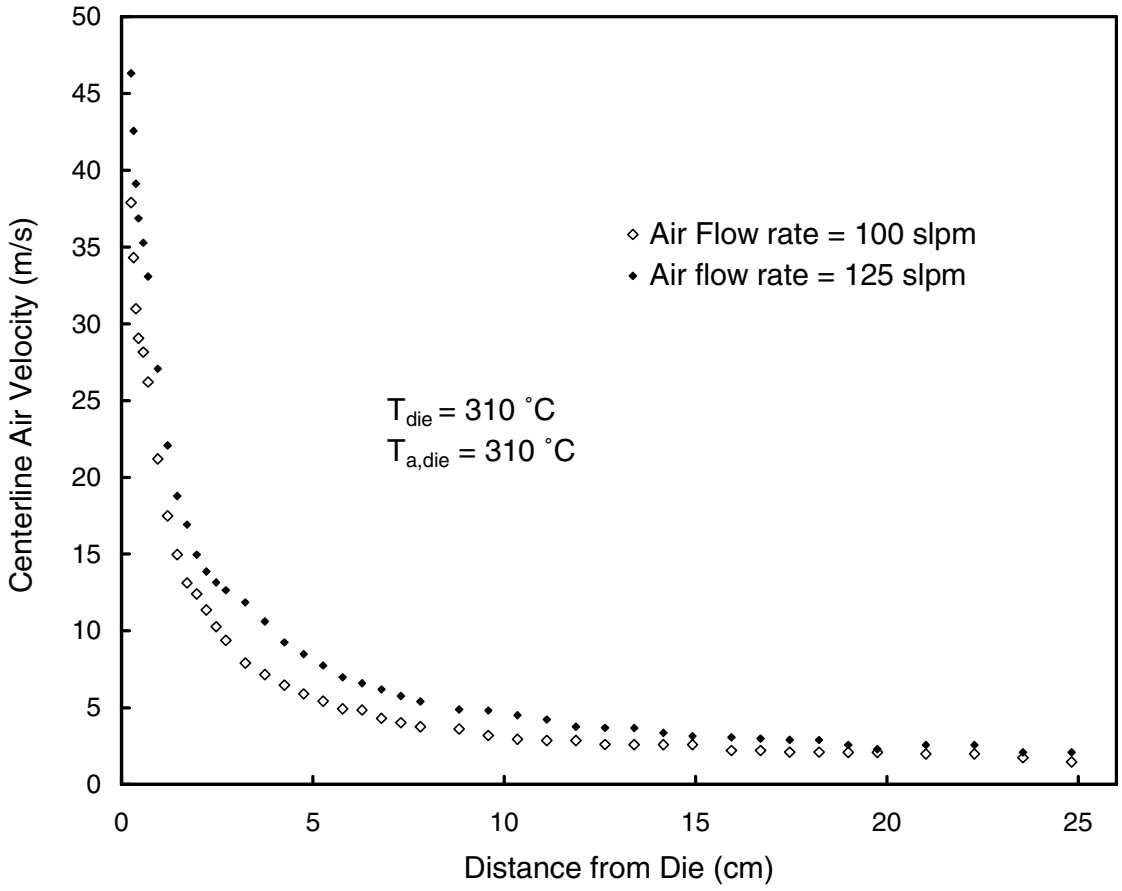

Figure 14. Centerline air velocity for different flowrates below the 60˚ slot die used in the melt blowing experiments. The die slot length was 7.46 cm, the air gap was 0.65 mm , and the die had a single polymer orifice.

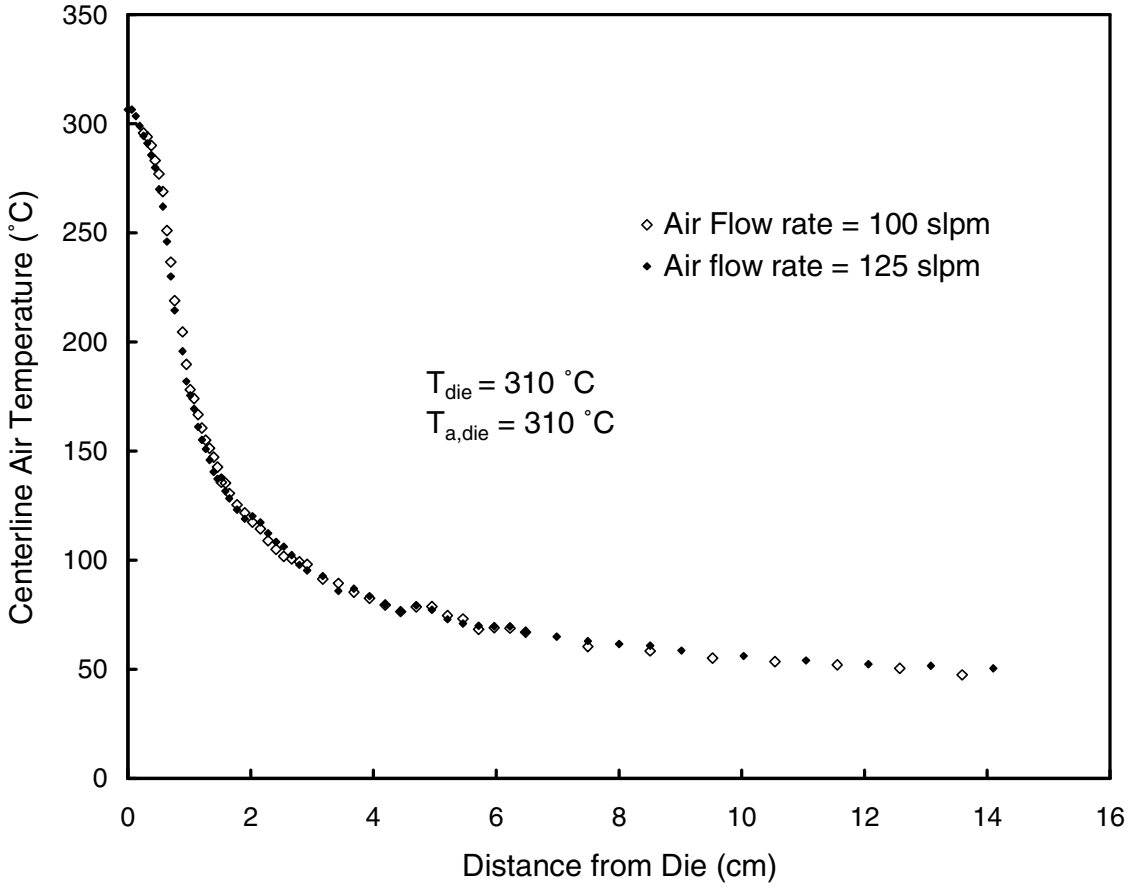

Figure 15. Centerline air temperature for different flowrates below the 60˚ slot die used in the melt blowing experiments. The die slot length was 7.46 cm, the air gap was 0.65 mm , and the die had a single polymer orifice.

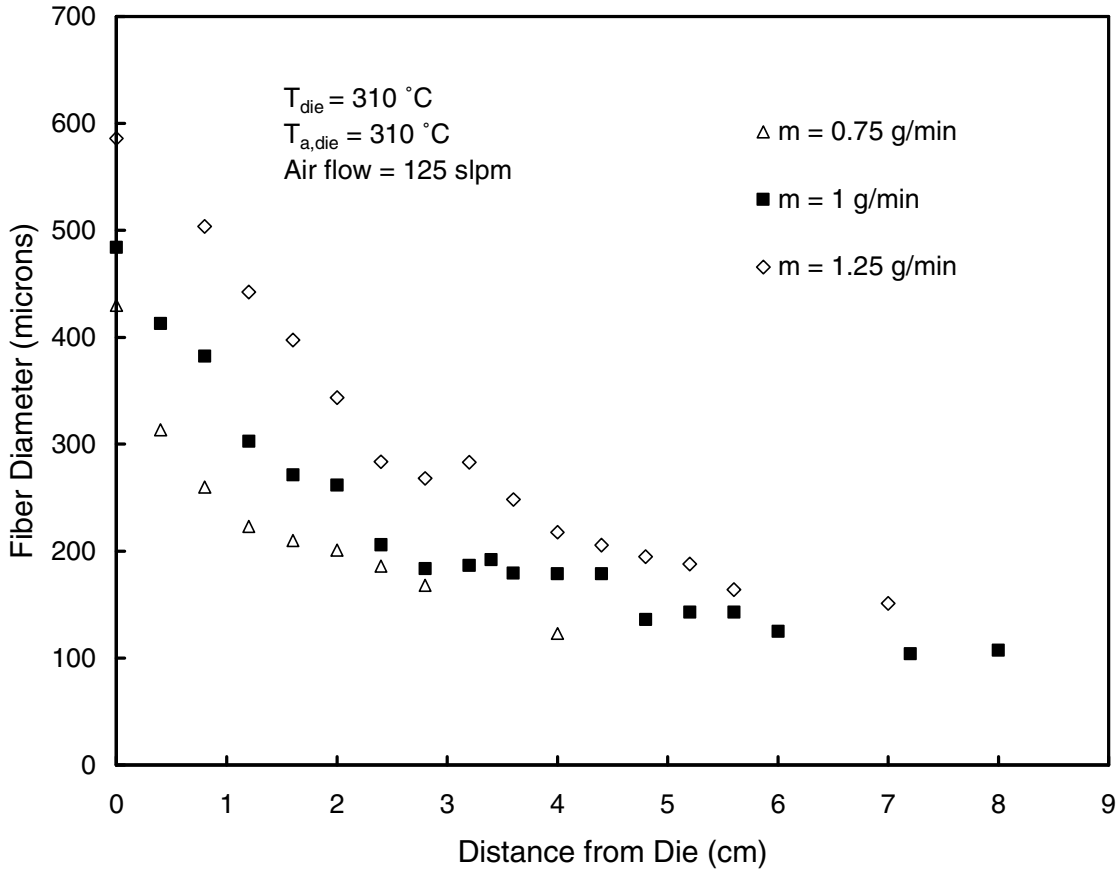

Figure 16. The fiber diameter profile obtained using high speed photography for polymer flowrates of 0.75, 1 and 1.25 g/min.

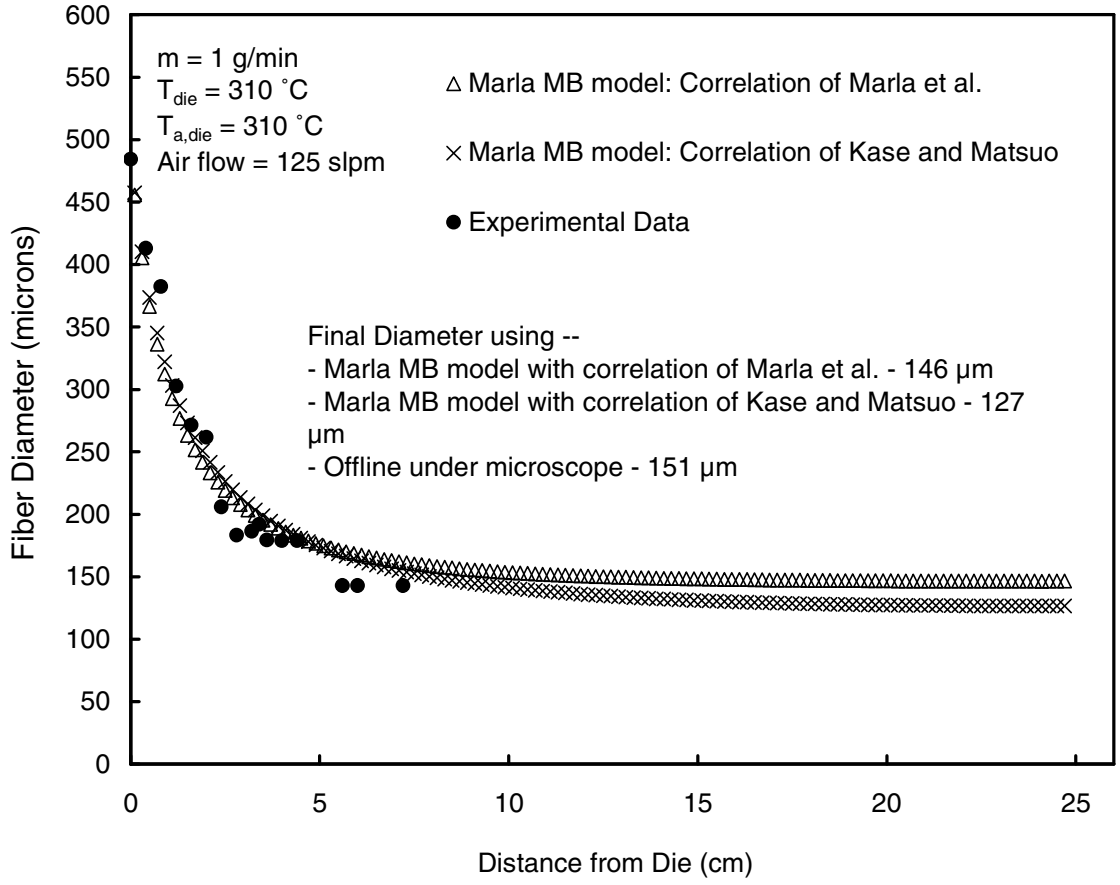

Figure 17. Fiber diameter predictions obtained from the melt blowing model of Marla and Shambaugh[30] when different correlations are used for calculating the heat transfer coefficient. For comparison, the experimental data obtained using high speed photography is also plotted for the operating conditions shown in the figure.

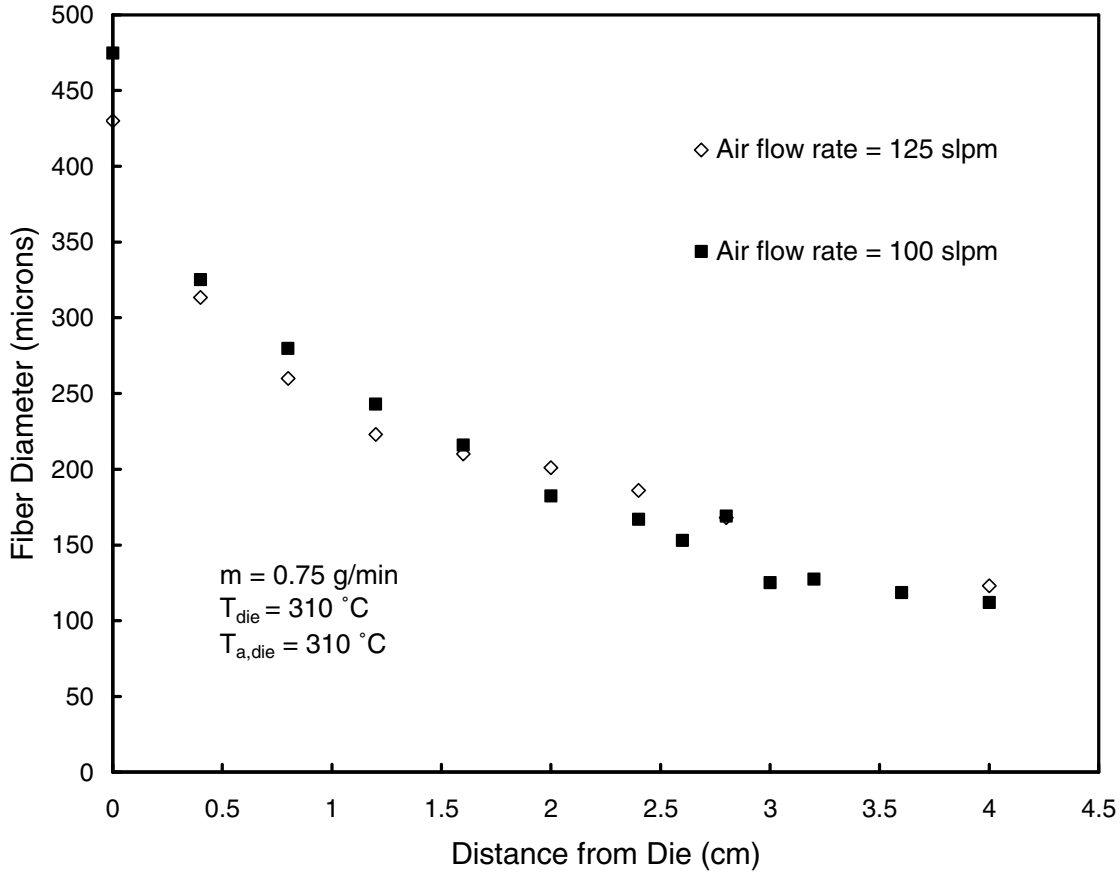

Figure 18. The fiber diameter profile obtained using high speed photography for air flowrates of 100 slpm and 125 slpm.

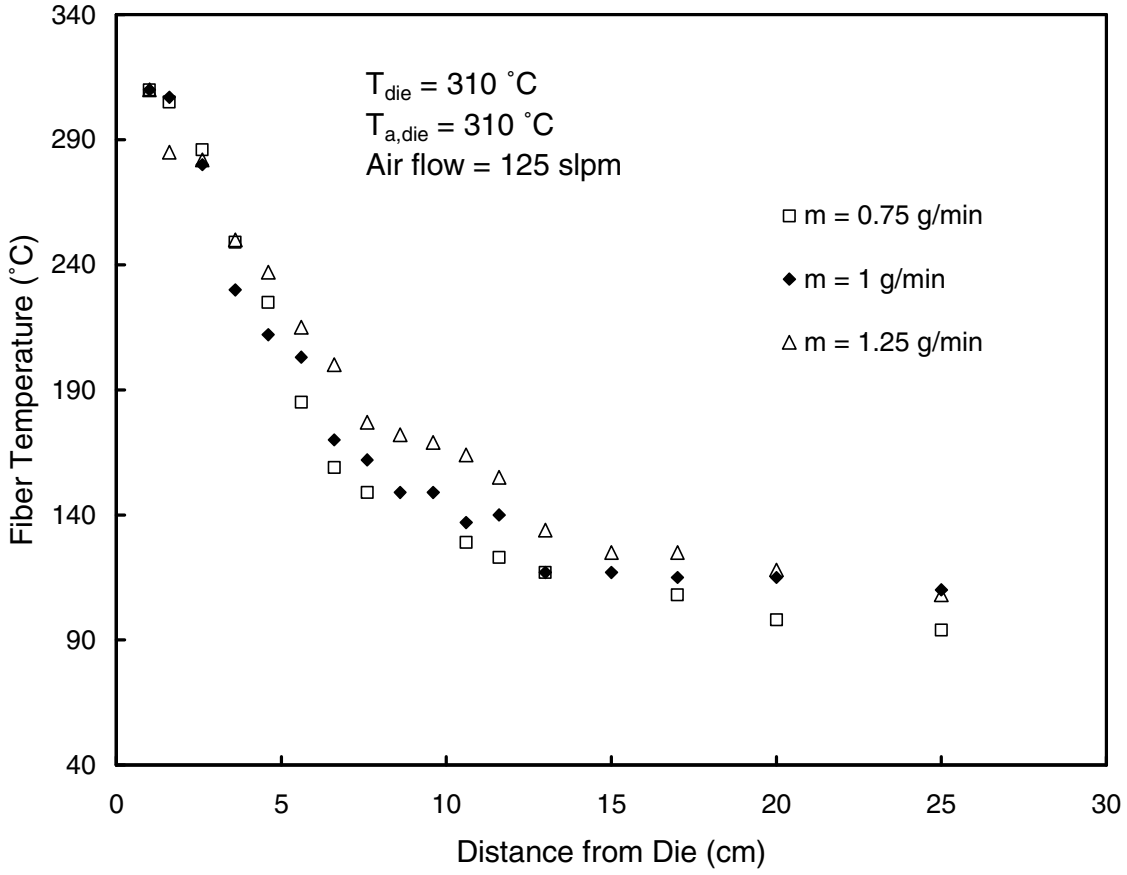

Figure 19. Fiber temperature profile when the mass flowrate of the polymer is varied while keeping all other operating conditions constant.

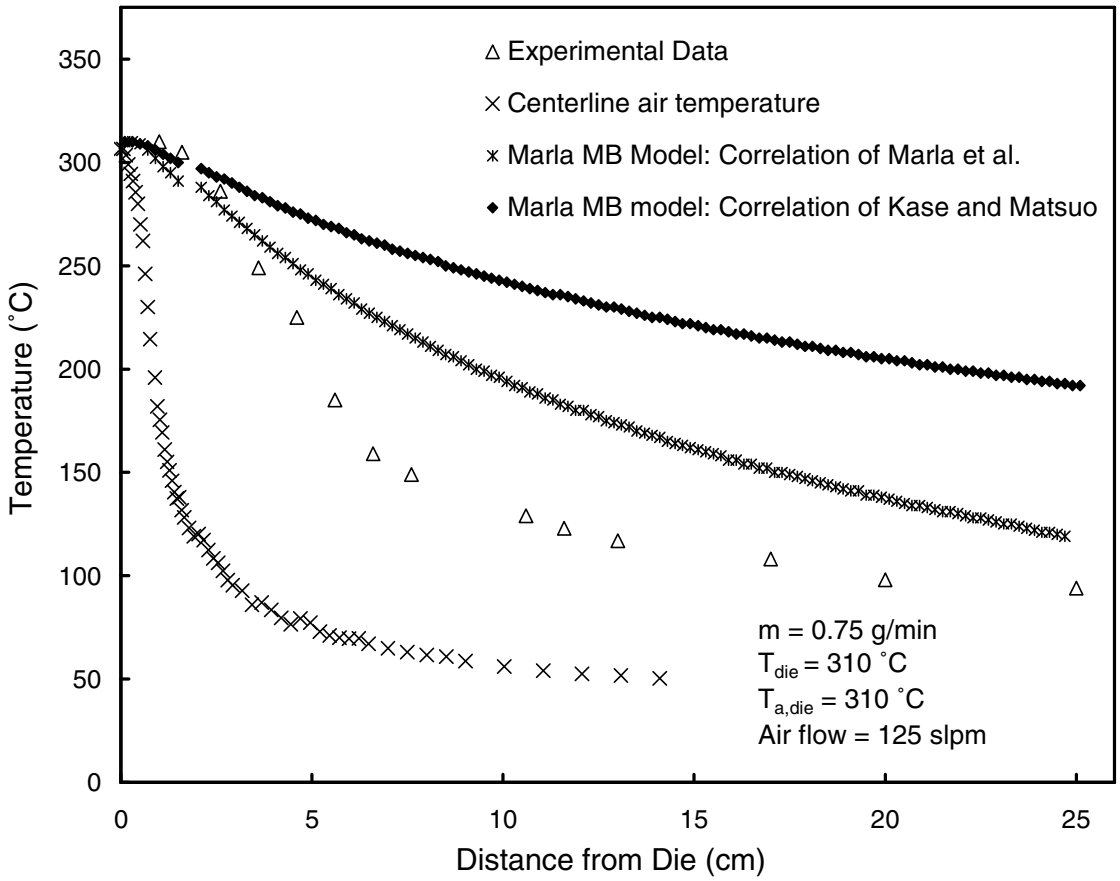

Figure 20. Fiber temperature predictions obtained from the melt blowing model of Marla and Shambaugh[30] when different correlations are used for calculating the heat transfer coefficient. For comparison, the experimental data is also shown. The base operating conditions were used.

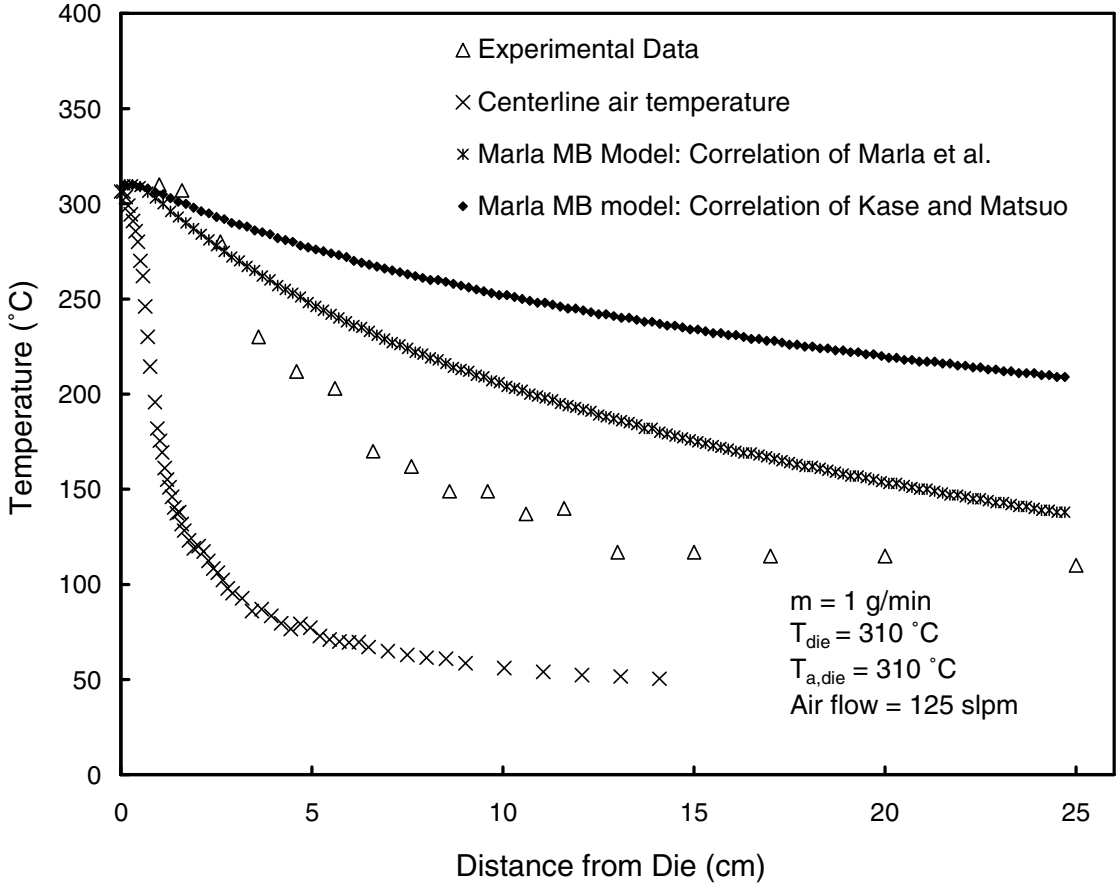

Figure 21. Fiber temperature predictions obtained from the melt blowing model of Marla and Shambaugh[30] when different correlations are used for calculating the heat transfer coefficient. For comparison, the experimental data is also shown. For this experiment, m = 1 g/min and the other conditions are the same as the base operating conditions.

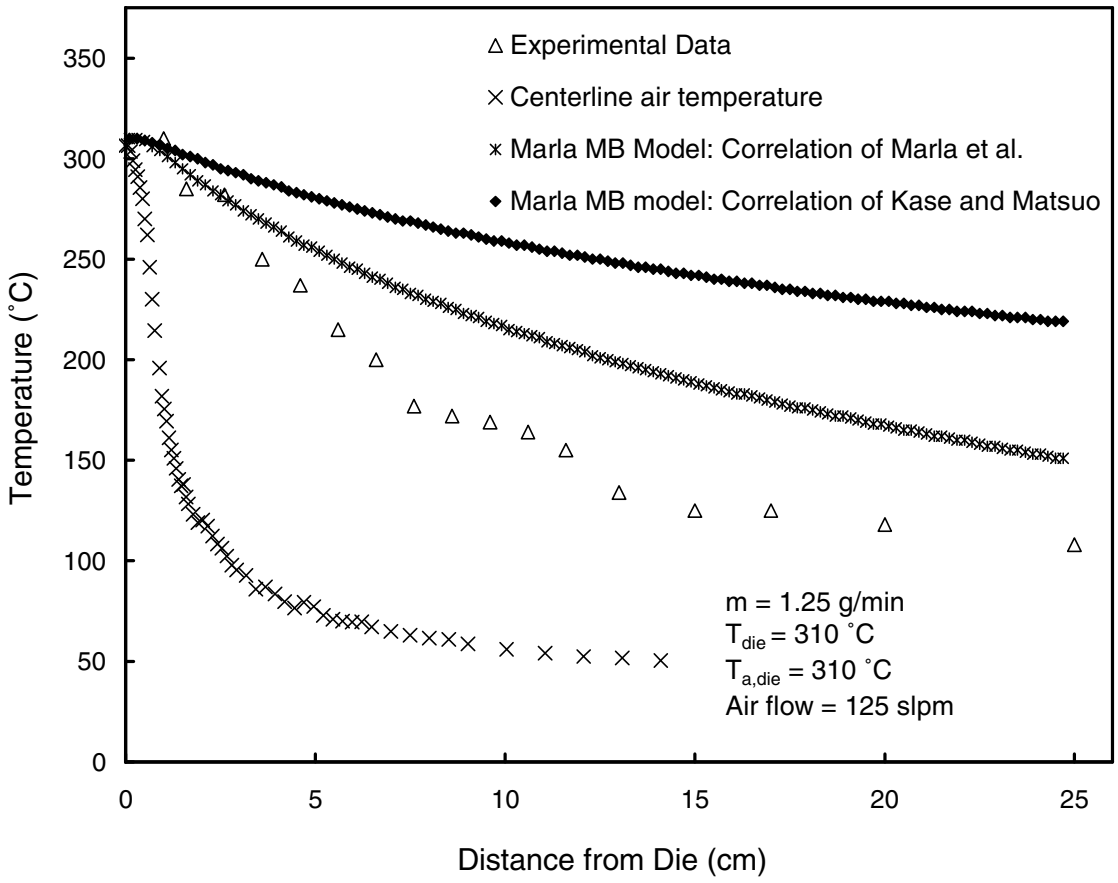

Figure 22. Fiber temperature predictions obtained from the melt blowing model of Marla and Shambaugh[30] when different correlations are used for calculating the heat transfer coefficient. For comparison, the experimental data is also shown. For this experiment, m = 1.25 g/min and the other conditions are the same as the base operating conditions.

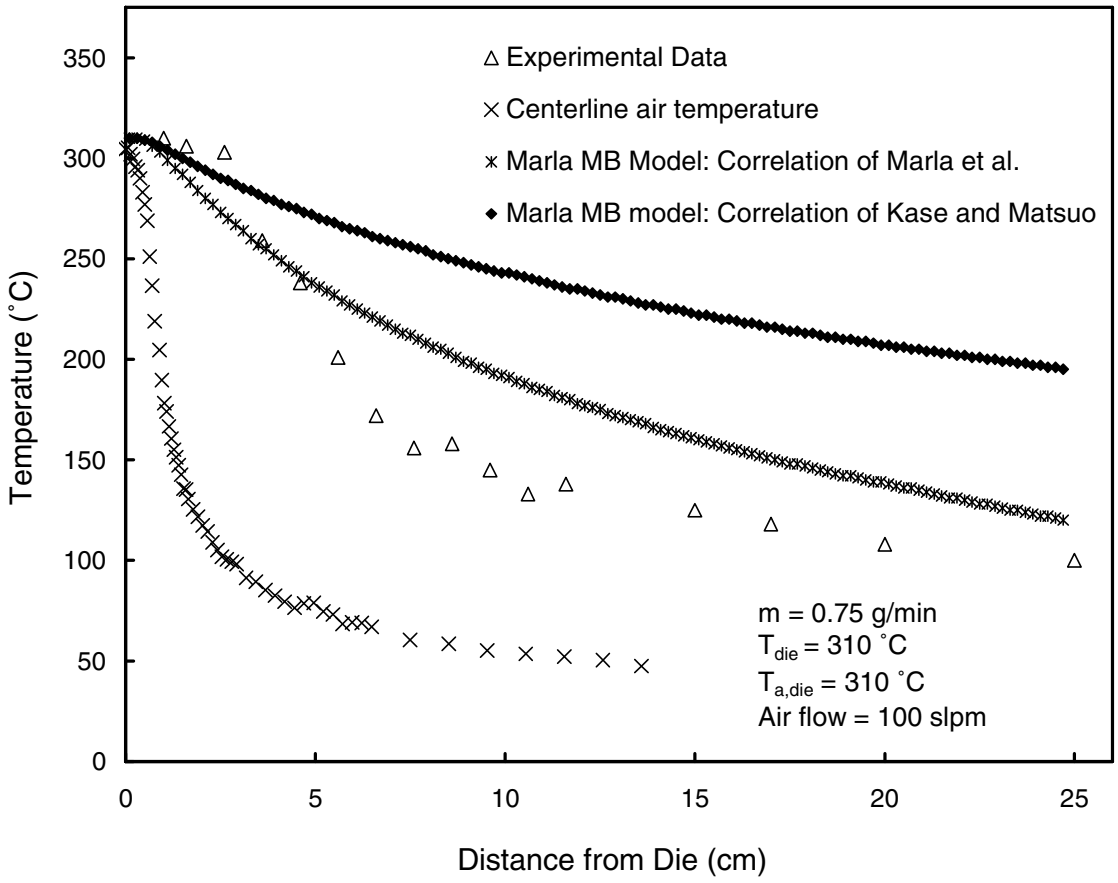

Figure 23. Fiber temperature predictions obtained from the melt blowing model of Marla and Shambaugh[30] when different correlations are used for calculating the heat transfer coefficient. For comparison, the experimental data is also shown. For this experiment, air flowrate = 100 slpm and the other conditions are the same as the base operating conditions.

CHAPTER 8

CONCLUSIONS

8.1 Summary of Work

The present study has made significant advances in the area of melt blowing. A comprehensive model for describing the fiber motion in 3 space was developed. The model predictions were compared with experimental data of fiber diameter and favorable agreement was obtained both with annular dies and slot dies. The model accurately predicted the fiber diameter profile and the final fiber diameter. It was found that the model qualitatively captured the cone-shaped structure characteristic of fiber motion as observed over a period of time using a multiple exposure photograph of the vibrating fiber. The model equations were modified to account for hollowness and a new process involving melt blowing for producing hollow fibers was simulated. The effect of hollowness on the fiber properties such as diameter, temperature stress etc was investigated. Similar to hollow fibers made from melt spinning, it was found that in melt blown hollow fibers, the stress in the fiber increases with increase in the hollowness. It is believed that this increased stress could result in better mechanical properties of melt blown fabrics. In addition, it was also found that beyond a hollowness of 50 %, melt fracture was a possibility as the tremendous stresses in the fiber are on the same order as that reported in literature for melt fracture of polypropylene. The most important result obtained from the simulations was that for a given polymer flowrate, the outer fiber diameter and the vibration frequency increase with increase in the hollowness. This

powerful result paved the way for the experiments with the swirl die in an attempt to address a practical engineering problem. Solid fibers were spun using the swirl die which is used in the deposition of adhesives. The effect of changing the primary operating variables in melt blowing - the mass flowrate of polymer, the air flowrate, the polymer temperature and the air temperature on the diameter and swirl frequency of the fiber was investigated. It was found that fibers spun from the swirl die behave in a manner similar to conventional melt blowing dies as a response to a change in one of the four primary operating variables in melt blowing. The quality of the helical loops formed by the fiber are an indication of the accuracy of the laydown pattern. By constructing a moving belt, the deposition pattern was analyzed and the range of operating conditions were defined over which the highly-defined and well-controlled helical structure was intact. It was found that reducing the mass flowrate of the polymer and increasing the air flowrate result in a decrease in the final fiber diameter and an increase in the rate of swirl formation. Since it is a rule of thumb in adhesive deposition that larger fibers form stronger bonds with the substrate, the challenge was to try and increase line speeds without a reduction in the fiber diameter. By using the results obtained from the modeling of melt blown hollow fibers as the basis for design of experiments, the swirl die was modified such that a lumen fluid was introduced in the polymer orifice to induce hollowness in the fibers. Experiments were carried out where the effect of hollowness on the swirl frequency was investigated. Experimental data showed that for a fixed outer diameter, by inducing hollowness in the fiber up to 40 %, it was possible to obtain a 55 % increase in line speeds or swirl frequency over solid fibers. Since, for a fixed outer

diameter, hollow fibers require less polymer than solid fibers, this was a significant breakthrough in processing adhesives to achieve higher line speeds without compromising on the quality of the swirling pattern and the outer fiber diameter. Thus by using the results of the mathematical model as the basis for subsequent design of experiments with the swirl die, a technique to improve line speeds as much as 55 % with our resin was shown.

Since the melt blowing model overpredicted the fiber temperature compared to experimental data when the heat transfer correlation of Kase and Matsuo[1] was used in the model, an experimental campaign to develop an accurate heat transfer correlation was started. The first step was the calibration of the Infrared (IR) camera and a test station was built to account for the error involved in temperature measurement of small objects due to the limitation in the spatial resolution of the IR camera. It was found that the emissivity of a polymer fiber was dependent on its diameter. A universal response curve or slit response factor curve (SRF) was developed to quantify the error involved while measuring the temperature of small objects. By observing the transient heating of a polymer fiber suddenly introduced in a heated flow field of air with plug flow characteristics, the heat transfer coefficient was measured for different Reynolds numbers. These data were then converted into Nusselt – Reynolds number plots for both heat transfer from polymer filaments to air in cross flow and parallel flow. The results from the present study for the case of heat transfer from filaments to air in cross flow compared favorably with the well-established results of McAdams.[2] The correlation developed for heat transfer from polymer filaments to air in parallel flow was used in the

melt spinning and melt blowing models. On-line measurements of fiber diameter and fiber temperature in melt spinning and melt blowing were made using high-speed flash photography and an IR camera respectively. These measurements were compared with the predictions of the melt spinning and melt blowing models obtained by using the heat transfer correlation developed above. For melt spinning, excellent agreement was found between experimentally measured fiber temperature and the model predictions. This was observed over several spinning speeds with both polypropylene and polybutylene. For melt blowing, the choice of heat transfer correlation did not significantly affect the diameter profile and the model predictions using the both the correlation developed in the present study and that of Kase and Matsuo[1] accurately predicted the fiber diameter profile. However, the temperature profile predicted by the melt blowing model using the correlation of Kase and Matsuo severely overpredicted the temperature compared to experimental data. On the other hand that the model predictions using the correlation developed in the present study compared better with experimental data. Thus, using modeling and experiments, an accurate heat transfer correlation for both melt spinning and melt blowing was developed. Since the predictions of the melt blowing model depends on the accuracy of the empirical correlations used to estimate the transport properties, this correlation greatly improved the accuracy of the model.

8.2 Recommended Directions for Future Work

The model developed in the present study was used to simulate novel scenarios and the model predictions were used as the basis for subsequent design of experiments. Furthermore, the accuracy of the model predictions was improved by developing a new heat transfer correlation for heat transfer from fine filaments to air in parallel flow. With this powerful model in place, there are several exciting possibilities one could investigate. While the present study involved spinning hollow fibers using the swirl die, it would be interesting to observe the effect of hollowness on fibers made from the slot die. Since hollow fibers result in a higher frequency of vibration, this would mean that hollow fibers made from a slot die would increase the laydown frequency and result in increased rates of production. Recently, a rapid framing camera capable of capturing images at 150,000 frames/s was acquired and this could be a useful tool in analyzing fiber motion both near the melt blowing die and on the collection screen. Using this camera, the fiber vibration frequency, amplitude of vibration and the lateral velocity of the fiber can be measured. These results can then be compared with the predictions of the mathematical model developed in this work. This rapid framing camera can also be used to analyze the laydown pattern of fibers made from a slot die. Since the laydown pattern from slot dies is random, it would be interesting to see if statistics can be used to describe the fiber laydown pattern.[3] The melt blowing model developed in this study analyzes fibers only up to the stop point which, depending on the operating conditions, is typically 8-15 cm below the die. However, the collection screen may sometimes be placed much below this distance from the die. The rapid framing camera can be used to study the fiber motion

from the stop point to the collection screen. Such a study may be helpful in extending the present model to describe the fiber motion from the die to the collection screen.

Krutka et al.[4-6] used computational fluid dynamics (CFD) to investigate the air flow field below melt blowing dies. However, these simulations were performed in the absence of the polymer in the flow field. The 3D model developed in this study could be used as input to the CFD simulations to investigate the effect of the presence of the fiber in the air flow field. Such a study could lead to a better understanding of the air flow pattern below melt blowing dies and eventually into more efficient melt blowing dies.

References

(1) Kase, S.; Matsuo, T. Studies on Melt Spinning. I. Fundamental Equations on the Dynamics of Melt Spinning. *J. Polym. Sci., Part A*. **1965,** *3*, 2511-2554.

(2) McAdams, W. H. *Heat Transmission*, 3rd ed.; Kirkpatrick S. D., Ed; McGraw-Hill Series in Chemical Engineering; McGraw-Hill Book Company, Inc.: New York, NY, 1954; pp 258-260

(3) Chhabra, R.; Shambaugh, R. L. Experimental Measurements of Fiber Threadline Vibrations in the Melt-Blowing Process. *Ind. Eng. Chem. Res.* **1996**, *35*(11), 4366-4374.

(4) Krutka, K. M.; Shambaugh, R. L.; Papavassiliou, D. V. Analysis of a Melt-Blowing Die: Comparison of CFD and Experiments. *Ind. Eng. Chem. Res.* **2002,** *41*(20), 5125-5138.

(5) Krutka, K. M.; Shambaugh, R. L.; Papavassiliou, D. V. Effects of Die Geometry on the Flow Field of the Melt-Blowing Process. *Ind. Eng. Chem. Res.* **2003,** *42*(22), 5541-5553.

(6) Krutka, K. M.; Shambaugh, R. L.; Papavassiliou, D. V. Effects of Temperature and Geometry on the Flow Field of the Melt Blowing Process. *Ind. Eng. Chem. Res.* **2004,** *43*(15), 4199-4210.